University of Copenhagen

Doctoral Thesis

An ATLAS Search for Sterile Neutrinos

Fabian A.J. Thiele

This thesis has been supervised by:

Assoc. Prof. Stefania Xella

January 10th, 2019

This thesis has been submitted to the PhD School of The Faculty of Science, University of Copenhagen.

KØBENHAVNS UNIVERSITET

Abstract

Several outstanding problems currently not addressed by the Standard Model (SM) of particle physics including neutrino masses, matter-antimatter asymmetry and dark matter could be succesfully addressed by the addition of right-handed neutrinos with Majorana masses below the electroweak scale.

In this thesis leptonic decays of the W boson produced in $36.1\,\text{fb}^{-1}$ of $\sqrt{s} = 13\,\text{TeV}$ proton-proton collisions at the Large Hadron Collider (LHC) are searched for Heavy Neutral Leptons (HNLs). The HNLs are produced through mixing with muon or electron neutrinos, and detected in the ATLAS detector through their leptonic decays. The HNL Majorana nature is used to find the smoking-gun signature of three leptons $\ell^{\pm}\ell^{\pm}\ell'^{\pm}$, $\ell, \ell' = e, \mu$ otherwise not observed in decays of SM particles. This signature allows a search for HNLs in mass ranges of 5 to 50 GeV that decay close to the beamline.

This search sets best constraints on the mixing angle in the HNL mass range 15 to 42 GeV for the mixing of HNLs with muon neutrinos and for 25 to 50 GeV for the mixing with electron neutrinos and is the first result in the mass range 5 to 50 GeV using data measured by ATLAS.

Synopsis

Flere udestående problemer, som i øjeblikket ikke er løst af partikelfysikkens Standardmodellen (SM), herunder masserne af neutrinoer, stof-antistof asymmetri og mørkt stof, kan muligvis adresseres med success ved at indføre en højre-håndet neutrino med en Majorana masse under den elektrosvage skala.

I denne afhandling søges tunge neutrale leptoner (HNLs) igennem leptoniske henfald af W-bosonen produceret i 36.1 fb^{-1} proton-proton kollisioner ved $\sqrt{s} = 13\,\text{TeV}$ på LHC. HNLs bliver produceret gennem blandingen af myon- og elektron-neutrinoer, og bliver opdaget i ATLAS detektoren via leptoniske henfald. HNL Majoranas natur bliver benyttet til at finde den smoking gun signatur med tre leptoner $\ell^{\pm}\ell^{\pm}\ell'^{\pm}$, $\ell, \ell' = e, \mu$, som ellers ikke ville blive observeret i henfald af Standardmodellens partikler. Denne signatur tillader at søge efter HNLs i en masse interval mellem 5 og 50 GeV og som henfalder tæt på beamline.

Denne søgning giver de bedste begrænsninger på blandings vinklen i HNL masse intervallen mellem 15 og 42 GeV for blandingen af HNLs med myon-neutrinoer og mellem 25 og 50 GeV for blandingen med elektron-neutrinoer; disse resultater er de første i masse intervallet mellem 5 og 50 GeV med data målt i ATLAS.

Acknowledgements

This thesis has been my life for the last three years, and although I have worked hard on making this search for neutrinos my very own it is undeniably clear that a lot of work, knowledge and support from so many others have been an essential part of it.

First and foremost I would like to thank my supervisor Stefania Xella for her constant trust in me, the stimulating discussions and her indespensible advise. Further I would like to thank Hass AbouZeid for his in-depth reading of my thesis and the highly valuable feedback. This extends to Christian Bourjau, and Rosanna Ignazzi who did not only give suggestions but also helped me with the danish abstract.

I would also like to acknowledge ATLAS as well as LHC and everyone that contributes constantly and tirelessly in helping them run and function.

My work at the Niels Bohr Institute and CERN would not have been possible without all the people supporting, motivating and sharing their life with me. I choose to not list them here but if you, dear Reader, came here looking and wondering whether you would be on that list then you most certainly are, and I hope you know I am grateful to you. The single exception I would like to make for my parents Monika and Jürgen who I owe everything to. To all my friends, near and far, the ones I saw daily and the ones I've barely seen during this time: I am incredibly grateful and proud to be a part of your life. Thank you for the constant and neverending support, especially in my times of need.

This has been an adventure, and thanks to all of you, I would do it all over again!

Abstract thinking, which throughout the ages has been one of the most powerful of man's aids in lifting the veil that shrouds the laws of Nature from the eyes of the uninitiated observer, has proved of the utmost importance for enabling the insight into the structure of atoms so obtained to be applied practically in elucidating the properties of those elements that are immediately accessible to our perceptions.

– Niels Henrik David Bohr
December 10, 1922
Speech at the Nobel Banquet in Stockholm [1]

Contents

Chapter 1.

Introduction

Neutrinos, first postulated in 1930 as a possible explanation to the continuous energy spectra in beta decay [2], and discovered in 1956 [3] were long thought to have zero mass and as such included as massless particles in the SM. Observations of neutrino oscillations [4–6] have shown strong evidence of a very small but non-zero neutrino mass. In fact, the masses are much smaller than the remaining particles of the SM [7] by at least six orders of magnitude [8].

While fermions obtain mass in the SM by Yukawa interactions with the Higg's field, the masses couple left- and right-handed chirality states of the particles. Experiments [9, 10] have shown though that neutrinos are exclusively left-handed while anti-neutrinos have right-handed chirality.

The so called *see-saw* mechanism [11] provides an elegant solution for the existence of neutrino masses and their relatively small value by including a heavy right handed neutrino HNL with a large Majorana mass. The size of active neutrino[1] mass is then balanced by the large mass of the HNL while the latter does not practically contribute to the weak interaction. An inclusion of three HNLs would also reinstate a natural symmetry in the fermion sector as all other fermions already exist in both chirality states.

Models like the Neutrino Minimal Standard Model (νMSM) [12] form a natural extension of the SM by introducing three HNLs with masses smaller than the electroweak scale and which satisfy the conditions for the see-saw mechanism. By careful choice of parameters, the νMSM offers a possible explanation to neutrino oscillations as well as baryon asymmetry and provides a dark matter candidate.

Several experimental signatures are suggested to probe HNL existence [13, 14], usually in dependence on lifetime and mass of the HNL. An interesting candidate within the νMSM is of GeV mass scale and within reach of LHC experiments. With the large amount of data collected e.g. by the A Toroidal LHC ApparatuS (ATLAS) experiment in the second run of the LHC, excellent use can be made of the experiment as a general purpose detector to search for signatures of HNLs.

The viability of collider experiment searches is strongly dependent on the HNL lifetime. For HNLs the lifetime depends only on mass and the mixing angle where generally HNLs of low masses are longer lived (compare Figure 4.2). To reduce the large amounts of SM background processes, powerful discriminants are needed. While for longer lifetimes at low masses HNLs could be found by searching for displaced decay vertices; current exclusion limits in the 5 to 80 GeV range set by DELPHI and CMS experiments are in the short-lived range with little to no observable decay length.

The Majorana nature of the HNLs offers a convenient *smoking-gun* signature as it allows the search for three leptons with special charge requirements only allowed by decay of Majorana particles [15]. The analysis presented here uses this *prompt trilepton* signature with no opposite-sign and same-flavor lepton pairs to search for HNL mixing with muon and electron neutrinos in data measured by the ATLAS experiment in 2015 and 2016.

[1] *active* neutrinos participate in the weak interaction in contrast to HNLs which are also called *sterile* neutrinos

Chapter 2.

Theory

Why does water not admit its bulk of every kind of gas alike? - This question I have duly considered, and though I am not yet able to satisfy myself completely, I am nearly persuaded that the circumstance depends upon the weight and number of the ultimate particles *of the several gases*

— John Dalton, 1805 [16]

In order to include neutrino masses and their small value, in comparison with other fermions, in the SM one approach introduces *heavy* neutral leptons which *see-saw* the small neutrino masses. Models like the νMSM propose three HNLs, two of which would be in reach for accelerator experiments like ATLAS with which this search is conducted. This chapter introduces HNLs as an extension to the SM and points towards an interesting parameter space for a prompt lepton search in which HNLs of GeV scale could be discovered or excluded experimentally.

2.1. Standard Model of particle physics

What matter is made of and whether there indeed exist *fundamental* particles that are the constituents of every*thing* is a question that has been revisited over centuries and dates back to at least Democritus in the 5th century BC. Comprehensive experiments proving the existence of electrons and further fundamental particles unveiled a variety of particles that are considered nowadays fundamental in the energy scales reachable. Using large particle accelerators to supply the energy needed to create these particles, humans are striving for a more complete understanding of what the universe is made of. The findings of this search are summarized in a theoretical framework commonly referred to as the *standard model of particle physics*.

The SM is hugely successful in describing a wide variety of phenomena based on the interactions between particles that have been discovered and even predicted the existence of new particles. With the discovery of the Higgs boson by the Compact Muon Solenoid (CMS) and ATLAS experiments in 2012 [17, 18]

a major milestone was achieved and an essential part of the SM experimentally confirmed.

It is often visualized as in Figure 2.1 and includes three groups of particles: quarks, leptons and gauge bosons. The SM constituents are in the following referred to as *elementary particles* or simply *particles*.

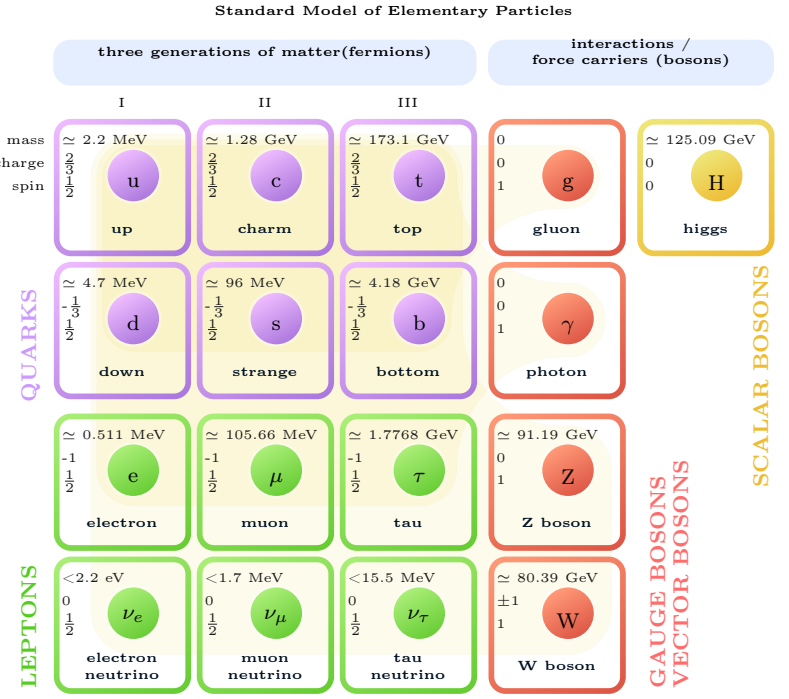

Figure 2.1.: Visualization SM of elementary particles. From [19], under creative commons license CC-BY[20], adapted to natural units.

The SM describes three out of the four known fundamental forces: Strong interaction, electromagnetic interaction and weak interaction. The last remaining one, gravitation, is not described. In itself the SM is a formulation of the more general theoretical framework called Quantum Field Theory (QFT). It models particles as excited states of an underlying field. Interactions between particles are therefore interactions between fields. The fields themselves are described via Lagrangians, spatial integrals over the Lagrangian density of the field containing kinetic terms in form of derivatives and potential terms.

2.1.1. Helicity and chirality

Given a particle with spin $\vec{S}$ and momentum $\vec{p}$ the helicity is defined as [21]

$$h := \frac{\vec{S} \cdot \vec{p}}{|\vec{p}|} \tag{2.1}$$

where $\cdot$ denotes the usual scalar product. A particle is therefore said to have right-handed helicity if the spin and momentum point in the same direction. Otherwise it is said to have left-handed helicity.

Chirality is defined as the eigenstates of the $\gamma^5 = i\gamma^0\gamma^1\gamma^2\gamma^3$ operation and does not have an intuitive physical representation. The γ^i with $i = 0, \ldots, 3$ denotes here one of the *gamma matrices* which are $\mathbb{C}^{4\times4}$ matrices obeying specific anticommutation relations stated in [21, p. 90]. However helicity eigenstates (left- and right-handed helicity) are also chiral eigenstates for massless particles or consequently for relativistic particles ($E \gg m$).

While the helicity can change depending on the reference frame, the chirality is an intrinsic property to a particle.

The SM is a chiral theory in which particles behave differently depending on whether they are part of the left- or right-handed class. From now on the handedness of a particle is referring for simplicity to the chiral eigenstate.

2.1.2. Spontaneous symmetry breaking

Consider a scalar doublet

$$\phi = \begin{pmatrix} \phi^+ \\ \phi^0 \end{pmatrix}, \quad \phi^+, \phi^0 \in \mathbb{C}. \tag{2.2}$$

The scalar field ϕ has then the potential of form

$$U(\phi) = \mu^2\phi^\dagger\phi + \lambda(\phi^\dagger\phi)^2, \quad \lambda \in \mathbb{R}_+, \tag{2.3}$$

with Lagrangian

$$\mathcal{L} = (\partial_\mu\phi)^*(\partial^\mu\phi) - U(\phi). \tag{2.4}$$

The field will have its minimum, also called non-zero vacuum expectation value, at

$$\langle\phi\rangle = \frac{|\mu|}{\sqrt{\lambda}} =: v \tag{2.5}$$

for $\mu^2 < 0$. As $U(\phi)$ has a symmetry on ϕ's real and imaginary parts, the minimum is degenerated with all of the states satisfying:

$$\phi^\dagger\phi = \frac{v^2}{2}. \tag{2.6}$$

A choice of vacuum state is known as *spontaneous symmetry breaking*.

2.1.3. Masses in the Standard Model

In the SM, mass is not intrinsic to the particles but particles acquire mass through Yukawa couplings with the Higgs field upon spontaneous electroweak symmetry breaking with a non-zero vacuum expectation value v.

Gauge bosons of the electroweak interaction The required invariance of the Lagrangian on the $\mathrm{SU}(2)_L \times \mathrm{U}(1)_Y$ local gauge symmetry of the electroweak sector would be broken by Lagrangian terms corresponding to particle masses. While left-handed particles transform as weak isospin doublets the right-handed ones transform as singlets, a mass term breaks this invariance. Gauge bosons mediating the weak force would therefore be massless.

Upon adding a complex $\mathrm{SU}(2)_L$ scalar field (2.2) to the electroweak Lagrangian one again needs to require it to be gauge invariant. This invariance can be achieved by substituting (2.4) with the appropriate covariant derivates

$$\partial_\mu \to D_\mu = \partial_\mu i g_W \boldsymbol{T}\cdot\boldsymbol{W}_\mu + ig'\frac{Y}{2}B_\mu \tag{2.7}$$

where $\boldsymbol{T} = \frac{1}{2}\boldsymbol{\sigma}$ are the generators of the SU(2) symmetry, g_W the coupling constant of $\mathrm{SU}(2)_L$ and g' the coupling of $\mathrm{U}(1)_Y$. Y denotes the weak hypercharge.

Once spontaneous symmetry breaking occurs[1] a mass term arises between the SM gauge bosons as the covariant derivative couples them to the scalar field. Following Goldstone's theorem [22] three massless Goldstone bosons will also arise: one for each generator. They are removed from the Lagrangian by choice of a so-called unitary gauge which sets ϕ^+ to zero.

By therefore choosing the scalar field to be

$$\phi = \frac{1}{\sqrt{2}} \begin{pmatrix} 0 \\ v + h(x) \end{pmatrix}, \tag{2.8}$$

which will be associated with the Higgs field, one can determine the effect of the covariant derivative on ϕ as

$$D_\mu \phi = \frac{1}{2}\frac{1}{\sqrt{2}} \begin{pmatrix} 2\partial_\mu + i g_W W_\mu^{(3)} + i g' B_\mu & i g_W (W_\mu^{(1)} - i W_\mu^{(2)}) \\ i g_W (W_\mu^{(1)} + i W_\mu^{(2)}) & 2\partial_\mu - i g_W W_\mu^{(3)} + i g' B_\mu \end{pmatrix} \begin{pmatrix} 0 \\ v + h \end{pmatrix} \tag{2.9}$$

and the W boson

$$W_\mu^\pm = \frac{1}{\sqrt{2}} \left[W_\mu^{(1)} \mp i W_\mu^{(2)} \right] \tag{2.10}$$

mass is then given by the terms quadratic in $W^{(1)}, W^{(2)}$,

$$\frac{1}{2} m_W^2 W_\mu^{(1)} W^{(1)\mu} \tag{2.11}$$

and can therefore be identified as [21]

$$m_W = \frac{1}{2} g_W v. \tag{2.12}$$

The photon and Z boson fields are then obtained by writing the terms in the Lagrangian depending quadratically on $W_\mu^{(3)}$ and B and solving for the physical states (diagonalizing the mass matrix) obtaining finally the relation [23]

$$\begin{pmatrix} W_\mu^{(3)} \\ B_\mu \end{pmatrix} = \begin{pmatrix} \cos\theta_W & \sin\theta_W \\ -\sin\theta_W & \cos\theta_W \end{pmatrix} \begin{pmatrix} Z_\mu \\ A_\mu \end{pmatrix} \tag{2.13}$$

and $\tan\theta_W = \frac{g'}{g_W}$. While the photon, associated with A_μ is still massless the Z boson mass can then be expressed as [21]

$$m_Z = \frac{1}{2} \frac{g_W}{\cos\theta_W} v. \tag{2.14}$$

Fermions In an analogous manner Yukawa couplings with the Higg's field can give rise to fermion masses. The Lagrangian of the Yukawa interaction for fermions is given by [24]

$$-\mathcal{L}_Y = h_{ij}^u \bar{Q}_{Li} u_{Rj} \tilde{H} + h_{ij}^d \bar{Q}_{Li} d_{Rj} H + f_{ij}^e \bar{l}_{Li} e_{Rj} H + \text{h.c.} \tag{2.15}$$

where $\bar{Q}_{Li}$ denote left-handed quark doublets, $\bar{l}_{Li}$ left-handed lepton doublets and the right-handed fields are written as u_{Rj}, d_{Rj}, e_{Rj} for up- and down-quarks and leptons respectively. The i, j indices denote the different generations

[1] see Section 2.1.2

and $h.c.$ abbreviates the Hermitian conjugate terms in the Lagrangian ensuring the eigenvalues of the Hermitian operator to be real numbers.

When the electroweak symmetry is now broken by $v \neq 0$ the Yukawa couplings are taking the form:

$$h^u_{ij} v = (m_u)_{ij}, \quad h^d_{ij} v = (m_d)_{ij}, \quad f^e_{ij} v = (m_e)_{ij} \tag{2.16}$$

which denotes the masses of the up- and down-type quarks u, d as well as the charged leptons e in the generations i, j. The Lagrangian therefore becomes

$$-\mathcal{L}_Y = (m_u)_{ij} \bar{Q}_{Li} u_{Rj} + (m_d)_{ij} \bar{Q}_{Li} d_{Rj} + (m_e)_{ij} \bar{l}_{Li} e_{Rj} + \text{h.c.} \tag{2.17}$$

where it becomes clear that the mass terms couple the left- and right handed components (see Section 2.1.4). As can be noticed there is no mass term for neutrinos added to the Lagrangian, which will lead to one of the limitations of the SM described in Section 2.2. First one needs to understand though the difference between Dirac and Majorana particles.

2.1.4. Majorana particles

For fermions that acquired masses through interaction with the Higgs field the mass couples to both left- and right handed components:

$$m\bar{\Psi}\Psi = (\overline{\Psi_L + \Psi_R})(\Psi_L + \Psi_R) = \bar{\Psi}_L \Psi_R + \bar{\Psi}_R \Psi_L \tag{2.18}$$

for a field $\Psi = \Psi_L + \Psi_R$.

One can now define two classes of fields that are distinguished by the relationship of the left-handed and right-handed field components. The two classes will have wide implications for their compatibility with the standard model.

For a Majorana field it holds that

$$\Psi_R = (\Psi_L)^C \tag{2.19}$$

where C denotes the image of the anti-particle operation $\hat{C}$ given by

$$\hat{C} : \Psi \mapsto \Psi^C = C\bar{\Psi}^T = i\gamma_2\gamma_0\bar{\Psi}^T. \tag{2.20}$$

And hence $\Psi^C = \eta^*\Psi$ which implies that a Majorana particle is its own anti-particle.

A Dirac field instead has independent components Ψ_L, Ψ_R where no such implication exists. While a Dirac field can be described by a set of four spinors, two are identified with the helicity of the particle and two with the helicity of the anti-particle under (2.20), a Majorana field can instead be described by only two spinors. This follows from (2.19) and the spinors parameterize solely the helicity therefore having only two degrees of freedom.

2.2. Neutrinos

It has been well established in experiments (see [9, 10]) that neutrinos exist only in left-handed chirality states while anti-neutrinos are intrinsically of right-handed chirality. Upon interaction with the Higgs field, chirality is changed which shows that neutrinos would not have mass in the SM and indeed they are included as massless particles.

From the previous Section it also becomes clear that Majorana particles can not carry a charge as it would be inverted upon the $\hat{C}$ operation. For the fermions of our SM this leaves only the neutrino as a possible Majorana candidate. Whether this is indeed the case has not yet been established and indeed this has wide consequences as shown in Section 2.3.

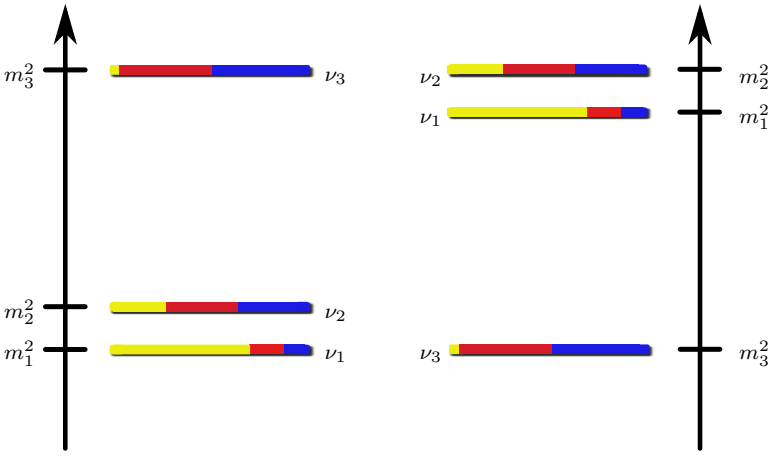

Figure 2.2.: Neutrino mass eigenstate hierarchies showing the different mass-splitting orderings. The colours correspond to the relative flavor eigenstate content: yellow=ν_e, red=ν_μ, blue=ν_τ. From [25] under creative commons license CC-BY[20].

Originally included as massless particles in the SM neutrinos have been opening questions over the last decades. Among this are atmospheric [4] and solar neutrino puzzles [5, 6]. Both of them are understood by oscillation of neutrino flavors. For this to occur an interaction needs to take place. The flavor eigenstate of neutrinos (used in the weak interaction where the neutrino interacting with the W boson and an electron is labeled ν_e) is therefore perceived to be written as a superposition of mass eigenstates:

$$\nu_\alpha = \sum_{i=1,2,3} U^*_{\alpha i}\nu_i, \quad \alpha = e,\mu,\tau \tag{2.21}$$

the so-called Pontecorvo-Maki-Nakagawa-Sakata (PMNS) matrix U relates the flavor and mass eigenstates of the neutrinos:

$$U = \begin{pmatrix} U_{e1} & U_{e2} & U_{e3} \\ U_{\mu 1} & U_{\mu 2} & U_{\mu 3} \\ U_{\tau 1} & U_{\tau 2} & U_{\tau 3} \end{pmatrix}. \tag{2.22}$$

and a common parameterization is given as in [7]:

$$U = \begin{pmatrix} c_{12}c_{13} & s_{12}c_{13} & s_{13}e^{i\delta} \\ -s_{12}c_{23} - c_{12}s_{23}s_{13}e^{i\delta} & c_{12}c_{23} - s_{12}s_{23}s_{13}e^{i\delta} & s_{23}c_{13} \\ s_{12}s_{23} - c_{12}c_{23}s_{13}e^{i\delta} & -c_{12}s_{23} - s_{12}c_{23}s_{13}e^{i\delta} & c_{23}c_{13} \end{pmatrix} \times \mathrm{diag}\left(1, e^{i\frac{\alpha_{21}}{2}}, e^{i\frac{\alpha_{31}}{2}}\right),$$

where abbreviated notation is used in which $c_{ij} = \cos\theta_{ij}$, $s_{ij} = \sin\theta_{ij}$, $\theta_{ij} = [0, \frac{\pi}{2}[$ and $\delta = [0, 2\pi]$, α_{21}, α_{31} are CP violating phases.

The oscillating flavor states as superpositions of mass eigenstates allow for the explanation of a variety of appearance and disappearance findings. It is so far established that at least three neutrino mass eigenstates exist that need to be light and different, so

$$m_i \neq m_j, \forall i \neq j, \quad m_i \leq 1\,\mathrm{eV} \tag{2.23}$$

for $i, j = 1, 2, 3$ [7]. Assuming only three neutrinos one obtains two independent mass splittings $\Delta m^2_{ij} = (m^2_i - m^2_j)$. By convention ν_1 denotes the smaller of $1, 2$ mass splitting and ν_3 the remaining one. Current measurements of the mass splittings are noted in Table 2.1.

Table 2.1.: Mass splitting of neutrino mass eigenstates for three neutrinos. Table excerpt from [7].

Mass splitting	best-fit	3σ range
$\Delta m^2_{21}[10^{-5}\ \mathrm{eV}^2]$	7.37	6.93 - 7.96
$\Delta m^2_{31}[10^{-3}\ \mathrm{eV}^2]$	2.56	2.45 - 2.69

The splittings are visualized in Figure 2.2. A mass ordering (ν_1, ν_2, ν_3) is referred to as *normal neutrino mass hierarchy* and an ordering (ν_3, ν_1, ν_2) as *inverted* hierarchy.

2.3. Type-I see-saw mechanism

In order to explain the very low neutrino masses as observed through the neutrino oscillations (see Section 2.2) different expansions of the SM are possible. These commonly called Beyond the Standard Model (BSM) theories take different approaches to incorporate the observations with already verified and precisely measured elements of the SM (see Section 2.1).

One of them is called the *see-saw* mechanism and is presented here. The description follows closely [26] and is reduced to the essential parts.

First it needs to be noticed that in the SM no more fundamental reason is used for not introducing right-handed neutral particles (neutrinos) other than they were not observed. Once one adds right-handed neutral fields (implying also $Y = 0$) and assumes them to be $\mathrm{SU}(2)_L$ singlets no interaction with gauge bosons takes place. However their presence has wide reaching implications for the model. As mentioned before in Section 2.1.3 masses in the SM are generated by Yukawa interactions with the Higg's field, where we have a chirality switch upon interaction. Now that this is possible with a right-handed field one obtains for the Yukawa interaction another term:

$$-\mathcal{L}'_Y = \sum_{\ell,\ell'} f_{\ell\ell'} \bar{\Psi}_{\ell L} H^C N_{\ell' R} + \mathrm{h.c.} \tag{2.24}$$

where H is the Higg's multiplet, $\Psi_{\ell L}$ the lepton doublet $(\nu_{\ell L}, \ell_L)^T$ with a (2, -1) representation of $\mathrm{SU}(2) \times \mathrm{U}(1)_Y$ and $f_{\ell\ell'}$ a new coupling constant. Following electroweak symmetry breaking Equation (2.24) can be rewritten as

$$-\mathcal{L}_{\mathrm{mass}} = \sum_{\ell,\ell'} M_{\ell\ell'} \bar{\nu}_{\ell L} N_{\ell' R} + \mathrm{h.c.} \tag{2.25}$$

with a *mass matrix*

$$M_{\ell\ell'} = \frac{v}{\sqrt{2}} f_{\ell\ell'}. \tag{2.26}$$

As the fields $\nu_{\ell L}$, $N_{\ell' R}$ are not generally corresponding to the chiral projections of the physical fields the mass matrix can not be assumed to be diagonal. In order to find eigenvectors of $M_{\ell\ell'}$ one can though diagonalize it via

$$U^\dagger M V = m \tag{2.27}$$

where

$$m = \mathrm{diag}\,(m_1, \ldots, m_n)\,. \tag{2.28}$$

By defining new states $\nu_{\ell L}, N_{\ell R}$ via

$$\nu_{\ell L} := \sum_{i\in\{1,\dots,n\}} U_{\ell i}\nu_{iL}, \tag{2.29}$$

$$N_{\ell R} := \sum_{i\in\{1,\dots,n\}} V_{\ell i}\nu_{iR}, \tag{2.30}$$

Equation (2.25) can be rewritten as

$$-\mathcal{L}_{\text{mass}} = \sum_{i\in\{1,\dots,n\}} \bar{\nu}_{iL} m_i \nu_{iR} + \text{h.c.} \tag{2.31}$$

with m_i as defined in (2.28).

However with the introduction of a right-handed neutral field additional terms appear in the Yukawa sector generating additional masses. As $N_{\ell\text{R}}$ was invariant under $\text{SU}(2)_L \times \text{U}(1)_Y$ so should be $N^C_{\ell L}$. An additional mass term to be considered for the Lagrangian would then be:

$$-\mathcal{L}_{\text{add. mass}} = \frac{1}{2}\sum_{\ell,\ell'} B_{\ell,\ell'}\overline{N^C}_{\ell L} N_{\ell' R} + \text{h.c.}, \tag{2.32}$$

which allows us to write this together with (2.25) as

$$-\mathcal{L}_{\text{mass}} = \frac{1}{2}\begin{pmatrix}\bar{\nu}_L & \bar{N}^C_L\end{pmatrix}\underbrace{\begin{pmatrix}0 & M\\ M^T & B\end{pmatrix}}_{\mathcal{M}}\begin{pmatrix}\nu^C_R\\ N_R\end{pmatrix} + \text{h.c.} \tag{2.33}$$

where $\mathcal{M}$ is the mass matrix with $M, B \in \mathbb{C}^{n\times n}$ for n generations. Assuming $n = 1$, $M, B \in \mathbb{R}$ and especially B positive shows by diagonalizing $\mathcal{M}$ where the see-saw mechanism obtains its name from.

Diagonalizing the mass matrix yields eigenvalues (and hence masses of the physical neutrinos)

$$m_{1,2} = \frac{1}{2}\left(B \pm B\sqrt{1+4\frac{M^2}{B^2}}\right) \tag{2.34}$$

which for $B \gg M$ yields

$$m_1 \approx \frac{M^2}{B}, \quad m_2 \approx B \tag{2.35}$$

creating a very small mass m_1 while allowing for a very heavy mass m_2. This see-sawing of masses can be translated to the active and HNL case where the *heavy* neutrino allows the active neutrino to be much lighter. The physical neutrino states as obtained from the eigenvalues from the mass matrix are [21]

$$\begin{aligned}\nu &\approx (\nu_L + \nu^C_L) - \frac{M}{B}(\nu_R + \nu^C_R)\\ N &\approx (\nu_R + \nu^C_R) + \frac{M}{B}(\nu_L + \nu^C_L)\end{aligned} \tag{2.36}$$

where for the approximation again $B \gg M$ was used. It becomes clear that due to the assumption of a much larger Majorana mass B than the Dirac mass M the light neutrino states are essentially the same ones as in the SM. The right-handed neutrino would only couple to a very small degree to the left-handed weak interaction (reduced by the factor $\frac{M}{B}$).

However if B would instead be zero, diagonalizing $\mathcal{M}$ results in the same mass eigenvalues as M, M^T form the anti-diagonal of $\mathcal{M}$ (see proof for this in [26, Ch. 4.5]) and the resulting eigenvectors would hence be Dirac particles. For $n = 1$ the 1×1 matrix (also called scalar) B is therefore sometimes referred to as Dirac mass matrix (determining the Dirac character, not equating it with the Dirac mass). Having $B = 0$ for $n = 1$ (or B being a $n \times n$ zero-matrix for higher dimensions) is the equivalent with assuming no summands $\overline{N^C}_{\ell L} N_{\ell' R}$ in (2.32).

2.4. Heavy Neutral Leptons and the νMSM

A minimal expansion in terms of number of particles is the νMSM that introduces gauge-singlet Majorana particles as right-handed partners to the left-handed so called *active* neutrinos. For the νMSM the Majorana masses of the right handed neutrinos are on the GeV-scale. This model can account for neutrino masses, oscillations as well as provide a dark-matter candidate and contribute to the baryon asymmetry in the universe [14].

The νMSM includes three singlet neutral Majorana fermions (also called sterile neutrino) N_I with the Lagrangian

$$L_{\text{singlet}} = i\bar{N}_I \partial_\mu \gamma^\mu N_I - Y_{I\alpha} \bar{N}_I^C \tilde{H} L_\alpha^C - M_I \bar{N}_I^C N_I + \text{h.c.}, \tag{2.37}$$

where the mass term allows the active and sterile neutrino to mix. The lightest N_1 is a dark-matter candidate in the νMSM due to its weak mixing with other leptons, it may have a mass of $\mathcal{O}(10)$ keV [13] and lifetime exceeding the age of the universe. In total an extension of the SM by these singlets offers 18 parameters, three of which are associated with Majorana masses, three with Dirac masses, six with mixing angles and finally six with CP-violating phases [27]. Observations of neutrino oscillations constrain these parameters. In the νMSM the requirement of having a low-mass dark-matter candidate as well as the aim to explain baryon asymmetry further fixes parameters so that N_2 and N_3 are much heavier than N_1 and of approximately the same mass. The HNLs searched for in this thesis would be a good candidate for $N_{2,3}$ in the νMSM. There are further constraints on the lifetime, and hence mixing angle, coming from big bang nucleosynthesis limiting the parameter space [12, 28]. Heavy neutrinos as searched for in this thesis could therefore be a natural and sensible addition to the SM solving several so far unexplained phenomena.

To help experimentally restrict the parameters as for instance the mixing angle to active neutrinos it is useful to analyze multiple signatures and channels as was done in this thesis. It has been shown that depending on the neutrino mass hierarchy, single mixing angles might be largely suppressed in the νMSM, while this does not hold for multiple mixing angles [29]. Knowing limits on several mixings is therefore beneficial in the phenomenological interpretation of results.

2.5. Existing experimental tests

The HNLs searched for in this thesis are of GeV mass below the electroweak scale. Several experiments probe a similar parameter space and a short overview of recent results is given here.

A selection of different experimental limits obtained mostly by accelerators on the muon mixing angle are shown in Figure 2.3 with almost identical results showing for the electron mixing in [30]. Not included here are recent results from the CMS experiment. In 2018 CMS published results [31] for $35.9\,\text{fb}^{-1}$ of proton-proton (pp) collisions at $\sqrt{s} = 13\,\text{TeV}$ which covers a similar mixing

angle and mass parameter range as this search. In absence of evidence of HNLs they report exclusion limits on muon- and electron mixing angles (see Figure 2.4) which will be subsequently shown together with results obtained in this search for better comparison.

Neutrinoless double beta decay[33] is the decay of a nucleus (A, Z) by

$$(A, Z) \rightarrow (A, Z + 2) + 2e^{-} \qquad (0\nu\beta\beta)$$

which as a lepton number violating process would confirm or exclude the Majorana nature of neutrinos. It uses the so-called effective Majorana mass $|m_{\beta\beta}|$ as parameter of interest [34]. As this mass can be comprised of active neutrino masses as well as HNLs, a non-observation of this decay will pose an upper restriction on HNL masses and mixing via (2.36) as indicated in Figure 2.5, and can be interpreted in models like the νMSM [35].

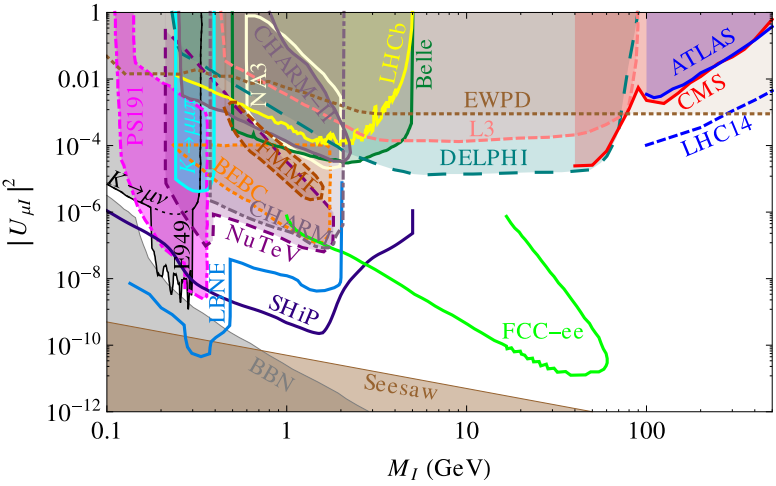

Figure 2.3.: Existing experimental limits $|U_{\alpha N}|^2$ for $\alpha = \mu$. A recent 2018 result from the CMS experiment is not shown here. Figure from [30].

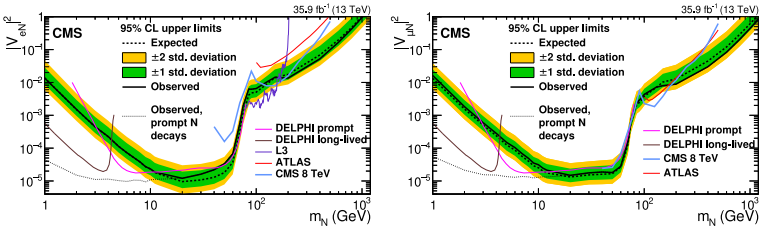

Figure 2.4.: Shown are CMS results obtained for a charged three lepton search comparable to the search presented here. Figure from [31].

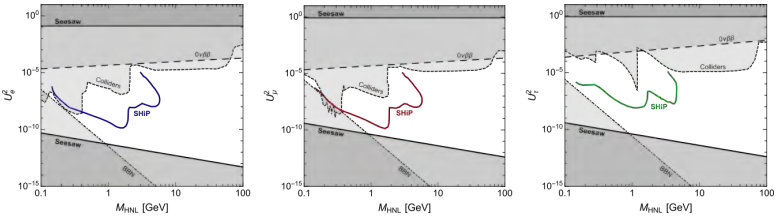

Figure 2.5.: Indication of upper limits from neutrinoless double beta decay on active-sterile mixing angles in the GeV HNL mass region. Bands are determined numerically. Figure from [32].

Chapter 3.

The ATLAS experiment

Atlas, who looks after the bottom of the ocean, and carries the great columns that keep heaven and earth asunder

— Homer, 800 BC[1]

The ATLAS detector [36] at the LHC is a multipurpose particle detector with a cylindrical geometry. As such it is constructed in radially layered design resembling somewhat an onion structure. The different layers or subdetectors are ensuring that a wide variety of particles with different properties can be detected and their properties measured as they are traversing the detector to various degrees. In Section 3.2 the different components of ATLAS are detailed.

In order to design the vast amount of components and also operate and maintain them a large collaboration as the ATLAS experiment is required. It consists of scientists and engineers from 181 institutions in 38 countries totalling a little more than 3000 scientific authors [37]. Such an incredible effort can naturally not be managed without uncountable supporting roles and funding opportunities. Since the original draft of the letter of intent for ATLAS more than 25 years ago [38] great achievements such as the discovery of the Higgs boson are part of the experiment. Plans to upgrade the experiment and operate it with the high-luminosity phase of the LHC (HL-LHC) (currently foreseen from 2026 onwards) are well underway [39] and will ensure highly interesting general-purpose particle physics data to be available.

The LHC is at the core of four large particle detectors at the European Organization for Nuclear Research (CERN) facilities. It accelerates protons, lead and xeon ions, collides them and therefore supplies the required hadron collisions at fixed interaction points around which the ATLAS, CMS, Large Hadron Collider beauty (LHC-b) and A Large Ion Collision Experiment (ALICE) detectors are built. The LHC is presented in Section 3.1.

[1] Hom. Od. 1.2

3.1. The Large Hadron Collider

The LHC is a 27 km long acceleration ring for hadrons located in the west of Geneva under the French/Swiss border. A detailed description of its design, infrastucture and services provided can be found in [40].

The CERN infrastructure complex for colliding hadrons (only *pp* collisions for this search) is sketched in Figure 3.1. In order to reach the design *pp* collision energy ($\sqrt{s}$) of 14 TeV, protons are first accelerated in different stages (namely Linear Accelerator (LINAC2), Proton Synchrotron Booster (BOOSTER), Proton Synchrotron (PS), Super Proton Synchrotron (SPS)) and finally injected into the LHC ring where they reach their final collision energy. For this search *pp* collisions in 2015 and 2016 were measured at $\sqrt{s} = 13$ TeV.

The beam supplied from SPS has an energy of 450 GeV and needs to be injected into the LHC main accelerator ring. For this the injected beam is approaching the beamline from below (at an angle of 0.85 mrad [40]) where a so called *injection kicker system* is aligning the incoming protons with the existing beams using four fast pulsed magnets. For this the timing of the previous SPS accelerator as well as rise- and fall-times for the injection kickers has to be taken into account.

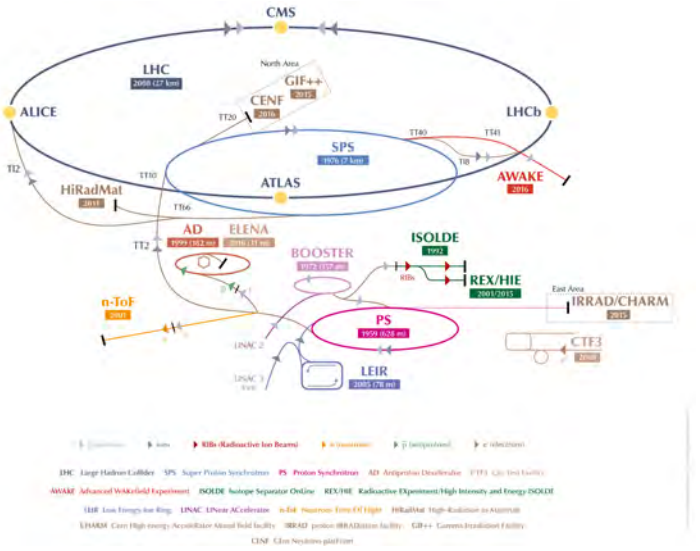

Figure 3.1.: The CERN accelerator complex. Shown are among others different stages of acceleration for protons for the LHC and the use made of older existing accelerators. Figure from [41].

Within the accelerator ring are two beamlines that accelerate protons in opposite directions to each other. The acceleration is performed by using so-called RF cavities which make the protons experience attraction towards the next ring segment while super-cooled magnets are used for bending the proton trajectory along the beamline. By steering the magnetic fields with very high precision the protons are bunched together in the RF cavities with a bunch-size of about 115 billion protons. Timing the two beamlines a synchronized bunch crossing from the two lines happens at determined so-called interaction or collision points. For the data collected in this analysis the average amount

of protons colliding called *interaction* in such a bunch crossing is 13.4 for 2015 and 25.1 for 2016. An overview of the mean number of interactions per crossing is shown in Figure 3.2. In the following the different technical aspects of such a circular accelerator are detailed.

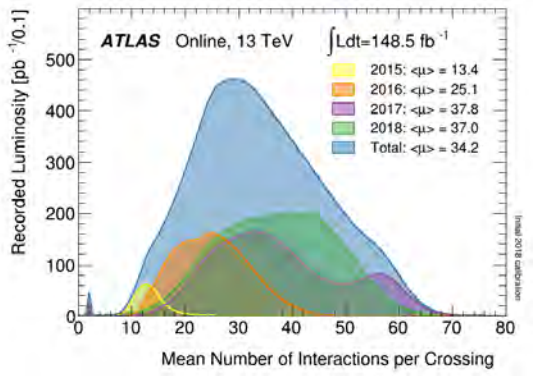

Figure 3.2.: Luminosity-weighted distribution of the mean number of interactions per crossing ($\langle\mu\rangle$) for the timeframe 2015 – 2018. All data recorded by ATLAS during stable beams is shown and total average value as well as per-year are noted in the figure. Figure from [42].

3.1.1. RF systems

When entering the LHC protons have an energy of about 450 GeV [40, 43]. In order to obtain the 13 TeV collision energy used for this search every proton has to be accelerated by the use of radiofrequency (RF) cavities from 450 GeV to 6.5 TeV. This *ramp* called procedure takes about 20 min.

Protons in the RF system experience a force due to the electromagnetic field induced. By using a hollow structure with cavities and connecting tubes as well as an oscillating electromagnetic field it is possible to let the protons be accelerated by a standing wave into the forward direction for each beamline. This way protons are experiencing a varying accelerating force depending on their present energy in the sense that protons with higher energy get less of a kick by the electromagnetic field. Additionally this helps in the bunching of protons which in turn is needed to increase the probability of collisions in a single bunch crossing as well as prevent migration of protons between bunches or the formation of intermediate *satellite* bunches.

The electromagnetic field in the RF cavitiy is oscillating at a frequency of 400 MHz [40]. At the LHC the two beampipes have independent RF systems, containing each two cryomodels which each contain four RF cavities. The cavities themselves are made out of copper and sputtered with niobium [40, 44] similar to the previous high energy version (beyond 172 GeV) of the Large Electron-Positron Collider (LEP) acccelerator in the same tunnel [44], though here sheets of niobium instead of sputtering was applied [45].

3.1.2. Superconducting electromagnets

In order to keep the accelerated particles on a circular path (they circle the ring more than eleven thousand times per second [46]) a large amount of *lattice*

magnets is used in order to bend the particle trajectories around the ring. The rather small circumference for the very high LHC energy makes it necessary to use superconductive magnets. The very high field strengths used ranging from 6.5 to 8.5 T requires therefore a cooling to temperatures below 2 K [40]. At LHC mostly dipole magnets are used (see Figures 3.3,3.4) to change the trajectory while symmetrically aligned quadrupoles (and higher alignment orders) are used to further focus the beam and tune beam parameters. The superconducting magnets are made from NbTi windings.

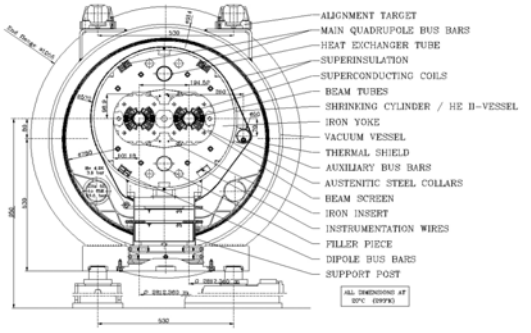

Figure 3.3.: Cross-section of the LHC line showing the two beamlines and dipole magnets. Figure from [40].

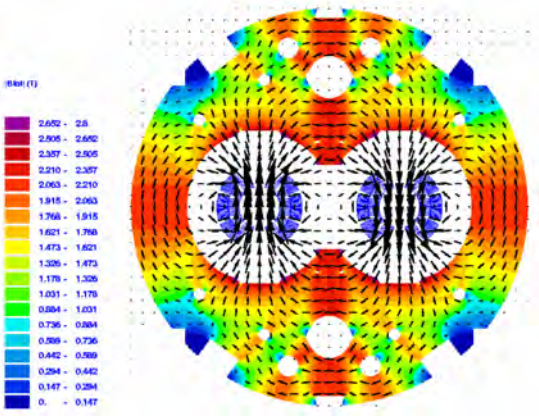

Figure 3.4.: Cross-section of the LHC line showing the computed dipole magnetic flux. Figure from [40].

3.1.3. Cryogenics and vacuum

The very high magnetic fields required to keep 6.5 TeV protons (for a total collision energy of $\sqrt{s} = 14$ TeV) within circular LHC accelerator with relatively small radius requires an operating temperature below 2 K. This low operation temperature is achieved by two-phase saturated superfluid helium

[47]. In a quasi-isothermal cooling scheme the heat is transported from the magnets using a dedicated Cryogenic Distribution Line (QRL) in the tunnel of the LHC. At eight dedicated points in the ring storage vessels for the helium, and refrigerators for the nitrogen are placed. Though the nitrogen is only used for precooling machine and the use of nitrogen is forbidden in the tunnel [40]. The separate refrigeration points or plants limit the distance cooling fluids are transported to 3.3 km underground and place a form of redundancy. The RF cavities are enclosed in a cryostat where every RF system cools four cavities.

The QRL and cryomagnets are both using an insulation vacuum and operate at around 10×10^{-4} Pa. The vacuum needed for the beam requirements is though much higher. Requirements are expressed as gas densitities and compared with hydrogen. The value is stated in [40] to be below 10×10^{15} H_2 m^{-3} which allows for more than 100 h beam lifetime. This lifetime is dominated by nuclear scattering effects of protons on residual gas.

3.2. ATLAS subdetectors

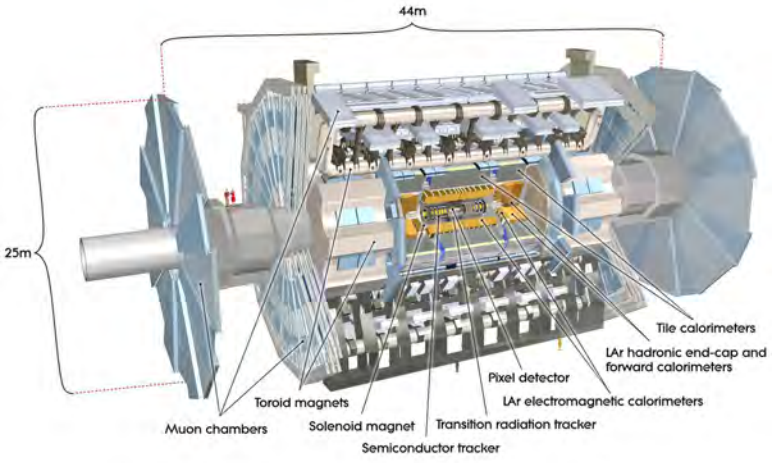

Figure 3.5.: The ATLAS detector and its subsystem. Computer generated rendering of the subdetector geometry and placement. Figure from [48].

The ATLAS detector, shown in a computer generated rendering in Figure 3.5, consists of: the inner tracking detector or Inner Detector (ID) at the core surrounded by a thin superconducting solenoid generating a 2 T axial magnetic field; the electromagnetic and hadronic calorimeters; and a Muon Spectrometer (MS) incorporating three large superconducting toroid magnets.

The ID consists of three sub-detectors which provide charged-particle tracking, charge sign and momentum measurements in the pseudorapidity range $|\eta| < 2.5$. A silicon Pixel Detector (PIX) supplies high-granularity measurements of the track, including the Insertable B-Layer (IBL) [49, 50] installed after Run 1 of the LHC, which is followed by a Semiconductor Tracker (SCT). At larger radii, a Transition Radiation Tracker (TRT) enables radially extended track reconstruction up to $|\eta| = 2.0$, which enhances the pattern recognition

and momentum resolution, and provides particle identification information over a wide range of energies.

The calorimeter system covers the pseudorapidity range $|\eta| < 4.9$. Electromagnetic calorimetry is provided by high-granularity lead/liquid-argon (LAr) detectors in the pseudorapidity range $|\eta| < 3.2$, and is extended to larger pseudorapidities by the forward calorimeter, which is also a LAr detector. Hadronic calorimetry is provided by the steel/scintillator-tiles calorimeter in the region $|\eta| < 1.7$, which is segmented into three barrels: a central barrel and two extended barrels. It is extended up to $|\eta| < 4.9$ by a copper/LAr detector and a copper-tungsten/LAr detector.

The MS includes separate trigger and high-precision chambers as the formers readout speed is too slow to supply information fast enough for triggering. The magnetic field for the muon spectrometer, which deflects the muon tracks, is generated by three large air-core toroid magnets. The chamber system covers the pseudorapidity region $|\eta| < 2.7$, where precision measurements of the track coordinates are provided by monitored drift tubes, and at large pseudorapidities $2 < |\eta| < 2.7$, the cathode strip chambers with higher granularity are used. The muon trigger system covers the range $|\eta| < 2.4$, where resistive plate chambers are used in the barrel and thin gap chambers in the end-cap regions.

3.2.1. ATLAS coordinate system and common quantities

Descriptions in this thesis and general ATLAS publications make use of the ATLAS coordinate system. It is a three-dimensional cartesian (x, y, z) space defined with origin in the nominal interaction point of pp collisions. The z-direction is defined by the beam line with consequently the $x - y$ plane being transverse to the beamline. The x-direction is parallel to ground-level and its axis points positively towards the center of the LHC. The positive y-direction points upwards towards the surface. As commonly done in high energy physics experiments the azimuthal angle is measured around the beam axis and denoted here by Φ, while the polar angle is defined respectively to the beam axis and denoted by θ.

Pseudorapdity is defined as

$$\eta = -\log\tan\left(\frac{\theta}{2}\right) \tag{3.1}$$

and converges in the relativistic limit to the common definition of rapidity. This can be seen when writing both as a function of the particles momentum $\vec{p}$ and the logitudinal momentum p_L, the projection of $\vec{p}$ along the beam-axis. It is then

$$\eta = \frac{1}{2}\log\left(\frac{|\vec{p}| + p_L}{\vec{p} - p_L}\right), \quad y = \frac{1}{2}\log\left(\frac{E + p_L}{E - p_L}\right) \tag{3.2}$$

for y rapidity.

So called transverse quantities are commonly denoted by a lower $_{\mathrm{T}}$ as for instance in p_{T}, E_{T} or $E_{\mathrm{T}}^{\mathrm{miss}}$. The transverse quantity is a projection on the $x - y$ plane.

3.2.2. Inner detector

The three detector systems forming the ID are shown in Figure 3.6 together with their relative placement around the interaction point in the center. The ID covers the range $|\eta| < 2.5$ and resolves the impact parameter with $< 15\,\mu\mathrm{m}$. It also offers good three-dimensional vertexing capabilities with a z-axial resolution for vertex reconstruction of $\sigma(z) < 1\,\mathrm{mm}$ hence enabling good b-jet tagging capabilities [52]. For its design tracks with a nominal p_{T} threshold of

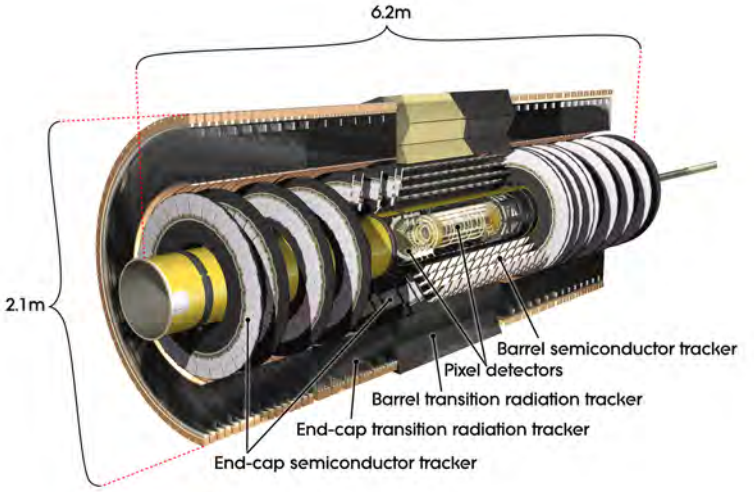

Figure 3.6.: The inner detector of ATLAS. Figure from [51].

0.5 GeV have been considered [36]. The inner detector offers excellent momentum resolution and is a crucial part in the identification of charged particles.

Silicon pixel detector The closest detector to the interaction point (located at radii 50.5 to 194.6 mm and in z-direction at 0 to 650 mm, both extremal values correspond to the forward/backward pixels shown in Figures 3.6, 3.7) are composed of silicon pixel sensors providing high granularity while measuring charged particles traversing at least three layers for trajectories with $|\eta| < 2.5$. The pixel detector consists of three layers parallel to the beampipe (referred to as the barrel) as well as three pixel rings in the forward- and backward region called the end-caps.

The semiconductors are $256 \pm 3\,\mu\text{m}$ thick oxygenated n-type wafers. It contains n^+ implants on the read-out side and the p-n junction on the back side. As the rest of the ID the sensors are strongly affected by raditation which influenced design choices especially regarding operation voltage. The type of semiconductor will change after about $F_{\text{neq}} \approx 2 \times 10^{13}\,\text{cm}^{-2}$ (neutron equivalent fluence [53]) and also increase the depletion voltage. Upon this inversion the junction will move to the front side [52]. The pixels offer a nominal $50 \times 400\,\mu\text{m}^2$ detection size.

Apart from the radiation sensitivity the temperature plays an active choice in the noise for the sensor measurements as well as for the aforementioned annealing. The sensors are hence cooled with a coolant of approximately 25 °C down to 5 to 10 °C for operation. The repated cooling and heating cycles with corresponding contraction and expansion of material has been taken into account for the planning of the detector.

In fact the alignment tolerances for the pixel sensors is at 10 to 20 µm for the radial and axial directions for the three layers and for the end-cap disks at 20 µm in radial and 100 µm in axial direction. They offer an accuracy of 10 µm in azimuthal direction and are all aligned within 7 µm tolerance.

After replacing the beam pipe with a reduced radius version (from 29 mm to 25 mm measuring the inner radius), enough space was available to insert a new

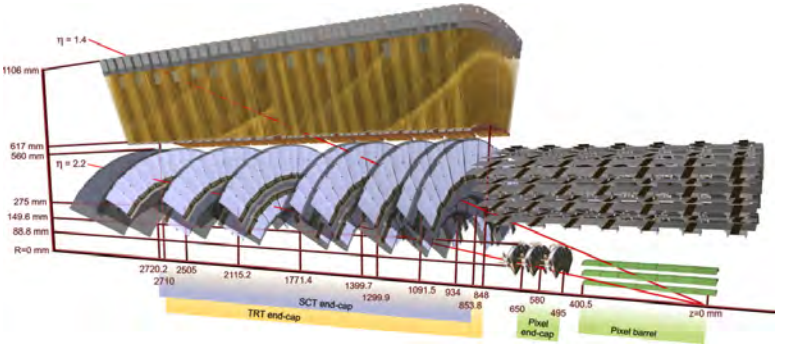

Figure 3.7.: Rendering showing sensors traversed by two charged tracks of 10 GeV p_{T} in the end-cap with $\eta = 1.4,\ 2.2$. Figure from [36].

pixel layer: the IBL between the innermost pixel layer and the beam pipe [49]. This was done in May of 2014 [54] and the search presented here has therefore been fully conducted using the improved track- and vertex reconstruction as well as b tagging performance. The gain for track- and vertex reconstruction can be seen in [49, Figures 20-22] where it is plotted in dependence of η, p_{T} and reaches in some bins almost to 40 % resolution improvement. Here the closer proximity of the sensors to the interaction point is a big advantage but can pose an additional difficulty in case of slightly further displaced HNLs as will be later discussed in Section 6.4. The tilted alignment of the sensors as shown in Figure 3.8 allows for a near complete coverage in azimuthal angle.

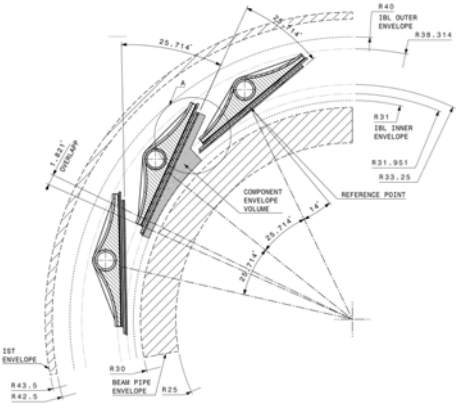

Figure 3.8.: IBL alignment of pixel sensors: $r\phi$ view. Figure from [49].

Silicon microstrip tracker In contrast to the silicon pixels the SCT consists of single sided p-n silicon sensors [55]. It supplies four barrel layers ($|\eta| <$ 1.1 to 1.4) and nine disks in each endcap ($|\eta| >$ 1.1 to 1.4). While initially the sensors operate at 150 V (like the pixel detector) the operation voltage will need to be increased to 250 to 350 V [36] due to strong radiation. The sensors are with 285 ± 15 µm thicker than the pixel detector and balance cost efficiency as well as operationability in terms of voltage and reliability. The SCT is an

extension of the pixel detector and is positioned between 299 to 560 mm radial distance to the interaction point, and expands in z-direction until 2720.2 mm for the disks and until 749 mm for the barrel. Every module consists of two times 768 active strips, where a strip are two daisy-chained 6 cm long sensors. The strip pitch was optimized for resolution to 80 µm. As the pixel detector it is designed to operate at low temperatures and is included in the ID cryostat.

Transition radiation tracker While the TRT is designed to operate at room temperature it is also contained in the ID cryostat. It extends radially from 563 to 1066 mm and axially in z-direction until 712 mm (barrel) and 2710 mm (end-cap). The detector consists of drift tubes with a diameter of 4 mm in which a gas mixture of 70 % Xe, 27 % CO_2 and 3 % O_2 is flushed with 5 to 10 mbar over-pressure [36]. The drift tubes form three rings in the barrel region and two sets of wheels in the end-cap. The first set consists of 12 wheels and the second of eight, while in both a wheel comprises eight successive drift tube layers. The set further from the interaction point uses a larger spacing between the layers. In Run-II of LHC only the third ring of the barrel used the aforementioned gas while the first wo layers were flushed with an Ar/CO_2 mixture. The O_2 content of the gas was brought down in 2018 to avoid sparks and is now at approximately 1.5 %.

The anode wire is made from tungsten with a diameter of 31 µm and in the barrel possesses an active length length of ± 71.2 cm. In the middle an additional support for the wire fixes it to the tube wall ensuring a wire sag of less than 15 µm. This support causes an inefficiency of 2 cm length near the center of the anode. The tubes are read out from each end and are operated at -1530 V obtaining a gain of 2.5×10^4. Electron collection time is approxaimtely 48 ns. The TRT end-caps do not extend beyond $|\eta| = 2$. While the barrel straw layers are interleaved wth fibres the end-cap planes are interleaved with foils to provide transition radiation upon the traversal of charged particles.

The used Xenon gas mixture plays an essential role and allows the TRT to combine the tracking information with additional particle identification based on transition radiation photon detection [56]. It has a low photon absorbtion range in the energy range relevant for the transition radition [57]. Hits in the inner detector that could be caused both by pions and electrons can be discriminated by the fraction of *high-threshold* hits of a track. The TRT outputs an extra bit for a signal that passes a specified higher threshold at any point within a 25 ns window.

As transition radiation depends on the γ factor, and electrons have a larger γ factor than pions, electrons are more likely to emit transition radiation photons. The opening angle between original track and transition radiation photon is highly colinear and therefore translates the amount of high-threshold hits to a property of the charged particle passing through it. In ATLAS a likelihood-based identification method is then applied to distinguish between the pion and electron hypotheses.

3.2.3. Electromagnetic calorimeters

The Electromagnetic Calorimeter (EM calorimeter) [58] is separated into the barrel $|\eta| < 1.475$ and the end-caps at $1.375 < |\eta| < 3.2$ providing therefore full azimuthal Φ coverage up to $|\eta| < 3.2$. It is designed to measure electrons, photons, jets and $E_{\mathrm{T}}^{\mathrm{miss}}$ with sufficient precision and provide triggering information.

The EM calorimeter consists of three absorbers with gaps in between. It uses an accordeon shape for the absorbers which are made out of lead with a thickness of 1.53 mm for $|\eta| < 0.8$ and 1.13 mm outside of it (limitting decrease

of sampling fraction in this area) [36]. This shape enables naturally the complete Φ coverage. Readout electrodes are made from conductive copper layers and are located in the gaps between the absorbers. In total three copper layers are used where the two outer form the high-voltage potential and the inner one reads out signal. The EM calorimeter uses LAr as the active medium.

The three independent readout layers exhibit different granularity in η direction, shown in Figure 3.9, and coarser granularity in later layers. Most energy is absorbed in layer two, leaving layer three with the tail of electromagnetic showers.

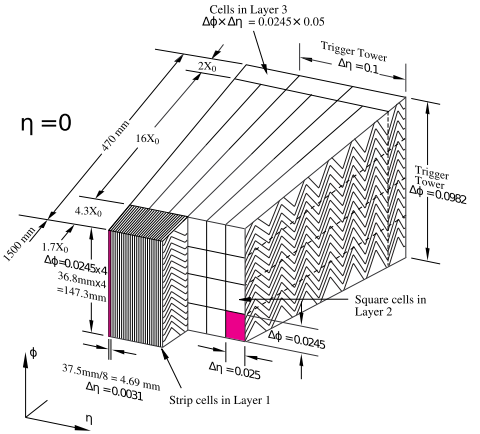

Figure 3.9.: Example of the EM calorimeter barrel module layout. Figure from [58].

The three components (barrel and two end-caps) are all housed in their own separate cryostats while the EM calorimeter and the solenoid magnet after the ID share the same vacuum vessel and therefore minimize the material budget by avoiding additional vacuum walls.

3.2.4. Hadronic calorimeters

ATLAS uses three hadronic calorimeters: tile calorimeter, LAr Hadronic Endcap Calorimeter (HEC) and LAr Forward Calorimeter (FCal).

Tile calorimeter The tile calorimeter [59] consists of a barrel and two *extended barrel* parts. It uses steel as absorber and scintillating tiles as active material. Between the central barrel and the extended parts lies a 600 mm gap in which cabling for the inner detector, LAr cables and supply electronics is located. The gap is partially filled by calorimeters or even only scintillators to recover parts of the energy otherwise lost in this region. The barrel extends until $|\eta| < 1$ while the extended barrel covers $0.8 < |\eta| < 1.7$ [60].

The main function of the tile calorimeter is to supply additional information for the energy reconstruction of jets produced in the pp collisions as well as measure missing transverse moment $p_{\mathrm{T}}^{\mathrm{miss}}$. It is constructed by 64 modules as shown in Figure 3.10a which each consist of scintillators as well as steel. The different layers consist of a 5 mm *master plate* with 4 mm thick spacer plates on top, assembled in a staggered fashion, giving room for the scintillators. The light is collected at the edges of the tile using two wavelength-shifting fibres, which are coupled to Photomultiplier Tube (PMT) at the top of each module.

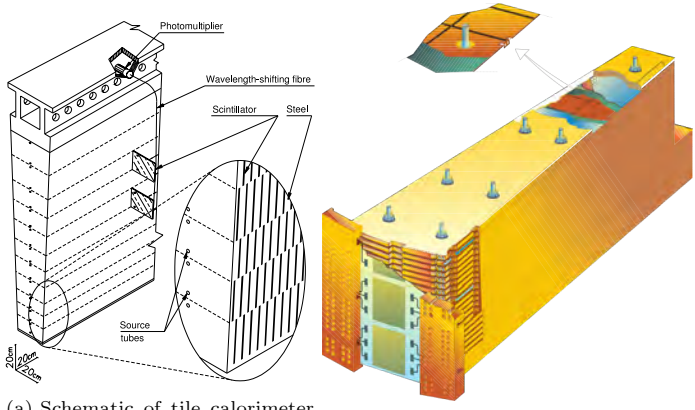

(a) Schematic of tile calorimeter module. Figure from [36].

(b) Schematic of HEC module. Figure from [36].

Figure 3.10.: Selection of hadronic calorimeter modules

The radial depth of a module is given by approximately 7.4 interaction lengths and a module offers a $\Delta\Phi \times \Delta\theta$ resolution of about 0.1×0.1.

Hadronic end-cap calorimeter The HEC [58] covers the η range between 1.5 to 3.2.It consists of two wheels (called *front-* and *rear-wheel*) which both have a radius of 2.03 m. Both wheels consist of copper plates with 8.5 mm gaps and use LAr as the active medium. The front-wheel uses 24 copper plates of 25 mm thickness while the rear-wheel uses 16 copper plates of 50 mm thickness. Within the gaps three parallel electrodes are placed similarly to the EM calorimeter in which the outer two electrodes have the high-voltage applied and the middle one is for readout.

Each wheel consists of identical modules (see Figure 3.10b), finer in the front- than the rear-wheel, which are wedge shaped and fixed to a central ring as well as the periphery fixture. The HEC supplies a $\Delta\Phi \times \Delta\theta$ resolution of 0.1×0.1 for the front- and 0.2×0.2 for the rear-wheel.

Forward calorimeter The FCal detector offers an η range coverage between 3.1 and 4.9. As it is close to beamline (and about 4.7 m away from the interaction point) it experiences a high particle flux which somewhat determines its design choices. For instance the LAr gaps are kept small in order to avoid ion build-up problems.

The calorimeter functions by the use of small-diameter rods in tubes which are parallel to the beam direction [61]. In total there are three 45 cm deep FCal modules enumerated by appending 1-3, the further from the interaction point they are. The absorber material for FCal 1 is copper while for FCal 2 and 3 tungsten is used to provide stronger containment of particles. Behind the last FCal module an additional brass shield is placed to reduce background and prevent damage from the end-cap muon system.

The FCal 1 consists of copper plates stacked behind each other. In total 12 260 holes are drilled through them, parallel to the beampipe in which an electrode structure consisting of a co-axial copper rod as shown in Figure 3.11a is installed. Around the rod between the copper plates gaps for the LAr are positioned. For FCal 2 and 3 two copper end plates with a thickness of 2.35 cm

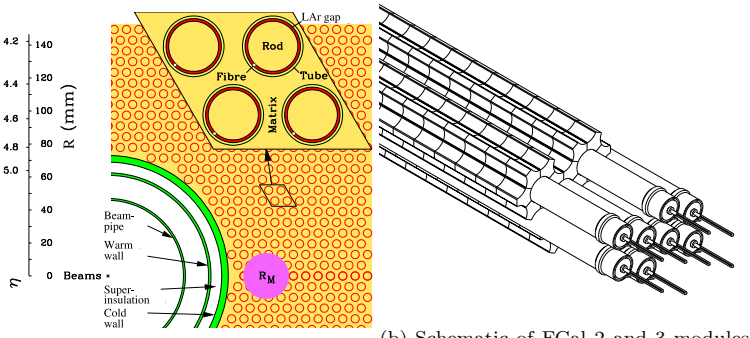

(a) Schematic of FCal 1 showing copper plates and tubes as well as LAr gaps for electrodes. Figure from [36].

(b) Schematic of FCal 2 and 3 modules showing structure and alignment of tungsten slugs with the contained rods also made from tungsten. Figure from [36].

Figure 3.11.: Schematics of FCal modules.

is filled with tungsten slugs. The rods spanned between them are similar to the FCal 1 but consist of tungsten.

3.2.5. Solenoid and toroid magnets

In order to determine the momentum of charged particles strong magnetic fields are needed that bend the trajectory of even high energy particles observably while they traverse the ATLAS detector. For this reason ATLAS uses in total four magnet systems which store a total of 1.6 GJ. It consists of one central solenoid after the ID, a central and two end-cap toroids as shown in Figure 3.12.

Solenoid magnet In order to balance the requirements of a strong magnetic field for the inner detector while reducing the amount of extra material budget in front of the calorimeters a single layer coil has been installed outside of the ID. The extra material introduced corresponds to approximately 0.66 radiation lengths and the solenoid magnet [36, 62] measures at a stored-energy-to-mass ratio of 7.4 kJ kg^{-1}. At the center the axial magnetic field provided is 1.998 T and uses a nominal operational current of 7730 kA.

The solenoid magnet consists of a wound high-strength Al-stabilised NbTi conductor and measures an inner and out diameter of 2.46 m and 2.56 m respectively. For charging and discharging the magnet only 30 min are needed.

Toroid magnets The magnetic field supplied for the calorimeters and muon detectors is supplied by the barrel and end-cap toroids [36, 63] and measures at 0.5 T and 1 T. The barrel toroid consists of eight coils encased in stainless-steel vacuum containers, which each have a length of 25.3 m. The diameter of the toroids measure at 9.4 m for the inner and 20.1 m for the outer. As the solenoid the toroids consist windings, which here are made of of Al-stabilised Nb/Ti/Cu conductors. The large size of the magnets requires a large time to cooldown which for 4.6 K is given by five weeks.

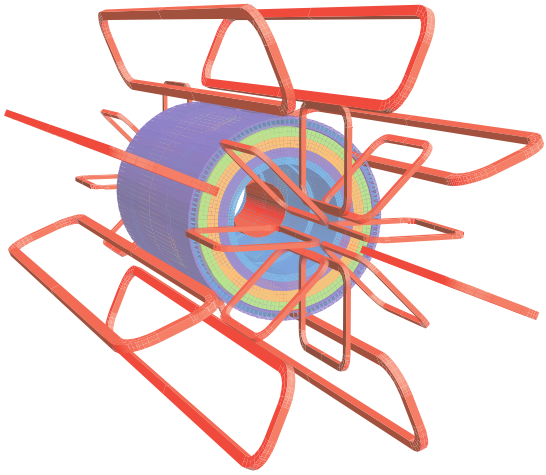

Figure 3.12.: Schematic of the ATLAS magnet windings and tile calorimeter steel. The solenoid windings are shown inside the tile calorimeter volumne. Figure from [36].

3.2.6. Muon spectrometers

The MS form the most outer part of the ATLAS detector. As muons are the only charged particle that cannot be stopped by the ATLAS calorimeters the MS offer a good opportunitiy to distinguish between them and other charged particles. This in turn makes the environment beyond the calorimeters comparably pure and free from most other particles created in the interaction point. In general the spectrometers are designed to detect charged particles (with $|\eta| < 2.7$) that traverse the whole ATLAS detector and measure its momentum. As high energy particles do not exhibit major bending in the magnetic field of ATLAS large spacing and distances are needed to get a good precision on the momentum. For this the MS offers a good resolution on tracks between 3 to 3000 GeV and ensures a 10 % p_{T} resolution for 1 TeV tracks.

The MS consists in the barrel region of three concentric cylindrical shells around the z-axis at radii of approximately 5, 7.5 and 10 m while in the end-cap region it is made from four wheels at z-distances of 7.4, 10.8, 14 and 21.5 m to the interaction point. Parts of the MS exhibit a gap at $|\eta| \approx 0$ to enable service lines for other detector parts.

The detectors consist mostly of MDT which make up the barrel region and all but the first (from the interaction point) layer of the end-cap MS. The first layer consists instead of a Cathode-strip Chamber (CSC) which is able to withstand a higher counting rate. The total MS offers a resolution of 40 µm into the bending plane and a resolution of 5 mm in the transverse plane due to differences in the readout. An important point is the required sagitta resolution for the p_{T} measurement: Along the z-axis of 500 µm a resolution of ≤ 50 µm is needed. This is achieved by knowing the position of strips and wires in the MDT and CSC to 30 µm resolution and requires a high-precision optical alignment system that constantly monitors the position and internal deformations (see also Figure 3.13). Additionally track-based alignment algorithms are used for cross-checks.

Every MDT consists of three to eight layers of drift tubes that are filled with Ar/CO_2 gas in a 93/7 ratio at 3 bar. The central anode wire is made of

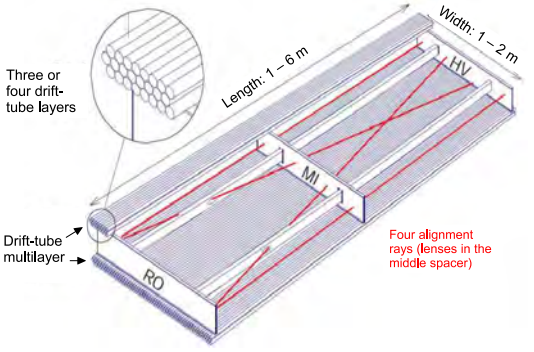

Figure 3.13.: Schematic showing MS Monitored Drift Tube Chambers (MDTs). Figure from [36].

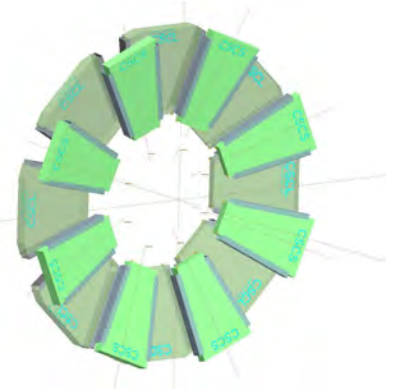

Figure 3.14.: Schematic showing MS CSCs. Figure from [36].

tungsten-rhenium and has a diameter of 50 µm. Every tube is operated at a potential of 3080 V. The tubes a very long drift time of 700 ns, which makes a separate triggering detector necessary, and resolves charged particles with a precision of 80 µm. In total a MDT can resolve 35 µm by using the combination of layered tubes.

In the forward region with $2 < |\eta| < 2.7$ the first wheel is using CSC as they are having a better rate capability: While MDTs can handle a rate of $150\,\mathrm{Hz\,cm^{-2}}$, for CSC this rate increases to $1000\,\mathrm{Hz\,cm^{-2}}$ which is especially required in the end-cap regions. The subsequent three wheels use then MDTs again. The end-cap MS only go until $|\eta| = 2.7$ for which such rate limitation is sufficient. Additionally CSCs offer a better time resolution. They are multiwire proportional chambers with cathode planes and are arranged in two disks with eight chambers each, see Figure 3.14. The wires are installed in radial direction but are parallel in each chamber with the central (radial) wire. The anode-cathode and wire-wire spacing is equidistant and a gas mixture of Ar/CO_2 in a ratio 80/20 is used. With an operation voltage of 1900 V a resolution of 60 µm is achieved.

As the readout of MDTs and CSCs is quite slow and triggering on muons with the MS is one of the design goals, additional fast trigger chambers are required

for triggering on muon tracks. They deliver information with 15 to 25 ns time resolution enabling triggering and also the tagging of beam-crossings which happen at 25 ns intervals. For this Resistive plate Chambers (RPCs) are used in the barrel region with $|\eta| < 1.05$ and in the end-cap (here with $1.05 < |\eta| < 2.4$) this is done by using Thin Gap Chambers (TGCs).

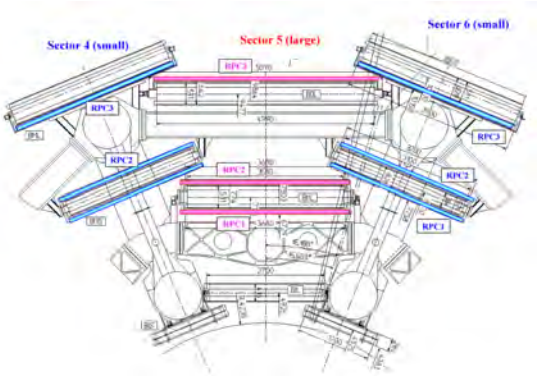

Figure 3.15.: Schematic showing MS RPCs. Figure from [36].

The RPC consists of three concentric cylindrical layers of gaseous parallel electrode-plate detectors. The two plates are made of phenolic-melaminic plastic laminate and separated at a distance of 2 mm by insulators. Similar to the multi-wire proportional chambers the electric field forms an avalanche along ionising tracks that will finally reach the anode and can be read-out. The gas in used between the plates is $C_2H_2F_4$/Iso-C_4H_{10}/SF_6 in a ratio of (94.7/5/0.3).

Finally the TGC offers beside a trigger signal also the azimuthal coordinate to compliment the MDTs in the three outer end-cap wheels (the MDTs are here aligned radially). They are also gaseous detectors filled with a quenching gas mixture of CO_2 and n-C_5H_{12}. The distance between the 50 µm wire and cathode is here smaller than the wire-to-wire distance with 1.4 mm in comparison to 1.8 mm. At an operational voltage of 2900 ± 100 V and with the comparably small wire-to-wire distance a good time resolution is achieved for triggering.

3.3. Triggering of event recording

As a bunch crossing at the LHC happens every 25 ns the data rate would exceed storage and processing capabilities available to the ATLAS experiment. A two-level trigger system is used to select events of interest [64] to reduce the rate of events written to data storage. The Level-1 Trigger (L1) is hardware implemented and uses a subset of detector information to reduce the event rate from the design bunch-crossing rate to an event rate of 75 to 100 kHz. After an event is accepted by the L1, the events are processed by the software-based High Level Trigger (HLT) with an output rate of about 1 kHz.

While a fast decision is important, information from different parts of the detector has to be taken into account as well as a variety of readout requirements. For instance does the time-of-flight of a charged particle to the MS exceed the bunch crossing interval and an EM calorimeter signal extends over about four bunch crossings. The multi-level triggering approach as well as local and central data buffers enable the selection of interesting events while keeping storage and bandwidth requirements reasonable.

The L1 is implemented by custom electronics and is designed to accept signatures as high p_{T} muons, electron/photon energy deposits, jets and hadronic decays of τ particles. Apart from particles it also accepts different thresholds of $E_{\mathrm{T}}^{\mathrm{miss}}$ or large deposits of E_{T}. In order to process the information fast it only handles a reduced subset of detector information. Namely for muons these are RPC and TGC in the MS and for the other signatures it is the EM calorimeter cluster information. The time restriction for the L1 is 2.5 µs after a bunch crossing. Within this timeframe the L1 system needs to make a decision whether to accept or reject the event. The ATLAS L1 has a target latency of 2 µs leaving the remaining time as contingency. Of this time about 1 µs is spent on signal propagation through cables alone. For this reason electronics are handling the decision as close to the subdetectors as possible and connection paths and cables to the central trigger processor are kept short.

The management of data and trigger information is handled by the Data Aquisition System (DAQ) which buffer the event data from subdetector specific readout electronics at the rate which the L1 provides. The data is buffered in pipeline memories and retained which also happens close to the detector. The HLT then requests data corresponding to pre-defined regions of interest. If a region of interest (characterized by coordinates, energy, or type of signatures) passes the HLT event-building is performed and passed by DAQ to the event filter. A positive HLT decision means that the event gets moved to data storage and is recorded.

In order to form its decision the L1 menu can contain up to 256 items where every item is a coarse requirement in input data. This can be the multiplicity of objects or flags indicating whether an event quantity like $E_{\mathrm{T}}^{\mathrm{miss}}$ has been passed. In contrast HLT can acces further information from the calorimets and spectrometers and also can combine them with the data from the ID to further refine the selection. This can for instance allow the reconstruction of decays as is required for detecting b decays. The HLT needs consequently more time to form a decision and consists largely of consumer networking hardware and computers making it highly configurable.

The time needed to process an event in the HLT is about 100 ms and reduces after its decision the event rate to less than 1 kHz.

Chapter 4.

Search outline

Why does the universe exist? *If we find the answer to that, it would be the ultimate triumph of human reason - for then we would know the mind of God*
— S. Hawking, A Brief History Of Time 1988

This chapter gives an outline of the search designed. It details the signal model used and its cross-section as well as the MC generation process. Since the work presented here is an indirect search, decays of the HNL used as *analysis channels* are presented and the overall search strategy for defining a signal region is summarized.

4.1. Signal model

The HNL considered for this analysis interacts with matter solely by mixing with active neutrinos as described in detail in Section 2.3. Production and decay of the HNL are therefore taking place through charged- and neutral-current interactions involving the active neutrino.

An ATLAS analysis can therefore focus the search on production mechanisms that are abundantly taking place in proton-proton collisions at $\sqrt{s} = 13\,\text{TeV}$ and that rely on the excellent final state particle identification of the ATLAS experiment. For this purpose on-shell W boson decays have been selected as a mean to produce HNLs. They decay to two quarks or to a lepton and neutrino from the same generation.

Figure 4.1 shows the corresponding Feynman diagrams of the selected analysis strategy: The active neutrino originating from the on-shell W boson mixes to the HNL N. The N decays itself by mixing back to an active neutrino which can then interact in a neutral or charged-current weak interaction. For this search only weak interaction is focused on as it generates a lepton whose charge is determined by the lepton number and chirality of the active neutrino to which N mixed to. This lepton is subsequently denoted by the term *subleading lepton*.

The signature described can directly probe the Majorana nature of the HNL (see also Section 2.1.4) by requiring that the lepton originating from the on-shell W should have the same charge as the subleading lepton. The W originating lepton is from now on denoted as *leading lepton*. Also originating from the charged weak interaction vertex is a virtual W^- boson (where the charge is

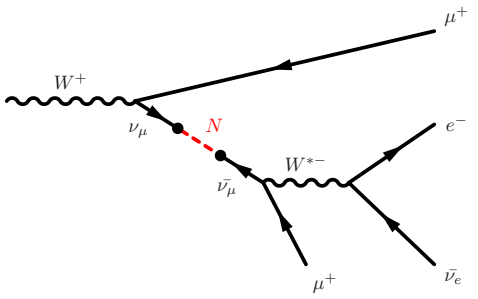

Figure 4.1.: Feynman diagram of the production and decay mechanism focused on in this analysis. Both production and decay takes place via mixing with active neutrinos. Shown is the muon-channel.

determined by the subleading lepton charge) which itself can decay leptonically or hadronically. By requiring it to decay leptonically to $e^-\bar{\nu}_e$ for the muon-channel and $\mu^-\bar{\nu}_\mu$ for the electron-channel a signature with no opposite-sign and same-flavor leptons is ensured. This largely helps reduce events originating from already known standard model processes and makes the analysis sensitive to the very weak HNL signal.

In this search a simplified model is considered in contrast to more complete ones as for instance the νMSM (see Section 2.4). The simplification lies in the exclusive mixing of HNLs with only one active neutrino flavor. As mixing angles under consideration are reduced the parameter space under scrutiny for the discovery or exclusion of HNLs is consisting only of the HNL mass and the single mixing angle $|U_{\alpha N}|^2$ for a flavor $\alpha \in \{\mu, e\}$. The mixing with τ flavor is also possible but has not been considered for this analysis due to the additional complications with τ identification.

Decays are therefore parameterized by the mass of the HNL and the mixing angle. In fact, as will be seen in Sections 4.1.2 and 4.1.3 these are the only two unknown parameters in the simplified model and results can therefore be represented on a two-dimensional plane of the two parameters as seen in Figure 4.2. The contours in the figure are calculated by the full sum of hadronic and leptonic HNL partial widths as is further described in 4.1.3.

4.1.1. MC signal sample production

As shown in Figure 4.2 the proper decay length of the HNLs is only dependent on the HNL mass itself and the mixing angle to active neutrinos. In order to measure HNLs with ATLAS, the proper decay length of the HNLs plays a major role as it has direct implications on the reconstruction and therefore detection efficiencies of the final state particles.

The samples are produced with Pythia 8.2 by simulating W production from proton-proton collisions with the `NNPDF 2.3 LO` Probability Density Function (PDF) and `A14` tune and forcing the gauge boson to decay to a lepton and a heavy neutral lepton. The heavy neutral lepton is then in turn forced to decay to the desired final state. For the latter decay, the proper decay length is specified in the configuration of Pythia. This has several advantages: for one, the travel distance of the HNL can be fully controlled and samples can be reweighed depending on theoretical calculations which are performed in Sections 4.1.2 and 4.1.3. To test the model, several samples are generated, each for a certain mass hypothesis with fixed proper decay length $c\tau$. The

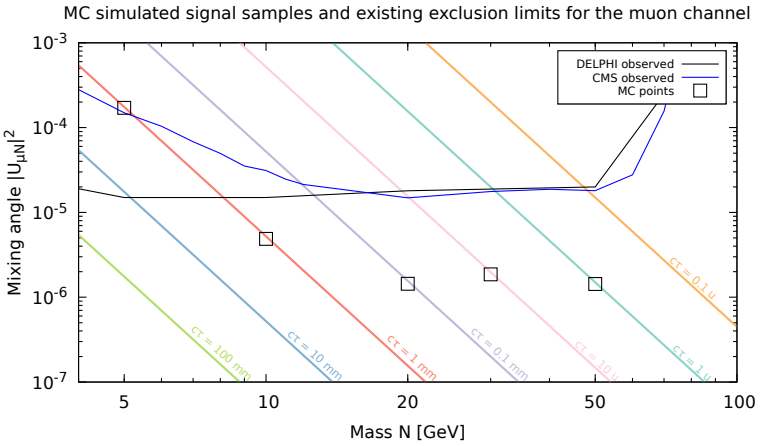

Figure 4.2.: Contours of the proper decay length $c\tau$ depending on the two free parameters $|U_{\alpha N}|^2$ in the model considered for this analysis. Also shown are existing exclusion limits from the Detector with Lepton, Photon and Hadron Identification (DELPHI) and CMS experiment for $\alpha = \mu$. The $|U_{\alpha N}|^2$ values plotted as *MC points* are noted in Table 4.1.

samples are hereafter weighted in order to represent the rectangles in Figure 4.2.

As will be shown in the next sections, the cross section (and therefore the weight normalization of each sample) is dependent on the mixing angle and the branching ratio of the HNL to $l_\alpha^\pm l_\beta^\mp \nu_\beta$ decay.

4.1.2. Cross-section

Following Figure 4.1 and generalizing it to both muons and electrons the cross-section of producing the aforementioned HNL signature can be determined. The cross section of the process of interest can therefore be parameterized as follows:

$$\sigma(pp \to l_\alpha^\pm l_\alpha^\pm l_\beta^\mp \nu_\alpha) = \sigma(pp \to W^\pm) \cdot \mathrm{BR}(W^\pm \to l_\alpha^\pm \nu_\alpha) \tag{4.1}$$

$$\cdot |U_{\alpha N}|^2 \cdot \left(1 - \frac{m_N^2}{m_W^2}\right)^2 \left(1 + \frac{1}{2}\frac{m_N^2}{m_W^2}\right) \tag{4.2}$$

$$\cdot \mathrm{BR}(N \to l_\alpha^\pm l_\beta^\mp \bar{\nu}_\alpha), \alpha \neq \beta \tag{4.3}$$

where $\alpha, \beta \in \{e, \mu\}$ for this analysis and $|U_{\alpha N}|^2$ is the mixing angle of the HNL to the active neutrino of flavor α. σ denotes the cross-section, BR the branching ratio and m_N, m_W the HNL and W masses respectively.

The cross-section for

$$\sigma(W^\pm \to l_\alpha^\pm \nu_\alpha) = \sigma(pp \to W^\pm) \cdot \mathrm{BR}(W^\pm \to l_\alpha^\pm \nu_\alpha) \tag{4.4}$$

is approximately $20.64 \pm 0.70\,\mathrm{nb}$ [65], while the branching ratio of the HNL decay as well as the mixing angle $|U_{\alpha N}|^2$ need to be calculated in dependence

of the mass and proper decay length $c\tau$. Assuming a Majorana neutrino the typical branching ratio for $\alpha = \mu$, $\beta = e$ is

$$\mathrm{BR}(N \to \mu^+ e^- \bar{\nu}_e) \approx 5.3\,\%. \tag{4.5}$$

The phase space term

$$\left(1 - \frac{m_N^2}{m_W^2}\right)^2 \left(1 + \frac{1}{2}\frac{m_N^2}{m_W^2}\right) \tag{4.6}$$

is of higher importance for $m_N \geqslant 20\,\mathrm{GeV}$ due to the more comparable masses of the HNL to the W boson.

In Section 4.1.3 further details are given on how the calculations are performed.

4.1.3. HNL decay

Decays of the HNL are treated in several phenomenological articles. With HNLs of masses below the weak scale being increasingly within reach of the LHC experiments, papers describing possible searches (e.g. [15, 66, 67]), HNL phenomenological and experimental constraints are now more focused on this part of the parameter space.

For the experimental considerations it is important to fully describe the HNL decay. Since the total decay width Γ is related to the proper decay length $c\tau$ via

$$c\tau = \frac{c\hbar}{\Gamma} \tag{4.7}$$

and the total width is a sum of the partial widths of it's decays

$$\Gamma = \sum_i \Gamma_i \left(m_N, |U_{\alpha N}|^2\right), \tag{4.8}$$

where $\{\Gamma_i\}$ is the set of partial widths for states the HNL can decay to, it is important to note that the partial widths are all depending on the mixing angle and HNL mass (compare e.g. [13]). Correspondingly there exists a relationship between the proper decay length and the two free parameters in the simplified model. For finding e.g. the mixing angle corresponding to

$$c\tau = 0.1\,\mathrm{mm} \tag{4.9}$$

it is therefore important to know the partial widths for every decay channel of the HNL. The $|U_{\alpha N}|^2$ corresponding to the total decay width

$$\Gamma = 1.973\,27 \times 10^{-9}\,\mathrm{GeV} = \frac{c\hbar}{0.1\,\mathrm{mm}} \tag{4.10}$$

can therefore be found by calculating all partial widths in its dependence to $|U_{\alpha N}|^2$ and m_N.

The decay channels are opened via charged- and neutral-current weak interactions. Hence, possible decays can be purely leptonic, completely invisible ($\nu\nu\nu$) or hadronic. An overview of the leptonic, invisible and hadronic decays to single mesons is given in [13, 68].

For this analysis, as mentioned before, the proper decay length of the HNL is important to determine the signal reconstruction efficiency with the ATLAS detector. A consequent treatment of all partial widths Γ_i is, as seen above, necessary to determine the HNL displacement from the interaction point in the detector. While [68] finds that for masses below 1 GeV the partial widths for

Table 4.1.: Overview of mixing angles corresponding to the simulated MC signal samples for the muon channel. The mixing angles are associated with the nominal signal strength $\mu_{\mathrm{SIG}} = 1$ in the exclusion fits. The best limits set by DELPHI in this mass range are at $|U_{\mu N}|^2 \approx 1 \times 10^{-5}$ to 3×10^{-5} .

m_N	5 GeV	10 GeV	20 GeV	30 GeV	50 GeV
$c\tau$	1 mm	1 mm	0.1 mm	10 µm	1 µm
$\lvert U_{\mu N}\rvert^2$	1.7×10^{-4}	4.9×10^{-6}	1.4×10^{-6}	1.9×10^{-6}	1.4×10^{-6}

single meson final states are sufficient in describing the hadronic decays, this analysis requires the full hadronic decay width as HNL masses investigated here span the 5 to 50 GeV range.

Given the multitude of possible decays and their contribution to the total width, the decay channels for this analysis are calculated by use of the `cHNLdecay` program. It has been written by the Author of this thesis [69]. For a given mass hypothesis $|U_{\alpha N}|^2$ is calculated for a fixed $c\tau$. The computed mixing angles for all mass hypotheses considered in this analysis are shown in Table 4.1. As a last step the branching ratio BR $\left(N \to l_\alpha^\pm l_\beta^\mp \nu_\beta\right)$, $\alpha \neq \beta$ can be determined as mixing angle $|U_{\alpha N}|^2$, the partial width and total width are known.

4.2. Analysis channels

As the mixing angle $|U_{\alpha N}|^2$ might be strongly suppressed for any α, depending on the active neutrino mass hierarchy [29, Table 2], the search is conducted for mixing to muons and electrons separately. While the search is performed for the simplified model with exclusive mixing to one angle, the two-channel approach enables the more exact interpretation for different HNL models and allows to set limits even if one mixing angle is possibly strongly suppressed.

As the focus of this analysis is a signal with very low cross section, an excellent identification of the final state leptons is necessary. For this reason, muons have traditionally been regarded as a good detection candidate. Here the two channels are comprised of muons and electrons in the final state due to the additional difficulties of correctly identifying the τ decay.

The two channels need separate treatment as the reconstruction and correct identification of electrons and muons differ within the ATLAS experiment. These differences include selection triggers, identification requirements, isolation of the leptons and scale factors between MC and measured data.

4.3. MC sample generation

The signal Monte Carlo (MC) samples used in the ATLAS simulations were generated using `Pythia8` [70] with a model of W production (of both charges) in 13 TeV pp collisions, with the W forced to decay into ℓ and a newly defined HNL particle N ($W^\pm \to \ell^\pm N$). N is assigned a mean proper decay length $c\tau = 0.001$, 0.01, 0.1 or 1 mm and decays as shown in Figure 4.1. The samples for the background are generated using `Sherpa` [71], `Powheg-Box` [72–74] and `Pythia` in versions `6` [75] and `8`. More specialized external packages as `EvtGen` [76] for bottom and charm hadronic decays, `Tauola` [77] for τ decays and `Photos` [78] for QED corrections are used and perform event reweighting. When `Powheg-Box` and `Pythia` are used in combination the generation of events

is done by using the former whereas the parton showers are modeled with the latter. The MC generators, external packages and the applied parton distribution functions used to produce the individual processes are listed in Table 4.2.

The signal samples used have been undergoing the full Geant-4 ATLAS detector simulation (FULLSIM) as a slight displacement may occur for a proper decay length of 0.1 to 1 mm. ATLAS also uses a fast alternative simulation approach (ATLAS Fast Simulation (ATLFAST)) which uses templates for calorimeter clusters instead of simulating the detailed contained showers. Background samples can be produced both with fully simulated events as with ATLFAST where correct simulation behavior was previously verified by the experiment. As this search uses electrons and also the isolation of charged objects the full simulation of signal samples was used as a precaution. In later internal ATLAS comparisons ATLFAST samples were also produced for the experiment but not used in this thesis. Tests concluded that the prompt signature is nearly identical in both cases and reconstruction efficiency is not mentionably affected. Later searches can therefore make use of a reduction of simulation costs.

4.4. Optimization approach

As will be described in more detail in later sections this search consists of requirements on the objects it selects (Section 5) and cuts on event properties measured. Together they form the signal region (Section 6) and determine how many events from known standard model processes (from now on called *background*)are contaminating the expected signal events.

It is desirable to maximize the ratio of the signal to the background contamination which in turn maximizes the significance of the result of this search. This ratio is for now called significance and is an approximation of the expected discovery potential of a Poisson counting experiment. Most of the backgrounds are simulated by the use of MC samples that inherently carry a statistical uncertainty. As the analysis will cover a phase space with little available MC, the significance can be estimated, compare to [86] eq. (20), by

$$S = \left\{ 2 \cdot \left((s+b) \cdot \ln\left(\frac{(s+b)\cdot(b+\sigma_b^2)}{b^2 + (s+b)\cdot\sigma_b^2} \right) - \frac{b^2}{\sigma_b^2} \cdot \ln\left(1 + \frac{\sigma_b^2 \cdot s}{b\cdot(b+\sigma_b^2)} \right) \right) \right\}^{\frac{1}{2}} \tag{4.11}$$

where s denotes the amount of signal events, b the total amount of background events and σ_b the statistical uncertainty on b. This equation behaves approximately as $s/\sqrt{b+\sigma_b^2}$ which ensures that optimized cuts are not simply favoring weakly modeled phase spaces with high uncertainty σ_b.

Optimization of the selection in the two channels is determined after establishing a set of preliminary cuts. In addition to the basic object selection described in Section 5, and selection triggers, leptons must satisfy flavor and charge requirements, such that the visible event consists of exactly $l_\alpha^\pm l_\alpha^\pm l_\beta^\mp$.

Furthermore, a requirement is imposed on the three-lepton invariant mass:

$$40\,\text{GeV} < M(_\alpha, l_\alpha, l_\beta) < 90\,\text{GeV}. \tag{4.12}$$

This is the signal region of interest where $M(_\alpha, l_\alpha, l_\beta)$ is chosen to be consistent with the mass of the W boson after allowing for missing energy being caried away by the neutrino.

The optimization of lepton p_T, isolation requirement of the lepton object and E_T^miss are then performed in sequence after applying these preliminary

Table 4.2.: MC generators and parton distribution functions applied to produce the signal and background processes.

Process	**MC generator**	**PDF sets and tunes**
Signal ($\ell = \mu$)	`Pythia8` (v8.210) [70]	NNPDF 2.3 LO [79], A14 tune [80]
	`EvtGen` (v1.2.0) [76]	
Signal ($\ell = e$)	`Pythia8` (v8.212)	NNPDF 2.3 LO, A14 tune
	`EvtGen` (v1.6.0)	
$t\bar{t}$	`Powheg-Box v2` (r3026) [72–74]	NLO CT10 in the ME calculation [81]
	`Pythia` (v6.428) [75]	CTEQ6L1 [82], Perugia 2012 tune [83]
	`EvtGen` (v1.2.0)	
	`Tauola` (v27feb06) [77]	
	`Photos` (v2.09) [78]	
single top	`Powheg-Box v1` (r2856)	NLO CT10 in the ME calculation
	`Pythia` (v6.428)	CTEQ6L1, Perugia 2012 tune
	`EvtGen` (v1.2.0)	
	`Tauola` (v27feb06)	
	`Photos` (v2.09)	
ttV, $V = W, Z$	`MadGraph5_aMC@NLO` (v2.2.2.p6) [84]	NNPDF 2.3 LO, A14 tune
	`Pythia8` (v8.186)	NNPDF 2.3 LO α_s 130 QED, A14 tune
	`EvtGen` (v1.2.0)	
WW, ZZ, WZ (semi-leptonic decay)	`Sherpa` (v2.1.1) [71]	CT 10
WZ, ZZ (leptonic decay)	`Powheg-Box v2` (r2819)	NLO CT10 in the ME calculation
	`Pythia8` (v8.210)	CTEQ6L1, AZNLO tune [80]
	`EvtGen` (v1.2.0)	
Z+jets ($m_{ll} \geq 40\,\text{GeV}$), W+jets	`Sherpa` (v2.2.1)	NNPDF 3.0 NNLO [85]
Z+jets ($10 \leq m_{ll} \leq 40\,\text{GeV}$)	`Sherpa` (v2.1.1)	CT 10
Triboson	`Sherpa` (v2.2.1)	NNPDF 3.0 NNLO

cuts. The detailed procedure for the optimization is described in Sections 6.2 and 6.3.

Chapter 5.

Object requirements

The important thing is to not stop questioning.
Curiosity has its own reason for existing.
— A. Einstein, 1955 [87]

5.1. Reconstruction of leptons and their identification

Particles created in the *pp* collisions in the ATLAS detector are traversing the detector and leave signals in different layers of the detector components. The ability to accurately reconstruct and identify objects based on these signals is crucial for analysis of the data. In order to optimize the selection criteria, the algorithms are developed to keep up with the changing energy and pile-up conditions of the collisions. In this section, the reconstruction and identification algorithms for muons, electrons, jets and missing transverse energy are presented. Furthermore, the methods used for isolation criteria and overlap removal are examined.

Charged leptons in ATLAS consist of a track that has been reconstructed from hits in the inner detector [88].

For the tracking in the inner detector hits form three dimensional space points (in the SCT and PIX clusters are formed that make up space points), which are used to find the seeds of possible tracks and to actually create the candidate tracks matching with the created seeds. Among the track candidates a likelihood selection is applied in form of a *track scoring* strategy taking into account different quality criteria as for instance the existence and position of holes in different subdetectors. This is done to avoid mis-identification of uncorrelated hits and reduce the amount of overlapping tracks that share a large amount of hits. The latter is achieved by attributing shared hits mostly to the track with the highest score followed by a refit of the tracks given the newly assigned hit configurations. Given a certain cut-off value, tracks can this way be removed from the candidates iteratively.

5.1.1. Muon reconstruction and identification

Muons are reconstructed in the inner detector as described above for general charged objects. Additionally information from the MS is though used [89]

in order to create a muon object. There are various muon types defined in ATLAS that rely on different information from the MS, ID, and additional detector information. Tracks reconstructed in the MS need to have at least two hits located there to do so. The general requirements on muon tracks and are listed in table 5.2. One distinguishes between four types of muons as they influence the track reconstruction. The exact requirements for the different types are shown in table 5.1.

Table 5.1.: Muon type classifications of track requirements for reconstructing muon objects in the ATLAS experiment. As stated in [89].

Type	**Track requirements**
Combined	reconstruct MS and ID tracks separately first, then form combined track from both and refit with all hits (MS hits may be added to improve fit goodness)
Segment-tagged	reconstruct track in ID and extrapolate to MS, needs to have track segment in monitored drift tube chamber or cathode strip chamber (for $\|\eta\| > 2$) of the MS
Calorimeter-tagged	reconstruct track in ID that is matched in space to energy deposited in calorimeter that needs to be compatible with a minimally-ionizing particle
Extrapolated	reconstruct MS track that needs to be compatible with the interaction point and take into account energy loss in calorimeters, three hits in the MS are required for the forward region

The type is though uniquely resolved with preference given to what is called a *combined* muon over segment- and calorimeter-tagged objects. Finally the distinction between combined and extrapolated type is performed based on fit quality and hits.

The object identification criteria that was chosen for this analysis requires that the muons are *combined* as this offers the best object quality. Apart from the track reconstruction muons for this analysis are required to pass an identification Working Point (WP) called *loose* where loose is defined by the MuonSelectorTool and is intended to keep a very high fraction of prompt (signal-like) muon objects while rejecting candidates from light-hadron decays (background-like) such as pions or kaons. Given the combined muon type required for this analysis the variables used to differentiate between the different WPs are

- $\frac{\left|\left(\frac{q}{p}\right)_{\mathrm{MS}} - \left(\frac{q}{p}\right)_{\mathrm{ID}}\right|}{\sqrt{\Delta\left(\frac{q}{p}\right)^2_{\mathrm{MS}} + \left(\frac{q}{p}\right)^2_{\mathrm{ID}}}}$
- $\frac{|p_{\mathrm{T}}^{\mathrm{MS}} - p_{\mathrm{T}}^{\mathrm{ID}}|}{p_{\mathrm{T}}^{\mathrm{combined}}}$
- normalized χ^2 of combined track fit.

Additional requirements are imposed on the transverse momentum and pseudorapidity of the muons such that $p_{\mathrm{T}} > 4\,\mathrm{GeV}$ and $|\eta| < 2.5$. No further requirements are made apriori on the Impact Parameter (IP) of the track, although in the muon channel the muon with leading p_{T} will be required to pass a selection requirement on the IP (see Section 6.4).

Table 5.2.: Technical requirements for a track identified as a muon. The requirements are defined by the hits in the three inner detector subdetectors: PIX, SCT and TRT. The number of TRT outliers on the muon track is denoted $n_{\mathrm{TRT}}^{\mathrm{outliers}}$, the number of TRT hits on the muon track is denoted $n_{\mathrm{TRT}}^{\mathrm{hits}}$, and n is defined as the sum $n := n_{\mathrm{TRT}}^{\mathrm{outliers}} + n_{\mathrm{TRT}}^{\mathrm{hits}}$.

Variable	**Condition**
Number of PD hits+number of crossed dead PD sensors	> 0
Number of SCT hits+number of crossed dead SCT sensors	> 4
Number of PD holes + number of SCT holes	< 3
n, where $0.1 < \|\eta\| < 1.9$	> 5
$n_{\mathrm{TRT}}^{\mathrm{outliers}}$, where $0.1 < \|\eta\| < 1.9$	$< 0.9 \cdot n$

5.1.2. Electron reconstruction and identification

Electron reconstruction in the central region of ATLAS is performed by matching energy deposits in the electromagnetic calorimeter with tracks formed in the inner detector. The electron reconstruction procedure consists of four steps: seed-cluster reconstruction; track reconstruction, electron specific track fit, and electron candidate reconstruction [90].

In the seed-cluster reconstruction, a sliding window algorithm is used to search in $\phi \times \eta$ space for energy clusters with total cluster E_{T} above 2.5 GeV called *seeds*, where the size of the window corresponds to the granularity of the second layer of the electromagnetic calorimeter. For the energy calculation the energy deposited in the different layers of the calorimeter are summed up. The actual clusters are then formed from the candidates around the seeds using a clustering algorithm [91]. The clustering algorithm allows the removal of duplicates where the candidate with the highest E_{T} remains.

The track reconstruction is achieved in three steps: pattern recognition, ambiguity resolution and TRT extension. First, the pattern recognition uses the pion hypothesis for energy loss due to interactions with the detector material. If a track seed fails the track requirements by the pion hypothesis (seed cannot be extended to at least seven hits in different layers of the silicon detector), but has $p_{\mathrm{T}} > 1$ GeV the electron hypothesis is attempted. This one allows for up to 30 % energy loss at intersections of the track with detector material. Track candidates originating from the pattern recognition are used in the global ATLAS χ^2 track fitter [92] using the hypothesis used for the pattern recognition. If a track fails this using the pion hypothesis a retry is attempted with the electron hypothesis. After this the track is used as an input to find compatible TRT measurements and therefore extend the track [93].

In the electron specific track fit, the fitted tracks are matched to electromagnetic clusters using the distance in η and ϕ between the position of the track after extrapolation in the calorimeter middle layer and the cluster barycentre. The matching condition accounts for both energy loss and the number of precision hits in the silicon detector. Finally, the electron candidate is reconstructed using a matching of the track candidate to the cluster seed.

Electron Identification Criteria (EID) are applied on the reconstructed electron candidates in order to select electron samples with different levels of background contamination. The identification is done by a likelihood tool which is based on a multivariate analysis technique that evaluates several properties of the electron candidate simultaneously in order to distinguish between prompt (signal-like) and non-prompt or secondary (background-like) objects for instance originating from hadronic jets or photon conversion. The proper-

ties used for the likelihood calculation are listed in [90, Table 1]. The WPs also make use of the IBL hence requiring a hit in it. Default ATLAS working points are named *Loose + B-layer*, *Medium*, *Tight* and are referring to the rejection levels of non-prompt objects. The three working points are in a subset relationship to each other, meaning that all objects passing *Tight* identification requirements will also pass *Medium* identification.

The base WP used in this analysis for the electron identification is *Loose + B-layer* (sometimes shortened to `Loose` as the B-layer hit is required). The EID working point requires a signal efficiency of 90 % for electrons candidates with $E_{\mathrm{T}} \approx 25\,\mathrm{GeV}$.

Additionally a selection is made on the kinematics of an object requiring $p_{\mathrm{T}} > 7\,\mathrm{GeV}$ for data measured in 2015 and $p_{\mathrm{T}} > 4.5\,\mathrm{GeV}$ for data measured in 2016. The pseudorapidity is required to be within the calorimeter acceptance $|\eta| < 2.47$. Electrons with tracks within the region where the barrel and end-cap calorimeters meet, the so-called calorimeter transition region, are also vetoed. This region is characterized by $1.37 < |\eta| < 1.52$.

5.2. Jets

The experimental signature of jets is characterized by locally-calibrated topological clusters (topo-cluster), which are built from calorimeter cells, associated with bundles of tracks in the ID. The anti-k_t algorithm is used to perform jet reconstruction with radius parameter $R = 0.4$, with the topo-clusters as input. Jet energies are determined by a calibration scheme using the Jet Energy Scale (JES) correction to recover the true 4-vector of the original jet and the electromagnetic scale to calibrate calorimeter level energies [94]. Jets are in this analysis required to have p_{T} of at least 20 GeV and to be contained in a range of $|\eta| < 4.5$.

To select jets from pile-up a Jet Vertex Tagger (JVT) tool [95] is used. The tool performs a multi-variate differentiation that is largely based on the fraction of p_{T} of a given track associated to the jets that originates from the primary interaction point in contrast to the total scalar p_{T} sum of a jet. The JVT tool is operated for this search at a working point corresponding to a 92 % efficiency in tagging jets and allowing for a observed fake rate of 2 % from pile-up jets.

To filter out and tag b jets specifically, a multi-variate approach is used [96]. The tagger used for this analysis (the so-called `FixedCutBEff_77` working point) is at a working point efficiency of 76.97 % in tagging b jets and a purity of 95.17 %, hence allowing for 4.83 % jets that are mistakenly defined as b jets.

5.3. Missing transverse momentum

Missing transverse momentum is defined as the negative vector sum of transverse momenta of reconstructed physics objects and $E_{\mathrm{T}}^{\mathrm{miss}}$ is the magnitude of such vector. The physics objects considered are electrons, photons, muons, taus and jets (hard terms). It is an essential variable for many physics analyses, since SM neutrinos and some theorized beyond the SM particles escape the detector without producing a signal. Using the SM background only hypothesis, the $E_{\mathrm{T}}^{\mathrm{miss}}$ will only originate from SM neutrinos. Ideally, the $E_{\mathrm{T}}^{\mathrm{miss}}$ should be determined using the final state particles from the hard pp interaction only. In practice, the detector phase space, reconstruction efficiencies, and the presence of pile-up interaction from other pp vertices in the same bunch crossing event will affect the measurement [97].

The missing transverse energy can be algorithmically calculated and candidates for this in ATLAS are Calorimeter-based Soft Term (CST) and ID Track-based Soft Term (TST) calculations.

The $E_{\mathrm{T}}^{\mathrm{miss}}$ applied in the analysis uses a track-based soft-term in combination with calorimeter-based measurements TST which is the primary method of $E_{\mathrm{T}}^{\mathrm{miss}}$ calculation in Run 2 for ATLAS. The main advantage of this approach is the excellent energy resolution in the calorimeters and the wide coverage in $|\eta|$, it is also more stable with increasing pile-up.

5.4. Isolation

Further rejection of background is obtained by requesting objects to be isolated. Isolation criteria for a certain track are defined around a chosen spatial cone around the track where the input is the p_{T} of other tracks or calorimeter deposits E_{T} in the cone. Particles originating from a jet are likely to have many other tracks in close proximity, so objects originating from a jet are characterized as poorly isolated.

There are mainly two variables used for defining the isolation of an object: *Calorimetric isolation* $E_{\mathrm{T}}^{\Delta R}/E_{\mathrm{T}}$ where the nominator denotes the scalar sum of E_{T} for tracks in a spatial radius of $\Delta R = \sqrt{\Delta\eta^2 + \Delta\phi^2}$ around the electron cluster after correcting for electron leakage and pile-up. *Track isolation* $p_{\mathrm{T}}^{\Delta R}/E_{\mathrm{T}}$ where the nominator denotes the sum of p_{T} for tracks in a spatial radius of

$$\Delta R = \min\left\{0.2, \frac{10\,\mathrm{GeV}}{E_{\mathrm{T}}}\right\}. \tag{5.1}$$

For the latter the track needs to originate from the primary interaction vertex and needs to pass track quality requirements ensuring that the isolation is calculated from actual tracks in the detector rather than coincidentally matched patterns. Detailed requirements are listed in [90].

The isolation WPs are then defined as either targeted efficiency requirements given a certain background (usually $Z \to ee$ samples) or fixed cut requirements that define an upper limit on one or both of the two variables.

Isolation WPs considered here using a targeted efficiency are `Loose Track Only`, `Loose`, `Gradient Loose` and `Gradient`. They are therefore parameterized by η and p_{T} of the track to achieve in all bins of this two-dimensional space the efficiency.

For this analysis we are using a `Loose` isolation working point for all leptons. This is the case for both analysis channels. The impact of the pre-defined isolation working points on signal and background MC samples is examined in detail in Sections 6.2.2 and 6.3.2.

5.5. Overlap removal

Intrinsic to the pattern recognition and reconstruction of tracks in the detector is the possibility to construct different particles from the observed hits. When the same physical particle is reconstructed as different analysis objects, it is necessary to resolve the ambiguity which is called *overlap removal*. The technique for obtaining this is based on proximity ΔR considerations of the objects. The overlap removal is performed for muons, electrons and jets with respect to each other. In table 5.3, the procedure for overlap removal is schematically described.

It is important to note that b jets are protected against overlap removal as b decays can create rather isolated muons or electrons with arbitrary charge configuration leading to a bigger pollution of our signal region by heavy quark backgrounds. The potential b jet is therefore preserved and at a later step the whole event will be vetoed on as it contains a b jet (see Section 6).

Table 5.3.: Overlap removal requirements between reconstructed muons, electrons and jets with respect to each other. No overlap removal is performed with reconstructed τ objects or between b-jets and jets.

Overlap removal: electrons and jets		
1.	Jet removed	Jets within $\Delta R < 0.2$ of an electron track. Unless it is a b-jet or has 20% higher p_T than the electron.
2.	Electron removed	Electrons within the jet sliding cone defined by $\Delta R < \min\left\{0.04 + \frac{10\,\text{GeV}}{p_\text{T}(e)}, 0.4\right\}$.
Overlap removal: muons and jets		
1.	Jet removed	Same requirement as for electrons. Unless it is a b-jet or the jet has three or more tracks.
2.	Muon removed	Same requirement as for electrons.
Overlap removal: muons and electrons		
1.	Muon removed	When a calorimeter tagged muon shares the same tracks as an electron.
2.	Electron removed	If it shares the same track with a remaining muon.

5.6. Minimal kinematic requirements for lepton objects

This analysis requires a set of minimal requirements that are applied to all objects before the definition of a signal region. By doing so, we comply with predefined working points which allows us to take full advantage of so called Scale Factors (SFs) which are derived by the ATLAS experiment to account for differences in the simulated and measured data.

Therefore we are requiring

- $p_\text{T}(\mu) \geq 4\,\text{GeV}$
- $p_\text{T}(e) \geq 7\,\text{GeV}$ for 2015 datasets
- $p_\text{T}(e) \geq 4.5\,\text{GeV}$ for 2016 datasets
- $|\eta(e)| \leq 2.47, |\eta(\mu)| \leq 2.5$
- veto $1.37 < |\eta(e)| < 1.52$

as a baseline definition.

Chapter 6.

Signal selection

To seek out one line in his books would be to go looking for a needle in a meadow
— Thomas More, 1532 [98]

The search for HNL is conducted in the $W^{\pm} \to \ell^{\pm}\ell^{\pm}\ell'^{\mp}\nu_{\ell'}$ final states for $\ell, \ell' = \mu, e$ with $\ell \neq \ell'$, which exploit the Majorana nature of the HNL. By requiring the final state to have three isolated leptons and no opposite-sign same-flavor lepton pairs, background processes as Drell-Yan pair production, W+jets and $t\bar{t}$ are efficiently rejected. Furthermore, the trilepton invariant mass is an important variable variables in the signal selection. The trilepton invariant mass is constructed from the three visible final state leptons, which will peak just below the mass of the W boson at 80 GeV as the neutrino is removing some of the energy from the system which appears as $E_{\mathrm{T}}^{\mathrm{miss}}$. The dilepton invariant mass is determined as the invariant mass of the subleading ℓ and the additional ℓ' which will again result in a mass distribution peaking slightly below the mass of the HNL. When the mass of the HNL is much smaller than the mass of the W boson, the leading lepton will arise from the W decay and the subleading lepton is originating from the HNL decay. In this search the dilepton invariant mass distribution is used as the final discriminant to perform hypothesis tests on the background and signal+background models. In appendix C the correct classification of the leading ℓ as originating from the W boson is studied. As the final discriminant is only applied to bin the sample distributions and no cut is applied a possible impact on this search is therefore negligible.

The proper decay length, see Section 4.1.1, used to generate the signal samples is: $c\tau = 1\,\mathrm{mm}$ for $m_N = 5$ and 10 GeV, $c\tau = 0.1\,\mathrm{mm}$ for $m_N = 20\,\mathrm{GeV}$, $c\tau = 10\,\mu\mathrm{m}$ for $m_N = 30\,\mathrm{GeV}$, and $c\tau = 1\,\mu\mathrm{m}$ for $m_N = 50\,\mathrm{GeV}$. The relatively *long* lifetime for the $m_N = 5$ and 10 GeV samples is chosen in order to

investigate the particular mass versus mixing parameter space region which is not yet excluded by previous experiments.

The signal selection, which optimizes the number of signal events relative to the number of background events, is defined for the muon and electron channels separately in this section.

The SM backgrounds that can lead to a signature mimicking that of the prompt heavy neutral lepton particle consist of two broad categories, irreducible and reducible types. The irreducible background is composed of exactly three leptons, where the only SM source is diboson events of the type WZ or ZZ, with all bosons decaying leptonically. In the case of ZZ, one lepton must fall out of detector acceptance. This background type is largely negligible due to the small cross section of such events, and the need for reconstructed charge mis-identification when selecting two same flavor and same charge leptons.

Reducible background events all contain sources of mainly *fake* leptons, that is muons or electrons originating from hadronic jets which are not identified as such but reconstructed as separate lepton objects. A large proportion of such events come from W+jets data. Additional contributions from Z+jet, $t\bar{t}$, single top, and diboson events (WW, WZ and ZZ) with hadronic decays must also be accounted for.

All backgrounds discussed above are evaluated and analyzed with MC, as described in Section 4.3. The final selection of a signal region in which models are tested is optimized based on the significance. As the search covers a phase space with little available Monte Carlo, the significance is estimated by equation (4.11) as referenced in Section 4.4. This equation behaves approximately as

$$s/\sqrt{b+\sigma_b^2} \tag{6.1}$$

tries to ensure that optimized cuts are not simply favoring weakly modeled phase spaces with high uncertainty σ_b. However as a hypothesis based search strategy for background-only and signal-plus-background models is used (see Section 7) the estimated significance is not the only discriminat for optimizing the signal region. The statistics available for the background-only model and the relative uncertainty on it are taken into account as well. This importance arises especially as a data-driven template fit of the backgrounds with more than one fake lepton is applied. Hints for the benefit of this approach are already visible in some of the optimization plots in this section that exhibit discontinuities due to the low statistical sample size of e.g. the W+jets sample.

The signal yield is specific to each mass point and decay length in consideration.

While the triggers used for the preselection to optimize the signal region cuts are listed in Section 6.1 the final decision for triggers was made in regard to lowest possible single lepton or dilepton trigger thresholds. For the muon channel this is the lowest possible dimuon trigger while for the electron channel this is the single electron trigger. For the electron channel additional higher electron thresholds have to be requested as SF needed for the correct scaling of MC were derived only for certain trigger combinations.

For the muon channel, final events are selected with `HLT_mu18_mu8noL1` for the 2015 datasets and `HLT_mu22_mu8noL1` for the 2016 ones. For the electron channel events are selected with a logical OR between `HLT_e24_lhmedium`, `HLT_e60_lhmedium` and `HLT_e120_lhloose` for the 2015 dataset and `HLT_e26_lhtight_nod0_ivarloose`, `HLT_e60_lhmedium_nod0` and `HLT_e140_lhloose_nod0` for the 2016 dataset for all mass points.

6.1. Preselection for optimization

Events are selected using single- and multi-lepton triggers in muon and egamma stream. For the optimization of lepton p_{T} and $E_{\mathrm{T}}^{\mathrm{miss}}$ cut all triggers selected by a previous data processing step were allowed, not filtering between the channels. These triggers have been used to reduce the amount of data storage and processing time considerably and are listed in Table 6.1. Triggers listed there encode in their name the object they trigger on and the p_{T} threshold in GeV. For instance `mu18` stands for a muon with a p_{T} of at least 18 GeV. Additionally encoded are the following attributes: `noL1` does not require the associated L1 trigger to have passed, `lhmedium` encodes the medium likelihood requirement on the electron identification and `nod0` foregoes the requirement of a maximal $\mathring{0}$ separation from the beamline. The HLT has a turn-on curve depending on the object p_{T}. Usually objects are requested to have a p_{T} of about 1 GeV above the specified trigger threshold to be positioned on top of the curve. This is in later sections referred to the as *trigger offline requirement*.

Table 6.1.: Triggers used for preselection: Selecting events on these triggers reduces data storage and processing time considerably for cut optimization and further processing.

Trigger name	**Dataset**
`HLT_mu18_mu8noL1`	2015
`HLT_mu22_mu8noL1`	2016
`HLT_e24_lhmedium`	2015
`HLT_e60_lhmedium`	2015
`HLT_e120_lhloose`	2015
`HLT_e26_lhtight_nod0_ivarloose`	2016
`HLT_e60_lhmedium_nod0`	2016
`HLT_e140_lhloose_nod0`	2016
`HLT_e17_lhloose_nod0_mu14`	2016
`HLT_e17_lhloose_mu14`	2016

Apart from the triggers listed above, optimization is conducted while requiring all objects to pass the default requirements listed in the previous section. Requirements for the transverse momentum and pseudorapidity of the leptons are imposed according to the efficiency SF recommendations for the 2015 and 2016 datasets. The lower p_{T} threshold for electrons is 7 GeV for 2015 data and 4.5 GeV for 2016 data. For muons, the lower p_{T} threshold is 4 GeV for both 2015 and 2016 data. The pseudorapidity requirement for electrons is $|\eta| < 2.47$ and further electrons inside the crack regions $1.37 < |\eta| < 1.52$ are vetoed. For muons, the pseudorapidity requirement is $|\eta| < 2.5$.

6.2. Muon channel

Optimization of the muon channel selection is determined after establishing a set of preliminary cuts. In addition to the basic object selection described in Section 5.1, leptons must satisfy flavor and charge requirements, such that the event consists of exactly $\mu^{\pm}\mu^{\pm}e^{\mp}$.

Furthermore, a requirement is imposed on the three-lepton invariant mass $M(\mu_{\mathrm{lead}}, \mu_{\mathrm{sublead}}, e)$ in form of a lower and upper boundary of 40 GeV and 90 GeV respectively. This is the interesting signal region where the three-lepton invariant mass is consistent with the mass of the W boson.

An important variable is the dilepton invariant mass, $M(\mu_{\text{sublead}}, e)$, which is correlated with the mass of the HNL. For the final background-only and signal-plus-background models, shown in Section 7, no separate dilepton invariant mass cut is applied for the different masses. Instead the final observable is defined as a $M(\ell_{\text{sublead}}, \ell')$ plot from 0 to 50 GeV.

In appendix E, the simulated events are compared to measured data collected by ATLAS in 2015 and 2016. The plots are produced for preselection cuts in order to stay blinded. Further signal region cuts are also applied but the plots are blinded by an additional blind-cut that inverts the trilepton mass $M(\mu_{\text{lead}}, \mu_{\text{sublead}}, e)$. One can observe an agreement in terms of total events but also a slight shape difference at all levels. At later cut stages the limited statistics in each bin of the variables are visible.

The optimization of the different cuts applied for the muon channel selection, is based on the preliminary cuts shown in the top of Table 6.2 while the final cut selection is comprised of all the cuts in the same table.

Table 6.2.: Summary of the final optimal cuts for the muon channel. The d_0 significance is only applied to the *leading* muon. The first five cuts form the preliminary cuts which were used as a starting point for the cut optimization.

	Muon channel: Final signal region requirements
	Preselection triggers as listed in Table 6.1
Prelim. cuts	$\mu == 2$ (loose, combined) and $e == 1$ (loose LLH) $\lvert\Delta z_0 \sin(\theta)\rvert(l) < 1\,\text{mm}$, $\lvert d_0/\sigma(d_0)\rvert(\mu_{\text{lead}}) < 3$ $p_{\text{T}}(e) \geq 4.5$ (2016), 7 (2015), $p_{\text{T}}(\mu) \geq 4$ $\lvert\eta(e)\rvert \leq 2.47, \lvert\eta(\mu)\rvert \leq 2.5, \text{veto} : 1.37 < \lvert\eta(e)\rvert < 1.52$ $M(\mu, \mu, e) < 90\,\text{GeV}$ $M(\mu, \mu, e) > 40\,\text{GeV}$
Trigger	`HLT_mu18_mu8noL1` (2015) `HLT_mu22_mu8noL1` (2016)
	Trigger matching $\mu^{\pm}\mu^{\pm}e^{\mp}$ $p_{\text{T}}(\mu_1) \geq 23\,\text{GeV}$ $p_{\text{T}}(\mu_2) \geq 14\,\text{GeV}$ μ_1 `loose` isolation μ_2 `loose` isolation e `loose` isolation b jet veto $E_{\text{T}}^{\text{miss}} < 60\,\text{GeV}$

6.2.1. Lepton p_{T}

In this section, the transverse momentum requirements on the leading and subleading muon as well as the electron are examined. Ideally, the optimal cut on p_{T} is determined as the cut that yields the highest significance as defined in Eq. (4.11).

Due to the applied triggers for the 2015 and 2016 datasets, which impose requirements on the lepton p_{T}, there is a lower threshold for which p_{T} cuts can be applied. For the muon channel, the triggers which are found to give the largest percentage of signal events recorded are shown in Table 6.3. Due to

technical requirements a preselection of a variety of triggers has been applied at this step that include the final triggers for the muon- and electron channel. Plots in this section therefore show a wide baseline of triggers. This is also responsible for little variation of significance at lower p_{T}.

Table 6.3.: Trigger requirements and relevant p_{T} requirements for the trigger used in the event selection for the muon channel for m_N = 5 to 50 GeV. The requirements imposed on both the 2015 and 2016 datasets are shown.

Trigger for $W \to \mu^{\pm} N \to \mu^{\pm}\mu^{\pm}e^{\mp}\nu_{\mu}$	
2015:	Combined trigger: `HLT_mu18_mu8noL1`
	$p_{\mathrm{T}}(\mu_{\mathrm{lead}}) \geq 19$ GeV
	$p_{\mathrm{T}}(\mu_{\mathrm{sublead}}) \geq 9$ GeV
2016:	Combined trigger: `HLT_mu22_mu8noL1`
	$p_{\mathrm{T}}(\mu_{\mathrm{lead}}) \geq 23$ GeV
	$p_{\mathrm{T}}(\mu_{\mathrm{sublead}}) \geq 9$ GeV

First, the p_{T} distribution of the leading muon is examined. The signal selection requirements applied before the p_{T} study are the preliminary cuts, see Table 6.2.

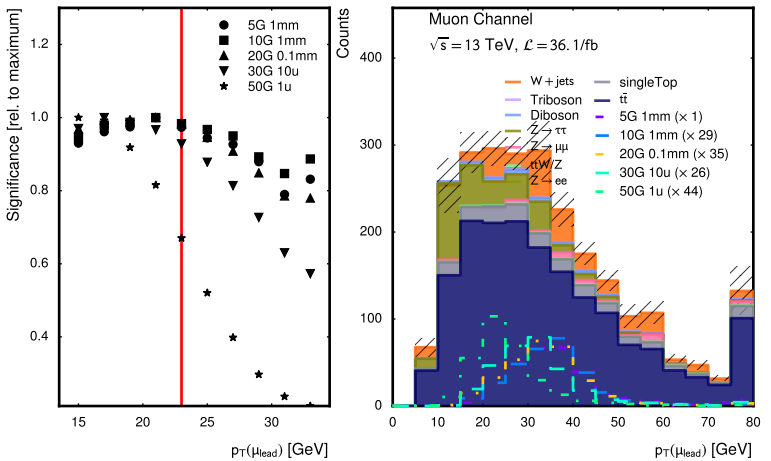

Figure 6.1.: On the right hand side: The $p_{\mathrm{T}}(\mu_{\mathrm{lead}})$ distribution for MC backgrounds and all signal mass points. The signal events are scaled by a factor indicated in the legend for visibility. On the left hand side: Significance for the different signal samples as a function of the $p_{\mathrm{T}}(\mu_{\mathrm{lead}})$ requirement. A point x_0 on the x-axis represents the requirement $p_{\mathrm{T}} \geq x_0$. The HLT offline p_{T} requirement, given by $p_{\mathrm{T}}(\mu_{\mathrm{lead}}) \geq 23$ GeV, is shown by the red line. The error bands show combined statistical uncertainties.

Figure 6.1 shows both the $p_{\mathrm{T}}(\mu_{\mathrm{lead}})$ distribution for the signal and background events and the significance as a function of the $p_{\mathrm{T}}(\mu_{\mathrm{lead}})$ requirement. The significance given at the value x_0 represents the requirement:

$p_{\mathrm{T}}(\mu_{\mathrm{lead}}) \geq x_0$. On the significance plots, the red line represents the HLT offline p_{T} requirement for the leading muon, given by $p_{\mathrm{T}}(\mu_{\mathrm{lead}}) \geq 23\,\mathrm{GeV}$.

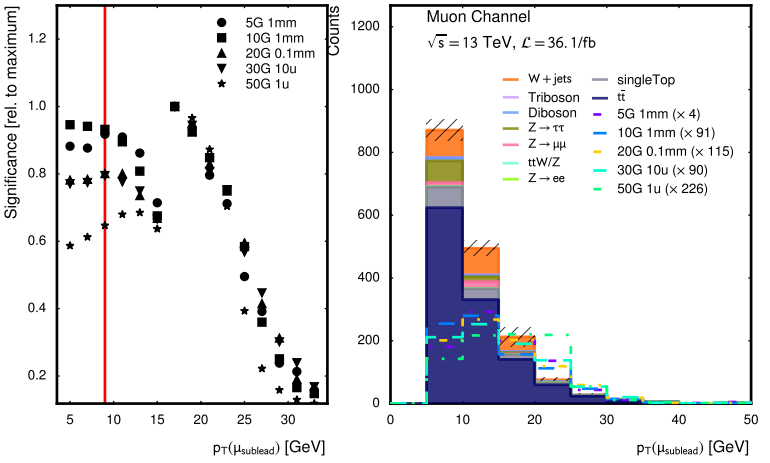

Figure 6.2.: On the right hand side: The $p_{\mathrm{T}}(\mu_{\mathrm{sublead}})$ distribution for MC backgrounds and all signal mass points. The signal events are scaled by a factor indicated in the legend for visibility. On the left hand side: Significance for the different signal samples as a function of the $p_{\mathrm{T}}(\mu_{\mathrm{sublead}})$ requirement. A point x_0 on the x-axis represents the requirement $p_{\mathrm{T}} \geq x_0$. The HLT offline p_{T} requirement, given by $p_{\mathrm{T}}(\mu_{\mathrm{sublead}}) \geq 9\,\mathrm{GeV}$, is shown by the red line. The error bands show combined statistical uncertainties.

It is found that the significance decreases for all mass points when the minimal p_{T} is higher than the HLT offline requirement. Therefore, the p_{T} requirements is chosen as: $p_{\mathrm{T}}(\mu_{\mathrm{lead}}) \geq 23\,\mathrm{GeV}$.

Prior to the study of the p_{T} distribution of the subleading muon, both the preliminary event selection in Table 6.2 and the p_{T} requirement for the leading muon, $p_{\mathrm{T}}(\mu_{\mathrm{lead}}) \geq 23\,\mathrm{GeV}$, are applied.

Similarly as above, Figure 6.2 shows the $p_{\mathrm{T}}(\mu_{\mathrm{sublead}})$ distribution and the significance as a function of the $p_{\mathrm{T}}(\mu_{\mathrm{sublead}})$ requirement. Since the multi-fake background events from W+jets often have relatively large weights, this background component can have a large impact on the acquired significance and cause rapid jumps in the distribution. The W+jets process participates due to multiple (≥ 2) non-prompt leptons that are usually characterized by a lesser isolation and lower p_{T}. Jumps in the distributions are consequently caused by a reduction of W+jets events and the subsequent removal of a large fraction of relative uncertainty in (4.11). The same plot can be found in Figure 6.3 where no W+jets sample was included. It is clear that the description of multiple fake leptons through the W+jets MC sample is poorly modelled.

The p_{T} cut on the subleading muon is set to $p_{\mathrm{T}}(\mu_{\mathrm{sublead}}) \geq 14\,\mathrm{GeV}$ for all masses.

Analogous, the event selection applied before the study of the p_{T} distribution of the electron consists of the preliminary event selection and the leading and subleading muons p_{T} requirements given by $p_{\mathrm{T}}(\mu_{\mathrm{lead}}) \geq 23\,\mathrm{GeV}$ and $p_{\mathrm{T}}(\mu_{\mathrm{sublead}}) \geq 14\,\mathrm{GeV}$. Figure 6.4 shows the $p_{\mathrm{T}}(e)$ distribution and the significance as a function of the $p_{\mathrm{T}}(e)$ requirement. For all m_N signal regions it

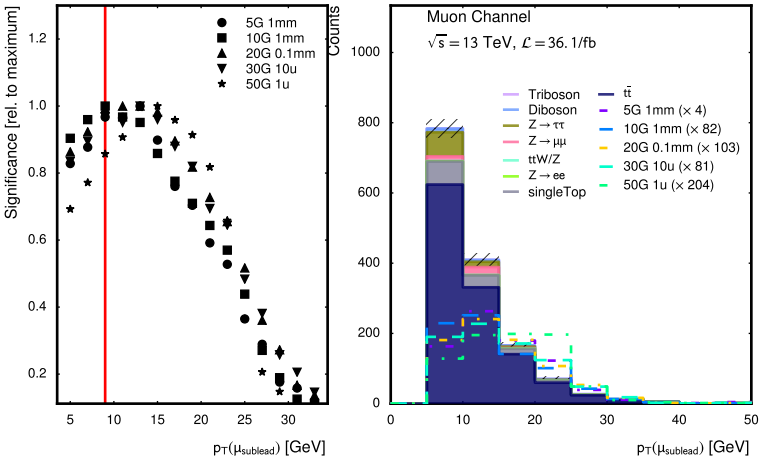

Figure 6.3.: Shown is Figure 6.2 with no W+jets sample included. It is clear that the poor statistical size of the MC sample causes the discontinuities in significance estimation and that the MC background describing multiple fake leptons is therefore poorly modelled. The error bands show combined statistical uncertainties.

is found that there is not an appreciable gain in significance when applying a lower threshold for $p_T(e)$, so no further requirement on the electron p_T is used.

6.2.2. Lepton isolation

All signal leptons in this HNL search are generally well isolated. There is variation dependent on m_N, where smaller mass points offer less phase space for the opening angle between the subleading muon and electron, resulting in their closer proximity. The leading muon is usually well isolated, as expected for any prompt lepton coming from W boson decay.

The two following sections investigate the impact of several isolation WPs, defined in Section 5.4, on the different signal samples and background events. Studied here is the significance on selecting different isolation requirements on the leading lepton, originating in most cases from the W boson (compare to Section C). Furthermore the significance and statistical sample size of background events remaining after selecting isolation WPs for the two remaining leptons is studied.

The signal selection applied before studying the impact of the isolation working points is summarized in Table 6.4.

Leading muon isolation requirements

The impact of the isolation working points for the leading muon is examined in Figure 6.5. Shown is the significance after selecting different isolation WPs for all mass hypotheses (see Table 4.1). The Figure shows the significance values as well as color-coded the relative differences in significance to the lowest value per mass point to help guide the eye. It can clearly be seen that for the leading lepton no meaningful increase in significance can be achieved as the lepton is coming in almost all cases from prompt decays for both the backgrounds as

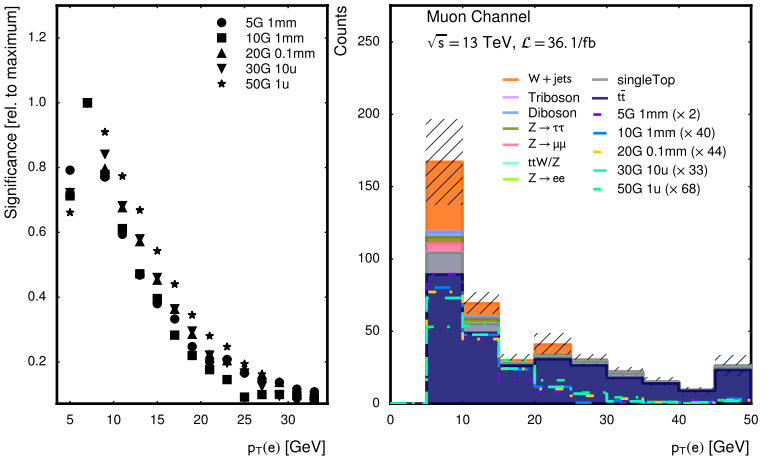

Figure 6.4.: On the right hand side: The $p_{\mathrm{T}}(e)$ distribution for MC backgrounds and all signal mass points. The signal events are scaled by a factor indicated in the legend for visibility. On the left hand side: Significance for the different signal samples as a function of the $p_{\mathrm{T}}(e)$ requirement. A point x_0 on the x-axis represents the requirement $p_{\mathrm{T}} \geq x_0$. The error bands show combined statistical uncertainties.

Table 6.4.: Event selection requirements prior to studying the impact of the isolation working points in the muon channel.

Cuts used for optimizing isolation WPs
Preliminary cuts from Table 6.2
`HLT_mu18_mu8noL1` (2015) and `HLT_mu22_mu8noL1` (2016)
$p_T(\mu_{\mathrm{lead}}) \geq 23\,\mathrm{GeV}$
$p_T(\mu_{\mathrm{sublead}}) \geq 14\,\mathrm{GeV}$
b jet veto

well as the signal. Differences can be seen to range only up to approximately 6.5 % favoring a more relaxed isolation as it keeps the statistical sample size of the MC samples high and therefore reduces σ_b in (4.11). To maintain a rich sample size the working point `Loose` is selected for μ_{lead}.

Subleading muon and electron isolation requirements

The impact of the isolation working points for the subleading muon and electron is examined in all possible combinations for each of the signal mass hypotheses $m_N = 5$, 10, 20, 30 and 50 GeV. In addition to the requirements listed in Table 6.4, `Loose` isolation is required for the leading muon. An example for the 30 GeV mass point can be seen in Figure 6.6a.

While significance is a good indicator of discrimination between signal and background processes the final background-only model used in this search relies on a data-driven template fit and MC description therefore prompting for sufficient statistical sample sizes. This helps constrain fit parameters and ob-

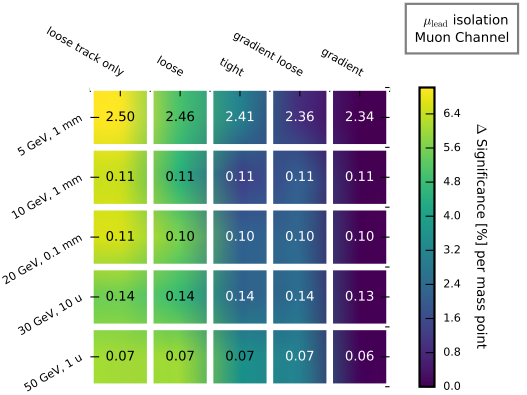

Figure 6.5.: *Muon Channel.* Effect of implementing the possible isolation requirement WPs for the leading muon in the muon channel. Values shown are significance values for the different mass hypotheses. The color-coding helps to guide the eye and denotes relative differences in significance to the lowest value per mass point. The luminosity corresponds to 36.1 fb^{-1}.

tain better signal discrimination results . For this reason the precision of the samples is also plotted, as the inverted relative uncertainty (so a 5 % relative uncertainty would yield a value of 20). This is exemplarily shown in Figure 6.6b.

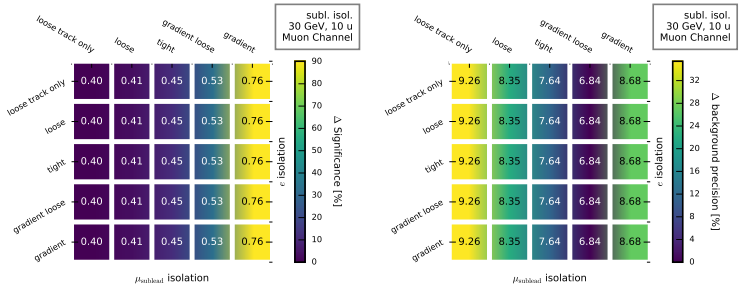

(a) Significance (b) Inverted rel. uncertainty

Figure 6.6.: *Muon Channel.* 30 GeV signal point. Effect of implementing the possible isolation requirement WPs for the subleading leptons in the muon channel. The luminosity corresponds to 36.1 fb^{-1}. All mass points can be found in Appendix A

The plots for all mass hypotheses can be found in Appendix A.

In order to allow for a reasonable amount of MC statistics in the control- and validation regions as well as to unify the selection between the two channels of this search, the final choice of isolation working points is `Loose` for all leptons.

6.2.3. Missing transverse energy

The signal region optimization of setting an upper level of $E_{\mathrm{T}}^{\mathrm{miss}}$ is studied after applying the preliminary cuts in Table 6.2 and the two muon p_{T} cuts: $p_{\mathrm{T}}(\mu_{\mathrm{lead}}) \geq 23\,\mathrm{GeV}$ and $p_{\mathrm{T}}(\mu_{\mathrm{sublead}}) \geq 14\,\mathrm{GeV}$ as well as isolation criteria derived in Section 6.2.2..

The plot on the right hand side of Figure 6.7 shows the $E_{\mathrm{T}}^{\mathrm{miss}}$ distribution for the signal as well as backgrounds. The left hand plot shows the significance as a function of an upper limit on the $E_{\mathrm{T}}^{\mathrm{miss}}$ requirement. Again, the significance given at value x_0 represents the requirement: $E_{\mathrm{T}}^{\mathrm{miss}} \leq x_0$.

For all signal samples, $E_{\mathrm{T}}^{\mathrm{miss}}$ is below 60 GeV, as expected from a signal event that consists of a single SM neutrino in the final state carrying a fraction of the event momentum. Whereas the various backgrounds are scattered, ranging to 200 GeV. The requirement $E_{\mathrm{T}}^{\mathrm{miss}} < 60\,\mathrm{GeV}$ is chosen for all mass points as it retains reasonable statistical sizes for background and signal samples whereas lower values would not relevantly increase the estimated significance.

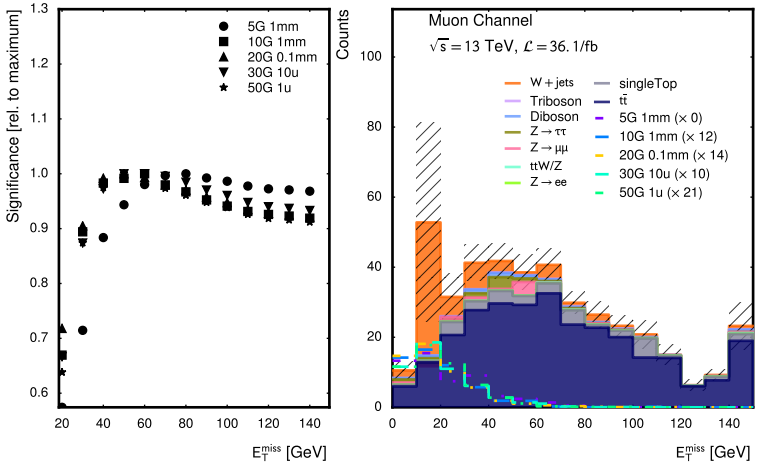

Figure 6.7.: On the right hand side: The $E_{\mathrm{T}}^{\mathrm{miss}}$ distribution for MC backgrounds and all signal mass points. The signal events are scaled by a factor indicated in the legend for visibility. On the left hand side: Significance for the different signal samples as a function of the upper $E_{\mathrm{T}}^{\mathrm{miss}}$ boundary. The error bands show combined statistical uncertainties.

6.2.4. Impact parameter

As discussed in Section 4.1.3 this search is conducted for several HNL signal mass hypotheses using different proper decay lengths. Depending on the boost of the HNL a slight displacement between the beam pipe and the vertex of HNL decay may exist. This is rather pronounced for the $c\tau = 1\,\mathrm{mm}$ signals with 5 GeV and 10 GeV mass while for 0.1 mm and shorter proper decay lengths a displacement is not noticeable.

The effect of IP requirements defined by the two variables

$$|d_0^{\mathrm{BL}}/\sigma(d_0)|, \quad |\Delta z_0^{\mathrm{BL}} \sin(\theta)| \tag{6.2}$$

are studied for the final state region of the signal samples. For this purpose two signal samples 10 GeV and 50 GeV have been selected to study both slightly displaced as well as prompt signal. All requirements of the signal region, shown in Table 6.2 are applied. The effect of the IP requirements is studied for all leptons: μ_{lead}, μ_{sublead} and e.

In Figure 6.8 the distributions for signals and backgrounds are presented as well as the impact of requiring an upper cut on either of the two IP on the significance relative to the maximal achievable significance. Discontinuities in the significance distributions are due to the cut removal of MC samples with very high relative weights, emphasizing the low statistical sample size of some samples. In Figures 6.9 and 6.10 the same is shown for the subleading muon and electron.

The optimization study for the IP requirements shows, that tighter requirements for the IPs will in general decrease the number of signal events and the significance obtained. The final selected ip cuts are stated shown in Table 6.10.

6.2.5. Final cut selection

The impact of the final event selection on the signal and total background is exemplarily shown for the 30 GeV mass point in Table 6.5. The full cutflow table for all signal points and backgrounds can be found in Appendix B in Table B.1.

Table 6.5.: *Muon channel:* Impact of cuts on the number of 30 GeV signal and total background events. The samples are scaled by $\mathcal{L} = 36.1\,\text{fb}^{-1}$. The last cuts are indicating the impact of a *possible* upper cut on the di-lepton mass for different mass hypothesis. This is to indicate the significance that a simple cut and count experiment would yield. However the dilepton mass variable is used as a final signal search variable.

Selection	30G 10u	ε_{tot}	S	$\sum$ Bkg
Initial	24 876.00 ± 0.00	1.00	0.00	592 737 020.78 ± 0.00
After obj. def. (weighted)	13.29 ± 0.28	0.27	0.00	721 364.07 ± 4480.10
μ == 2 (loose, combined) and e == 1 (loose LLH), $\lvert\Delta z_0 \sin(\theta)\rvert(l) < 1\,\text{mm}$, $\lvert d_0/\sigma(d_0)\rvert(\mu_{\text{lead}}) < 3$	12.60 ± 0.28	0.25	0.01	143 545.52 ± 1857.13
$p_{\text{T}}(e) \geq 4.5$ (2016), 7 (2015), $p_{\text{T}}(\mu) \geq 4$	12.49 ± 0.27	0.25	0.01	138 983.95 ± 1824.76
$\lvert\eta(e)\rvert \leq 2.47$, $\lvert\eta(\mu)\rvert \leq 2.5$, veto : $1.37 < \lvert\eta(e)\rvert < 1.52$	11.84 ± 0.27	0.24	0.01	130 172.43 ± 1746.28
Trigger	7.89 ± 0.22	0.16	0.01	109 734.41 ± 1405.76
Trigger matching	7.88 ± 0.22	0.16	0.01	109 692.65 ± 1405.73
$\mu^{\pm}\mu^{\pm}e^{\mp}$	7.85 ± 0.22	0.16	0.09	2747.77 ± 66.03
$p_{\text{T}}(\mu_1) \geq 23\,\text{GeV}$	7.81 ± 0.22	0.16	0.09	2731.17 ± 65.91
$p_{\text{T}}(\mu_2) \geq 14\,\text{GeV}$	4.95 ± 0.18	0.10	0.09	1306.91 ± 38.11
μ_1 loose isolation	4.87 ± 0.18	0.10	0.10	1182.30 ± 37.31
μ_2 loose isolation	4.77 ± 0.18	0.10	0.14	779.46 ± 20.14
e iso loose isolation	4.74 ± 0.18	0.10	0.15	679.59 ± 18.56
$M(\mu\mu e) < 90\,\text{GeV}$	4.62 ± 0.18	0.09	0.28	152.25 ± 10.48
$M(\mu\mu e) > 40\,\text{GeV}$	4.61 ± 0.18	0.09	0.29	145.08 ± 9.83
bJets: 0	4.52 ± 0.18	0.09	0.41	61.30 ± 7.34
$E_{\text{T}}^{\text{miss}} < 60\,\text{GeV}$	4.40 ± 0.17	0.09	0.52	28.50 ± 6.09
$M(\mu, e) < 50\,\text{GeV}$	4.37 ± 0.17	0.09	0.54	24.58 ± 6.00
$M(\mu, e) < 30\,\text{GeV}$	4.12 ± 0.16	0.08	0.59	16.69 ± 5.16
$M(\mu, e) < 20\,\text{GeV}$	2.20 ± 0.12	0.04	0.36	9.80 ± 4.83
$M(\mu, e) < 10\,\text{GeV}$	0.39 ± 0.05	0.01	0.08	2.58 ± 4.37
$M(\mu, e) < 5\,\text{GeV}$	0.06 ± 0.02	0.00	0.01	4.66 ± 3.74

At this point it is useful to look at the impact the final cuts have on data and MC events. As the search is still blinded at this point, the signal region will not be shown but instead the $M(\ell, \ell, \ell')$ sideband outside the signal region between 40 to 90 GeV. Shown are the trilepton invariant mass and $p_{\text{T}}(\ell')$ in

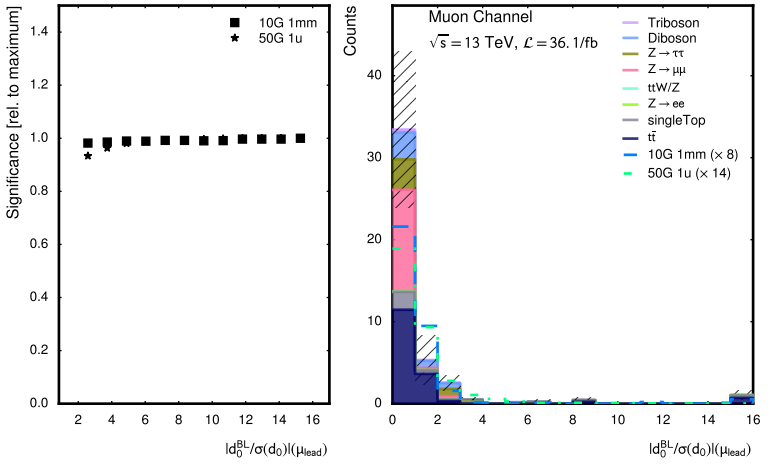

(a) $|d_0^{\mathrm{BL}}/\sigma(d_0)|(\mu_{\mathrm{lead}})$

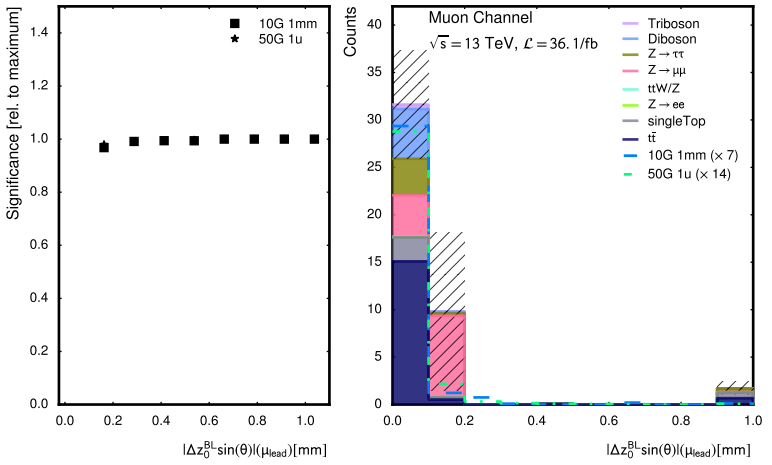

(b) $|\Delta z_0^{\mathrm{BL}} \sin(\theta)|(\mu_{\mathrm{lead}})$

Figure 6.8.: *Muon channel.* IPs for μ_{lead}. The error bands show combined statistical uncertainties.

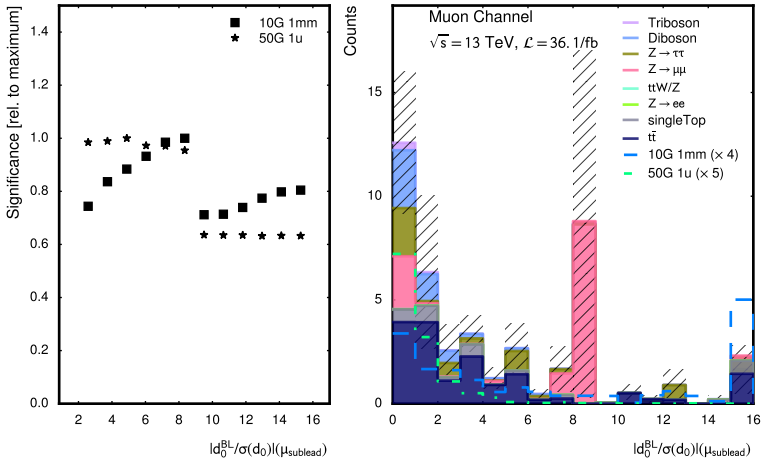

(a) $|d_0^{\mathrm{BL}}/\sigma(d_0)|(\mu_{\mathrm{sublead}})$

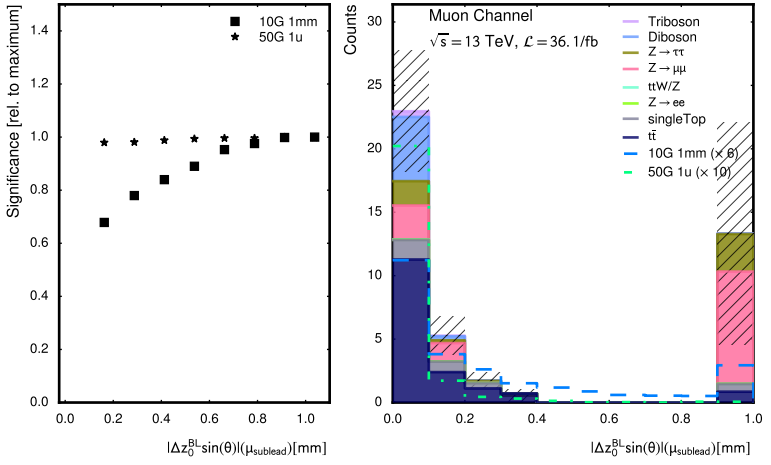

(b) $|\Delta z_0^{\mathrm{BL}} \sin(\theta)|(\mu_{\mathrm{sublead}})$

Figure 6.9.: *Muon channel.* IPs for μ_{sublead}. The error bands show combined statistical uncertainties.

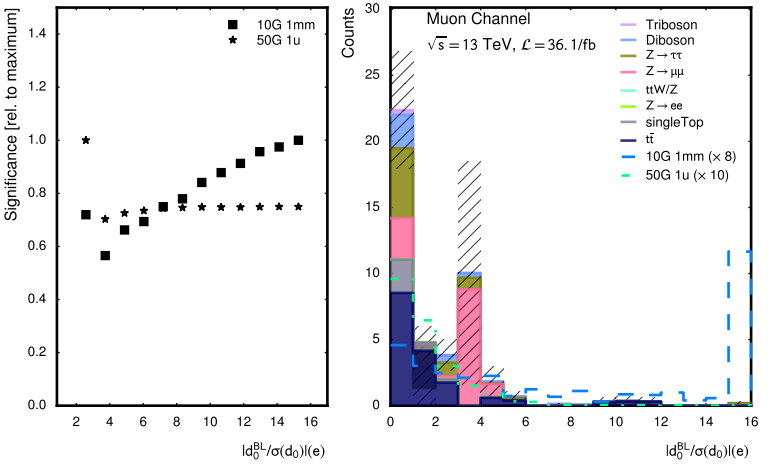

(a) $|d_0^{\mathrm{BL}}/\sigma(d_0)|(e)$

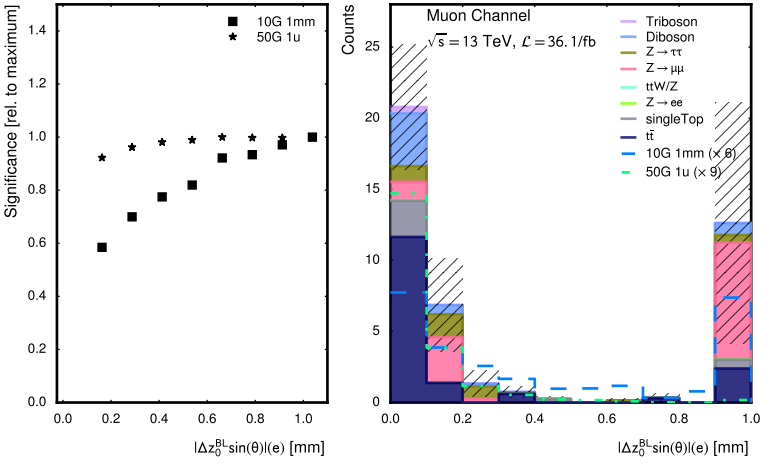

(b) $|\Delta z_0^{\mathrm{BL}} \sin(\theta)|(e)$

Figure 6.10.: *Muon channel.* IPs for e. The error bands show combined statistical uncertainties.

Figure 6.11. This search is clearly a low statistics search due to the exotic phase space it covers. The low statistical sample size of the MC events is clearly visible by the large uncertainty bands representing the statistical uncertainty. The population in this region as well as the signal region was therefore a key concern during the optimization of signal region cuts. A selection of plots for different regions comparing data and MC are shown in Appendix E.

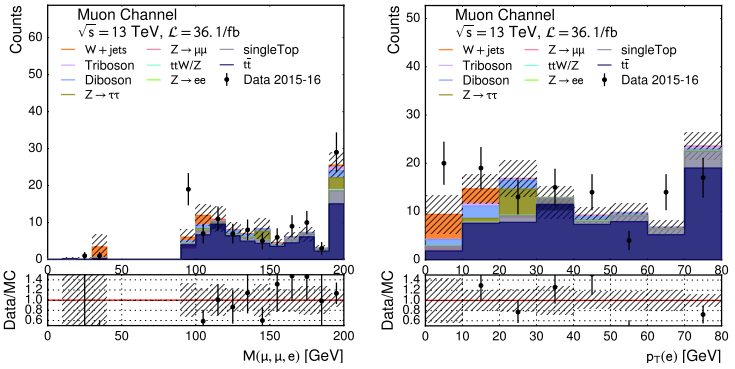

(a) $M(\ell, \ell, \ell')$ (b) p_{T} muon

Figure 6.11.: *Muon Channel.* Comparison of agreement between data and MC backgrounds in the $M(\ell, \ell, \ell')$ sideband region outside of 40 to 90 GeV. The error bands show combined statistical uncertainties.

6.3. Electron channel

Similarly to the muon channel, the optimization of the electron channel is determined after establishing a set of preliminary cuts. The basic object selection and identification described in Section 5.1 is implemented for all leptons. In addition, the leptons must satisfy flavor and charge requirements, such that the event consists of exactly $e^{\pm}e^{\pm}\mu^{\mp}$, and the three-lepton invariant mass is again required to be consistent with the mass of the W boson.

The procedure used to determine the optimal signal region selection for the electron channel closely follows the procedure applied for the muon channel. One of the main differences is the larger amount of background samples which contain electrons with a misidentified charge. This amount has been determined to be negligable in the final signal region after applying a Z veto cut on the invariant mass of the two electrons.

The electron channel cut optimization is based on the preliminary cuts as shown at the top of Table 6.8. The complete table shows a summary of the cuts comprising the signal region for the electron channel.

6.3.1. Lepton p_{T}

In this section, the transverse momentum requirements on the leading and subleading electron as well as the muon are examined. Ideally, the optimal cut on p_{T} is determined as the cut that yields the highest significance as defined in Eq. (4.11). This section follows closely Section 6.2.1.

Table 6.6.: Trigger requirements and relevant offline requirement used in the event selection for the electron channel for $m_N = 5$ to 50 GeV. The requirements imposed on both the 2015 and 2016 datasets are shown.

Trigger for $W \to e^{\pm}N \to e^{\pm}e^{\pm}\mu^{\mp}\nu_e$	
2015:	`HLT_e24_lhmedium` or `HLT_e60_lhmedium` or `HLT_e120_lhloose` $p_T(e_{\text{lead}}) \geq 25$ GeV Medium Likelihood Identification
2016:	`HLT_e26_lhtight_nod0_ivarloose` or `HLT_e60_lhmedium_nod0` or `HLT_e140_lhloose_nod0` $p_T(e_{\text{lead}}) \geq 27$ GeV Tight Likelihood Identification

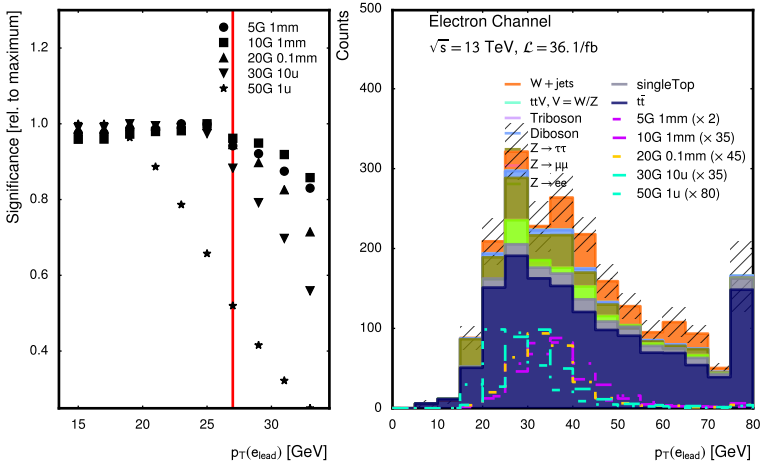

Figure 6.12.: On the right hand side: The $p_T(e_{\text{lead}})$ distribution for MC backgrounds and all signal mass points. The signal events are scaled by a factor indicated in the legend for visibility. On the left hand side: Significance for the different signal samples as a function of the $p_T(e_{\text{lead}})$ requirement. A point x_0 on the x-axis represents the requirement $p_T \geq x_0$. The HLT offline p_T requirement, given by $p_T(e_{\text{lead}}) \geq 27$ GeV, is shown by the red line. The error bands show combined statistical uncertainties.

For the electron channel, the triggers which are found to give the largest percentage of signal events recorded are shown in Table 6.6.

First, the p_T distribution of the leading electron is examined. The signal selection requirements applied before the p_T study are the preliminary cuts, see Table 6.8.

Figure 6.12 shows both the $p_T(e_{\text{lead}})$ distribution for the signal and background events and the significance as a function of the $p_T(e_{\text{lead}})$ requirement. The significance given at the value x_0 represents the requirement: $p_T(e_{\text{lead}}) \geq x_0$. On the significance plots, the red line represents the HLT offline p_T requirement for the leading electron, given by $p_T(e_{\text{lead}}) \geq 27$ GeV.

It is found that the significance decrease for all mass points when the minimal p_{T} is higher than the HLT offline requirement. Therefore, the p_{T} requirements is chosen as: $p_{\mathrm{T}}(e_{\mathrm{lead}}) \geq 27\,\mathrm{GeV}$.

Prior to the study of the p_{T} distribution of the subleading electron, both the preliminary event selection in Table 6.8 and the p_{T} requirement for the leading electron, $p_{\mathrm{T}}(e_{\mathrm{lead}}) \geq 27\,\mathrm{GeV}$, are applied.

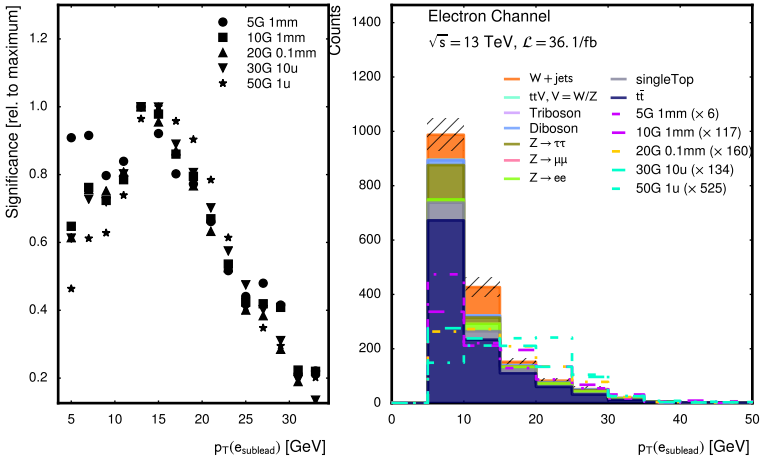

Figure 6.13.: On the right hand side: The $p_{\mathrm{T}}(e_{\mathrm{sublead}})$ distribution for MC backgrounds and all signal mass points. The signal events are scaled by a factor indicated in the legend for visibility. On the left hand side: Significance for the different signal samples as a function of the $p_{\mathrm{T}}(e_{\mathrm{sublead}})$ requirement. A point x_0 on the x-axis represents the requirement $p_{\mathrm{T}} \geq x_0$. The error bands show combined statistical uncertainties.

Similarly as above, Figure 6.13 shows the $p_{\mathrm{T}}(e_{\mathrm{sublead}})$ distribution and the significance as a function of the $p_{\mathrm{T}}(e_{\mathrm{sublead}})$ requirement. Since the multi-fake background events from W+jets often have relatively large weights, this background component can have a large impact on the acquired significance and cause rapid jumps in the distribution. The W+jets process participates due to multiple (≥ 2) non-prompt leptons that are usually characterized by a lesser isolation and lower p_{T}. Jumps in the distributions are consequently caused by a reduction of W+jets events and the subsequent removal of a large fraction of relative uncertainty in (4.11).

The p_{T} cut on the subleading electron is set to $p_{\mathrm{T}}(e_{\mathrm{sublead}}) \geq 10\,\mathrm{GeV}$ for all masses.

Analogous, the event selection applied before the study of the p_{T} distribution of the electron consists of the preliminary event selection and the leading and subleading electrons p_{T} requirements given by $p_{\mathrm{T}}(e_{\mathrm{lead}}) \geq 27\,\mathrm{GeV}$ and $p_{\mathrm{T}}(e_{\mathrm{sublead}}) \geq 10\,\mathrm{GeV}$. Figure 6.14 shows the $p_{\mathrm{T}}(\mu)$ distribution and the significance as a function of the $p_{\mathrm{T}}(\mu)$ requirement. For all m_N signal regions it is found that there is not an appreciable gain in significance when applying a lower threshold for $p_{\mathrm{T}}(\mu)$, so no further requirement on the muon p_{T} is used.

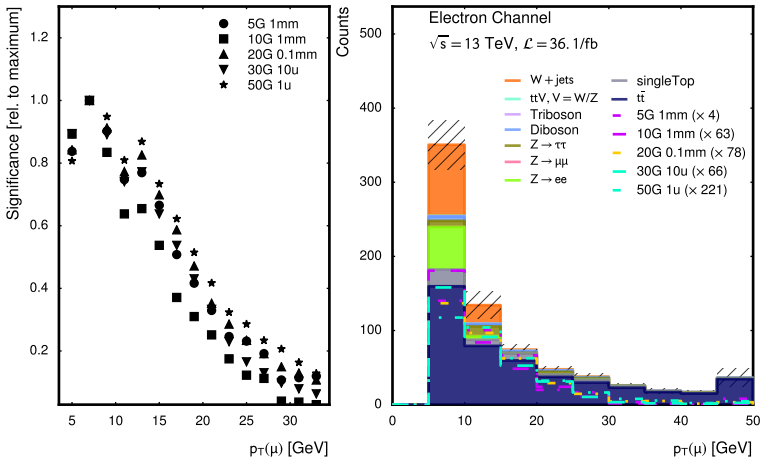

Figure 6.14.: On the right hand side: The $p_{\mathrm{T}}(\mu)$ distribution for MC backgrounds and all signal mass points. The signal events are scaled by a factor indicated in the legend for visibility. On the left hand side: Significance for the different signal samples as a function of the $p_{\mathrm{T}}(\mu)$ requirement. A point x_0 on the x-axis represents the requirement $p_{\mathrm{T}} \geq x_0$. The error bands show combined statistical uncertainties.

6.3.2. Lepton isolation

All signal leptons in this HNL search are generally well isolated. There is variation dependent on m_N, where smaller mass points offer less phase space for the opening angle between the subleading muon and electron, resulting in their closer proximity. The leading muon is usually well isolated, as expected for any prompt lepton coming from W boson decay.

Table 6.7.: Event selection requirements prior to studying the impact of the isolation working points in the electron channel.

Cuts used for optimizing isolation WPs
Preliminary cuts from Table 6.8
HLT from Table 6.6
$p_{\mathrm{T}}(e_{\mathrm{lead}}) \geq 27$ GeV
$p_{\mathrm{T}}(e_{\mathrm{sublead}}) \geq 10$ GeV
b jet veto

The two following sections investigate the impact of several isolation WPs, defined in Section 5.4, on the different signal samples and background events. Studied is here the significance on selecting different isolation requirements on the leading lepton, originating in most cases from the W boson (compare to Section C). Furthermore the significance and statistical sample size of background events remaining after selecting isolation WPs for the two remaining leptons is studied.

The signal selection applied before studying the impact of the isolation working points is summarized in Table 6.7.

Leading electron isolation requirements

The impact of the isolation working points for the leading electron is examined in Figure 6.15. Shown is the significance after selecting different isolation WPs for all mass hypotheses (see Table 4.1). The Figure shows the significance values as well as color-coded the relative differences in significance to the lowest value per mass point to help guide the eye. It can clearly be seen that for the leading lepton no meaningful increase in significance can be achieved as the lepton is coming in almost all cases from prompt decays for both the backgrounds as well as the signal. Differences can be seen to range only up to approximately 8 % favoring a more relaxed isolation as it keeps the statistical sample size of the MC samples high and therefore reduces σ_b in (4.11). To maintain a rich sample size the working point `Loose` is selected for e_{lead}.

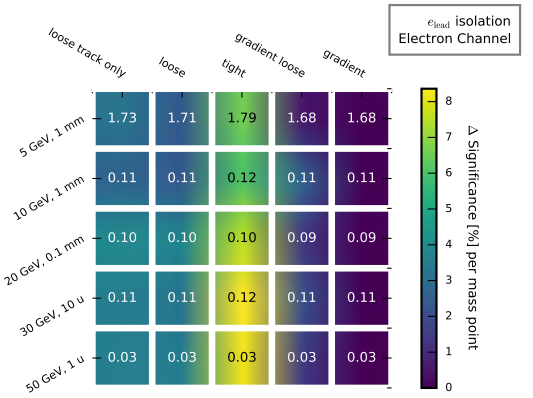

Figure 6.15.: *Electron Channel.* Effect of implementing the possible isolation requirement WPs for the leading electron in the electron channel. Values shown are significance values for the different mass hypotheses. The color-coding helps to guide the eye and denotes relative differences in significance to the lowest value per mass point. The luminosity corresponds to 36.1 fb^{-1}.

Subleading electron and muon isolation requirements

Just as for the muon channel the isolation WPs for the subleading electron and muon is examined in all possible combinations for each of the signal mass hypotheses m_N = 5, 10, 20, 30 and 50 GeV. In addition to the requirements listed in Table 6.7, `Loose` isolation is required for the leading electron.

While an example for the 30 GeV mass point is preseented here in Figure 6.16a and the precision on the background in Figure 6.6b, all mass point plots can be found in Appendix A.

In order to allow for a reasonable amount of MC statistics in the control- and validation regions as well as to unify the selection between the two channels of this search, the final choice of isolation working points is `Loose` for all leptons.

6.3.3. Electron Z-mass veto

Additionally a tighter cut on the $M(e,e)$ variable is applied in order to eradicate most of the $Z \to ee$. In Figure 6.17a a large $Z \to ee$ contribution with $M(e,e) \gtrapprox$

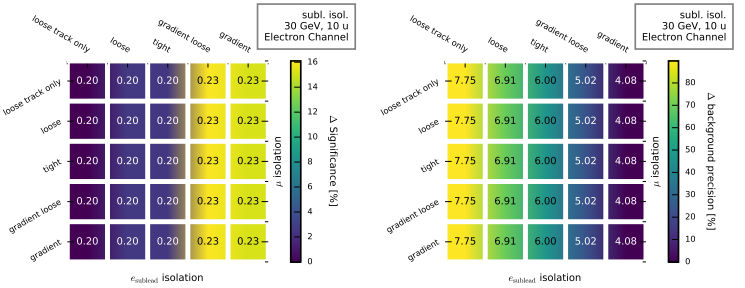

(a) Significance (b) Inverted rel. uncertainty

Figure 6.16.: *Electron Channel.* 30 GeV signal point. Effect of implementing the possible isolation requirement WPs for the subleading leptons in the electron channel. The luminosity corresponds to 36.1 fb^{-1}. All mass points can be found in Appendix A

80 GeV is shown that is disjoint from the signal distributions in Signal Region (SR). This contribution exhibits low statistics with relatively high uncertainties. While comparing it also with 6.17b it motivates an additional cut of $M(e,e) \leq 78\,\text{GeV}$ which does not harm the signal yield but removes some of the high weights associated with $Z \to ee$ background.

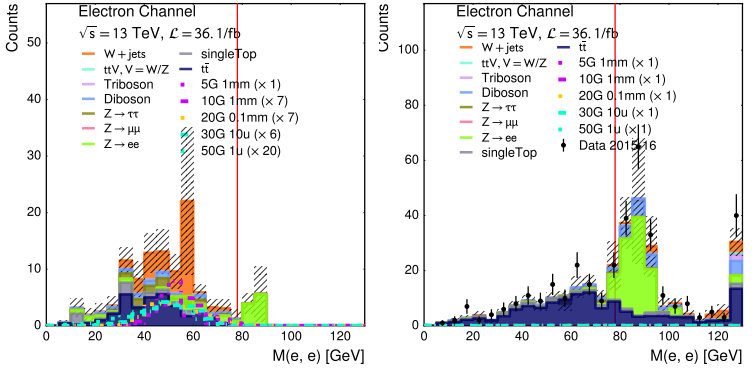

(a) SR: $M(e,e)$ (b) CR-1: $M(e,e)$

Figure 6.17.: $M(e,e)$ distributions for the blinded SR and CR-1 demonstrating the newly placed cut on $\leq 78\,\text{GeV}$ used in order to remove high-weight $Z \to ee$ samples. The error bands show combined statistical uncertainties.

6.3.4. Missing transverse energy

The signal region optimization of setting an upper level of $E_{\text{T}}^{\text{miss}}$ is studied after applying the preliminary cuts in Table 6.8 and the two electron p_{T} cuts: $p_{\text{T}}(e_{\text{lead}}) \geq 27\,\text{GeV}$ and $p_{\text{T}}(e_{\text{sublead}}) \geq 10\,\text{GeV}$ as well as isolation criteria derived in Sections 6.3.2 and 6.3.2. The Z veto from Section 6.3.3 is also applied.

The plot on the right hand side of Figure 6.18 shows the $E_{\mathrm{T}}^{\mathrm{miss}}$ distribution for the signal as well as backgrounds. The left hand plot shows the significance as a function of an upper limit on the $E_{\mathrm{T}}^{\mathrm{miss}}$ requirement. Again, the significance given at value x_0 represents the requirement: $E_{\mathrm{T}}^{\mathrm{miss}} \leq x_0$.

For all signal samples, $E_{\mathrm{T}}^{\mathrm{miss}}$ is below 60 GeV, as expected from a signal event that consists of a single SM neutrino in the final state carrying a fraction of the event momentum. Whereas the various backgrounds are scattered, ranging to 200 GeV. The requirement $E_{\mathrm{T}}^{\mathrm{miss}} < 60$ GeV is chosen for all mass points as it retains reasonable statistical sizes for background and signal samples whereas lower values would not relevantly increase the estimated significance.

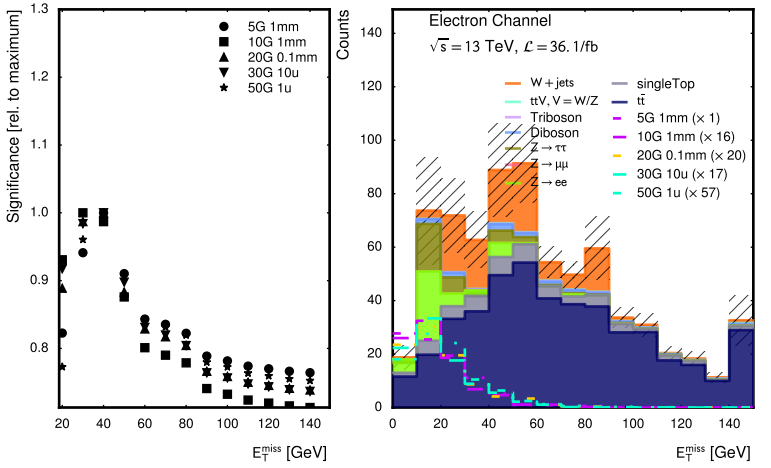

Figure 6.18.: On the right hand side: The $E_{\mathrm{T}}^{\mathrm{miss}}$ distribution for MC backgrounds and all signal mass points. The signal events are scaled by a factor indicated in the legend for visibility. On the left hand side: Significance for the different signal samples as a function of the upper $E_{\mathrm{T}}^{\mathrm{miss}}$ boundary. The error bands show combined statistical uncertainties.

6.3.5. Impact parameter

The effect of the IP requirements is studied for the electron channel for all leptons: e_{lead}, e_{sublead} and μ.

In Figure 6.19 the distributions for signals and backgrounds are presented as well as the impact of requiring an upper cut on either of the two IP on the significance relative to the maximal achievable significance. Discontinuities in the significance distributions are due to the cut removal of MC samples with very high relative weights, emphasizing the low statistical sample size of some samples.

In Figures 6.20 and 6.21 the same is shown for the subleading muon and electron.

As for the muon channel it can be concluded that applying IP cuts on other objects than the leading leptin is harmful for the statistics available as well as the overall estimated significance in the signal region. The final selected ip cuts are stated shown in Table 6.10.

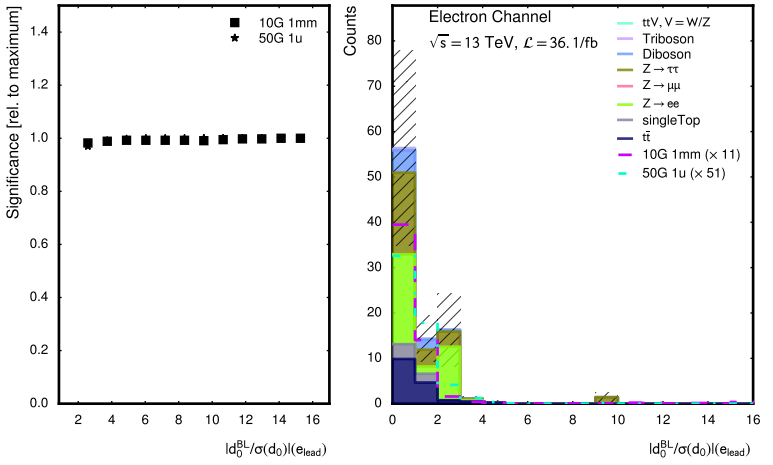

(a) $|d_0^{\mathrm{BL}}/\sigma(d_0)|(e_{\mathrm{lead}})$

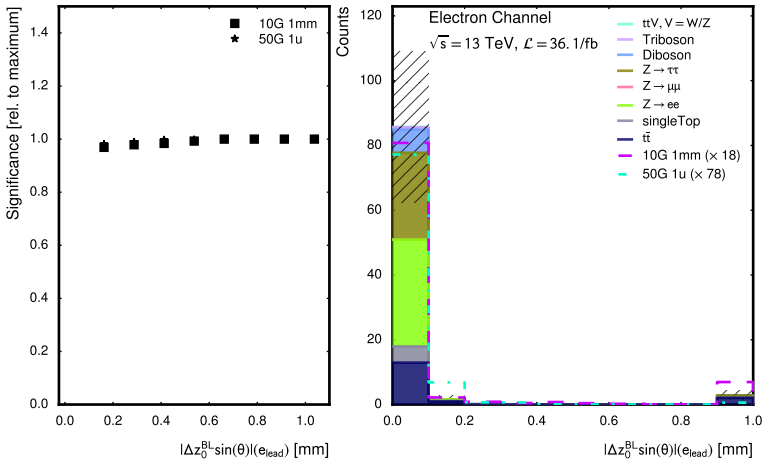

(b) $|\Delta z_0^{\mathrm{BL}} \sin(\theta)|(e_{\mathrm{lead}})$

Figure 6.19.: *Electron channel.* IPs for e_{lead}. The error bands show combined statistical uncertainties.

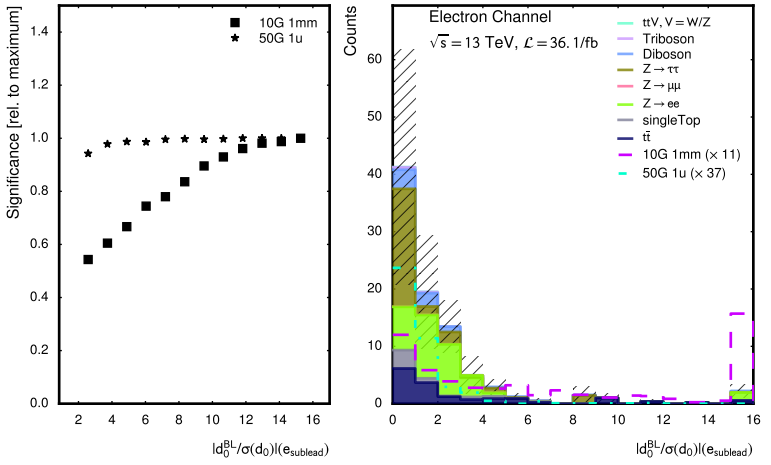

(a) $|d_0^{\mathrm{BL}}/\sigma(d_0)|(e_{\mathrm{sublead}})$

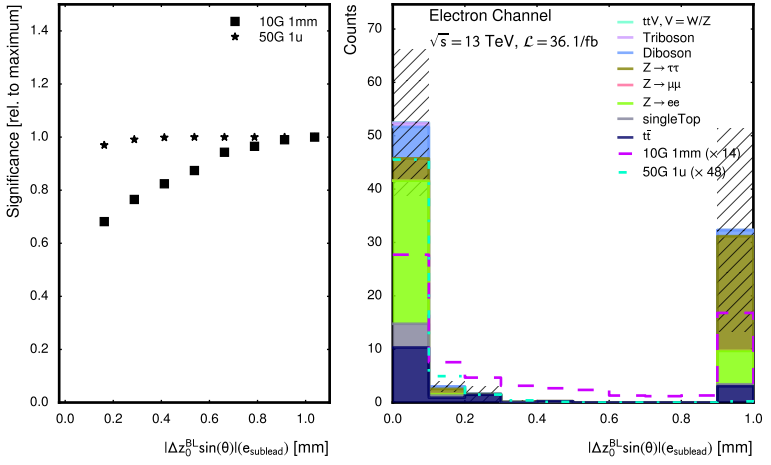

(b) $|\Delta z_0^{\mathrm{BL}} \sin(\theta)|(e_{\mathrm{sublead}})$

Figure 6.20.: *Electron channel.* IPs for e_{sublead}.The error bands show combined statistical uncertainties.

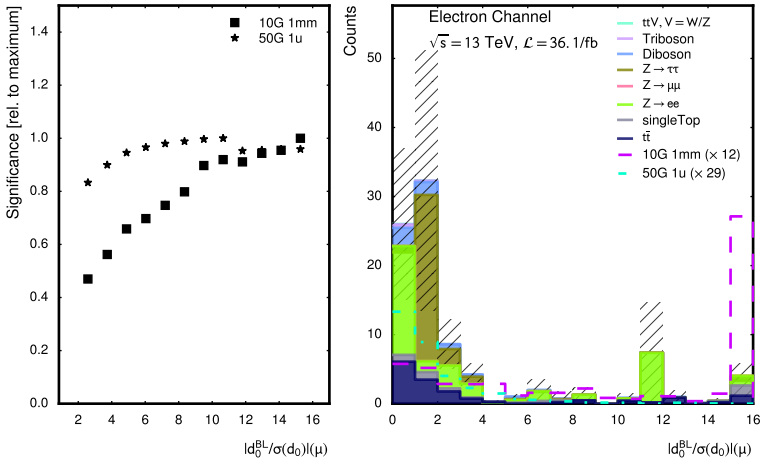

(a) $|d_0^{\mathrm{BL}}/\sigma(d_0)|(\mu)$

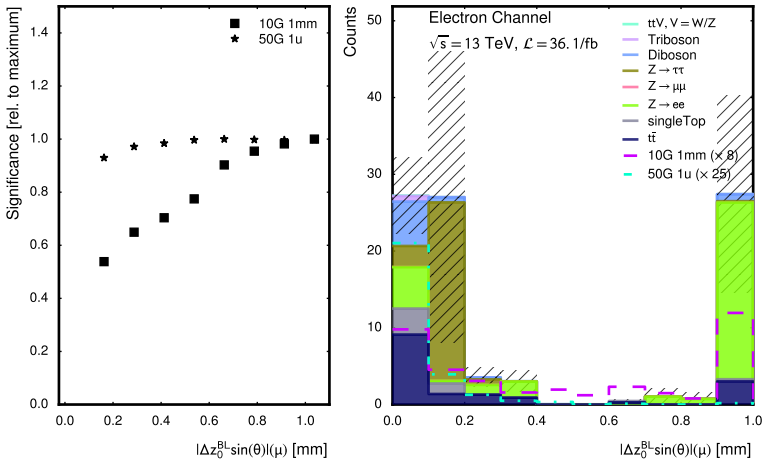

(b) $|\Delta z_0^{\mathrm{BL}} \sin(\theta)|(\mu)$

Figure 6.21.: *Electron channel.* IPs for μ. The error bands show combined statistical uncertainties.

6.3.6. Final cut selection

The impact of the final event selection on the signal and total background is exemplarily shown for the 30 GeV mass point in Table 6.9. The full cutflow table for all signal points and backgrounds can be found in Appendix B in Table B.5.

Table 6.8.: Summary of the final optimal cuts for the electron channel. The d_0 significance is only applied to the *leading* electron.

	Electron channel: Final signal region requirements
	Preselection triggers as listed in Table 6.1
Prelim. cuts	$\mu == 1$ (loose, combined) and $e == 2$ (loose LLH), e_{lead} tight LLH $\lvert\Delta z_0^{\text{BL}} \sin(\theta)\rvert(l) < 1\,\text{mm}$, $\lvert d_0^{\text{BL}}/\sigma(d_0)\rvert(e_{\text{lead}}) < 5$ $p_{\text{T}}(e) \geq 4.5$ (2016), 7 (2015), $p_{\text{T}}(\mu) \geq 4$ $\lvert\eta(e)\rvert \leq 2.47, \lvert\eta(\mu)\rvert \leq 2.5$, veto : $1.37 < \lvert\eta(e)\rvert < 1.52$ $M(e_{\text{lead}}, e_{\text{sublead}}, \mu) < 90\,\text{GeV}$ $M(e_{\text{lead}}, e_{\text{sublead}}, \mu) > 40\,\text{GeV}$
Trigger	`HLT_e24_lhmedium_L1EM20VH` (2015) or `HLT_e60_lhmedium` (2015) or `HLT_e120_lhloose` (2015) `HLT_e26_lhtight_nod0_ivarloose` (2016) or `HLT_e60_lhmedium_nod0` (2016) or `HLT_e140_lhloose_nod0` (2016)
	Trigger matching $e^{\pm}e^{\pm}\mu^{\mp}$ $p_{\text{T}}(e_{\text{lead}}) \geq 27\,\text{GeV}$ $p_{\text{T}}(e_{\text{sublead}}) \geq 10\,\text{GeV}$ e_{lead} `loose` isolation e_{sublead} `loose` isolation μ `loose` isolation Z veto: $M(e_{\text{lead}}, e_{\text{sublead}}) < 78\,\text{GeV}$ b jet veto $E_{\text{T}}^{\text{miss}} < 60\,\text{GeV}$

At this point it is useful to look at the impact the final cuts have on data and MC events. As the search is still blinded at this point, the signal region will not be shown but instead the $M(\ell, \ell, \ell')$ sideband outside the signal region between 40 to 90 GeV. Shown are the trilepton invariant mass and $p_{\text{T}}(\ell')$ in Figure 6.22. This search is clearly a low statistics search due to the exotic phase space it covers. The low statistical sample size of the MC events is clearly visible by the large uncertainty bands representing the statistical uncertainty. The population in this region as well as the signal region was therefore a key concern during the optimization of signal region cuts. A selection of plots for different regions comparing data and MC are shown in Appendix E.

6.4. Impact parameter scale factors

Object IPs for the ATLAS experiment are based on the two variables

$$|d_0^{\text{BL}}/\sigma(d_0)| \tag{6.3}$$

and

$$|\Delta z_0^{\text{BL}} \sin(\theta)| \tag{6.4}$$

Table 6.9.: *Electron channel:* Impact of cuts on the number of 30 GeV signal and total background events. The samples are scaled by $\mathcal{L} = 36.1\,\text{fb}^{-1}$. The last cuts are indicating the impact of a *possible* upper cut on the di-lepton mass for different mass hypothesis. This is to indicate the significance that a simple cut and count experiment would yield. However the dilepton mass variable is used as a final signal search variable.

Selection	30G 10u	ε_{tot}	S	$\sum$ Bkg
Initial	24 000.00 ± 0.00	1.00	0.00	592 737 020.78 ± 0.00
After obj. def. (weighted)	12.02 ± 0.26	0.24	0.01	242 989.76 ± 2226.91
μ == 1 (loose, combined) and e == 2 (loose LLH), e_{lead} tight LLH, $\lvert\Delta z_0 \sin(\theta)\rvert(l) < 1\,\text{mm}$, $\lvert d_0/\sigma(d_0)\rvert(e_{\text{lead}}) < 5$	10.61 ± 0.24	0.21	0.01	78 962.57 ± 914.44
$p_{\text{T}}(e) \geq$ 4.5 (2016), 7 (2015), $p_{\text{T}}(\mu) \geq 4$	10.48 ± 0.24	0.21	0.01	78 523.01 ± 913.82
$\lvert\eta(e)\rvert \leq 2.47$, $\lvert\eta(\mu)\rvert \leq 2.5$, veto : $1.37 < \lvert\eta(e)\rvert < 1.52$	9.48 ± 0.23	0.19	0.01	69 473.37 ± 865.28
Trigger	7.28 ± 0.20	0.15	0.01	63 812.11 ± 810.83
Trigger matching	6.23 ± 0.18	0.13	0.01	56 639.56 ± 747.04
$e^{\pm}e^{\pm}\mu^{\mp}$	6.16 ± 0.18	0.12	0.05	4474.09 ± 89.98
$p_{\text{T}}(e_1) \geq 27\,\text{GeV}$	6.16 ± 0.18	0.12	0.05	4474.09 ± 89.98
$p_{\text{T}}(e_2) \geq 10\,\text{GeV}$	4.35 ± 0.14	0.09	0.06	2196.01 ± 62.48
e_1 loose isolation	4.30 ± 0.14	0.09	0.06	2134.26 ± 62.27
e_2 loose isolation	4.23 ± 0.14	0.09	0.07	1039.95 ± 51.09
μ loose isolation	4.13 ± 0.14	0.08	0.09	786.71 ± 36.26
Z veto $M(e_1, e_2) < 78\,\text{GeV}$	4.08 ± 0.14	0.08	0.14	455.58 ± 20.19
$M(ee\mu) < 90\,\text{GeV}$	4.05 ± 0.14	0.08	0.19	178.91 ± 16.36
$M(ee\mu) > 40\,\text{GeV}$	4.03 ± 0.14	0.08	0.19	174.31 ± 16.30
bJets: 0	3.98 ± 0.14	0.08	0.21	103.20 ± 15.42
$E_{\text{T}}^{\text{miss}} < 60\,\text{GeV}$	3.91 ± 0.14	0.08	0.29	59.79 ± 10.61
$M(\mu, e_2) < 50\,\text{GeV}$	3.89 ± 0.14	0.08	0.29	58.06 ± 10.57
$M(\mu, e_2) < 30\,\text{GeV}$	3.65 ± 0.13	0.07	0.36	40.95 ± 7.58
$M(\mu, e_2) < 20\,\text{GeV}$	2.15 ± 0.10	0.04	0.28	19.11 ± 5.93
$M(\mu, e_2) < 10\,\text{GeV}$	0.44 ± 0.04	0.01	0.09	7.00 ± 3.81
$M(\mu, e_2) < 5\,\text{GeV}$	0.05 ± 0.01	0.00	0.02	1.29 ± 1.85

where the *BL* notes the measurement of the variables in respect to the beamline.

The SF provided for the muon- and electron identification WPs are derived under the assumption of the full recommended IP requirements:

$$|d_0^{\text{BL}}/\sigma(d_0)|(e) < 5, \quad |d_0^{\text{BL}}/\sigma(d_0)|(\mu) < 3 \tag{6.5}$$

and

$$|\Delta z_0^{\text{BL}} \sin(\theta)|(l) < 0.5\,\text{mm}, \quad l = e, \mu. \tag{6.6}$$

For the muon- and electron-channel separate studies were conducted to understand the impact of certain IP cuts on the signal. The corresponding sections are 6.2.4 and 6.3.5.

From the studies it can be concluded that the IP cuts would greatly diminish the HNL signal for mass points 5 and 10 GeV, where the proper decay length is given by $c\tau = 1\,\text{mm}$ and which consequently are further displaced. The requirement on leptons for this search are therefore as shown in Table 6.10.

Table 6.10.: Loosened IP requirements applied in this search after optimization in Sections 6.2.4 and 6.3.5.

Lepton	$\lvert d_0^{\text{BL}}/\sigma(d_0)\rvert$	$\lvert\Delta z_0^{\text{BL}} \sin(\theta)\rvert$
ℓ_{lead}	$< 3(\ell = \mu), < 5(\ell = e)$	$< 0.5\,\text{mm}$
ℓ_{sublead}	none	$< 1\,\text{mm}$
ℓ'	none	$< 1\,\text{mm}$

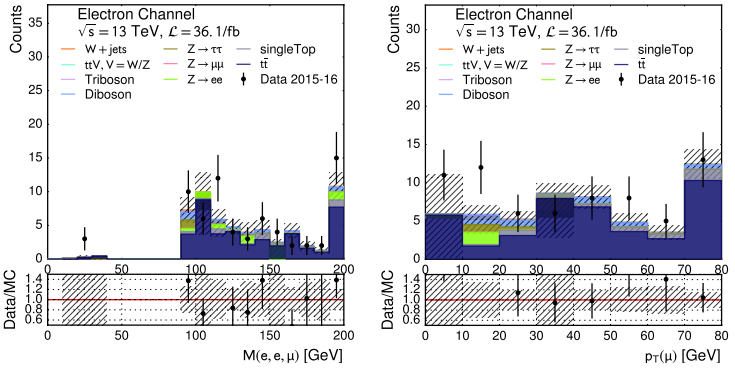

(a) $M(\ell, \ell, \ell')$ (b) p_{T} muon

Figure 6.22.: *Electron Channel.* Comparison of agreement between data and MC backgrounds in the $M(\ell, \ell, \ell')$ sideband region outside of 40 to 90 GeV. The error bands show combined statistical uncertainties.

As the SF are intended to account for known differences between the modeling and reconstruction of MC samples and data a study has therefore been performed to check the impact of the loosened IP requirements (as stated in Section 6.4) on the ratio between data and MC.

This is achieved by comparing the efficiency loss between applying the loosened IP cuts and the full IP cuts both on data and MC. By comparing the ratio between the efficiency loss it can be seen whether data and MC behave differently and accordingly whether the use of the same SF is justified. To stay blinded for this study while staying close to the signal region, a region has been selected which is constructed of the sidebands of the trilepton invariant mass distribution $M(l_\alpha, l_\alpha, l_\beta)$, $\alpha \neq \beta$. To increase statistics the b veto and $E_{\mathrm{T}}^{\mathrm{miss}}$ cuts are not applied. MC and data distributions of this region can be found in Appendix E where the region is notated by `DM-2`.

The result is presented in figures 6.23 and 6.24 for the muon and electron channel respectively. The difference in efficiency and the ratio of data and MC efficiency loss are presented in different p_{T} bins of the subleading leptons. Throughout it can be observed that the ratio of efficiency loss is compatible with unity within statistical uncertainties. It can therefore be concluded that using loosened IP cuts for this search is justified to increase the signal yield while still being able to leverage the appropriate SF derived for muon and electron objects.

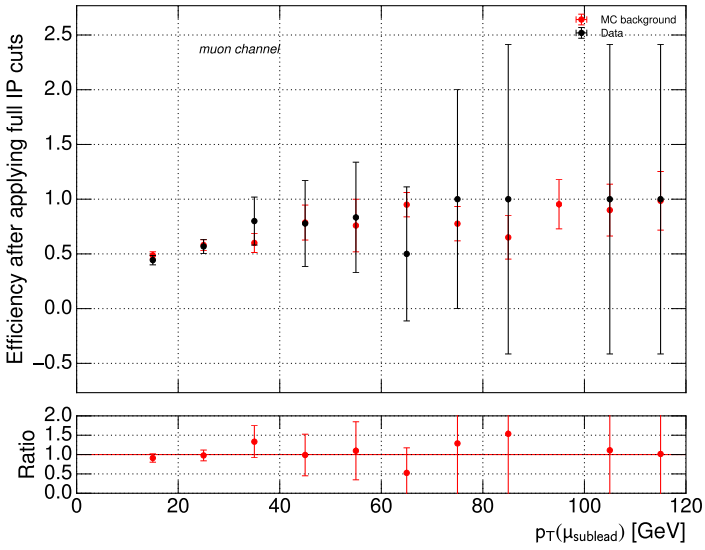

(a) $p_{\mathrm{T}}(\mu_{\mathrm{sublead}})$

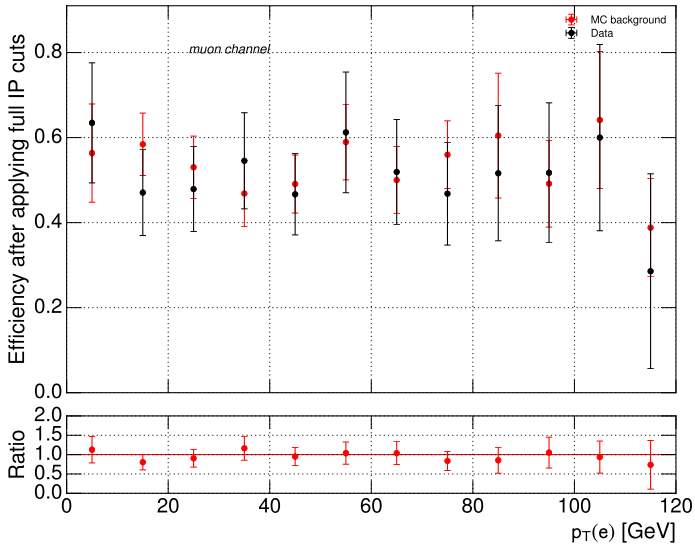

(b) $p_{\mathrm{T}}(e)$

Figure 6.23.: *Muon channel.* The effect of using loosened IP cuts on μ_{sublead} and e is studied in bins of p_{T} of the two lepton objects. Shown is `CR-1` without b veto or $E_{\mathrm{T}}^{\mathrm{miss}}$ cut applied to increase statistics. The error bands show combined statistical uncertainties.

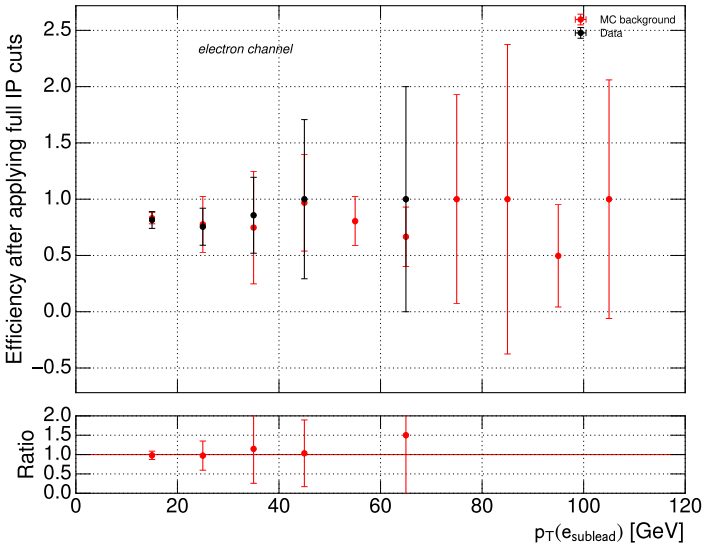

(a) $p_{\mathrm{T}}(e_{\mathrm{sublead}})$

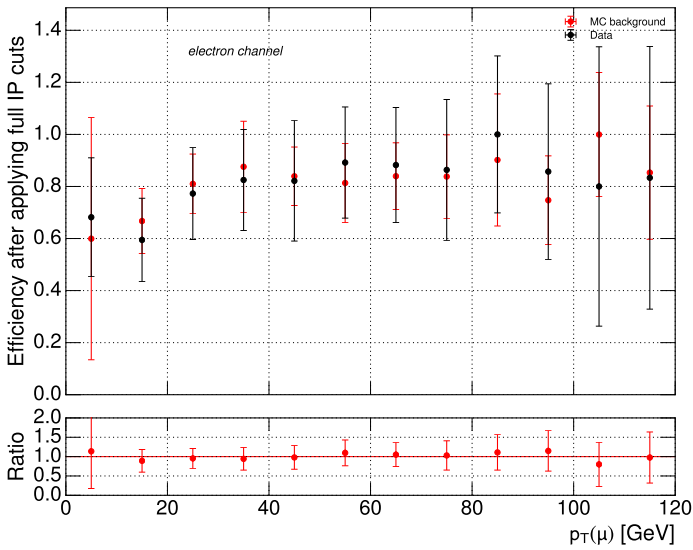

(b) $p_{\mathrm{T}}(\mu)$

Figure 6.24.: *Electron channel.* The effect of using loosened IP cuts on e_{sublead} and μ is studied in bins of p_{T} of the two lepton objects. Shown is `CR-1` without b veto or $E_{\mathrm{T}}^{\mathrm{miss}}$ cut applied to increase statistics. The error bands show combined statistical uncertainties.

Chapter 7.

Background estimation

But I don't feel secure enough to publish anything about this idea, so I first turn confidently to you, dear radioactives, with the question as to the situation concerning experimental proof of such a neutron, if it has something like about 10 times the penetrating capacity of a γ ray.

— W. Pauli, 1930 [2]

For the background estimation in the SR a multi-region fit is performed. Background samples are normalized in Control Regions (CRs) directly adjacent to the SR and hypothesis tests for background-only and signal-plus-background models can be conducted to discover or exclude certain amounts of signal. A partial data-derived estimation of samples is used where the shape and yield of processes with one or fewer real leptons are estimated in regions where all three leptons carry the same charge. By validating in multiple distributions of the control regions this shape and performing compatibility tests through the regions participating in the fit a robust background description translatable into the SR is performed.

7.1. Standard-Model backgrounds

In this analysis SM backgrounds participate due to a mixture of prompt leptons originating from boson decays which are labelled as *real* leptons and misidentification of non-prompt leptons originating from jets and leptons from pileup events that are labeled *fake leptons*. Though MC simulation and the ATLAS detector response simulation can account to some degree for fake leptons, it is advisable to check or account for the actual probability of a fake lepton entering the control- and signal regions in data.

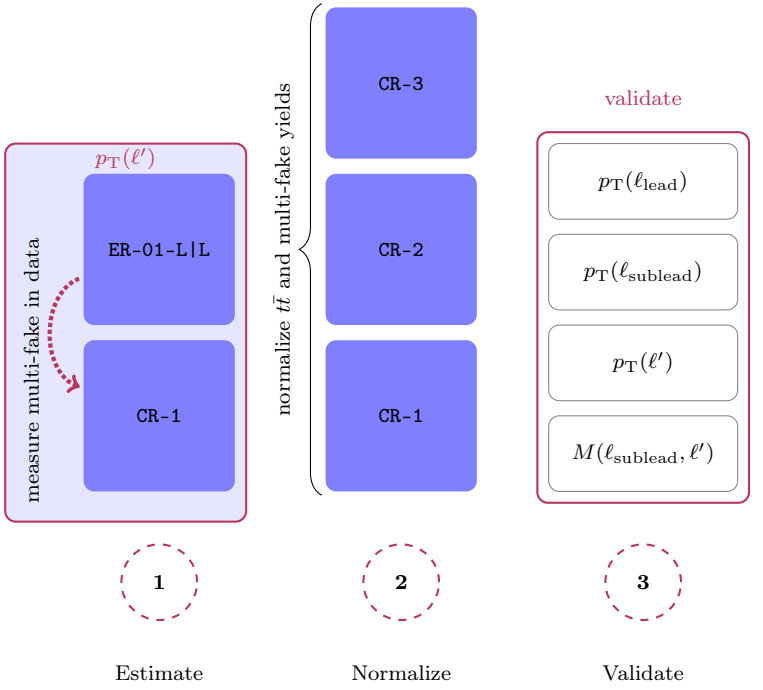

Figure 7.1.: The backgrond model before unlinding the signal region is constructed by SM processes and multi-fake shape estimation from step 1. Herafter the most dominant background $t\bar{t}$ and multi-fake yield are normalized and the result validated in the lepton p_{T} distributions as well as the dilepton invariant mass distribution. The estimation region for measuring the multi-fake contribution is denoted by `ER-01-L|L`.

Processes with two or more real leptons (Z+jets, $t\bar{t}$, diboson, single top etc.) are estimated by using MC generated samples. To ensure that the modeling of backgrounds is performed correctly in the narrow phase space of this search, the dominant background samples are normalized in several regions. This is applied for $t\bar{t}$ as it is the main MC background.

For processes with only one or fewer real leptons (W+jets, QCD), referred to as *multi-fake*, shape and yield are estimated in a region where all leptons have the same charge. For each control region the multi-fake yield and shape is correspondingly translated from a corresponding same charge region.

7.2. Fit approach

The shape and yield of multi-fake samples is measured in data in so called Estimation Regions (ERs) and translated to the CRs as well as the SR.

The control regions have been defined by single cut inversions from the signal region in order to ensure a close proximity with the phase space in the signal region. By performing a simultaneous fit in the control regions for the most dominant MC background $t\bar{t}$ and the multi-fake normalization it is ensured that the backgrounds are correctly normalized and that this normalization is invariant under inverting the control region cuts back to the signal region.

The procedure for constructing and validating the background model while remaining blinded in the signal region is shown in Figure 7.1. At first the SM processes for one or less fakes are used to measure the shape of the multi-fake sample in data. For this the calculation data minus MC is performed in the estimation regions while propagating all statistical uncertainties. The resulting shape is transferred to the corresponding control region CR. Herafter the $t\bar{t}$ MC sample yield as well as the multi-fake sample yield is normalized in the three control regions and the result verified in all lepton p_{T} distributions as well as the $M(\ell_{\mathrm{sublead}}, \ell')$ distribution.

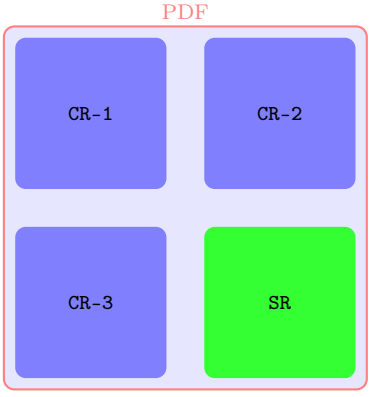

Figure 7.2.: A visualization of the PDF: For the final signal search a combined PDF is built of three control-regions rich in backgrounds and a signal region capable of discriminating background and signal-plus-background hypothesis models.

After unblinding the signal region a combined PDF is formed in which the backgrounds and signal can be normalized (see Figure 7.2). By using Log-Likelihood (LLH) ratio tests hypotheses for background-only and signal-plus-background models can be tested.

An overview of all regions involved in the background estimation is given in Table 7.1.

7.3. Construction of background fit regions

The most important backgrounds are normalized to data by using CR created upon inversion of one SR cut. In order to allow a reliable translation of the normalization from one background type from a CR to a SR, the CRs are neighboring the signal region and are separated by exactly one orthogonal cut.

By using several CRs an increase in available statistical sample size of the background samples is achieved and simultaneously the approach shows the invariance of the background estimation upon the definition of CRs.

A visualization of the cut-inversions is shown in Figure 7.3.

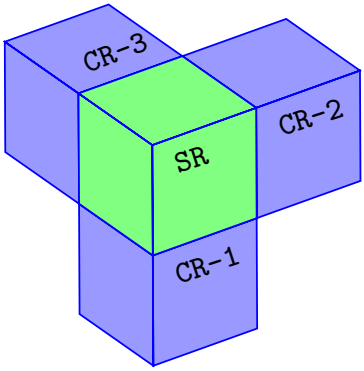

Figure 7.3.: Definition of control regions upon signal region cut inversion. A simultaneous fit of the backgrounds validates that the background estimated is invariant upon cut inversions back to the signal region.

7.3.1. Control Regions

Following the strategy described, control-regions are constructed by the following procedure. The signal region is defined as shown in Tables 6.2 and 6.8.

The cuts not corresponding to object requirements or the triggers applied are defining the invertible signal region cuts. Namely:

- s_0: no-OSSF lepton pairs
- s_1: $40\,\text{GeV} < M(l_\alpha l_\alpha l_\beta) < 90\,\text{GeV}$, $\alpha \neq \beta$, $\alpha, \beta \in \{\mu, e\}$
- s_2: b jet veto
- s_3: $E_\text{T}^\text{miss} < 60\,\text{GeV}$

The logically inverted cuts are defined as cuts c_i for $i \in \{0, \ldots, 3\}$ and are listed below:

- c_0: all leptons same charge
- c_1: $40\,\text{GeV} \geq M(l_\alpha, l_\alpha, l_\beta)$, **or** $M(l_\alpha, l_\alpha, l_\beta) \geq 90\,\text{GeV}$, $\alpha \neq \beta, \alpha, \beta \in \{\mu, e\}$
- c_2: at least one b jet
- c_3: $E_\text{T}^\text{miss} \geq 60\,\text{GeV}$

Used as control regions are all regions that differ from the signal region by inversion of a single cut. The region CR-i, $i \in \{0, \ldots, 3\}$ is hence defined as:

$$\texttt{CR} - \texttt{i} := \{s_j | j \in \{0, \ldots, 3\}, i \neq j\} + \{c_i\}, \tag{7.1}$$

while using the same object and trigger requirements.

Table 7.1.: Overview of what cuts the regions are comprised of. **s** stands for signal region cut and **c** stands for the control region cut (inverted version of cut s). For the electron channel no lepton isolation is required for the estimation regions.

Region	Charge	$M(l_\alpha, l_\alpha, l_\beta)$	b jet	$E_{\mathrm{T}}^{\mathrm{miss}}$	$\mu_{\mathrm{sublead}}, e$ isolation	$e_{\mathrm{sublead}}, \mu$ isolation
SR	**s**	**s**	**s**	**s**	Loose and Loose	Loose and Loose
CR-1	**s**	**c**	**s**	**s**	Loose and Loose	Loose and Loose
CR-2	**s**	**s**	**c**	**s**	Loose and Loose	Loose and Loose
CR-3	**s**	**s**	**s**	**c**	Loose and Loose	Loose and Loose
ER-0-L|L	**c**	**s**	**s**	**s**	Loose **or** Loose	none
ER-01-L|L	**c**	**c**	**s**	**s**	Loose **or** Loose	none
ER-02-L|L	**c**	**s**	**c**	**s**	Loose **or** Loose	none
ER-03-L|L	**c**	**s**	**s**	**c**	Loose **or** Loose	none

7.3.2. Estimation Regions

As control regions are denoted by `CR-i` with $i = 1, \ldots, 3$ via inversions of signal region cuts, in the same notation regions `CR-0i` can be constructed that have the additional requirement that all leptons have the same charge. They will be denoted as `ER-0i` in order to underline their purpose as multi-fake shape ***ER***.

Additionally region `ER-0i-L|L` $\supset$ `ER-0i` are defined which are identical to `ER-0i` but enriched with further fakes by loosening the isolation requirement on the subleading leptons. This is indicated by appending the L/L suffix (short for loosened isolation).

In the region `ER-0i-L|L` the statistical size is therefore increased in order to estimate the shape of data-derived backgrounds with lower statistical uncertainty.

7.4. Likelihood fits

A PDF is a function parameterizing the relative likelihood of a continuous random variable that the value of the random variable would equal its value. Its integral therefore maps to the value that a random variable falls within a particular range. It has therefore the important property that for the PDF f

$$\int f(x)\ \mathrm{d}x = 1 \tag{7.2}$$

holds. For complex probabilities with additional parameters $\boldsymbol{\alpha}$ entering the PDF one usually is interested in

$$f(x|\boldsymbol{\alpha}) \tag{7.3}$$

and calls this the *probability model* or *model* [99]. $\boldsymbol{\alpha}$ denotes here a whole set of parameters. The one of specific interest for the model, as for instance signal strength parameterization, are called *parameter of interest* while the other ones are usually referred to as *nuisance parameters*. All of them can be referred to as *fit parameters*. A common notation is μ for a parameter of interest and $\boldsymbol{\theta}$ for nuisance parameters.

The likelihood function in turn is defined as

$$\mathcal{L}(\boldsymbol{\alpha}|x) = f(x|\boldsymbol{\alpha}) \tag{7.4}$$

for x fixed and hence its integral on all of $\boldsymbol{\alpha}$ space is not generally unity. A likelihood function can include several physics analysis channels and parameters which, assuming they are statistically independent, are entering the liklihood as a factors. For this reason the logarithm of the likelihood is often used in order to use the multiplicative property of logarithms

$$\log(a \cdot b) = \log(a) + \log(b) \tag{7.5}$$

which makes it numerically easier to solve.

Terms constraining the fit parameters are estimated by so called *auxiliary measurements* and included in the likelihood. They are usually idealized estimations of the constraint by knowledge of a central value and some form of uncertainty (usually a standard deviation).

Instead of finding a parameter set $\boldsymbol{\alpha}$ for which the likelihood $\mathcal{L}$ becomes maximal, one minimizes $-\log(\mathcal{L})$ often referred to as LLH or sometimes abbreviated nLLH. Minimization of the negative Log-Likelihood (nLLH) is performed for this search using `Minuit2` [100, 101].

7.5. Hypothesis testing

Common models in experimental particle physics involve several fit parameters, each with pre- and post-fit uncertainties. Rejecting a hypothesis is therefore more involved than comparing model and observed data plots but needs to be properly quantified. A common approach is the comparison of models which for searches within ATLAS often consist of a background-only model describing the SM processes and a signal-plus-background model in which the signal under investigation is added on top of the SM background. An overview of the terms is given is given in an exemplification in Table 7.2.

Table 7.2.: Exemplification of background-only and signal-plus-background model terms in a Poisson counting experiment. n denotes the observed events, while B stands for the background model events and S for the signal events. Table from [99].

Symbol	**Statistical name**	**Physics name**	**Probability model**
H_0	null hypothesis	background-only	$\text{Pois}\,(n\|B)$
H_1	alternate hypothesis	signal-plus-background	$\text{Pois}\,(n\|S+B)$

Following the notation from the previous section one can consider the likelihood $\mathcal{L}(\mu, \boldsymbol{\theta})$ that is minimized in regard to measured data $\boldsymbol{x}$.

For simplicity the likelihood $\mathcal{L}(\mu, \boldsymbol{\theta}|\boldsymbol{x})$ is here written as $\mathcal{L}(\mu, \boldsymbol{\theta})$ omitting the data to which it corresponds. For maximum likelihood estimates (or simply called fit-results) given the data a "^" is now used.

The *profile likelihood ratio* is then given by

$$\lambda(\mu) = \frac{\mathcal{L}(\mu, \hat{\hat{\boldsymbol{\theta}}}(\mu))}{\mathcal{L}(\hat{\mu}, \hat{\boldsymbol{\theta}})} \tag{7.6}$$

where $\hat{\hat{\boldsymbol{\theta}}}(\mu)$ is the maximum estimate of $\mathcal{L}$ given $\boldsymbol{x}$ for fixed μ. Note that λ does not depend on $\boldsymbol{\theta}$ anymore as the denominator contains only the likelihood of the maximum likelihood estimates of fit parameters.

The test statistic for hypothesis testing, as a mapping of data to a real number, is then defined as

$$\tilde{q}_\mu = \begin{cases} -2\log\tilde{\lambda}(\mu), & \hat{\mu} \leq \mu \\ 0, & \hat{\mu} > \mu \end{cases} \tag{7.7}$$

where $\tilde{\lambda}$ is a simple extension of λ limiting $\hat{\mu} \geq 0$ via

$$\tilde{\lambda}(\mu) = \begin{cases} \lambda(\mu), & \hat{\mu} \geq 0 \\ \frac{\mathcal{L}(\mu, \hat{\hat{\boldsymbol{\theta}}}(\mu))}{\mathcal{L}(0, \hat{\hat{\boldsymbol{\theta}}}(0))}, & \hat{\mu} < 0. \end{cases} \tag{7.8}$$

Depending on whether a discovery or exclusion hypothesis test should be performed the test statistic considered is $\tilde{q}_0$ or $\tilde{q}_\mu$ respectively. If one would repeat the experiment the test statistic, as it depends on the observed data, would map to different values. It also depends on $\mu, \boldsymbol{\theta}$. One can now perform pseudo-experiments with MC techniques to obtain the distribution of the test statistic given a model $\mu, \boldsymbol{\theta}$ denoted

$$f(\tilde{q}_\mu|\mu, \boldsymbol{\theta}). \tag{7.9}$$

The p-value for measured data under a certain hypothesis with a parameter of interest μ is then given by

$$p(\mu) = \int_{\tilde{q}_\mu}^{\infty} f(\tilde{q}_\mu|\mu, \boldsymbol{\theta}) \, \mathrm{d}\tilde{q}_\mu \tag{7.10}$$

and therefore denotes the probability of obtaining a more extreme result assuming the hypothesis. Following Willk's theorem [102] for asymptotic test sizes (7.6) is independent of $\boldsymbol{\theta}$ [103] and can therefore be chosen as the fit result $\hat{\hat{\boldsymbol{\theta}}}(\mu)$ for a chosen parameter of interest μ.

For the CL_s method [104] the p-values corresponding to the signal-plus-background and background-only model are then defined analogously:

$$CL_{s+b} = \int_{\tilde{q}_\mu}^{\infty} f(\tilde{q}_\mu|\mu, \hat{\hat{\boldsymbol{\theta}}}(\mu)) \, \mathrm{d}\tilde{q}_\mu \tag{7.11}$$

$$CL_b = \int_{\tilde{q}_0}^{\infty} f(\tilde{q}_0|0, \hat{\hat{\boldsymbol{\theta}}}(0)) \, \mathrm{d}\tilde{q}_0 \tag{7.12}$$

and the CL_s value is obtained via

$$CL_s = \frac{CL_{s+b}}{CL_b}. \tag{7.13}$$

A discovery hypothesis test in this search is a rejection of the background-model as done in $\tilde{q}_0$ given a low p-value (see also Section 8.3), while setting exclusion limits on the signal-plus-background model is performed via the CL_s method for usually a p-value below 5 %.

7.6. Uncertainties

Uncertainties considered for the background estimation are consisting of statistical uncertainties due to the amount of measured data and MC events in the control- and signal region as well as experimental systematic uncertainties.

Systematic uncertainties are derived by the different working groups inside ATLAS and parameterize uncertainties in a wide variety of areas. This includes detector effects as well as algorithmic uncertainties upon the reconstruction of objects (see Section 5). ATLAS programs responsible to discriminate objects as jets, muons, electrons, $E_{\mathrm{T}}^{\mathrm{miss}}$ return beside their decision given a candidate also a decision considering a $\pm 1\sigma$ variation of the systematics associated with the objects. For this search systematic uncertainties do not exhibit a large impact on the fits as can be seen for instance in the best-fit Normalization Factor (NF) for the background-only hypotheses in Table 7.6. Systematics associated with jets contain a `JET_` prefix, while muon systematics start with `MUON_`, electron systematics start with `EG_` for E/gamma and $E_{\mathrm{T}}^{\mathrm{miss}}$ systematics include `MET_`. Besides the systematics associated with the ATLAS objects, the SFs applied also give a variation of their returned value. As they usually depend on identification and/or isolation WPs which are appended here to the name the systematic associated with it contains a lot of characters. The SF systematics all contain `SF` in their name. Systematics entering the fit that have no shape or yield differences for any sample involved are removed by the software and do not appear in the final list of systematics. An overview of the remaining systematic uncertainty names can be seen in Figure 8.23.

As will be seen later the systematic uncertainties do not exhibit a dominat impact on the signal strength obtained in signal-plus-background fits. From Figures 8.11 and 8.12 it can be seen that the largest impacts are obtained by the systematics listed in Table 7.3.

Table 7.3.: Systematics with the largest effect on signal strength for both channels.

Systematic name	Effect
MUON_MS	variation in the smearing of the MS track
MUON_ID	variation in the smearing of the ID track
EG_SCALE_ALL	variation of energy scale for electron calibration
MET_SoftTrk_RESO	$E_{\mathrm{T}}^{\mathrm{miss}}$ soft term resolution based on data and MC comparisons
JET_JER_SINGLE_NP	jet energy resolution calibration variation
JET_GroupedNP_1	jet energy scale calibration variation

As the systematic uncertainties are applied to MC samples the sample size can increase the relative effect of the $\pm\sigma$ variations associated with the systematic. This can happen if in one bin of the distribution the up- and down variations are further apart due to chance in a low statistical sample. An example of this can be seen in Section D where the jet energy resolution systematic variations display a discontinuous distribution due to statistical fluctuation. This was observed for this search in the muon channel only. By the use of kernels the distributions were smoothened, which is a standard procedure for ATLAS in this case [105].

As part of the likelihood function, auxiliary measurements parameterizing the uncertainties enter. For systematic uncertainties they are mostly assumed to be of Gaussian shape. When one considers the measurement of a single bin as an auxiliary measurement which is strictly positive, using the truncated Gaussian for the statistical uncertainty may lead to an underestimation of the uncertainty [106]. Instead a Poisson distribution with a uniform prior leads to a Gamma constraint term as noted in [99] hence the name *gamma* (γ) factor. For a counting experiment (as for instance in one bin of a distribution) n events were measured with a relative uncertainty of σ^{rel}.

As the Poisson mean value is not apriori known one measures it instead as $\tau\alpha$ where

$$\tau = \left(\frac{1}{\sigma^{\mathrm{rel}}}\right)^2 \tag{7.14}$$

and α is the uncertainty parameter allowed to varied in the LLH fit. The Poisson distribution is then given by

$$\mathrm{Pois}(n|\tau\alpha) = \frac{(\tau\alpha)^n e^{-\tau\alpha}}{n!}. \tag{7.15}$$

Finally the discrete Poisson distribution is generalized by using the Gamma distribution P_Γ with

$$P_\Gamma\left(\alpha|A=\tau, B=n-1\right) \tag{7.16}$$

as noted in [99].

For multiple MC samples a common statistical uncertainty parameter is used which is abbreviated in this search by γstat_. This is justified when the statistical uncertainties of the MC samples involved are approximately of the same order. For this reason separate γ-factors are used for the multi-fake sample and the HNL signal samples as here the available statistical size varies.

7.7. Multi-fake estimation

The underlying assumption is that leptons from multi-jets can end up by pure chance in control region CR-i or its electron charge inverted counterpart esti-

mation region ER-0i. This is well motivated upon inspection of the p_{T} distributions for subleading leptons in CR-1 and its charge inverted counterpart ER-01-L|L as shown in Figure 7.4.

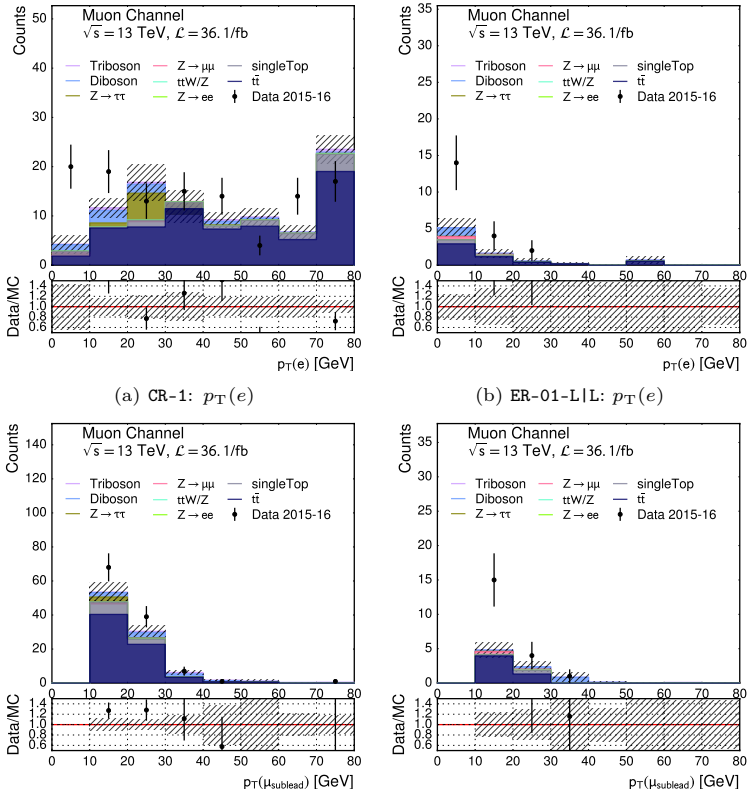

(a) CR-1: $p_{\mathrm{T}}(e)$ (b) ER-01-L|L: $p_{\mathrm{T}}(e)$

(c) CR-1: $p_{\mathrm{T}}(\mu_{\mathrm{sublead}})$ (d) ER-01-L|L: $p_{\mathrm{T}}(\mu_{\mathrm{sublead}})$

Figure 7.4.: Comparison of data and MC prediction in control region CR-1 (left) and estimation region ER-01-LL (right). The location of missing Monte Carlo events in low $p_{\mathrm{T}}(e)$ events is notable. The difference between the ER and CR is the charge on the electron: $\mu^{\pm}\mu^{\pm}e^{\mp}$ (left) vs. $\mu^{\pm}\mu^{\pm}e^{\pm}$ (right) and a slightly loosened isolation requirement as noted in Table 7.1).

As described in Section 7.3.2 the shape and yield of the these backgrounds is measured in ER-0i-L|L due to the larger statistics available. The estimation and control regions are therefore forming pairs CR-i and ER-0i-L|L as shown in Table 7.4.

The measurement of the shape and yield is performed by subtracting the MC process contribution from SM backgrounds from the data measured. By doing this, backgrounds that enter through at least two non-prompt leptons are disregarded. As was checked in MC truth information, the leading lepton is in nearly all cases a real lepton. This lepton triggers also the L1 which is matched in this search to the trigger information and therefore apriori reduced possible fake-leptons. Practically this means that MC simulated W+jets contribution

Table 7.4.: Shown are corresponding multi-fake estimation regions to the signal and control regions.

Signal/Control reg.	SR	CR-1	CR-2	CR-3
Estimation reg.	ER-0-L|L	ER-01-L|L	ER-02-L|L	ER-03-L|L

are discarded when measuring the shape of these multi-fake events as they are included in the shape (their contribution to control- and signal regions is solely due to two fake leptons which has been checked in MC truth information). The sample is form now on referred to as *Multi-fake*.

The shape is then transferred into the CRs and yield-corrected via an additional normalization factor μ_{dd} for the possible differences between the two regions. The yield is determined in the p_{T} distribution of the e for the muon-channel and for the μ for the electron channel. In these distributions the multi-fakes are expected to be visible in the lower end of the distributions. The variable is accordingly binned so that most of the multi-fakes are in the lowest bin. This offers a reduction of the statistical uncertainty for the yield measurement to the lowest possible value.

The determination of multi-fakes can be verified by performing a simultaneous fit upon different inversions c_i, $i \in \{1, 2, 3\}$. Additionally cross-checks have been conducted with different distributions given the previously measured NFs of the same events in order to verify that the right shape is indeed correctly measured throughout different observables.

Herafter two fit configurations are run to normalize the samples, one with statistical uncertainties only while one uses the statistical uncertainty of the samples as well as the full systematic uncertainty available. All fit configurations consist of a simultaneous fit of the regions CR-i, $i \in \{1, \ldots, 3\}$. As fit distributions in the $\ell^{\pm}\ell^{\pm}\ell'^{\mp}$ channel the ℓ' was chosen as it exhibits a p_{T} spectrum in which multi-fakes will appear at low values. This enables a better distinction between the yield of multi-fakes and other backgrounds modeled by MC. This also means that per region only one distribution is participating in the fit and therefore all regions are statistically independent.

7.8. Muon channel

For the muon channel the $p_{\mathrm{T}}(e)$ distribution is chosen to distinguish multi-fakes from MC simulated samples.

In Figure 7.5 the shape of the data-derived background sample (multi-fake) is measured. The contribution from modelled MC contributions is rather small in all plots.

This shape is then applied to regions CR-i, $i \in \{1, \ldots, 3\}$ and distributions as shown in Figure 7.6 (left column) are obtained.

In Section 7.8.3 it is shown that the measured yields are fully compatible within statistical uncertainties in the $M(\mu, e)$ distribution which is used in the signal region to search for HNL signal. An overview of the control regions and the distribution used for normalizing the dominant backgrounds is given in Table 7.5. The post-fit NF values obtained are shown in Table 7.6 while the overall correlation of all parameters used in the fits can be seen in Section 7.10.

7.8.1. Extrapolation into signal-region

The charge-inverted region of the signal region is the CR-0 region in which the only difference to the signal is composed of the requirement that all leptons carry the same charge.

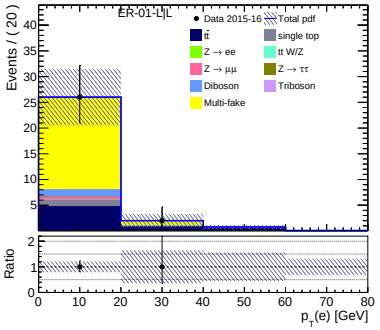

(a) ER-01-L|L: $p_{\mathrm{T}}(e)$

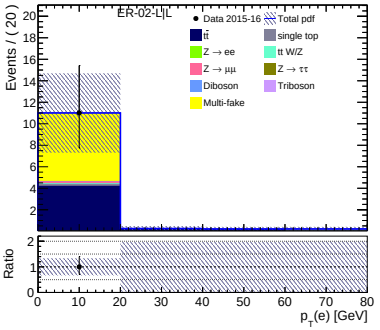

(b) ER-02-L|L: $p_{\mathrm{T}}(e)$

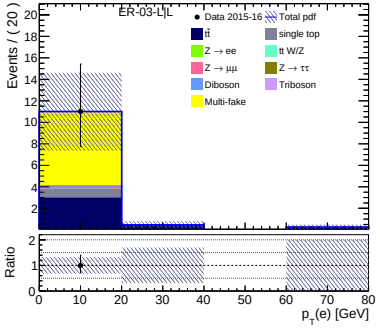

(c) ER-03-L|L: $p_{\mathrm{T}}(e)$

Figure 7.5.: Data-derived background shape estimation regions ER-0i-L|L. The yellow *Multi-Fake* sample shows the estimated contribution from data minus SM background samples contribution and the uncertainty on the total PDF pre-fit in the ERs.

Table 7.5.: Chosen control regions and fit distributions used for normalization of $t\bar{t}$ and multi-fake background.

Control region	**Difference to SR**	**Normalization distribution**
CR-1	$M(\mu,\mu,e) < 40\,\mathrm{GeV}$ or $M(\mu,\mu,e) > 90\,\mathrm{GeV}$	$p_{\mathrm{T}}(e)$
CR-2	at least one b-jet	$p_{\mathrm{T}}(e)$
CR-3	$E_{\mathrm{T}}^{\mathrm{miss}} > 60\,\mathrm{GeV}$	$p_{\mathrm{T}}(e)$

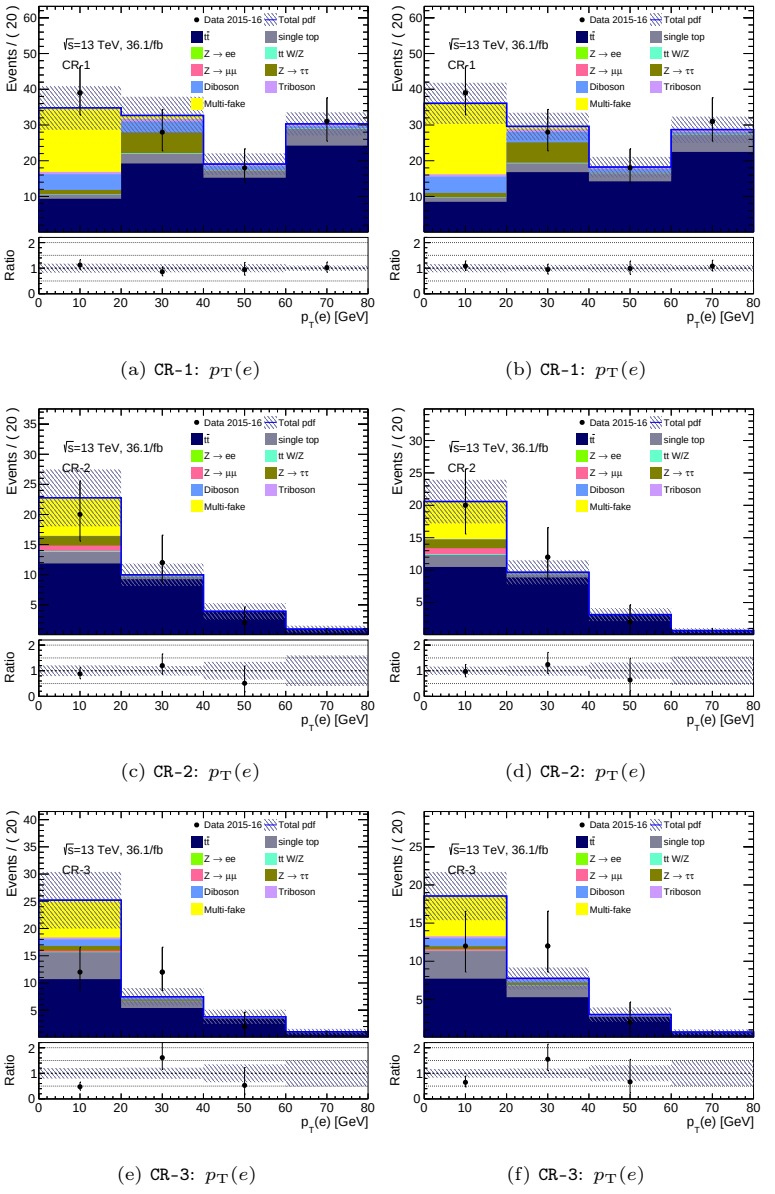

(a) CR-1: $p_{\mathrm{T}}(e)$

(b) CR-1: $p_{\mathrm{T}}(e)$

(c) CR-2: $p_{\mathrm{T}}(e)$

(d) CR-2: $p_{\mathrm{T}}(e)$

(e) CR-3: $p_{\mathrm{T}}(e)$

(f) CR-3: $p_{\mathrm{T}}(e)$

Figure 7.6.: Pre- (left column) and post-Fit distributions (right column) for CR-1 to CR-3 after normalizing the data-derived background and $t\bar{t}$ yield.

Table 7.6.: *Muon channel.* Normalization parameters obtained for multi-fake (μ_{dd}) and $t\bar{t}$ ($\mu_{t\bar{t}}$) for different uncertainty considerations.

Fit configuration	μ_{dd}	$\mu_{t\bar{t}}$
Statistical unc. only	0.84 ± 0.34	0.92 ± 0.13
Syst. and stat. unc.	0.97 ± 0.38	0.90 ± 0.14

Again the shape of the multi-fake background is measured in `ER-0-L|L` and apply it to the signal region as shown in Figure 7.7.

For a pre-unblinding background prediction in the signal region Figure 7.8 can be consulted. It shows the backround yield as normalized in the `CR`s only: The signal region itself is not used to normalize the samples and only poses as a validation region for the fit software. The dataset will be assumed to be equal to the background-only hypothesis (Asimov) and used to perform pre-unblinding sensitivity fits. In Table 7.7 the pre-unblinding yield of background samples is presented.

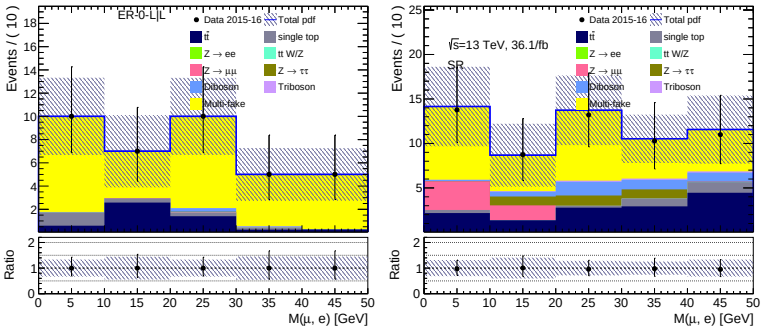

(a) $M(\mu, e)$ in `ER-0-L|L` (b) $M(\mu, e)$ in SR

Figure 7.7.: Measure multi-fake background in charge-inverted SR (left) and transfer the shape to the SR (right). The data shown in the signal region is the yield of background samples after applying the NFs derived in Table 7.6 (data=model). Background samples are pre-fit, so not scaled.

In order to make sure that the possible contribution to the multi-fake estimation region is negligible the values expected for the different mass hypotheses are quoted in Table 7.8. It can be clearly seen that only very few raw events made it into the estimation regions whose relative weighted contribution is negligible.

7.8.2. Statistical compatibility tests for normalization factors

For the statistical background model a simultaneous fit of the NFs associated with multi-fakes (μ_{dd}) and $t\bar{t}$ ($\mu_{t\bar{t}}$) is performed. The constraint obtained on the NFs is originating from up- and down-pulls experienced in the different `CR`s. For the muon channel e.g. the multi-fake normalization is pulled up by `CR-1` and down by `CR-3`.

To validate the background estimation method it therefore needs to be checked

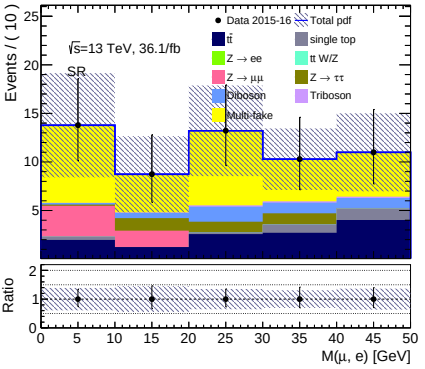

(a) $M(\mu, e)$

Figure 7.8.: Projected yield of background samples in signal region. Data points are the yield values of the background. The uncertainty of the normalization parameters $\mu_{t\bar{t}}$ and μ_{dd} are propagated and reflected in the final uncertainties.

Table 7.7.: Expected yield per background sample in signal region. Data shown is the background-only model prediction disregarding decimals. Apart from NFs also systematic and statistical uncertainty parameters were fitted and impact the yield.

Channel	SR
Observed events	56
Fitted bkg events	56.83 ± 6.51
Fitted $t\bar{t}$ events	12.31 ± 2.81
Fitted single top events	2.60 ± 0.51
Fitted Diboson events	4.37 ± 0.65
Fitted $Z \to ee$ events	0.00 ± 0.00
Fitted $Z \to \mu\mu$ events	4.88 ± 1.53
Fitted $Z \to \tau\tau$ events	3.63 ± 1.28
Fitted Triboson events	0.00 ± 0.00
Fitted ttW/Z events	0.04 ± 0.01
Fitted multi-fake (data-derived) events	28.49 ± 7.43
MC exp. SM events	58.63
MC exp. $t\bar{t}$ events	13.70
MC exp. single top events	2.61
MC exp. Diboson events	4.34
MC exp. $Z \to ee$ events	0.00
MC exp. $Z \to \mu\mu$ events	4.92
MC exp. $Z \to \tau\tau$ events	3.19
MC exp. Triboson events	0.00
MC exp. ttW/Z events	0.04
MC exp. multi-fake (data-derived) events	29.34

Table 7.8.: *Muon channel.* Shown are available statistics (and rel. uncertainty) in the `ER-0-L|L` which is used to measure the multi-fake template that is translated into the signal region. Also shown are the signal contamination of the various mass hypotheses in relative contributions (corresponding to a signal strength parameter of $\mu_{\mathrm{SIG}} = 1$) and total raw event count.

	Obs. events	**Stat. uncertainty**
Data	37.00 ± 6.08	$16.44\,\%$
	Rel. contamination	**Raw events**
HNL 5 GeV	$0.73 \pm 0.73\,\%$	1
HNL 10 GeV	$0.00 \pm 0.00\,\%$	0
HNL 30 GeV	$0.01 \pm 0.01\,\%$	3
HNL 20 GeV	$0.02 \pm 0.01\,\%$	4
HNL 50 GeV	$0.01 \pm 0.01\,\%$	3

whether there exists a *common* NF for multi-fake contributions that is compatible in all three control regions once one takes all statistical uncertainties into account. This factor translates the same-charge contribution into the no-OSSF control regions and finally also the signal region.

In this Section it is verified how *compatible* the NFs are if they are derived *separately* in `CR-1`, `CR-2` and `CR-3`. The test is performed statistically by calculating the LLH ratio of the background model with an expanded model using an additional degree of freedom that freely normalizes the multi-fakes *separately* in one of the regions.

The background model is now referred to as the null model H_0 and the expanded model as H_1 with $\mu^{\mathrm{alt}}_{\mathrm{dd}/t\bar{t}}$ in one of the control regions that also normalizes the yield of multi-fakes.

Assuming for illustration purposes that the additional NF for the *multi-fake* sample is added to `CR-3`, then the yields in bin i are for the different regions for multi-fakes (`dd`) are:

- `CR-1`: $\gamma_i \cdot \mu_{\mathrm{dd}} \cdot \mathrm{dd}^{\mathrm{yield}}_{\mathrm{prefit}}$
- `CR-2`: $\gamma_i \cdot \mu_{\mathrm{dd}} \cdot \mathrm{dd}^{\mathrm{yield}}_{\mathrm{prefit}}$
- `CR-3`: $\gamma_i \cdot \mu_{\mathrm{dd}} \cdot \mu^{\mathrm{alt}}_{\mathrm{dd}} \cdot \mathrm{dd}^{\mathrm{yield}}_{\mathrm{prefit}}$

where γ_i denotes the statistical uncertainty parameterization γ-factor, $\mathrm{dd}^{\mathrm{yield}}_{\mathrm{prefit}}$ the multi-fake pre-fit measured yield, μ_{dd} the NF of the background model and $\mu^{\mathrm{alt}}_{\mathrm{dd}}$ the extra NF of the expanded model.

And hereby the normalization of multi-fakes in `CR-3` is independent from the others as $\mu^{\mathrm{alt}}_{\mathrm{dd}}$ can invert any value of μ_{dd}.

If one chooses $\mu^{\mathrm{alt}}_{\mathrm{dd}} = 1$ it can be easily seen that $H_0 \subset H_1$. Therefore one can use

$$D = 2 \cdot [\mathcal{L}(H_1) - \mathcal{L}(H_0)]$$

as test statistic whose associated probability distribution is a chi-square distribution with one degree of freedom. Subsequently one can calculate then the percentage value to obtain a test statistic at least as extreme.

This test has been performed with additional NFs for multi-fake and $t\bar{t}$ in all regions and the results are shown in Table 7.9. It can be concluded that the NFs for the two samples are compatible in all regions as a usual cut off value for such test is located at $5\,\%$. However it is good to note the close proximity

of the μ_{dd} compatibility test in CR-3 to this cut-off value. The low amount of data points exhibited in this region in comparison to MC backgrounds gives rise to an artifical constrain on μ_{dd} which will be discussed in more detail in Section 8.2.

Table 7.9.: Compatibility test of separate NFs in one of the CRs with the overall normalization of the $t\bar{t}$ and multi-fake samples. The quoted 100 % value means that the LLH value obtained is within the precision of the fit. A usual cut-off value for such a test is 5 %.

Control region to use additional NF	$\mu_{\mathrm{dd}}^{\mathrm{alt}}$	$\mu_{t\bar{t}}^{\mathrm{alt}}$
CR-1	12.5 %	65.7 %
CR-2	84.8 %	100 %
CR-3	7.1 %	54.7 %

7.8.3. Validation of distribution choice

As described in Section 7.8.4 the shape of the dilepton invariant mass distributions is used in order to search for signal and exclusion limits on mixing angles for various HNL mass hypotheses.

In order to validate that the yield of the multi-fake backgrounds (as measured in the $p_{\mathrm{T}}(e)$ distribution) is fully compatible with $M(\mu, e)$ and other distributions the same yield is projected onto distributions not used in the normalization and presented in Figures 7.9 to 7.11.

Most notably is here the agreement in the distribution $M(\mu, e)$ which validates the approach to measure μ_{dd} and $\mu_{t\bar{t}}$ in a highly distinguishable distribution of MC and multi-fakes backgrounds with accordingly low statistical uncertainties.

To further show that the NFs measured in $p_{\mathrm{T}}(e)$ are fully compatible with the $M(\mu, e)$ distribution a statistical likelihood ratio test is performed.

For this test two fits are performed, one with the NFs freely floating and one with the NFs set constant to the values denoted in Table 7.6.

In Table 7.10 the probability for observing a result at least as extreme as the resulting χ^2 distribution is shown. It is clearly visible that the NFs are very compatible with the $M(\mu, e)$ distribution.

7.8.4. Performing exclusion fit

Assuming the observation of data equal to the background prediction shown in 7.8 (so exactly the background-only hypothesis) various fits can be performed for the signal-plus-background hypothesis with varying signal strength μ_{SIG} parameter. This way one can test the sensitivity of the analysis before unblinding the signal region.

Table 7.10.: LLH ratio test showing the compatibility of measured NFs with the $M(\mu, e)$ distributions. The advantage of using a LLH ratio test is that it can include all uncertainties on γ factors.

Control region	CR-1 - $M(\mu, e)$	CR-2 - $M(\mu, e)$	CR-3 - $M(\mu, e)$
p**-value**	57.7 %	88.2 %	49.8 %

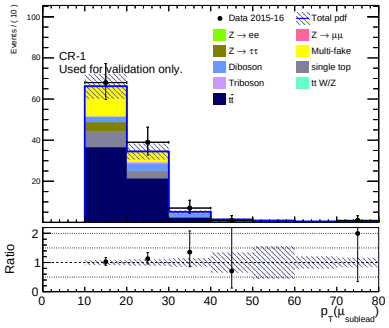

(a) CR-1: $p_{\mathrm{T}}(\mu_{\mathrm{sublead}})$

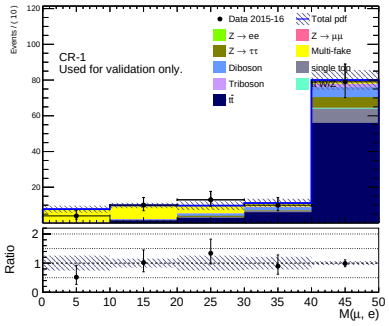

(b) CR-1: $M(\mu, e)$

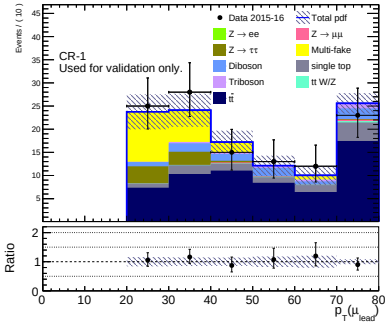

(c) CR-1: $p_{\mathrm{T}}(\mu_{\mathrm{lead}})$

Figure 7.9.: Post-Fit plots of CR-1 distributions not used in the normalization. The γ-factors in the plots (see Section 7.6) were also fitted and shown in their post-fit value.

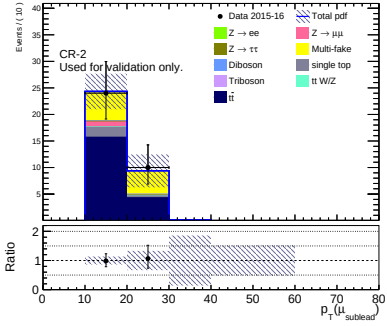

(a) CR-2: $p_{\mathrm{T}}(\mu_{\mathrm{sublead}})$

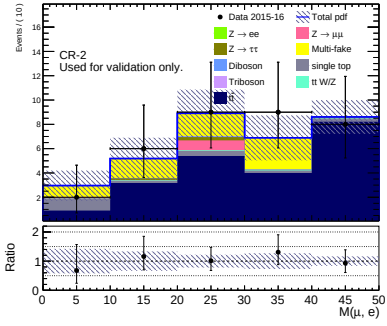

(b) CR-2: $M(\mu, e)$

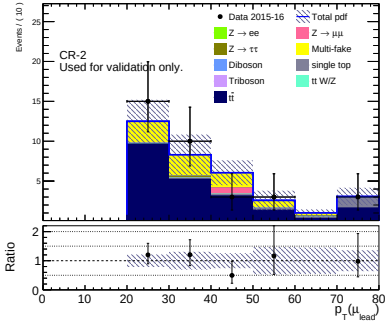

(c) CR-2: $p_{\mathrm{T}}(\mu_{\mathrm{lead}})$

Figure 7.10.: Post-Fit plots of CR-2 distributions not used in the normalization. The γ-factors in the plots (see Section 7.6) were also fitted and shown in their post-fit value.

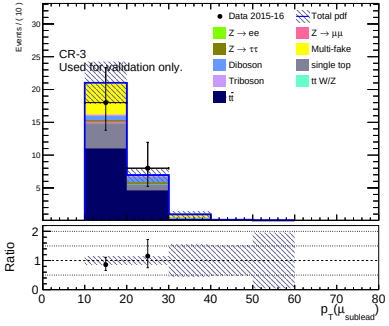

(a) CR-3: $p_{\mathrm{T}}(\mu_{\mathrm{sublead}})$

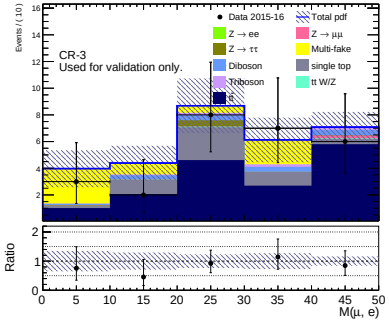

(b) CR-3: $M(\mu, e)$

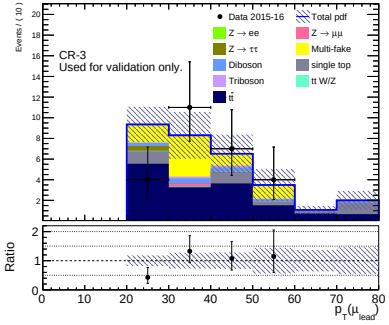

(c) CR-3: $p_{\mathrm{T}}(\mu_{\mathrm{lead}})$

Figure 7.11.: Post-Fit plots of CR-3 distributions not used in the normalization. The γ-factors in the plots (see Section 7.6) were also fitted and shown in their post-fit value.

A signal strength of $\mu_{\text{SIG}} = 1$ corresponds to the mixing angle of simulated Monte Carlo samples for a given proper decay length. An overview is shown in Figure 4.2 and the corresponding mixing angles are denoted in Table 4.1. These *exclusion* fits (using Asimov data) are performed in the variable distribution of $M(\mu, e)$.

The obtained exclusion strengths using an asymptotic formulae calculator are then presented in Figure 7.12. It has been checked separately that the asymptotic formulea do indeed give comparable results to frequentists calculators. The exclusion limits (sensitivity) on sterile-active mixing angles are presented in Figure 7.13 using all statistical and systematic uncertainties.

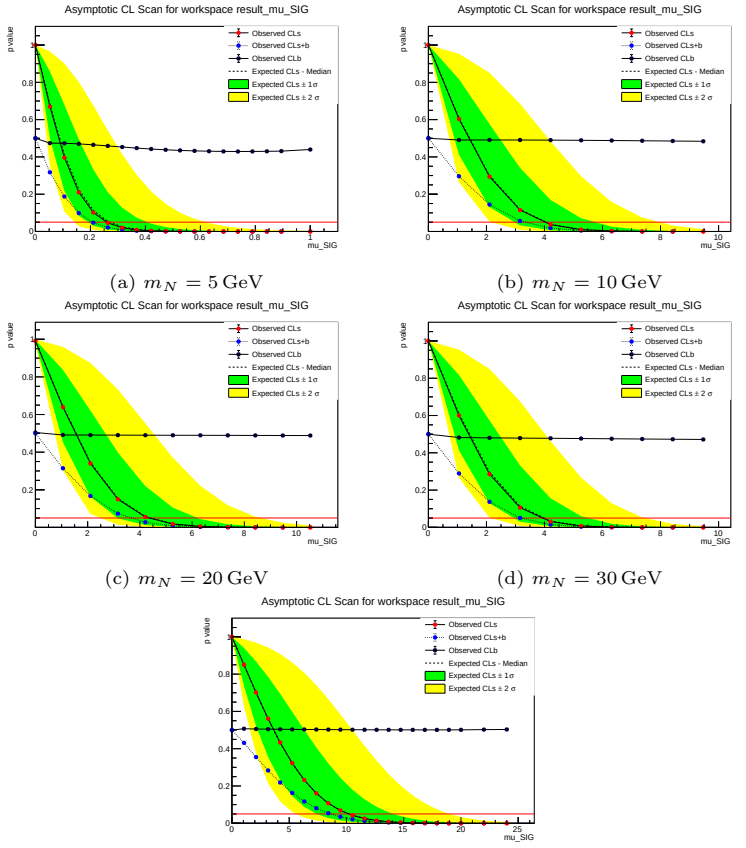

(a) $m_N = 5\,\text{GeV}$ (b) $m_N = 10\,\text{GeV}$

(c) $m_N = 20\,\text{GeV}$ (d) $m_N = 30\,\text{GeV}$

(e) $m_N = 50\,\text{GeV}$

Figure 7.12.: Exclusion levels obtained for the signal-plus-background hypothesis using data reflecting a background only model.

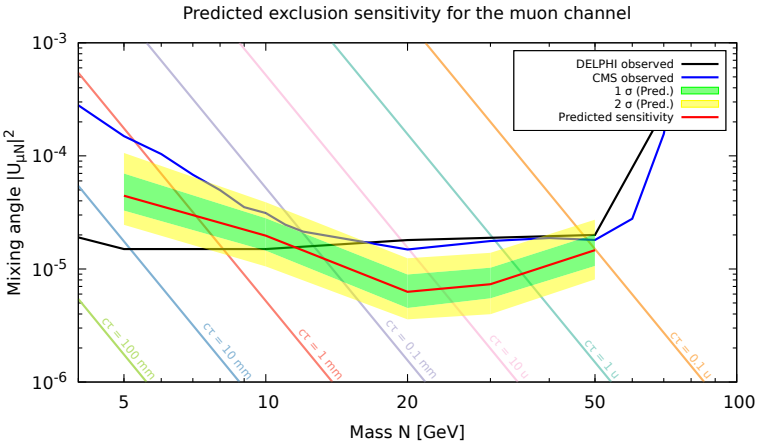

Figure 7.13.: Expected 95 % exclusion levels on $U_{\mu I}$ with statistical and systematical uncertainties.

7.9. Electron channel

The background fit for the electron channel is analogous to the muon channel described in Section 7.8. The variables chosen for distinguishing the multi-fake and MC background efficiently are stated in 7.12 and the normalization parameters Table 7.11.

As for the muon-channel the isolation requirement to measure the shape of the multi-fake background were also loosened in the `ER`s, however, instead of requiring only one of the leptons to pass the `Loose` isolation working point, for the electron channel no isolation is required for e_{sublead} or μ.

Table 7.11.: *Electron channel.* Normalization parameters obtained for multi-fake (μ_{dd}) and $t\bar{t}$ ($\mu_{t\bar{t}}$) for different uncertainty considerations.

Fit configuration	μ_{dd}	$\mu_{t\bar{t}}$
Using only stat. uncert.	1.09 ± 0.71	0.92 ± 0.17
Using stat. and syst. uncert.	0.42 ± 0.92	1.02 ± 0.16

Table 7.12.: Chosen control regions and fit distributions used for normalization of $t\bar{t}$ and multi-fake background.

Control region	**Difference to `SR`**	**Normalization distribution**
`CR-1`	$M(e,e,\mu) < 40\,\text{GeV}$ or $M(e,e,\mu) > 90\,\text{GeV}$	$p_{\text{T}}(\mu)$
`CR-2`	at least one b-jet	$p_{\text{T}}(\mu)$
`CR-3`	$E_{\text{T}}^{\text{miss}} > 60\,\text{GeV}$	$p_{\text{T}}(\mu)$

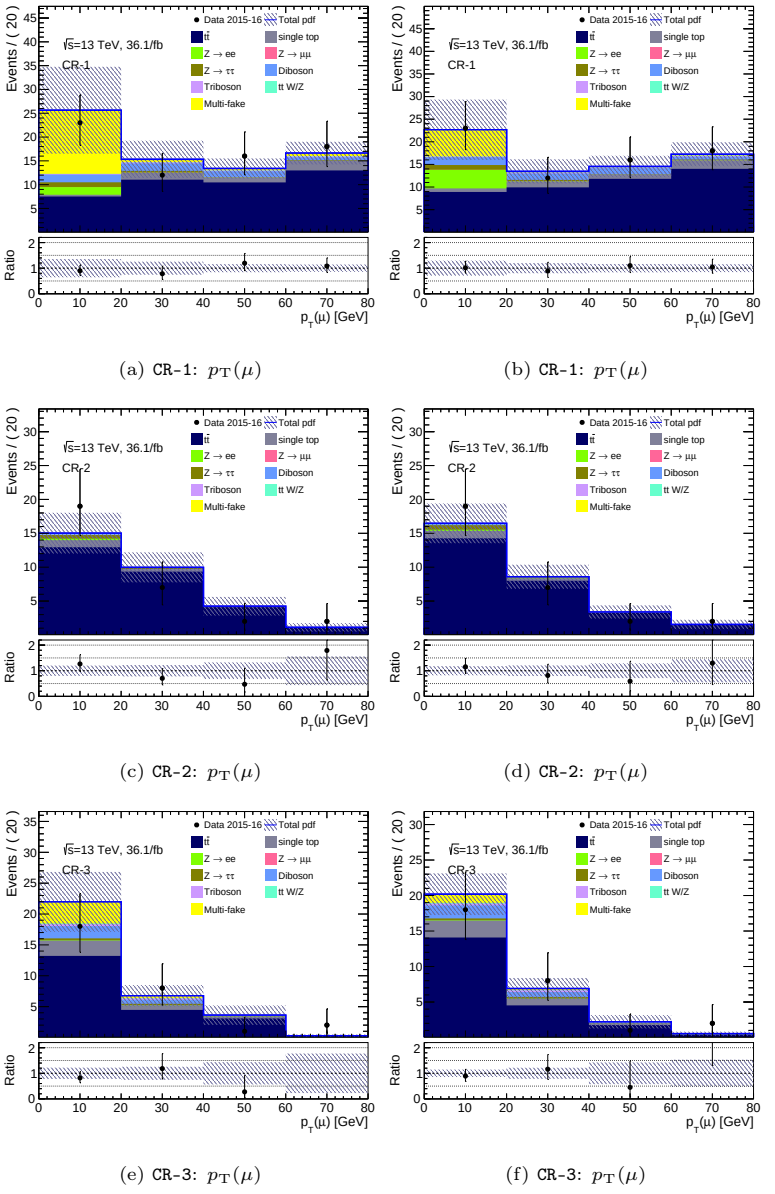

(a) CR-1: $p_{\mathrm{T}}(\mu)$ (b) CR-1: $p_{\mathrm{T}}(\mu)$

(c) CR-2: $p_{\mathrm{T}}(\mu)$ (d) CR-2: $p_{\mathrm{T}}(\mu)$

(e) CR-3: $p_{\mathrm{T}}(\mu)$ (f) CR-3: $p_{\mathrm{T}}(\mu)$

Figure 7.14.: Pre- (left column) and post-Fit distributions (right column) for CR-1 to CR-3 after normalizing the data-derived background and $t\bar{t}$ yield.

7.9.1. Extrapolation into signal-region

The charge-inverted region of the signal region is the CR-0 region in which the only difference to the signal is composed of the requirement that all leptons carry the same charge.

Again the shape of the multi-fake background is measured in ER-0-L|L, where isolation requirements on e_{sublead} and μ were dropped, and apply it to the signal region as shown in figure 7.15.

For a pre-unblinding background prediction in the signal region Figure 7.8 can be consulted. It shows the backround yield as normalized in the CRs only: The signal region itself is not used to normalize the samples and only poses as a validation region for the fit software. The dataset will be assumed to be equal to the background-only hypothesis (Asimov) and used to perform pre-unblinding sensitivity fits. In Table 7.13 the pre-unblinding yield of background samples is presented.

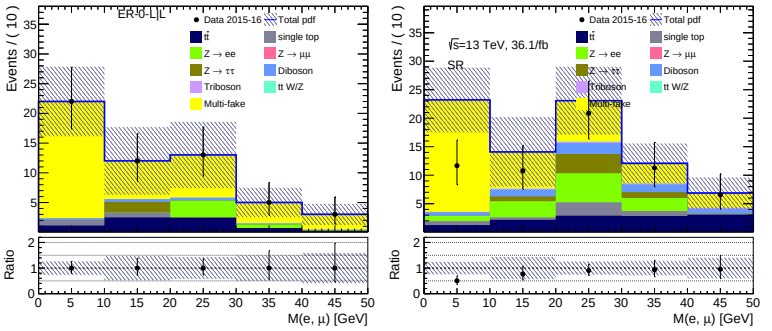

(a) $M(\mu, e)$ in ER-0-L|L

(b) $M(\mu, e)$ in SR-

Figure 7.15.: Measure multi-jet background in charge-inverted SR (left) and transfer the shape to the SR (right). The data shown in the signal region is the yield of background samples after applying the NFs derived in Table 7.11 (data=model). Background samples are pre-fit, so not scaled.

In order to make sure that the possible contribution to the multi-fake estimation region is negligible the values for the different mass hypotheses are quoted in Table 7.14. No signal events were contained in the estimation region.

7.9.2. Statistical compatibility tests for normalization factors

As already described in Section 7.8.2 a LLH ratio test was performed to confirm that the background model is compatible within statistical uncertainties in all CRs.

The results for including an additional NF for multi-fake and $t\bar{t}$ in all regions are shown in Table 7.15. It can be concluded that the NFs for the two samples are compatible in all regions.

7.9.3. Validation of distribution choice

Analogous to Section 7.8.4 the dilepton invariant mass distributions is used in order to determine the sensitivity of the search on mixing angles for various HNL mass hypotheses assuming a background only observation.

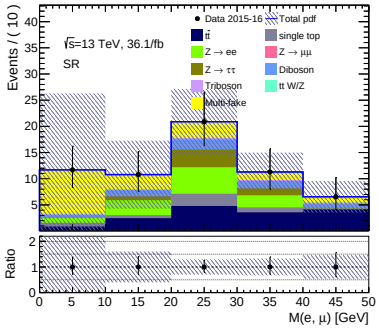

(a) $M(\mu, e)$

Figure 7.16.: Projected yield of background samples in signal region. Data points are the yield values of the background. The uncertainty of the normalization parameters $\mu_{t\bar{t}}$ and μ_{dd} are propagated and reflected in the final uncertainties.

Table 7.13.: Expected yield per background sample in the signal region. Data shown is the background-only model prediction disregarding decimals. Apart from NFs also systematic and statistical uncertainty parameters were fitted and impact the yield.

Channel	SR
Observed events	60
Fitted bkg events	60.68 ± 25.85
Fitted $t\bar{t}$ events	15.92 ± 5.29
Fitted single top events	4.77 ± 0.93
Fitted Diboson events	6.00 ± 0.96
Fitted $Z \to ee$ events	11.15 ± 2.06
Fitted $Z \to \mu\mu$ events	0.00 ± 0.00
Fitted $Z \to \tau\tau$ events	5.45 ± 1.26
Fitted Triboson events	0.00 ± 0.00
Fitted ttW/Z events	0.00 ± 0.00
Fitted multi-fake (data-derived) events	$16.50^{+26.58}_{-16.50}$
MC exp. SM events	79.26
MC exp. $t\bar{t}$ events	12.24
MC exp. single top events	4.56
MC exp. Diboson events	5.92
MC exp. $Z \to ee$ events	11.12
MC exp. $Z \to \mu\mu$ events	0.00
MC exp. $Z \to \tau\tau$ events	5.25
MC exp. Triboson events	0.00
MC exp. ttW/Z events	0.00
MC exp. multi-fake (data-derived) events	39.33

Table 7.14.: *Electron channel.* Shown are available statistics (and rel. uncertainty) in the `ER-0-L|L` which is used to measure the multi-fake template that is translated into the signal region. Also shown are the signal contamination of the various mass hypotheses in relative contributions (corresponding to a signal strength parameter of $\mu_{\text{SIG}} = 1$) and total raw event count.

	Obs. events	**Stat. uncertainty**
Data	55.00 ± 7.42	13.48 %
	Rel. contamination	**Raw events**
HNL 5 GeV	0.00 ± 0.00 %	0
HNL 10 GeV	0.00 ± 0.00 %	0
HNL 30 GeV	0.00 ± 0.00 %	0
HNL 20 GeV	0.00 ± 0.00 %	0
HNL 50 GeV	0.00 ± 0.00 %	0

Table 7.15.: Compatibility test of separate NFs in one of the `CR`s with the overall normalization of the $t\bar{t}$ and multi-fake samples. A usual cut-off value for such a test is 5 %.

Control region to use additional NF	$\mu_{\text{dd}}^{\text{alt}}$	$\mu_{t\bar{t}}^{\text{alt}}$
`CR-1`	68.6 %	79.6 %
`CR-2`	99.8 %	95.2 %
`CR-3`	64.5 %	80.1 %

In order to validate that the yield of the multi-fake background (as measured in the $p_{\text{T}}(\mu)$ distribution) is fully compatible with $M(e,\mu)$ and the lepton p_{T} distributions, in Figure 7.19 the distributions in the control regions that were not used in the blinded background normalization fits are presented. Most notably is here the agreement in the distribution $M(e,\mu)$ which validates the approach to measure μ_{dd} and $\mu_{t\bar{t}}$ in a highly distinguishable distribution of MC and multi-fakes backgrounds with accordingly low statistical uncertainties.

To further show that the NFs measured in $p_{\text{T}}(\mu_{\text{lead}})$ are fully compatible with the $M(e,\mu)$ distribution a statistical likelihood ratio test is performed. Further information regarding this likelihood ratio tests is given in Section 7.8.2.

For this test two fits are performed, one with the NFs freely floating and one with the NFs set constant to the values denoted in Table 7.11.

Table 7.16 shows then the probability for observing a result at least as extreme as the resulting χ^2 distribution. It is clearly visible that the NFs are very compatible with the $M(e,\mu)$ distribution.

Table 7.16.: LLH ratio test showing the compatibility of measured NFs with the $M(e,\mu)$ distributions. The advantage of using a LLH ratio test is that it can include all uncertainties on γ factors.

Control region	`CR-1` - $M(e,\mu)$	`CR-2` - $M(e,\mu)$	`CR-3` - $M(e,\mu)$
p**-value**	98.4 %	94.6 %	88.1 %

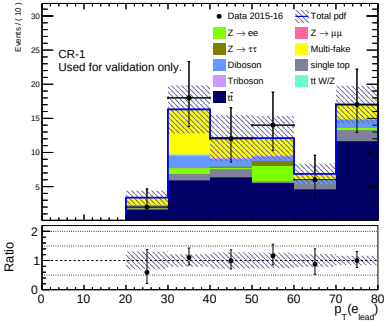

(a) CR-1: $p_{\mathrm{T}}(e_{\mathrm{lead}})$

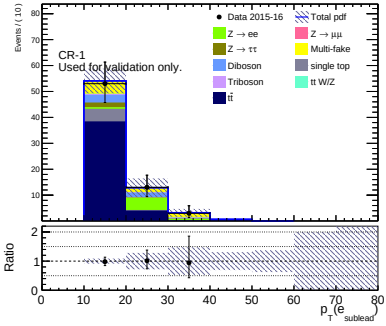

(b) CR-1: $p_{\mathrm{T}}(e_{\mathrm{sublead}})$

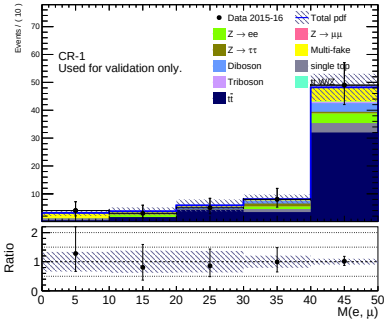

(c) CR-1: $M(e, \mu)$

Figure 7.17.: Post-Fit plots of CR-1 distributions not used in the normalization. The γ-factors in the plots (see Section 7.6) were also fitted and shown in their post-fit value.

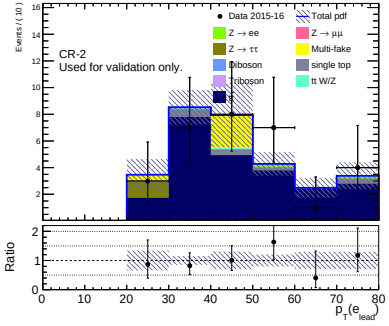

(a) CR-2: $p_{\mathrm{T}}(e_{\mathrm{lead}})$

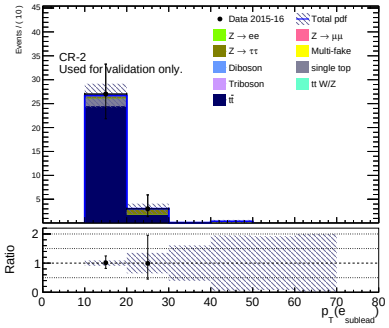

(b) CR-2: $p_{\mathrm{T}}(e_{\mathrm{sublead}})$

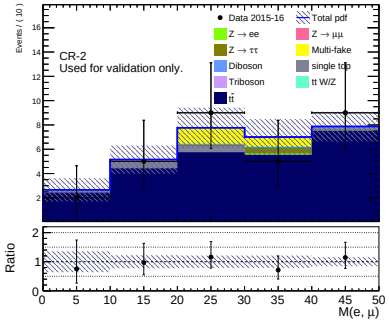

(c) CR-2: $M(e, \mu)$

Figure 7.18.: Post-Fit plots of CR-2 distributions not used in the normalization. The γ-factors in the plots (see Section 7.6) were also fitted and shown in their post-fit value.

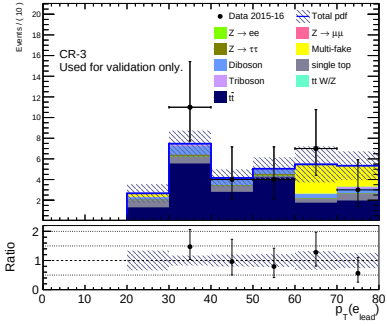

(a) CR-3: $p_{\mathrm{T}}(e_{\mathrm{lead}})$

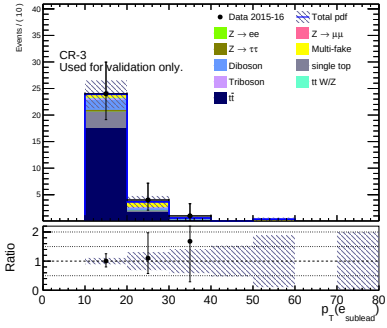

(b) CR-3: $p_{\mathrm{T}}(e_{\mathrm{sublead}})$

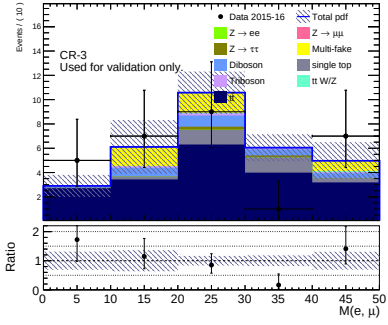

(c) CR-3: $M(e, \mu)$

Figure 7.19.: Post-Fit plots of CR-3 distributions not used in the normalization. The γ-factors in the plots (see Section 7.6) were also fitted and shown in their post-fit value.

7.9.4. Performing exclusion fit

Assuming the observation of data equal to the background prediction shown in 7.16 (so exactly the background-only hypothesis) various fits can be performed for the signal-plus-background hypothesis with varying signal strength μ_{SIG} parameter. This way one can test the sensitivity of the analysis before unblinding the signal region.

The obtained exclusion strengths using an asymptotic formulae calculator are then presented in Figure 7.20. It has been checked separately that the asymptotic formulea do indeed give comparable results to frequentists calculators. The exclusion limits (sensitivity) on sterile-active mixing angles are presented in Figure 7.21 using all statistical and systematic uncertainties.

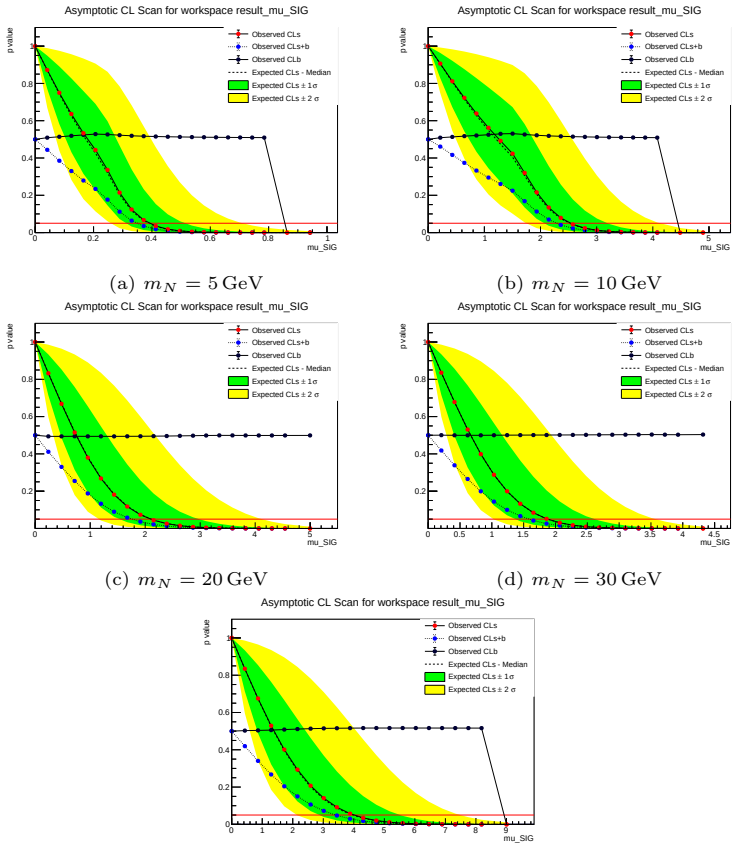

(a) $m_N = 5\,\mathrm{GeV}$ (b) $m_N = 10\,\mathrm{GeV}$

(c) $m_N = 20\,\mathrm{GeV}$ (d) $m_N = 30\,\mathrm{GeV}$

(e) $m_N = 50\,\mathrm{GeV}$

Figure 7.20.: Exclusion levels obtained for the signal-plus-background hypothesis using data reflecting a background only model.

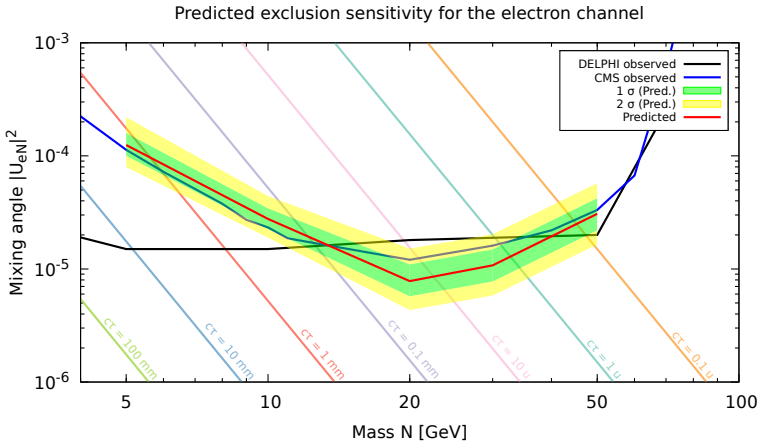

Figure 7.21.: Expected 95 % exclusion levels on $U_{\mu I}$ with purely statistical uncertainties.

7.10. Fit parameter correlation and pull plots

To give a detailed overview of the fit parameters, their correlation and their post-fit behavior, a background-only and signal-plus-background model has been fitted in the CRs and SR distributions in two versions.

Asimov in all regions This version uses Asimov data equal to the background-only hypothesis in all CRs and SR.

Asimov data in SR Actually measured data is used in the CRs. For the SR the normalized background samples are scaled with the values obtained from the CR background-only fit stated in Table 7.6. The Asimov dataset therefore corresponds as well to the background-only hypothesis.

For both versions pull plots of the fit parameters are presented for a background-only model and a correlation plot for a signal-plus-background model. The signal sample considered for correlation plots is the 20 GeV mass hypothesis.

The tests clearly show that no fit parameter is exhibiting large over- or underconstraints or deviations from their nominal value using Asimov datasets. Additionally the correlations between signal strength μ_{SIG} and other fit parameters can be studied. As expected an anti-correlation between the signal parameter-of-interest and the multi-fake normalization factor can be observed. This is consistent with later observations in Figures 8.11, 8.12 showing the impact of fit parameter variations on the signal strength.

7.10.1. Muon Channel

Asimov data in all regions In Figure 7.22 the pulls of a simultaneous fit in control- and signal region is presented. The data measured in the control region corresponds to a pre-fit Asimov dataset. Figure 7.23 shows the corresponding correlations of fit parameters.

Asimov data in SR In Figure 7.24 the pulls of a simultaneous fit in control- and signal region is presented. The data measured in the control region corresponds

to actual measured data. Figure 7.25 shows the corresponding correlations of fit parameters.

7.10.2. Electron Channel

Asimov data in all regions In Figure 7.26 the pulls of a simultaneous fit in control- and signal region is presented. The data measured in the control region corresponds to a pre-fit Asimov dataset. Figure 7.27 shows the corresponding correlations of fit parameters.

Asimov data in SR In Figure 7.28 the pulls of a simultaneous fit in control- and signal region is presented. The data measured in the control region corresponds to actual measured data. Figure 7.29 shows the corresponding correlations of fit parameters.

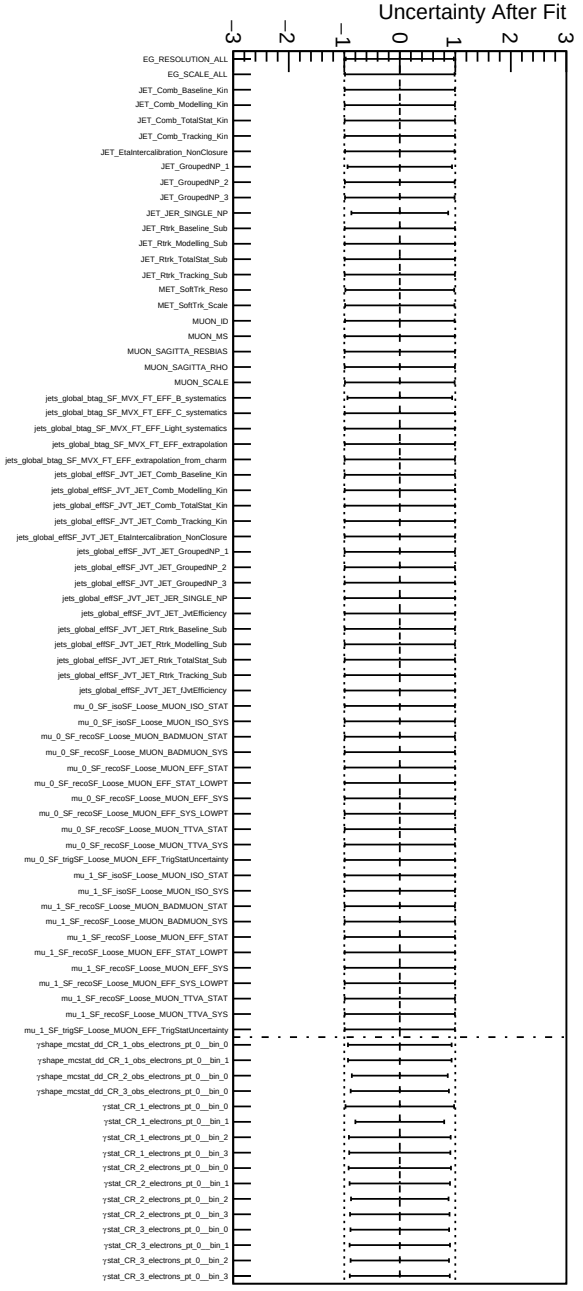

Figure 7.22.: *Muon channel.* Pulls of all parameters participating in the fit. The dataset is an Asimov dataset corresponding to the pre-fit model in both control and signal regions.

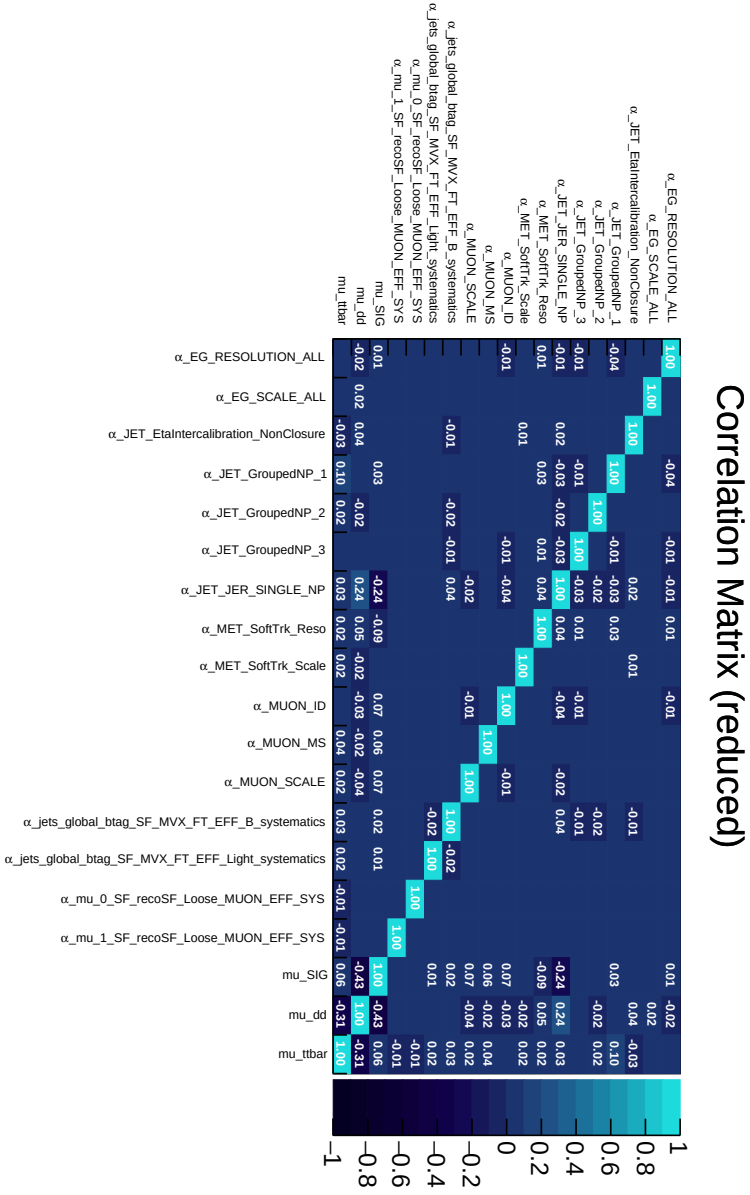

Figure 7.23.: *Muon channel.* Shown is the reduced correlation matrix of fit parameters for an exclusion fit including 20 GeV signal samples using an Asimov dataset corresponding to the pre-fit background-only model in both control and signal regions. Correlations c with $|c| < 0.01$ were removed from the matrix.

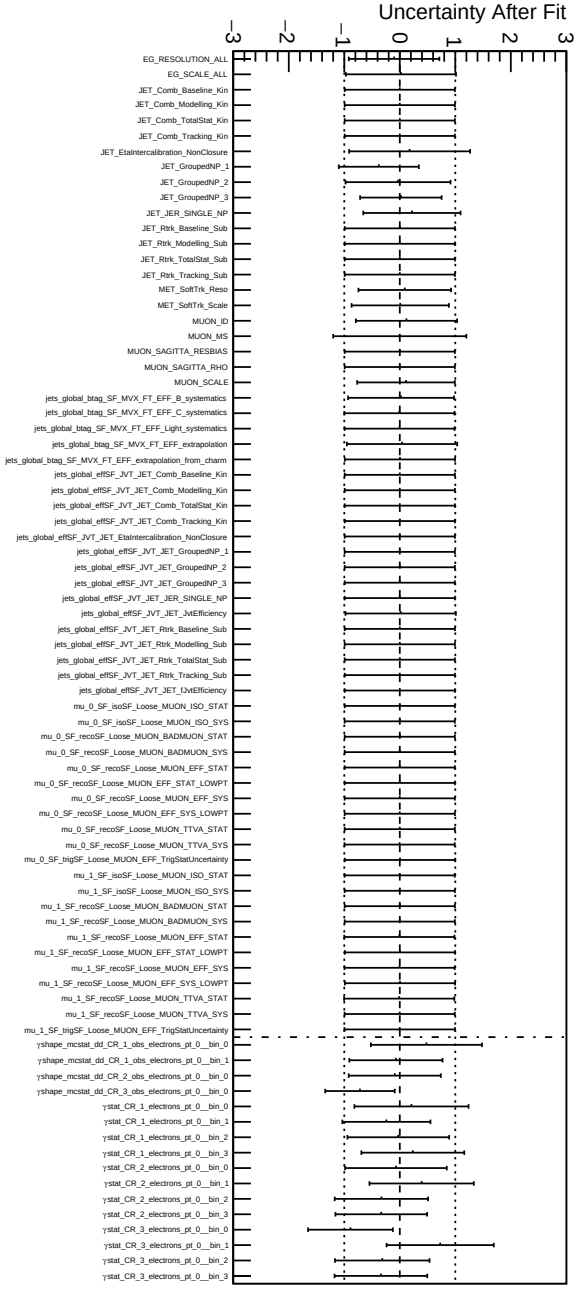

Figure 7.24.: *Muon channel.* Pulls of all parameters participating in the fit. The dataset is an Asimov dataset corresponding to the post-fit background-only model in the signal region and actual measured data in control regions.

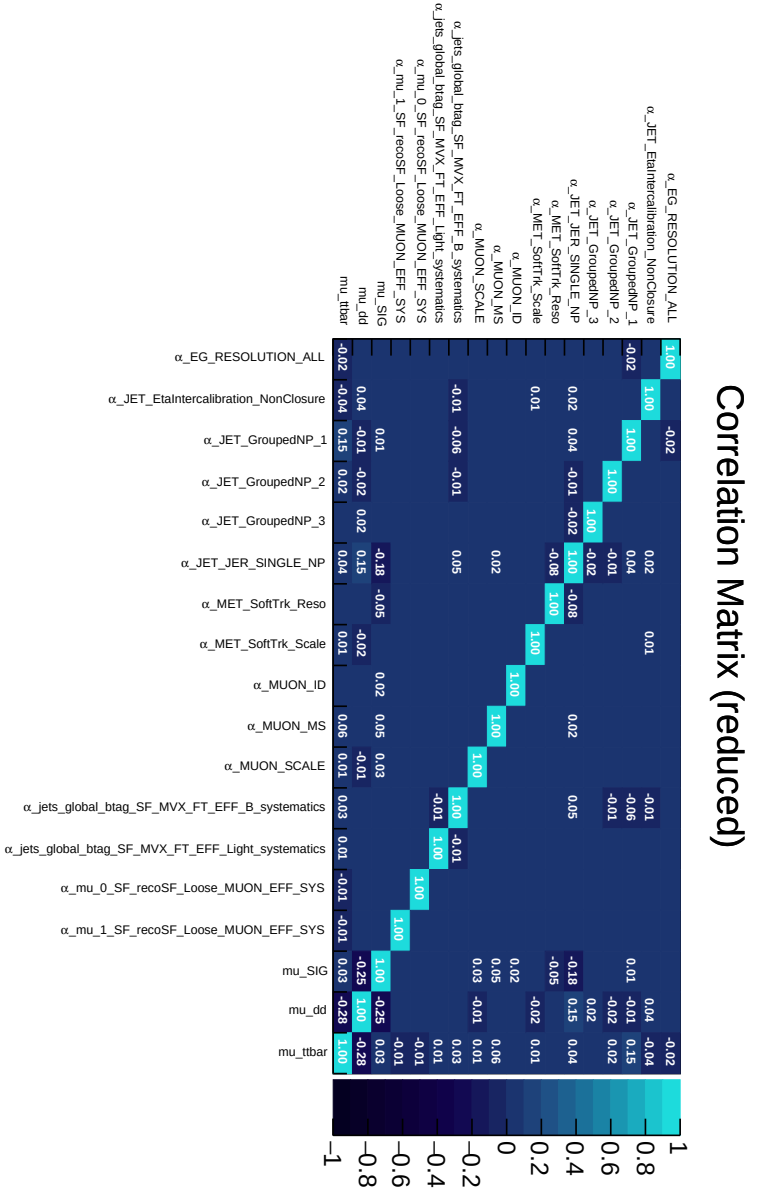

Figure 7.25.: *Muon channel.* Shown is the reduced correlation matrix of fit parameters for an exclusion fit including 20 GeV signal samples using an Asimov dataset corresponding to the post-fit background-only model. The data in the control regions is actual measured data. Correlations c with $|c| < 0.01$ were removed from the matrix.

Figure 7.26.: *Electron channel.* Pulls of all parameters participating in the fit. The dataset is an Asimov dataset corresponding to the pre-fit model in both control and signal regions.

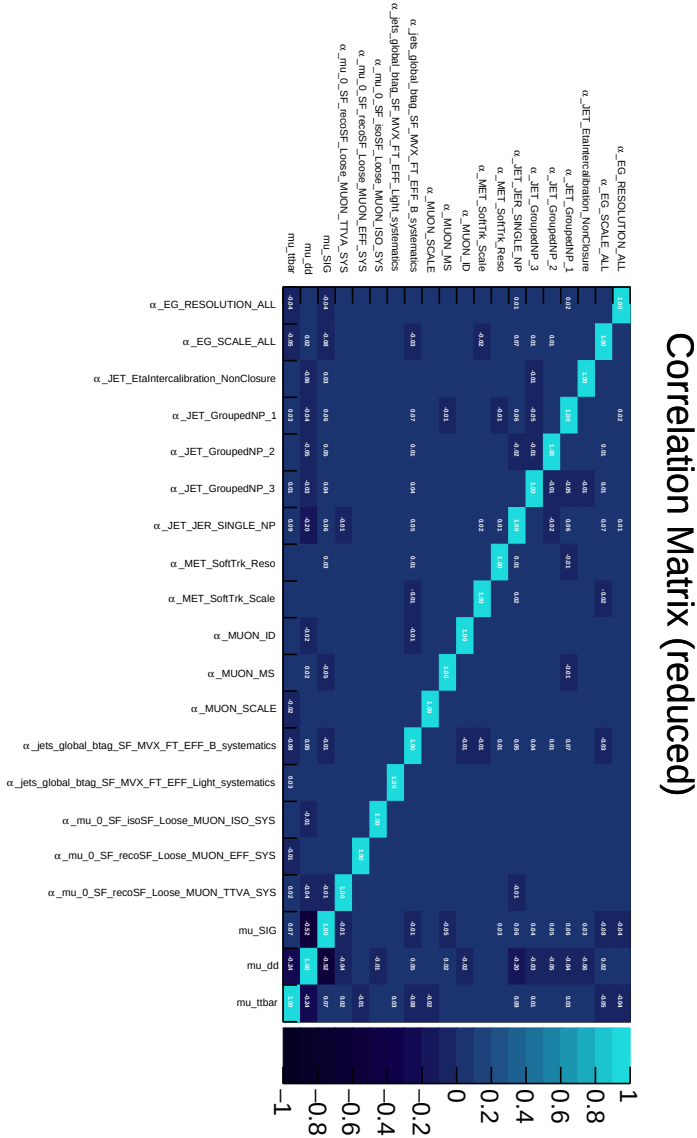

Figure 7.27.: *Electron channel.* Shown is the reduced correlation matrix of fit parameters for an exclusion fit including 20 GeV signal samples using an Asimov dataset corresponding to the pre-fit background-only model. The data in the control regions is actual measured data. Correlations c with $|c| < 0.01$ were removed from the matrix.

Figure 7.28.: *Electron channel.* Pulls of all parameters participating in the fit. The dataset is an Asimov dataset corresponding to the post-fit background-only model in the signal region and actual measured data in control regions.

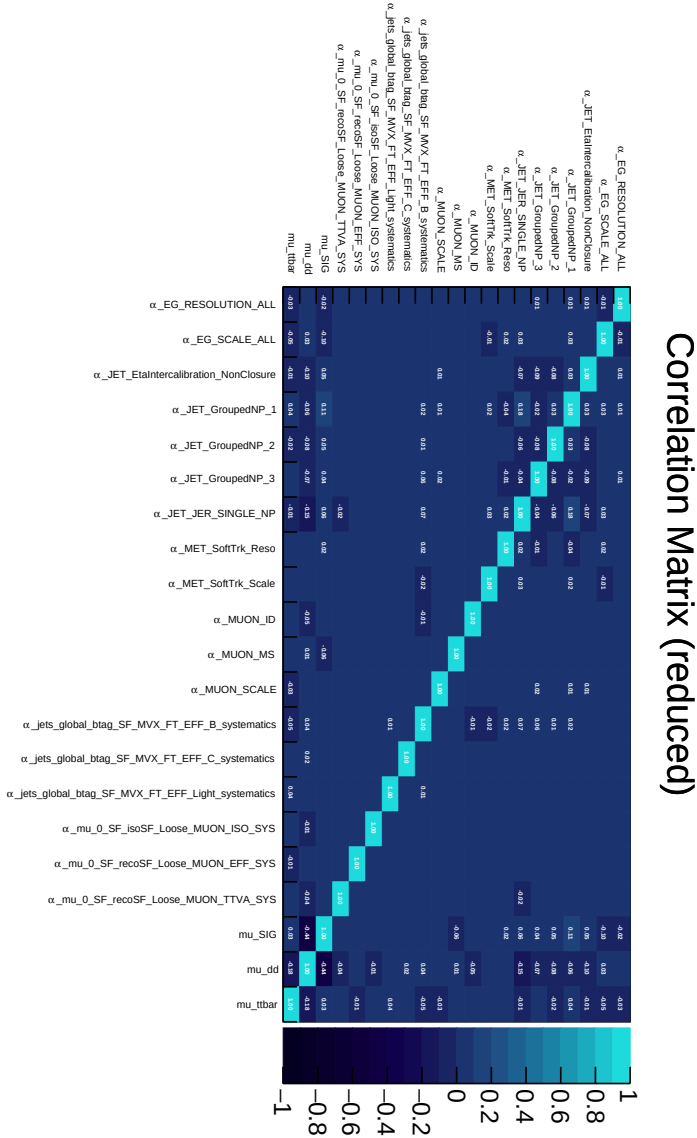

Figure 7.29.: *Electron channel.* Shown is the reduced correlation matrix of fit parameters for an exclusion fit including 20 GeV signal samples using an Asimov dataset corresponding to the post-fit background-only model. The data in the control regions is actual measured data. Correlations c with $|c| < 0.01$ were removed from the matrix.

Chapter 8.

Results

How wonderful that we have met with a paradox. Now we have some hope of making progress.

— N. Bohr, 1930 [107]

After determining the background shape as done in the previous chapter with a partial data-driven and MC based estimation method and performing cross-checks the unblinded signal region for both channels is presented forming here the results of this HNL search.

As can be seen in Table 7.6 the most dominant backgrounds $t\bar{t}$ and multi-fakes are scaled by a NF. This factor has been determined in the previous section solely in the control regions `CR-1` to `CR-3` as the signal region was kept blinded to avoid any bias.

This search is conducted for searching for a HNL signal and as such discovery is formulated in terms of hypothesis tests. The two hypotheses are the null hypothesis or *background-only* and the alternate hypothesis or *signal-plus-background*. For performing hypothesis tests a combined PDF will be built that combines `CR`s as well as the `SR` as a consequence of the unblinding. Hence a deviation from the previously observed normalization might be possible, especially considering the relative large statistical uncertainties in determining the multi-fake shape.

Below, plots will be shown for the background-only and signal-plus-background hypotheses. In Section 8.1 the difference in background estimation for a blinded and unblinded `SR` will be shown and NFs compared while in Section 8.3 the results of discovery and exclusion hypothesis testing are presented.

8.1. Background-only hypothesis

One might wonder how the background-only model, needed for hypothesis testing, compares in the `SR`. Observed is a good agreement, with a pull on the NF for the multi-fake sample which will be discussed in Section 8.2.

In order to quantify the impact of including the unblinded signal region into the background normalization of $t\bar{t}$ and the multi-fake sample, the signal region is presented in the following for two cases:

- using only `CR`s to normalize backgrounds: Figures 8.1a, 8.2a
- using `CR`s as well as `SR` to normalize backgrounds: Figures 8.1b, 8.2b

It is important to note that for the fit in Figure 8.1a the γ factors associated with the statistical uncertainties of the samples are not scaled from its nominal value. This means that approximately a ± 1 sigma variation of the order of the uncertainty bands shown can be adjusted in the fit as the largest uncertainty originates from low statistics. It can be seen from the ratio plots of background-only model and measured data that the data is located within one standard deviation of the CR-only background prediction. Furthermore it should be noticed that the deviation is trending towards the same direction in all bins indicating that the NF of the multi-fake sample will likely be higher once the SR is included in the fit. Table 8.1 shows the difference in NFs between using only the CRs to the case where the SR is included in the background fit normalization.

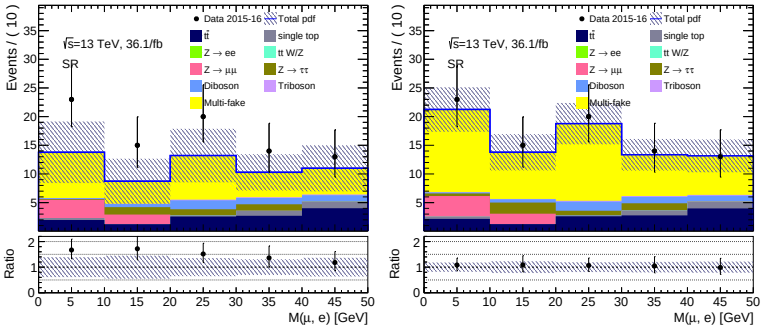

(a) Background fitted in CRs only.

(b) Background fitted in CRs and SR.

Figure 8.1.: *Muon Channel.* Unblinded signal region shows background-only model when normalized only in CRs (left) or in CRs as well as SR (right). Data shown was measured by ATLAS in 2015 and 2016.

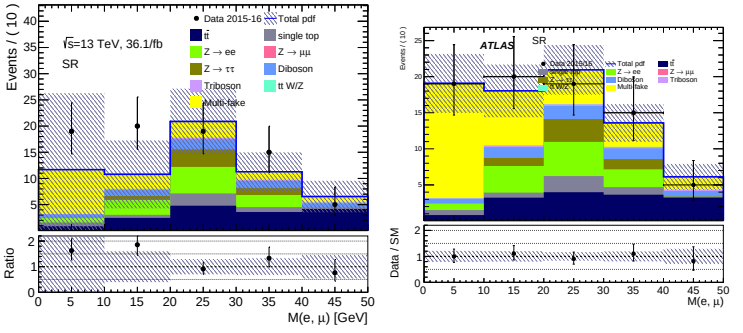

(a) Background fitted in CRs only.

(b) Background fitted in CRs and SR.

Figure 8.2.: *Electron Channel.* Unblinded signal region shows background-only model when normalized only in CRs (left) or in CRs as well as SR (right). Data shown was measured by ATLAS in 2015 and 2016.

In order to verify that no strong pulls exhist for other fit parameters that parameterize e.g. the systematic uncertainties, post-fit pull plots for the combined background-only fit in all regions (CRs and SR) are presented in Figure 8.23 for the muon channel and in Figure 8.24 for the electron channel.

Table 8.1.: NFs obtained for multi-fake (μ_{dd}) and $t\bar{t}$ ($\mu_{t\bar{t}}$) for different regions. The model used is a background-only model i.e. no signal model was included.

Fit configuration		μ_{dd}	$\mu_{t\bar{t}}$
Muon channel	only CRs	0.97 ± 0.38	0.90 ± 0.14
	CRs + SR	1.48 ± 0.34	0.88 ± 0.13
Electron channel	only CRs	0.42 ± 0.92	1.02 ± 0.16
	CRs + SR	0.81 ± 0.28	0.99 ± 0.15

Background CR distributions for different variables using the post-fit NFs as measured in control- and signal regions combined are plotted in Figures 8.3 and 8.4 for the muon channel and electron channel respectively. The SR plots for the same model are correspondingly shown in Figures 8.1b and 8.2b.

8.2. Discussion of background-only model

The pull on the multi-fake NF is understood to be anti-correlated with the γ factors parameterizing the statistical uncertainty in CR-3. This is understood to be the result of a statistical downfluctuation of data measured in the lowest bin of the control region. The parameterization of the uncertainty is hence not sufficient to address this downfluctuation as will be described here in detail, artificially constraining the multi-fake NF in a background-only fit using only CRs.

The previous Section showed the background-only model in two different fit configurations in- and excluding the SR for normalizing the background. As can be clearly seen from the NFs obtained in Table 8.1 the NFs for the $t\bar{t}$ sample are very robust upon inclusion of the SR. A slight decrease of relative uncertainty on $\mu_{t\bar{t}}$ is observable upon including the additional data from the SR showing in all cases a very good agreement of with unity normalization. This seems to further confirm the initial observation that samples with up to one non-prompt lepton are well simulated in MC. The multi-fake sample NF for the muon channel is pulled after the inclusion of the SR by about 1.34σ while for the electron channel with 0.42σ no pull over the original constraints of the uncertainty are observed.

The multi-fake sample normalization is strongly depending on the statistical uncertainty of each bin in the ERs. Total amount of a given sample per bin is dependent on a variety of fit parameters. I.e. these are

- pre-fit yield (y)
- normalization factor (μ)
- statistical uncertainty (γ)
- systematic uncertainty (α_i)

and the total amount of background is then determined as

$$y_{\mathrm{post-fit}} = y \cdot \mu \cdot \gamma \cdot \prod_i \alpha_i. \tag{8.1}$$

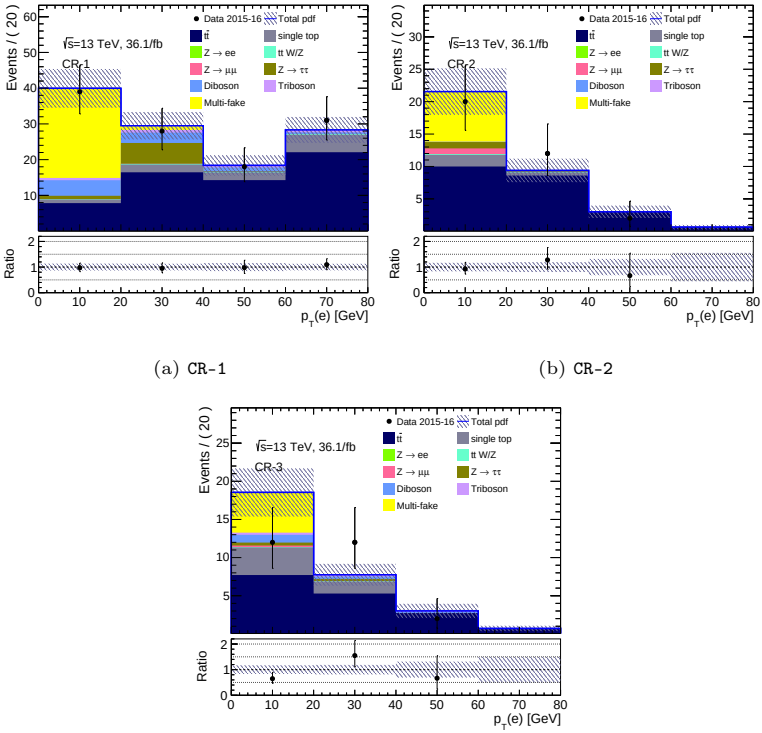

(a) CR-1 (b) CR-2

(c) CR-3

Figure 8.3.: *Muon Channel.* Control regions showing background-only hypothesis normalized in both CRs+SR.

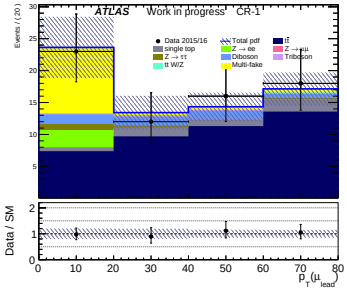

(a) CR-1

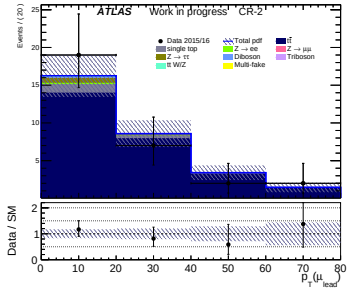

(b) CR-2

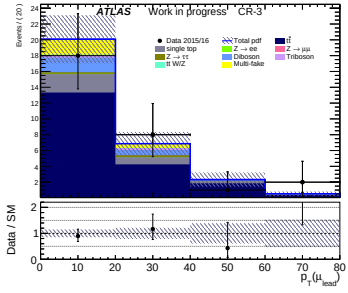

(c) CR-3

Figure 8.4.: *Electron Channel.* Control regions showing background-only hypothesis normalized in both CRs+SR.

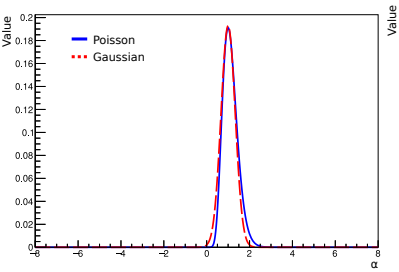

(a) PDFs in a low rel. stat. unc. scenario

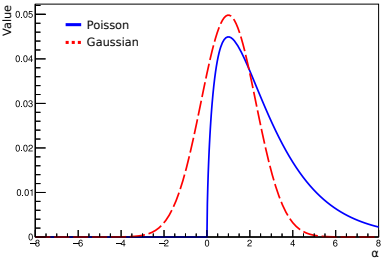

(b) PDFs in a high rel. stat. unc. scenario

Figure 8.5.: A comparison of the Gamma constraint terms for a Gaussian and Poisson PDF in a low (left) relative statistical uncertainty ($\tau = (1/\sigma^{\text{rel}})^2$) and high (right) relative statistical uncertainty scenerio.

In this case μ is of course constrained by several bin measurements, possibly throughout multiple regions. However if the statistical or systematic uncertainty in all of the bins is also relatively large it can "counteract" any movement of μ from unity in the fit. This leads to flat LLH curves and correspondingly large uncertainties on the fit parameter μ. For the multi-fake sample the same behavior can be observed in both channels. As the cuts required for the signal region to distinguish signal from background are reducing the available statistics both in measured data and MC significantly so are also the estimation regions low in statistics (the reduction of available statistics is also shown in Appendix E).

Upon proper propagation of the uncertainties of data and MC samples in the estimation region large relative statistical uncertainties are assigned to most of the multi-fake sample bins. To reduce this effect as much as possible the $p_{\text{T}}(\ell')$ distributions in which the multi-fake sample was measured were rebinned to contain most of the multi-fakes in a single bin. Despite this the large relative uncertainty shows in the normalization factor μ_{dd} for both channels. For the electron channel it is very large with 0.42 ± 0.92 showing the limited statistic available. Upon inclusion of the signal region it is clear that additional data will improve the relative uncertainty on the normalization factors.

However it can be clearly seen that the muon channel multi-fake sample normalization receives a pull into the up-direction where one can clearly see that this is improving the agreement between data and background model in the `SR` (Figure 8.1b) while it seems to be counteracted by the distribution in `CR-3` (Figure 8.3c). The inverted $E_{\text{T}}^{\text{miss}}$ cut region `CR-3` has shown in at least two distributions $p_{\text{T}}(\mu_{\text{lead}})$ and $p_{\text{T}}(e)$ a tendency to overestimate the background in the lowest bin in comparison to data (Figures 7.6e and 8.3c). This is a case where using Poisson constraints can be additionally restricting as shown in Figure 8.5: Low values on the γ-factor punish the LLH much more for Poisson constraint terms. A good agreement (within 1σ uncertainties) between the background-only model and data can be seen throughout `CR`s and `SR`.

In the fit parameter pull plots shown in Figures 8.23 and 8.24, the pull in `CR-3` on γ factors for both the MC and multi-fake sample are visible as well which are denoted by

γ_shape_mcstat_dd_CR_3_obs_electrons_pt_0__bin_0,
γ_stat_CR_3_electrons_pt_0__bin_0.

With the exception of the previously noted upwards pull on μ_{dd} no further pulls outside of 1σ are visible. Systematic uncertainties associated with jets show for both channels a deviation from the norm or slight constrainment and the muon spectrometer systematic shows a slight underconstraint for the muon channel. The γ factors, as they are inherently more volatile to changes, show an acceptable amount of variation within 1σ uncertainties.

It can therefore be concluded that the pull observed on μ_{dd} upon inclusion of `SR` into the normalization is expected from the `CR-3` statistical downfluctuation observed previously. This is also in agreement with low p-values shown in Table 7.9 that already indicated a friction between the high $E_{\mathrm{T}}^{\mathrm{miss}}$ control region and the other two.

8.3. Signal-plus-background hypothesis testing

Several hypothesis tests are performed to search for HNL signal. In order to test the compatibility of data given the background-only hypothesis a so-called discovery test is performed. The result is shown in Figure 8.6 where the p-value of rejecting the background-only hypothesis is translated into significance [99] using

$$Z = \Phi^{-1}(1 - p_0) \tag{8.2}$$

with Φ^{-1} being the cumulative distribution for a unit Gaussian. Traditionally a discovery threshold for discovery would be 5σ. For values larger around $2-3\ \sigma$ one speaks of *hints*. Correspondingly in the search conducted here the maximum significance observed was for the electron channel with 10 GeV with less than 1.4σ.

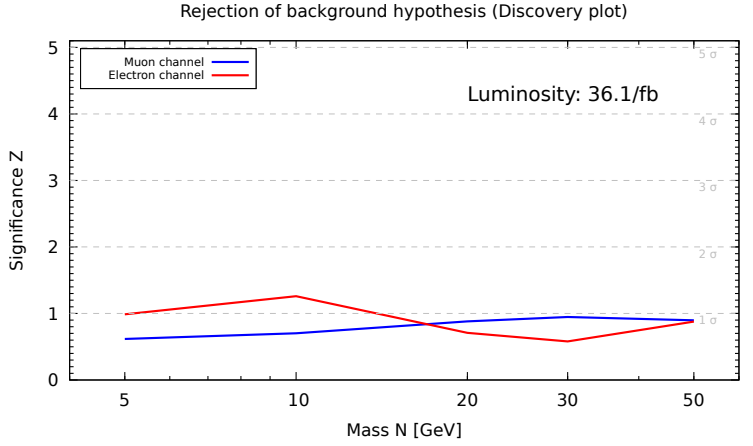

Figure 8.6.: For the various mass hypotheses discovery tests have been performed. Shown is the significance of rejecting the background hypothesis given the model for each mass.

In the absence of convincing evidence observed signal in the signal-plus-background hypothesis one sets instead exclusion limits. As described in Section 7.8.4 the signal strength parameter is proportionally related to the mixing angle of an active neutrino with the HNL and hence a limit on μ_{SIG} can be translated to an exclusion limit in the mixing-angle and HNL mass parameter space.

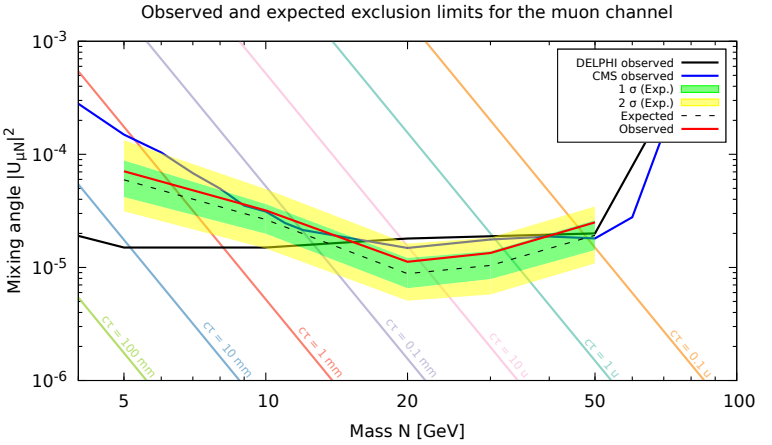

Figure 8.7.: *Muon Channel.* Shown are CMS limits (blue), DELPHI limit (black), ATLAS expected sensitivity (dotted with 1σ and 2σ bands) as well as actual observed limit (red).

The results for the exclusion tests are shown in Figures 8.7 and 8.8. The plots show past results from DELPHI and CMS as well as the expected and actually observed limit using ATLAS data. The observed limit on the mixing angle $|U_{\alpha N}|^2$ is shown in red for a 95 % confidence level while the expected limit assuming a perfect agreement of data with the background-only model is shown with a dotted black line. The corresponding upper limit plots for the exclusion search for the different HNL signal mass hypotheses are presented in Figures 8.9 and 8.10.

In order to gauge the impact of the different fit parameters on the excluded signal strength, plots are presented in Figures 8.11 and 8.12 showing the effect on μ_{SIG} once one of the parameters is varied (and fixed) at $\pm 1\sigma$. The difference in signal strength is obtained by calculating

$$\frac{\mu_{\mathrm{SIG}}(\mathrm{NP}) - \mu_{\mathrm{SIG}}(\text{best fit})}{\Delta\mu_{\mathrm{SIG}}(\text{best fit})} \tag{8.3}$$

where NP stands for the nuisance parameter and $\Delta\mu_{\mathrm{SIG}}$ for the uncertainty on the signal strength. Therefore the impact parameters show the difference in varying NP by $\pm 1\sigma$ normalized to the uncertainty of μ_{SIG}. The fit naturally has to be done for a signal-plus-background model where 30 GeV was exemplarily selected as it gives for both channels the best observed constraints on the mixing angle yet. The colored bars in the plot show the impact of fixing a fit parameter to $\pm 1\sigma$ on the signal strength for the signal-plus-background hypothesis and a value of 0.1 would for instance mean an increase of the signal strength by $0.1\sigma_{\mathrm{SIG}}$ where σ_{SIG} is the uncertainty on the unconstrained fit. The dots with their error bars are noting the post-fit systematic (usually between -1 and 1

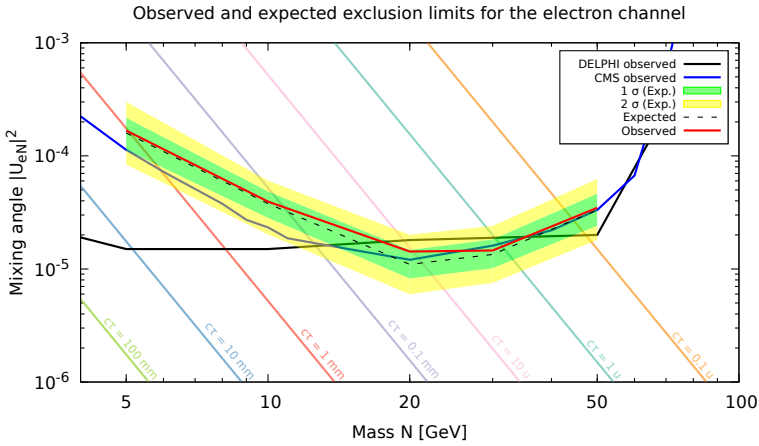

Figure 8.8.: *Electron Channel.* Shown are CMS limits (blue), DELPHI limit (black), ATLAS expected sensitivity (dotted with 1σ and 2σ bands) as well as actual observed limit (red).

denoting the σ value of the parameter) value (black) and the post-fit NF value (green) which is usually around 1. It can be clearly seen from the plots, as well as correlation matrices presented earlier, that the signal strength in the signal-plus-background fit is anticorrelated with the multi-fake NF. A better determination of the multi-fake sample yield and shape is therefore beneficial to discover HNLs or set stricter exclusion limits in the future.

8.4. Fit plots for all signal hypotheses

As the background-only model normalized only in the three CRs shows an underestimation of the data by about 1σ of the blinded NF it is educational to look at the signal-plus-background pre- and post-fit plots to gauge the signal contribution to the different dilepton invariant mass bins. Though for a correct treatment of discovery and exclusion hypothesis tests are needed the plots shows that the signal region could accompany HNL signal of various mass points.

This highlights as well the large statistical uncertainty accompanying the rather exotics phase space in which this search takes place. The obtained fit parameters for a signal-plus-background fit are also shown and underline the large relative uncertainties on the signal strength of approximately 100 %.

8.4.1. Muon channel

In Table 8.2 are the best fit values for the NFs of the multi-fake and $t\bar{t}$ background presented together with the signal NF for the five different mass hypotheses. In Figures 8.13 - 8.17 are then the signal region distributions both for pre- and post-fit parameters presented.

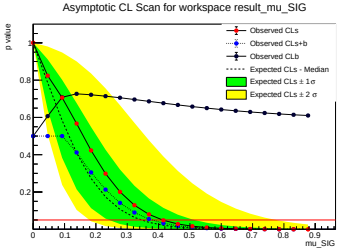

(a) $m_N = 5\,\text{GeV}$

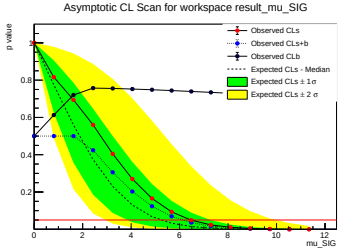

(b) $m_N = 10\,\text{GeV}$

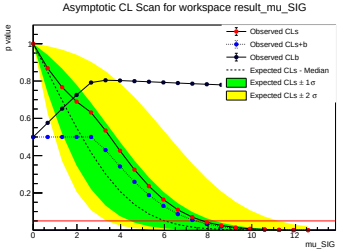

(c) $m_N = 20\,\text{GeV}$

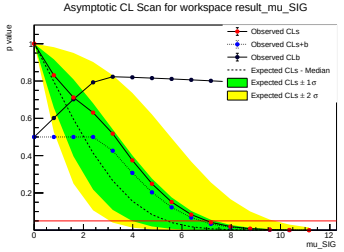

(d) $m_N = 30\,\text{GeV}$

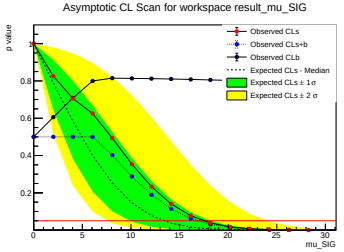

(e) $m_N = 50\,\text{GeV}$

Figure 8.9.: *Muon channel.* Exclusion levels obtained for the signal+background hypothesis.

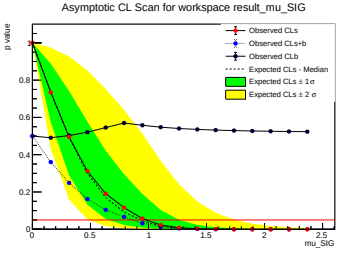

(a) $m_N = 5\,\mathrm{GeV}$

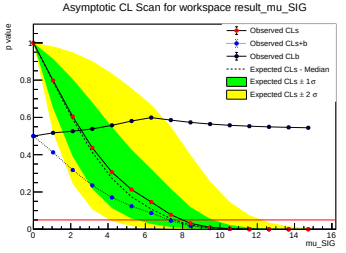

(b) $m_N = 10\,\mathrm{GeV}$

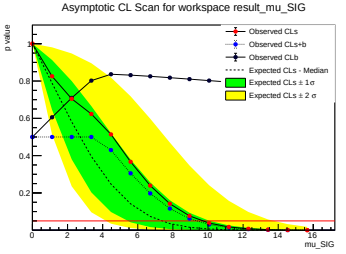

(c) $m_N = 20\,\mathrm{GeV}$

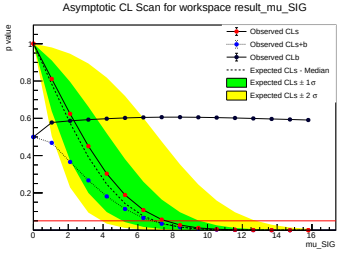

(d) $m_N = 30\,\mathrm{GeV}$

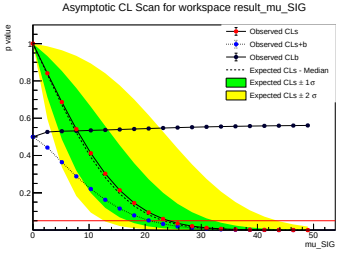

(e) $m_N = 50\,\mathrm{GeV}$

Figure 8.10.: *Electron channel.* Exclusion levels obtained for the signal+background hypothesis.

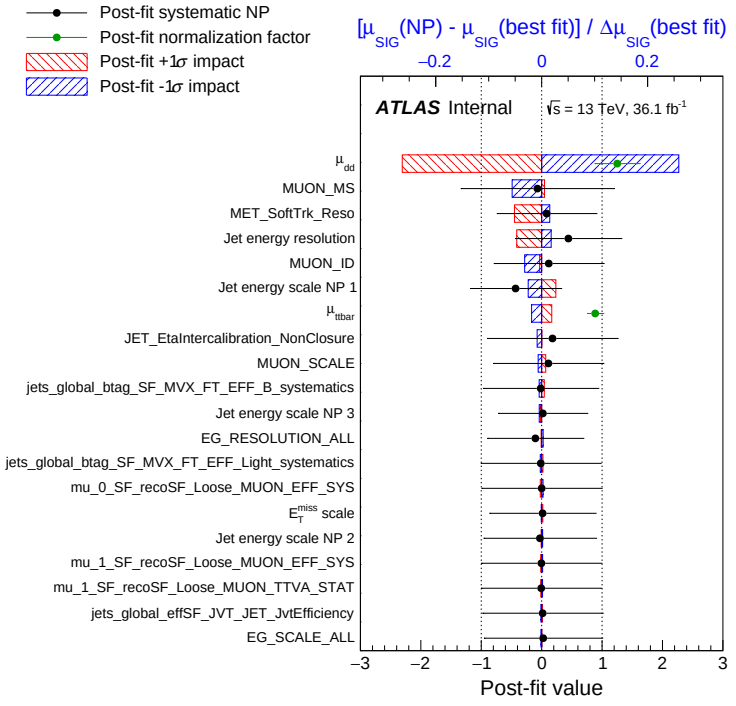

Figure 8.11.: *Muon channel.* Shown are impacts of $\pm 1\sigma$ variations of Nuisance Parameters (NPs) on the signal strength. Measured is the deviation of $\mu_{\mathrm{SIG}}(\mathrm{best} - \mathrm{fit})$ and $\mu_{\mathrm{SIG}}(NP)$ in ratio to the uncertainty on the POI.

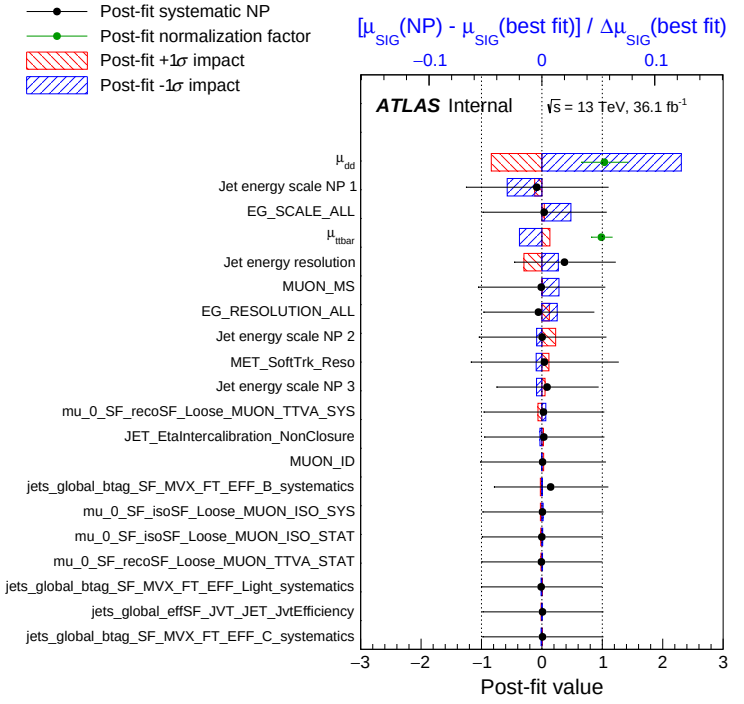

Figure 8.12.: *Electron channel.* Shown are impacts of $\pm 1\sigma$ variations of NPs on the signal strength. Measured is the deviation of $\mu_{\mathrm{SIG}}(\mathrm{best} - \mathrm{fit})$ and $\mu_{\mathrm{SIG}}(NP)$ in ratio to the uncertainty on the POI.

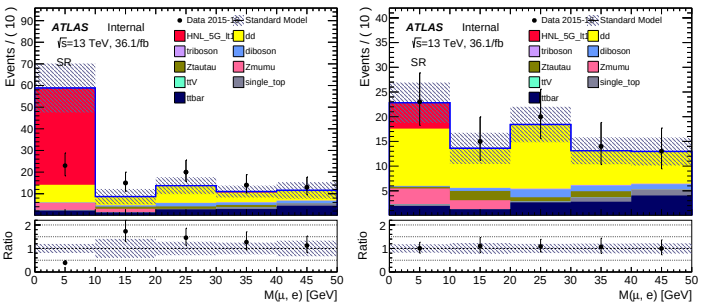

(a) Before fit (b) After fit

Figure 8.13.: *Muon Channel.* Signal-plus-background 5 GeV model. Fit parameters are shown in table 8.2

Table 8.2.: *Muon Channel.* Fit parameters obtained for different signal-plus-background mass hypotheses.

Signal	NF	Value
5 GeV	μ_{SIG}	0.11 ± 0.16
	μ_{dd}	1.38 ± 0.35
	$\mu_{t\bar{t}}$	0.88 ± 0.13
10 GeV	μ_{SIG}	1.94 ± 2.59
	μ_{dd}	1.36 ± 0.35
	$\mu_{t\bar{t}}$	0.88 ± 0.13
20 GeV	μ_{SIG}	2.84 ± 2.87
	μ_{dd}	1.33 ± 0.35
	$\mu_{t\bar{t}}$	0.88 ± 0.13
30 GeV	μ_{SIG}	2.71 ± 2.58
	μ_{dd}	1.25 ± 0.37
	$\mu_{t\bar{t}}$	0.90 ± 0.13
50 GeV	μ_{SIG}	6.49 ± 6.51
	μ_{dd}	1.21 ± 0.40
	$\mu_{t\bar{t}}$	0.88 ± 0.13

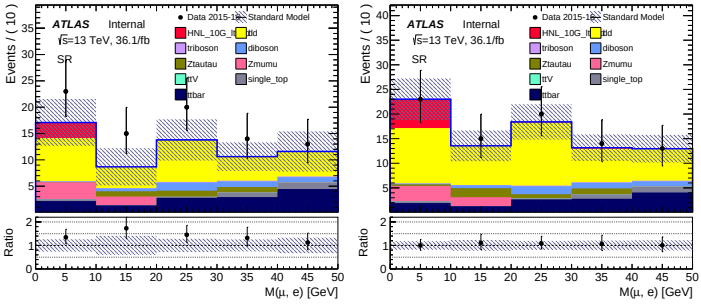

(a) Before fit (b) After fit

Figure 8.14.: *Muon Channel.* Signal-plus-background 10 GeV model. Fit parameters are shown in table 8.2

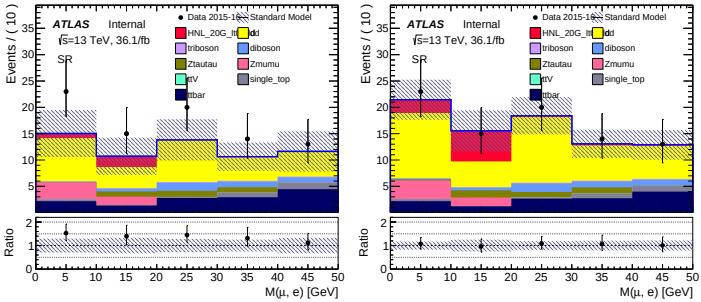

(a) Before fit (b) After fit

Figure 8.15.: *Muon Channel.* Signal-plus-background 20 GeV model. Fit parameters are shown in table 8.2

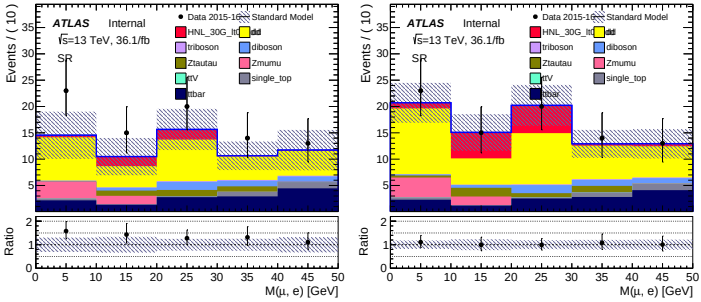

(a) Before fit (b) After fit

Figure 8.16.: *Muon Channel.* Signal-plus-background 30 GeV model. Fit parameters are shown in table 8.2

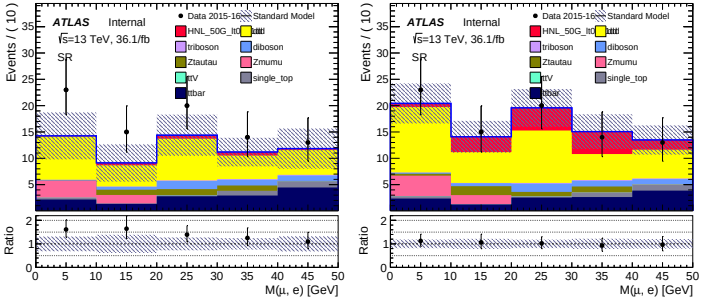

(a) Before fit (b) After fit

Figure 8.17.: *Muon Channel.* Signal-plus-background 50 GeV model. Fit parameters are shown in table 8.2

8.4.2. Electron channel

Analogous to the muon channel the best fit values for the multi-fake and $t\bar{t}$ background NFs are presented in Table 8.3. They are shown together with the signal NF for the five different mass hypotheses. Figures 8.18 - 8.22 show then the signal region distributions both for pre- and post-fit parameters.

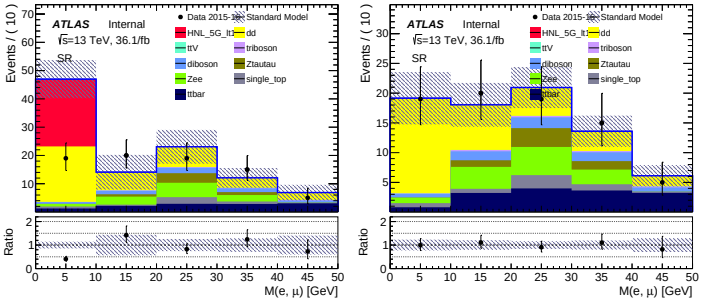

(a) Before fit (b) After fit

Figure 8.18.: *Electron Channel.* Signal-plus-background 5 GeV model. Fit parameters are shown in table 8.3

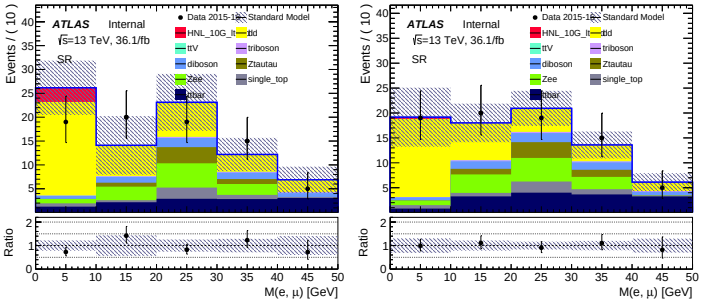

(a) Before fit (b) After fit

Figure 8.19.: *Electron Channel.* Signal-plus-background 10 GeV model. Fit parameters are shown in table 8.3

Table 8.3.: *Electron Channel.* Fit parameters obtained for different signal-plus-background mass hypotheses.

Signal	NF	Value
5 GeV	μ_{SIG}	0.00 ± 2.66
	μ_{dd}	0.81 ± 0.31
	$\mu_{t\bar{t}}$	0.99 ± 0.15
10 GeV	μ_{SIG}	0.12 ± 36.10
	μ_{dd}	0.80 ± 0.51
	$\mu_{t\bar{t}}$	0.99 ± 0.15
20 GeV	μ_{SIG}	3.88 ± 3.42
	μ_{dd}	0.61 ± 0.30
	$\mu_{t\bar{t}}$	0.99 ± 0.15
30 GeV	μ_{SIG}	0.78 ± 4.98
	μ_{dd}	0.78 ± 0.33
	$\mu_{t\bar{t}}$	0.99 ± 0.15
50 GeV	μ_{SIG}	0.86 ± 38.10
	μ_{dd}	0.81 ± 0.31
	$\mu_{t\bar{t}}$	0.99 ± 0.15

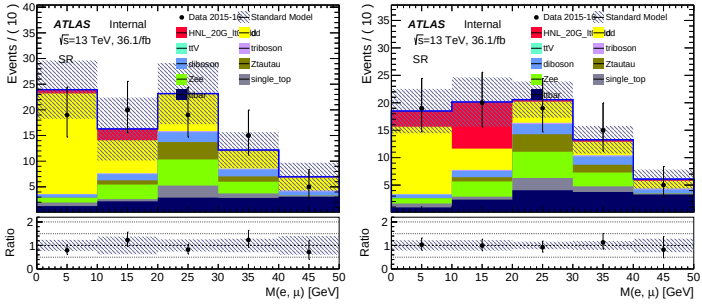

(a) Before fit

(b) After fit

Figure 8.20.: *Electron Channel.* Signal-plus-background 20 GeV model. Fit parameters are shown in table 8.3

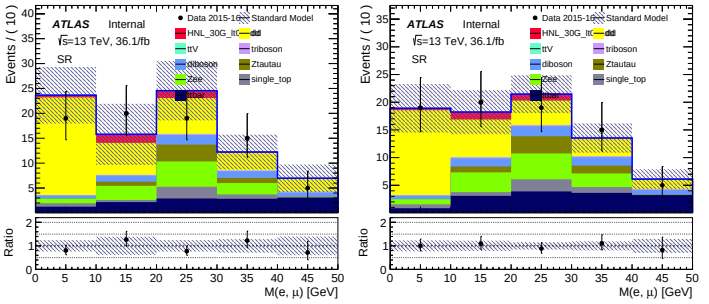

(a) Before fit (b) After fit

Figure 8.21.: *Electron Channel.* Signal-plus-background 30 GeV model. Fit parameters are shown in table 8.3

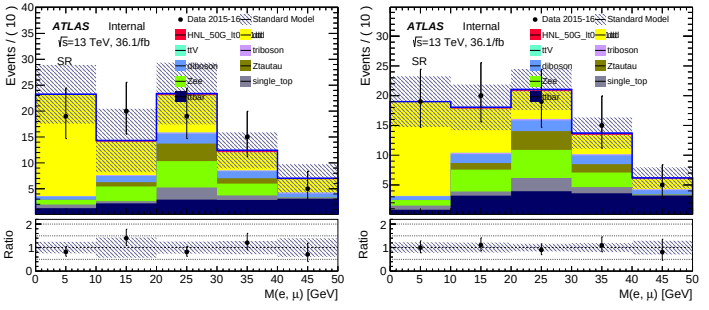

(a) Before fit (b) After fit

Figure 8.22.: *Electron Channel.* Signal-plus-background 50 GeV model. Fit parameters are shown in table 8.3

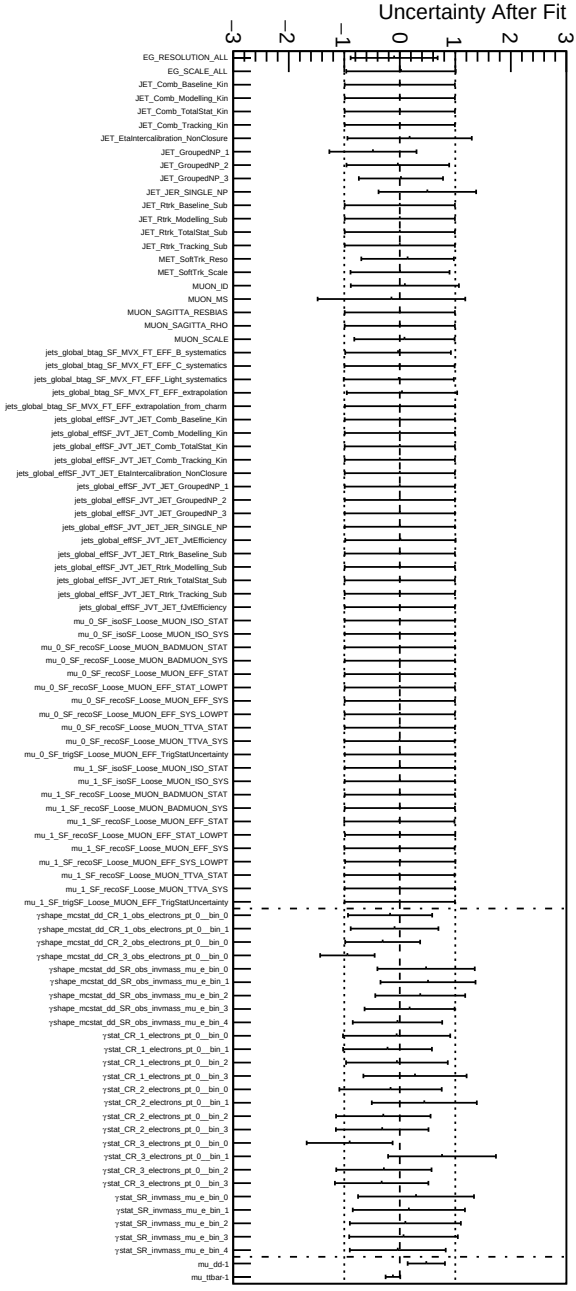

Figure 8.23.: *Muon channel.* Pull plot of bkg-only hypothesis in all fit regions CRs+SR. NFs to the right are plotted with additional summand −1 and uncertainties are not normalized to a pre-fit value.

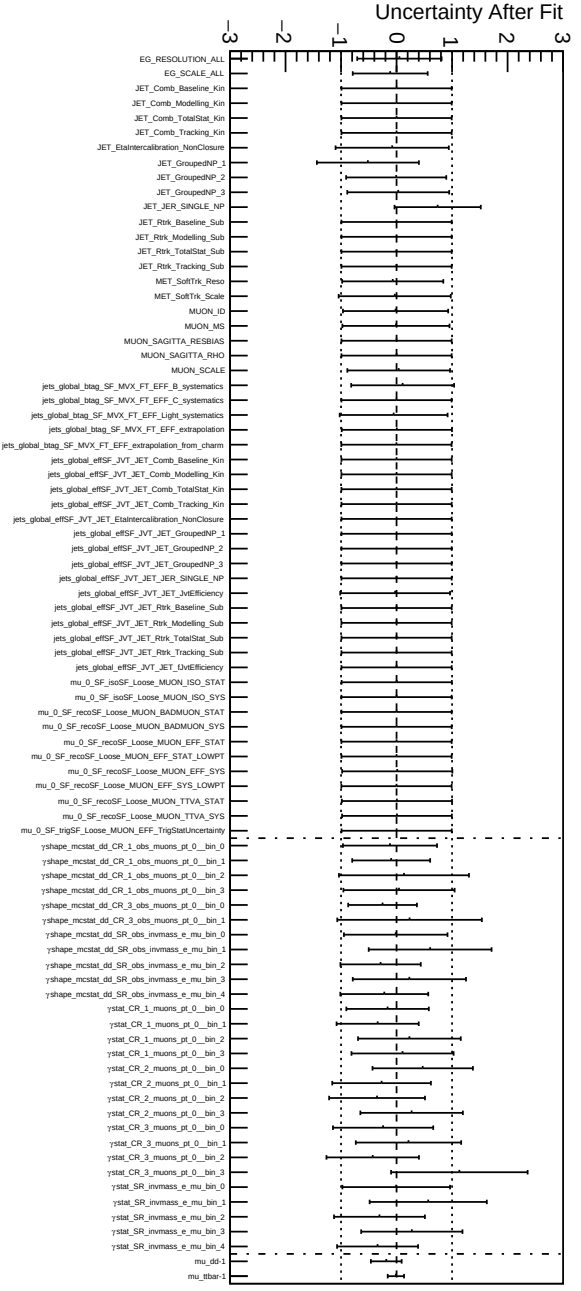

Figure 8.24.: *Electron channel.* Pull plot of bkg-only hypothesis in all fit regions `CRs+SR`. NFs to the right are plotted with additional summand −1 and uncertainties are not normalized to a pre-fit value.

Chapter 9.

Conclusion

It's about understanding! Understanding the world!

— P. Higgs, 2000 [108]

The results shown in Section 8 conclude the first search for HNLs in ATLAS data below the electroweak scale. It has been found that the background-only model described the data in the signal region accurately as no significant excess has been observed as underlined in Figure 8.6. In absence of convincing evidence for HNLs in the mass range 5 to 50 GeV at a mixing angle around 1×10^{-5} exclusion limits were set on the mixing angle. This search sets best constraints on the mixing angle in the HNL mass range 15 to 42 GeV for the mixing of HNLs with muon neutrinos and for 25 to 50 GeV for the mixing with electron neutrinos.

Ultimately this search is limited by several statistical sizes involved. For one the data used in this search was measured by ATLAS in 2015 and 2016 and corresponds to an integrated luminosity of 36.1 fb^{-1}. As can be seen in Appendix E as well as the `CR` and `SR` plots in Section 7 this limits the population of the `CR`s and `SR`. On the other hand the drastic cuts described in Section 6 are necessary to reduce SM backgrounds sufficiently to unveil a potential weak HNL signal. In fact the cuts finally chosen to comprise the signal region are selected also taking into account the final statistical size in the fit regions. The statistical uncertainty that limits the search is both originating from the low data population as well as the limited amount of MC statistics. As both need to be propagated for the measurement of the multi-fake sample shape the final NF for this sample is known only with large relative uncertainties.

However despite this limitation it is possible to set rather stringent limits on the mixing angle. This is achieved by multi-bin fits and the inclusion of multiple control regions to limit the background sample variations sufficiently. Despite sufficient fit flexibility to include most HNL shapes in the signal region as shown in Section 8.4 the hypothesis testing as well as post-fit signal NF (or parameter of interest) clearly show the limit on the mixing angle to which a HNL signal can be excluded with 95 % confidence in Figures 8.7 and 8.8.

As already discussed in Section 8.2 it should be noted however that a pull can be seen on the NF for the multi-fake sample in Table 8.1 which likely shows the consequence of an unexpected down-constraint on μ_{dd} originating in `CR-3` when performing a background-only fit only in the `CR`s. Due to the limited amount of statistics in that region and the fact that this describes the high $E_{\text{T}}^{\text{miss}}$ regime in contrast to the high statistics trilepton invariant mass sidebands in `CR-1`, where fake leptons are more likely to show, this has been concluded to be an artifact related to the limited statistical sample size discussed above. For all other regions in both channels no such constraint was observed.

9.1. Prospective future work

The ATLAS experiment has in run-2 of LHC, which is now completed, collected $140\,\mathrm{fb}^{-1}$ of good quality certified data (see Figure 9.1) which is almost a factor four compared to the luminosity used for this search.

The larger dataset would not only enable a more precise measurement of the multi-fake shape but also give the probability to search for a higher amount of HNLs as the potentially observable events containg HNLs would scale with luminosity. However in order to take full advantage of this increase a higher precision on the background estimation would be necessary and extremely beneficial. This could be achieved by producing higher amount of MC samples confined to the parameter space of interest or a dedicated rigorous data-driven background estimation to account for both prompt and non-prompt leptons.

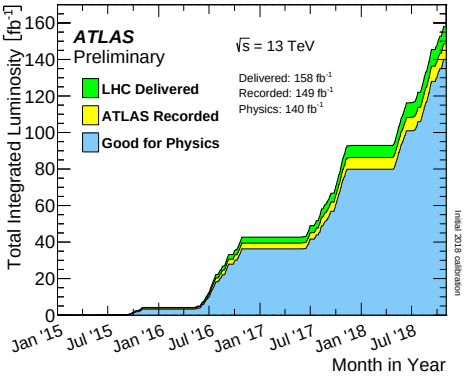

Figure 9.1.: Luminosity delivered by LHC, collected by ATLAS and certified to be good quality data during stable beams for 2015 – 2018. Figure from [42].

Though a larger luminosity allows the probing of mixing angles to unprecedented regions, the possibly highest gain remains in the further restriction of fit parameters related to statistical uncertainties. Improving and constraining the background model should therefore be of highest priority to conduct a full run-2 search for HNLs. The mass range for setting new exclusion limits (or discovering HNLs) should be shifted slightly higher as for low masses a further restriction of the parameter space means a probing into more displaced signals for which the signature scrutinized here becomes less favorable. Instead focusing the search efforts on the whole range 10 to 80 GeV would be a promising endavour that pushes ATLAS' multi-purpose character further to its limits.

Finally an additional analysis channel examining the mixing with τ neutrinos may be added. This was omitted here for time reasons as correct identification of τ leptons comes along with addititional difficulties.

Isolation of subleading leptons

The impact of the isolation working points for the subleading muon and electron is examined in all possible combinations for each of the signal mass hypotheses $m_N = 5$, 10, 20, 30 and 50 GeV. In addition to the requirements listed in Table 6.4, `Loose` isolation is required for the leading lepton.

The resulting significances for the muon channel are shown in Figures A.1a-A.5a. While significance is a good indicator of a good discrimination between signal and background our final background model relies on sufficient statistical sample sizes to reliably model control regions. For that matter the precision (inverted relative uncertainty) is plotted in Figures A.1b-A.5b.

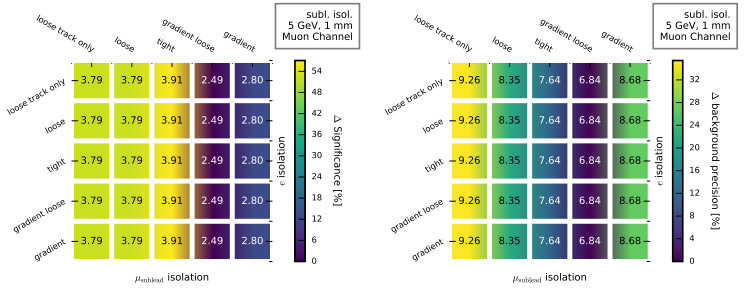

(a) Significance

(b) Inverted rel. uncertainty

Figure A.1.: *Muon Channel.* 5 GeV signal point. Effect of implementing the possible isolation requirement WPs for the subleading leptons. The luminosity corresponds to 36.1 fb^{-1}.

The resulting significances for the electron channel are shown in Figures A.6a-A.10a and the background sample precision is shown in Figures A.6b-A.10b.

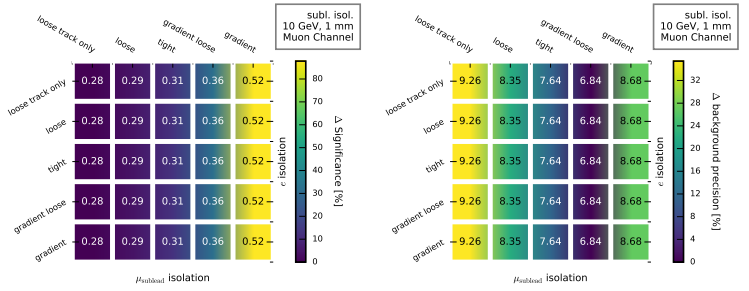

(a) Significance (b) Inverted rel. uncertainty

Figure A.2.: *Muon Channel.* 10 GeV signal point. Effect of implementing the possible isolation requirement WPs for the subleading leptons. The luminosity corresponds to 36.1 fb^{-1}.

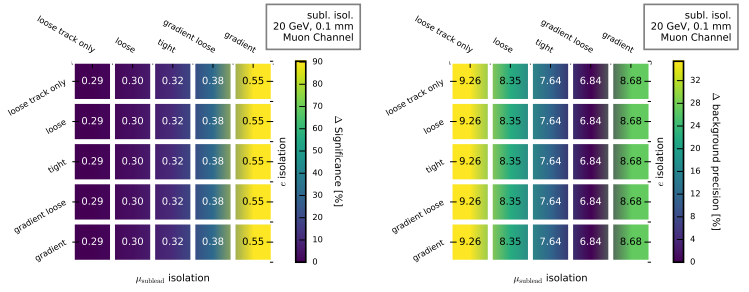

(a) Significance (b) Inverted rel. uncertainty

Figure A.3.: *Muon Channel.* 20 GeV signal point. Effect of implementing the possible isolation requirement WPs for the subleading leptons. The luminosity corresponds to 36.1 fb^{-1}.

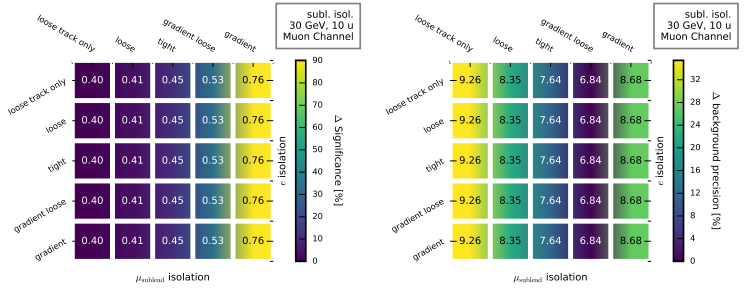

(a) Significance (b) Inverted rel. uncertainty

Figure A.4.: *Muon Channel.* 30 GeV signal point. Effect of implementing the possible isolation requirement WPs for the subleading leptons. The luminosity corresponds to 36.1 fb^{-1}.

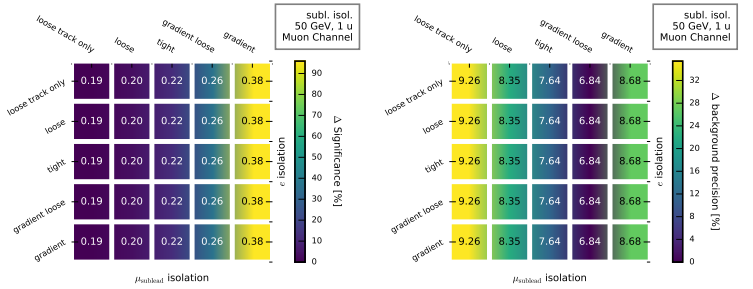

(a) Significance (b) Inverted rel. uncertainty

Figure A.5.: *Muon Channel.* 50 GeV signal point. Effect of implementing the possible isolation requirement WPs for the subleading leptons. The luminosity corresponds to 36.1 fb^{-1}.

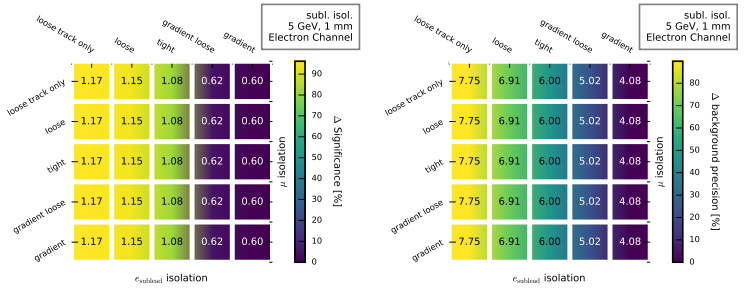

(a) Significance (b) Inverted rel. uncertainty

Figure A.6.: *Electron Channel.* 5 GeV signal point. Effect of implementing the possible isolation requirement WPs for the subleading leptons. The luminosity corresponds to 36.1 fb^{-1}.

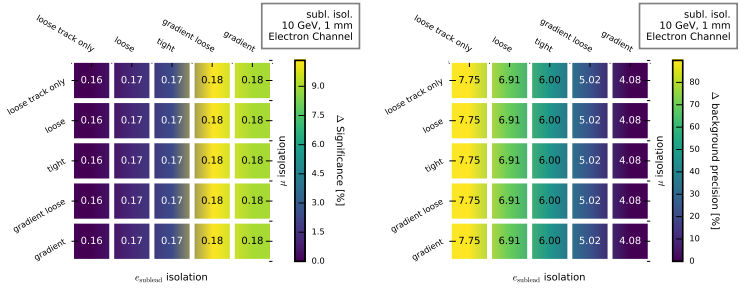

(a) Significance (b) Inverted rel. uncertainty

Figure A.7.: *Electron Channel.* 10 GeV signal point. Effect of implementing the possible isolation requirement WPs for the subleading leptons. The luminosity corresponds to 36.1 fb^{-1}.

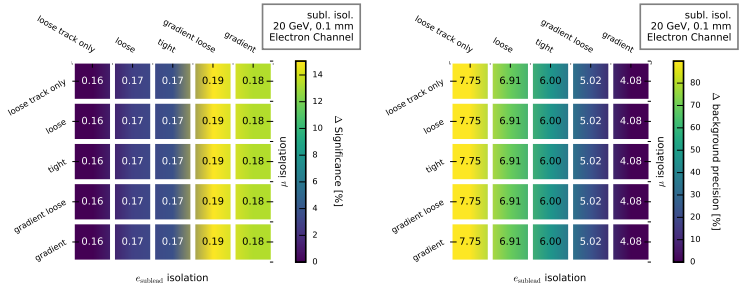

(a) Significance (b) Inverted rel. uncertainty

Figure A.8.: *Electron Channel.* 20 GeV signal point. Effect of implementing the possible isolation requirement WPs for the subleading leptons. The luminosity corresponds to 36.1 fb^{-1}.

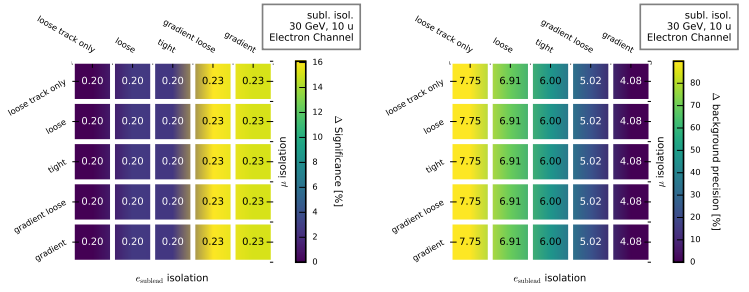

(a) Significance (b) Inverted rel. uncertainty

Figure A.9.: *Electron Channel.* 30 GeV signal point. Effect of implementing the possible isolation requirement WPs for the subleading leptons. The luminosity corresponds to 36.1 fb^{-1}.

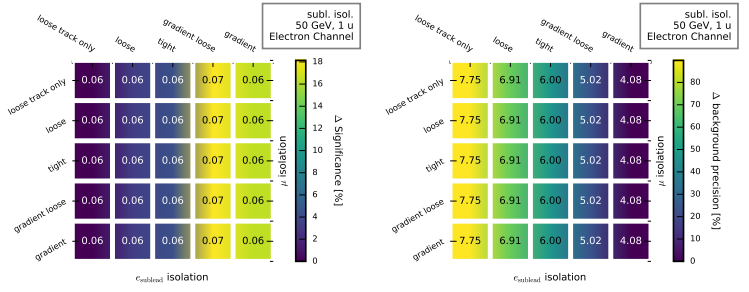

(a) Significance (b) Inverted rel. uncertainty

Figure A.10.: *Electron Channel.* 50 GeV signal point. Effect of implementing the possible isolation requirement WPs for the subleading leptons. The luminosity corresponds to 36.1 fb^{-1}.

Appendix B.

Full cutflow tables for signal region

Selection	10G 1mm	ε_{tot}	S	5G 1mm	ε_{tot}	S
Initial	24 996.00 ± 0.00	1.00	0.00	24 768.00 ± 0.00	1.00	0.00
After obj. def. (weighted)	16.43 ± 0.60	0.10	0.00	341.95 ± 16.68	0.05	0.07
μ == 2 (loose, combined) and e == 1 (loose LLH), $\lvert\Delta z_0 \sin(\theta)\rvert(l) < 1\,\text{mm}$, $\lvert d_0/\sigma(d_0)\rvert(\mu_{\text{lead}}) < 3$	11.41 ± 0.44	0.07	0.01	248.56 ± 14.30	0.03	0.13
$p_{\text{T}}(e) \geq 4.5$ (2016), 7 (2015), $p_{\text{T}}(\mu) \geq 4$	11.20 ± 0.44	0.07	0.01	242.85 ± 14.14	0.03	0.13
$\lvert\eta(e)\rvert \leq 2.47, \lvert\eta(\mu)\rvert \leq 2.5$, veto : $1.37 < \lvert\eta(e)\rvert < 1.52$	10.71 ± 0.43	0.06	0.01	234.23 ± 13.97	0.03	0.13
Trigger	7.24 ± 0.34	0.04	0.01	176.71 ± 11.98	0.02	0.12
Trigger matching	7.24 ± 0.34	0.04	0.01	176.71 ± 11.98	0.02	0.12
$\mu^{\pm}\mu^{\pm}e^{\mp}$	7.21 ± 0.34	0.04	0.09	175.04 ± 11.94	0.02	2.04
$p_{\text{T}}(\mu_1) \geq 23\,\text{GeV}$	7.19 ± 0.34	0.04	0.09	174.50 ± 11.93	0.02	2.04
$p_{\text{T}}(\mu_2) \geq 14\,\text{GeV}$	3.98 ± 0.24	0.02	0.08	106.50 ± 9.42	0.01	1.99
μ_1 `loose` isolation	3.82 ± 0.24	0.02	0.08	100.22 ± 9.24	0.01	1.93
μ_2 `loose` isolation	3.37 ± 0.22	0.02	0.10	68.85 ± 8.09	0.01	1.96
e iso `loose` isolation	3.26 ± 0.22	0.02	0.10	49.71 ± 7.18	0.01	1.53
$M(\mu\mu e) < 90\,\text{GeV}$	3.22 ± 0.22	0.02	0.20	48.43 ± 7.12	0.01	2.79
$M(\mu\mu e) > 40\,\text{GeV}$	3.22 ± 0.22	0.02	0.21	48.43 ± 7.12	0.01	2.90
bJets: 0	3.14 ± 0.22	0.02	0.29	47.49 ± 7.06	0.01	3.79
$E_{\text{T}}^{\text{miss}} < 60\,\text{GeV}$	3.10 ± 0.21	0.02	0.37	45.19 ± 6.92	0.01	4.20
$M(\mu, e) < 50\,\text{GeV}$	3.10 ± 0.21	0.02	0.39	45.19 ± 6.92	0.01	4.21
$M(\mu, e) < 30\,\text{GeV}$	2.99 ± 0.21	0.02	0.43	44.70 ± 6.91	0.01	4.48
$M(\mu, e) < 20\,\text{GeV}$	2.93 ± 0.21	0.02	0.47	44.70 ± 6.91	0.01	4.29
$M(\mu, e) < 10\,\text{GeV}$	2.93 ± 0.21	0.02	0.49	44.70 ± 6.91	0.01	3.06
$M(\mu, e) < 5\,\text{GeV}$	0.50 ± 0.09	0.00	0.11	44.70 ± 6.91	0.01	4.34

Table B.1.: *Muon channel:* Impact of cuts on the number of signal events. The samples are scaled by $\mathcal{L} = 36.1\,\text{fb}^{-1}$. The last cuts are indicating the impact of a *possible* upper cut on the di-lepton mass for different mass hypothesis. This is to indicate the significance that a simple cut and count experiment would yield. However the dilepton mass variable is used as a final signal search variable.

30G 10u	$\varepsilon_{\mathrm{tot}}$	S	20G 0.1mm	$\varepsilon_{\mathrm{tot}}$	S	50G 1u	$\varepsilon_{\mathrm{tot}}$	S
$24\,876.00 \pm 0.00$	1.00	0.00	$24\,233.00 \pm 0.00$	1.00	0.00	$25\,006.00 \pm 0.00$	1.00	0.00
13.29 ± 0.28	0.27	0.00	9.93 ± 0.24	0.21	0.00	8.44 ± 0.15	0.39	0.00
12.60 ± 0.28	0.25	0.01	9.46 ± 0.23	0.20	0.00	7.71 ± 0.14	0.36	0.00
12.49 ± 0.27	0.25	0.01	9.37 ± 0.23	0.20	0.01	7.68 ± 0.14	0.35	0.00
11.84 ± 0.27	0.24	0.01	8.86 ± 0.22	0.19	0.00	7.23 ± 0.13	0.33	0.00
7.89 ± 0.22	0.16	0.01	6.15 ± 0.18	0.13	0.00	3.53 ± 0.09	0.16	0.00
7.88 ± 0.22	0.16	0.01	6.15 ± 0.18	0.13	0.00	3.53 ± 0.09	0.16	0.00
7.85 ± 0.22	0.16	0.09	6.13 ± 0.18	0.13	0.07	3.52 ± 0.09	0.16	0.04
7.81 ± 0.22	0.16	0.09	6.09 ± 0.18	0.13	0.07	3.38 ± 0.09	0.16	0.04
4.95 ± 0.18	0.10	0.09	3.75 ± 0.14	0.08	0.07	2.42 ± 0.07	0.11	0.05
4.87 ± 0.18	0.10	0.10	3.64 ± 0.14	0.08	0.07	2.38 ± 0.07	0.11	0.05
4.77 ± 0.18	0.10	0.14	3.51 ± 0.14	0.08	0.10	2.36 ± 0.07	0.11	0.07
4.74 ± 0.18	0.10	0.15	3.44 ± 0.13	0.07	0.11	2.31 ± 0.07	0.11	0.07
4.62 ± 0.18	0.09	0.28	3.34 ± 0.13	0.07	0.21	2.24 ± 0.07	0.10	0.14
4.61 ± 0.18	0.09	0.29	3.33 ± 0.13	0.07	0.21	2.20 ± 0.07	0.10	0.14
4.52 ± 0.18	0.09	0.41	3.25 ± 0.13	0.07	0.30	2.16 ± 0.07	0.10	0.20
4.40 ± 0.17	0.09	0.52	3.18 ± 0.13	0.07	0.38	2.14 ± 0.07	0.10	0.26
4.37 ± 0.17	0.09	0.54	3.17 ± 0.13	0.07	0.39	2.13 ± 0.07	0.10	0.27
4.12 ± 0.16	0.08	0.59	3.01 ± 0.13	0.06	0.44	1.20 ± 0.05	0.06	0.18
2.20 ± 0.12	0.04	0.36	2.92 ± 0.12	0.06	0.47	0.55 ± 0.04	0.03	0.09
0.39 ± 0.05	0.01	0.08	0.89 ± 0.07	0.02	0.17	0.11 ± 0.02	0.00	0.02
0.06 ± 0.02	0.00	0.01	0.16 ± 0.03	0.00	0.04	0.02 ± 0.01	0.00	0.00

Selection	$t\bar{t}$	singleTop	$Z \to ee$
Initial	48 946 606.96 ± 0.00	9 971 400.35 ± 0.00	40 742 341.00 ± 0.00
After obj. def. (weighted)	26 509.58 ± 107.55	2691.15 ± 31.95	628.38 ± 106.09
μ == 2 (loose, combined) and e == 1 (loose LLH), $\lvert\Delta z_0 \sin(\theta)\rvert(l)$ < 1 mm, $\lvert d_0/\sigma(d_0)\rvert(\mu_{\text{lead}}) < 3$	17 064.95 ± 83.96	1602.06 ± 24.35	50.87 ± 24.08
$p_{\text{T}}(e) \geq$ 4.5 (2016), 7 (2015), $p_{\text{T}}(\mu) \geq 4$	16 887.05 ± 83.56	1585.33 ± 24.24	50.87 ± 24.08
$\lvert\eta(e)\rvert \leq 2.47, \lvert\eta(\mu)\rvert \leq 2.5$, veto : $1.37 < \lvert\eta(e)\rvert < 1.52$	15 744.24 ± 80.56	1482.90 ± 23.55	65.93 ± 15.79
Trigger	8552.23 ± 59.20	755.08 ± 17.07	−0.77 ± 1.98
Trigger matching	8536.25 ± 59.16	754.64 ± 17.06	−0.77 ± 1.98
$\mu^{\pm}\mu^{\pm}e^{\mp}$	2076.88 ± 29.42	196.99 ± 8.91	0.00 ± 0.00
$p_{\text{T}}(\mu_1) \geq 23$ GeV	2064.06 ± 29.28	195.66 ± 8.89	0.00 ± 0.00
$p_{\text{T}}(\mu_2) \geq 14$ GeV	1026.34 ± 20.99	91.03 ± 6.69	0.00 ± 0.00
μ_1 loose isolation	922.04 ± 19.97	84.76 ± 6.58	0.00 ± 0.00
μ_2 loose isolation	624.21 ± 16.24	57.32 ± 4.78	0.00 ± 0.00
e iso loose isolation	557.02 ± 15.48	47.85 ± 4.56	0.00 ± 0.00
$M(\mu\mu e) < 90$ GeV	113.12 ± 7.09	13.55 ± 3.39	0.00 ± 0.00
$M(\mu\mu e) > 40$ GeV	109.93 ± 6.96	12.85 ± 3.36	0.00 ± 0.00
bJets: 0	34.25 ± 3.19	8.82 ± 3.07	0.00 ± 0.00
$E_{\text{T}}^{\text{miss}} < 60$ GeV	13.70 ± 2.04	2.61 ± 0.74	0.00 ± 0.00
$M(\mu, e) < 50$ GeV	10.51 ± 1.81	1.91 ± 0.61	0.00 ± 0.00
$M(\mu, e) < 30$ GeV	6.32 ± 1.43	0.54 ± 0.29	0.00 ± 0.00
$M(\mu, e) < 20$ GeV	3.54 ± 1.17	0.35 ± 0.21	0.00 ± 0.00
$M(\mu, e) < 10$ GeV	2.17 ± 1.03	0.35 ± 0.21	0.00 ± 0.00
$M(\mu, e) < 5$ GeV	2.17 ± 1.03	0.35 ± 0.21	0.00 ± 0.00

Selection	$ttV, V = W/Z$	W+jets	$\sum$ Bkg
Initial	7 517 424.55 ± 0.00	289 050 049.08 ± 0.00	592 737 020.78 ± 0.00
After obj. def. (weighted)	226.11 ± 0.97	20 955.14 ± 1166.13	721 364.07 ± 4480.10
μ == 2 (loose, combined) and e == 1 (loose LLH), $\lvert\Delta z_0 \sin(\theta)\rvert(l)$ < 1 mm, $\lvert d_0/\sigma(d_0)\rvert(\mu_{\text{lead}}) < 3$	196.36 ± 0.88	2369.45 ± 321.25	143 545.52 ± 1857.13
$p_{\text{T}}(e) \geq$ 4.5 (2016), 7 (2015), $p_{\text{T}}(\mu) \geq 4$	195.67 ± 0.88	2289.83 ± 320.20	138 983.95 ± 1824.76
$\lvert\eta(e)\rvert \leq 2.47, \lvert\eta(\mu)\rvert \leq 2.5$, veto : $1.37 < \lvert\eta(e)\rvert < 1.52$	183.32 ± 0.85	2113.73 ± 318.71	130 172.43 ± 1746.28
Trigger	145.82 ± 0.74	907.62 ± 102.54	109 734.41 ± 1405.76
Trigger matching	145.26 ± 0.74	907.25 ± 102.54	109 692.65 ± 1405.73
$\mu^{\pm}\mu^{\pm}e^{\mp}$	20.11 ± 0.33	320.52 ± 55.17	2747.77 ± 66.03
$p_{\text{T}}(\mu_1) \geq 23$ GeV	20.08 ± 0.33	320.41 ± 55.17	2731.17 ± 65.91
$p_{\text{T}}(\mu_2) \geq 14$ GeV	16.82 ± 0.29	108.97 ± 29.94	1306.91 ± 38.11
μ_1 loose isolation	15.99 ± 0.28	102.78 ± 29.83	1182.30 ± 37.31
μ_2 loose isolation	15.00 ± 0.27	36.08 ± 8.36	779.46 ± 20.14
e iso loose isolation	14.00 ± 0.26	15.92 ± 6.16	679.59 ± 18.56
$M(\mu\mu e) < 90$ GeV	1.15 ± 0.07	6.23 ± 5.01	152.25 ± 10.48
$M(\mu\mu e) > 40$ GeV	1.09 ± 0.07	3.29 ± 3.73	145.08 ± 9.83
bJets: 0	0.13 ± 0.02	3.06 ± 3.71	61.30 ± 7.34
$E_{\text{T}}^{\text{miss}} < 60$ GeV	0.04 ± 0.01	0.89 ± 3.54	28.50 ± 6.09
$M(\mu, e) < 50$ GeV	0.03 ± 0.01	1.15 ± 3.53	24.58 ± 6.00
$M(\mu, e) < 30$ GeV	0.02 ± 0.01	0.58 ± 3.51	16.69 ± 5.16
$M(\mu, e) < 20$ GeV	0.01 ± 0.00	−0.65 ± 3.43	9.80 ± 4.83
$M(\mu, e) < 10$ GeV	0.00 ± 0.00	−3.23 ± 3.12	2.58 ± 4.37
$M(\mu, e) < 5$ GeV	0.00 ± 0.00	−1.09 ± 2.16	4.66 ± 3.74

$Z \to \mu\mu$	$Z \to \tau\tau$	Diboson	Triboson
37 954 205.73 ± 0.00	35 645 838.18 ± 0.00	122 653 547.50 ± 0.00	255 607.43 ± 0.00
657 890.69 ± 4308.08	6226.31 ± 357.47	6187.60 ± 15.48	49.11 ± 0.77
116 332.95 ± 1822.78	1269.48 ± 121.93	4613.35 ± 11.09	46.06 ± 0.74
112 108.20 ± 1790.03	1240.88 ± 121.38	4580.19 ± 11.03	45.94 ± 0.74
105 130.27 ± 1710.84	1135.24 ± 116.25	4273.92 ± 10.67	42.90 ± 0.71
95 611.75 ± 1399.43	465.55 ± 57.95	3263.55 ± 9.27	33.58 ± 0.61
95 588.87 ± 1399.40	465.54 ± 57.95	3262.04 ± 9.27	33.58 ± 0.61
39.24 ± 15.28	43.66 ± 11.68	41.65 ± 1.27	8.71 ± 0.32
39.24 ± 15.28	41.60 ± 11.34	41.42 ± 1.26	8.71 ± 0.32
9.93 ± 4.28	20.06 ± 7.15	26.19 ± 0.82	7.58 ± 0.31
8.91 ± 4.20	15.42 ± 6.44	25.06 ± 0.80	7.34 ± 0.30
4.64 ± 3.88	11.67 ± 5.75	23.49 ± 0.73	7.04 ± 0.29
4.65 ± 3.53	11.25 ± 5.74	21.99 ± 0.68	6.90 ± 0.29
5.76 ± 3.19	4.60 ± 3.56	6.57 ± 0.37	1.28 ± 0.13
5.89 ± 3.18	4.60 ± 3.56	6.20 ± 0.36	1.23 ± 0.12
5.00 ± 3.08	2.88 ± 3.31	5.98 ± 0.35	1.19 ± 0.12
4.77 ± 3.08	1.66 ± 3.21	4.34 ± 0.29	0.49 ± 0.07
4.77 ± 3.08	1.66 ± 3.21	4.10 ± 0.27	0.45 ± 0.07
4.74 ± 3.08	2.05 ± 1.63	2.24 ± 0.20	0.20 ± 0.05
4.89 ± 3.07	0.89 ± 0.82	0.70 ± 0.11	0.08 ± 0.03
3.22 ± 2.87	−0.11 ± 0.16	0.16 ± 0.04	0.02 ± 0.01
3.22 ± 2.87	0.00 ± 0.00	0.01 ± 0.01	0.00 ± 0.00

Table B.3.: *Muon channel:* Impact of cuts on the number of background events. The samples are scaled by $\mathcal{L} = 36.1\,\mathrm{fb}^{-1}$. The last cuts are indicating the impact of a *possible* upper cut on the di-lepton mass for different mass hypothesis. This is to indicate the significance that a simple cut and count experiment would yield. However the dilepton mass variable is used as a final signal search variable.

Selection	10G 1mm	ε_{tot}	S	5G 1mm	ε_{tot}	S
Initial	25 000.00 ± 0.00	1.00	0.00	24 000.00 ± 0.00	1.00	0.00
After obj. def. (weighted)	17.59 ± 0.60	0.10	0.01	366.36 ± 16.86	0.05	0.16
μ == 1 (loose, combined) and e == 2 (loose LLH), e_{lead} tight LLH, $\lvert\Delta z_0 \sin(\theta)\rvert(l) < 1\,\text{mm}$, $\lvert d_0/\sigma(d_0)\rvert(e_{\text{lead}}) < 5$	10.86 ± 0.47	0.06	0.01	237.25 ± 12.65	0.03	0.25
$p_{\text{T}}(e) \geq$ 4.5 (2016), 7 (2015), $p_{\text{T}}(\mu) \geq 4$	10.74 ± 0.47	0.06	0.01	229.54 ± 12.43	0.03	0.24
$\lvert\eta(e)\rvert \leq 2.47$, $\lvert\eta(\mu)\rvert \leq 2.5$, veto : $1.37 < \lvert\eta(e)\rvert < 1.52$	9.64 ± 0.44	0.05	0.01	205.37 ± 11.78	0.03	0.23
Trigger	8.34 ± 0.41	0.05	0.01	157.73 ± 10.10	0.02	0.19
Trigger matching	7.14 ± 0.38	0.04	0.01	136.96 ± 9.39	0.02	0.17
$e^{\pm}e^{\pm}\mu^{\mp}$	7.05 ± 0.38	0.04	0.06	135.12 ± 9.33	0.02	1.20
$p_{\text{T}}(e_1) \geq 27\,\text{GeV}$	7.05 ± 0.38	0.04	0.06	135.12 ± 9.33	0.02	1.20
$p_{\text{T}}(e_2) \geq 10\,\text{GeV}$	4.42 ± 0.27	0.02	0.06	68.95 ± 6.09	0.01	0.88
e_1 loose isolation	4.35 ± 0.27	0.02	0.06	67.84 ± 6.04	0.01	0.87
e_2 loose isolation	3.90 ± 0.26	0.02	0.06	41.84 ± 4.70	0.01	0.68
μ loose isolation	3.47 ± 0.25	0.02	0.08	23.76 ± 3.49	0.00	0.51
Z veto $M(e_1, e_2) < 78\,\text{GeV}$	3.42 ± 0.25	0.02	0.12	23.76 ± 3.49	0.00	0.80
$M(ee\mu) < 90\,\text{GeV}$	3.39 ± 0.25	0.02	0.16	23.76 ± 3.49	0.00	1.09
$M(ee\mu) > 40\,\text{GeV}$	3.39 ± 0.25	0.02	0.16	23.76 ± 3.49	0.00	1.09
bJets: 0	3.25 ± 0.22	0.02	0.17	23.76 ± 3.49	0.00	1.21
$E_{\text{T}}^{\text{miss}} < 60\,\text{GeV}$	3.15 ± 0.22	0.02	0.24	23.76 ± 3.49	0.00	1.64
$M(\mu, e_2) < 50\,\text{GeV}$	3.15 ± 0.22	0.02	0.24	23.76 ± 3.49	0.00	1.65
$M(\mu, e_2) < 30\,\text{GeV}$	3.02 ± 0.21	0.02	0.30	23.76 ± 3.49	0.00	2.11
$M(\mu, e_2) < 20\,\text{GeV}$	2.98 ± 0.21	0.02	0.39	23.76 ± 3.49	0.00	2.52
$M(\mu, e_2) < 10\,\text{GeV}$	2.97 ± 0.21	0.02	0.58	23.76 ± 3.49	0.00	3.12
$M(\mu, e_2) < 5\,\text{GeV}$	0.36 ± 0.07	0.00	0.15	23.76 ± 3.49	0.00	3.53

Table B.5.: *Electron channel:* Impact of cuts on the number of signal events. The samples are scaled by $\mathcal{L} = 36.1\,\text{fb}^{-1}$. The last cuts are indicating the impact of a *possible* upper cut on the di-lepton mass for different mass hypothesis. This is to indicate the significance that a simple cut and count experiment would yield. However the dilepton mass variable is used as a final signal search variable.

30G 10u	$\varepsilon_{\mathrm{tot}}$	S	20G 0.1mm	$\varepsilon_{\mathrm{tot}}$	S	50G 1u	$\varepsilon_{\mathrm{tot}}$	S
$24\,000.00 \pm 0.00$	1.00	0.00	$24\,000.00 \pm 0.00$	1.00	0.00	$25\,000.00 \pm 0.00$	1.00	0.00
12.02 ± 0.26	0.24	0.01	9.56 ± 0.23	0.21	0.00	5.45 ± 0.12	0.25	0.00
10.61 ± 0.24	0.21	0.01	8.40 ± 0.21	0.18	0.01	4.76 ± 0.11	0.22	0.00
10.48 ± 0.24	0.21	0.01	8.29 ± 0.21	0.18	0.01	4.73 ± 0.11	0.22	0.00
9.48 ± 0.23	0.19	0.01	7.41 ± 0.20	0.16	0.01	4.28 ± 0.10	0.20	0.00
7.28 ± 0.20	0.15	0.01	6.01 ± 0.17	0.13	0.01	2.07 ± 0.06	0.10	0.00
6.23 ± 0.18	0.13	0.01	5.18 ± 0.16	0.11	0.01	1.58 ± 0.06	0.07	0.00
6.16 ± 0.18	0.12	0.05	5.14 ± 0.16	0.11	0.05	1.56 ± 0.06	0.07	0.01
6.16 ± 0.18	0.12	0.05	5.14 ± 0.16	0.11	0.05	1.56 ± 0.06	0.07	0.01
4.35 ± 0.14	0.09	0.06	3.72 ± 0.14	0.08	0.05	1.31 ± 0.05	0.06	0.02
4.30 ± 0.14	0.09	0.06	3.68 ± 0.14	0.08	0.05	1.29 ± 0.05	0.06	0.02
4.23 ± 0.14	0.09	0.07	3.57 ± 0.13	0.08	0.06	1.28 ± 0.05	0.06	0.02
4.13 ± 0.14	0.08	0.09	3.48 ± 0.13	0.08	0.08	1.25 ± 0.05	0.06	0.03
4.08 ± 0.14	0.08	0.14	3.41 ± 0.13	0.07	0.12	1.22 ± 0.05	0.06	0.04
4.05 ± 0.14	0.08	0.19	3.37 ± 0.13	0.07	0.16	1.20 ± 0.05	0.06	0.06
4.03 ± 0.14	0.08	0.19	3.37 ± 0.13	0.07	0.16	1.16 ± 0.05	0.05	0.06
3.98 ± 0.14	0.08	0.21	3.27 ± 0.13	0.07	0.18	1.12 ± 0.05	0.05	0.06
3.91 ± 0.14	0.08	0.29	3.20 ± 0.13	0.07	0.24	1.10 ± 0.04	0.05	0.08
3.89 ± 0.14	0.08	0.29	3.17 ± 0.13	0.07	0.24	1.10 ± 0.04	0.05	0.08
3.65 ± 0.13	0.07	0.36	3.02 ± 0.13	0.07	0.30	0.61 ± 0.03	0.03	0.06
2.15 ± 0.10	0.04	0.28	2.93 ± 0.12	0.06	0.38	0.29 ± 0.02	0.01	0.04
0.44 ± 0.04	0.01	0.09	0.73 ± 0.05	0.02	0.15	0.04 ± 0.01	0.00	0.01
0.05 ± 0.01	0.00	0.02	0.09 ± 0.02	0.00	0.04	0.01 ± 0.00	0.00	0.00

)

Selection	$t\bar{t}$	singleTop	$Z \to ee$
Initial	48 946 606.96 ± 0.00	9 971 400.35 ± 0.00	40 742 341.00 ± 0.00
After obj. def. (weighted)	27 143.27 ± 111.52	2645.09 ± 31.91	184 597.22 ± 1959.54
μ == 1 (loose, combined) and e == 2 (loose LLH), e_{lead} tight LLH, $\lvert\Delta z_0 \sin(\theta)\rvert(l) < 1$ mm, $\lvert d_0/\sigma(d_0)\rvert(e_{\text{lead}}) < 5$	15 557.43 ± 82.64	1458.08 ± 22.96	54 897.87 ± 879.95
$p_{\text{T}}(e) \geq$ 4.5 (2016), 7 (2015), $p_{\text{T}}(\mu) \geq 4$	15 260.51 ± 81.92	1430.50 ± 22.78	54 903.86 ± 879.71
$\lvert\eta(e)\rvert \leq 2.47, \lvert\eta(\mu)\rvert \leq 2.5$, veto : $1.37 < \lvert\eta(e)\rvert < 1.52$	13 659.29 ± 77.71	1270.97 ± 21.42	48 517.51 ± 844.53
Trigger	11 802.32 ± 71.80	1112.54 ± 20.10	45 909.08 ± 795.80
Trigger matching	11 073.87 ± 69.74	1032.50 ± 19.23	39 972.00 ± 732.69
$e^{\pm}e^{\pm}\mu^{\mp}$	3244.10 ± 37.39	313.29 ± 10.59	310.68 ± 47.98
$p_{\text{T}}(e_1) \geq 27$ GeV	3244.10 ± 37.39	313.29 ± 10.59	310.68 ± 47.98
$p_{\text{T}}(e_2) \geq 10$ GeV	1452.56 ± 24.88	139.70 ± 6.89	286.76 ± 47.32
e_1 loose isolation	1408.81 ± 24.57	135.89 ± 6.82	279.06 ± 47.25
e_2 loose isolation	570.21 ± 15.52	55.63 ± 4.75	242.22 ± 43.57
μ loose isolation	486.73 ± 13.88	45.56 ± 4.50	130.59 ± 28.87
Z veto $M(e_1, e_2) < 78$ GeV	344.22 ± 11.63	32.29 ± 4.04	12.18 ± 5.82
$M(ee\mu) < 90$ GeV	102.02 ± 5.76	13.46 ± 2.86	10.31 ± 3.77
$M(ee\mu) > 40$ GeV	97.59 ± 5.66	13.12 ± 2.85	10.56 ± 3.75
bJets: 0	33.22 ± 3.32	8.13 ± 2.03	10.45 ± 3.73
$E_{\text{T}}^{\text{miss}} < 60$ GeV	12.24 ± 1.92	4.56 ± 1.69	10.40 ± 3.73
$M(\mu, e_2) < 50$ GeV	10.99 ± 1.71	4.35 ± 1.68	10.40 ± 3.73
$M(\mu, e_2) < 30$ GeV	6.33 ± 1.30	3.48 ± 1.62	8.84 ± 3.41
$M(\mu, e_2) < 20$ GeV	3.43 ± 1.00	1.13 ± 0.51	3.75 ± 2.83
$M(\mu, e_2) < 10$ GeV	1.25 ± 0.67	0.70 ± 0.40	0.92 ± 1.38
$M(\mu, e_2) < 5$ GeV	0.35 ± 0.35	0.44 ± 0.31	1.23 ± 1.05

Selection	$ttV, V = W/Z$	W+jets	$\sum$ Bkg
Initial	7 517 424.55 ± 0.00	289 050 049.08 ± 0.00	592 737 020.78 ± 0.00
After obj. def. (weighted)	228.32 ± 0.98	17 594.98 ± 1010.86	242 989.76 ± 2226.91
μ == 1 (loose, combined) and e == 2 (loose LLH), e_{lead} tight LLH, $\lvert\Delta z_0 \sin(\theta)\rvert(l) < 1$ mm, $\lvert d_0/\sigma(d_0)\rvert(e_{\text{lead}}) < 5$	188.74 ± 0.88	1904.23 ± 212.33	78 962.57 ± 914.44
$p_{\text{T}}(e) \geq$ 4.5 (2016), 7 (2015), $p_{\text{T}}(\mu) \geq 4$	187.90 ± 0.87	1855.98 ± 211.72	78 523.01 ± 913.82
$\lvert\eta(e)\rvert \leq 2.47, \lvert\eta(\mu)\rvert \leq 2.5$, veto : $1.37 < \lvert\eta(e)\rvert < 1.52$	168.54 ± 0.83	1452.36 ± 144.06	69 473.37 ± 865.28
Trigger	158.72 ± 0.80	1123.95 ± 119.96	63 812.11 ± 810.83
Trigger matching	151.34 ± 0.78	1038.56 ± 111.84	56 639.56 ± 747.04
$e^{\pm}e^{\pm}\mu^{\mp}$	21.91 ± 0.34	345.33 ± 55.54	4474.09 ± 89.98
$p_{\text{T}}(e_1) \geq 27$ GeV	21.91 ± 0.34	345.33 ± 55.54	4474.09 ± 89.98
$p_{\text{T}}(e_2) \geq 10$ GeV	17.92 ± 0.31	205.79 ± 30.50	2196.01 ± 62.48
e_1 loose isolation	17.41 ± 0.30	201.89 ± 30.45	2134.26 ± 62.27
e_2 loose isolation	15.70 ± 0.28	90.59 ± 20.33	1039.95 ± 51.09
μ loose isolation	14.56 ± 0.27	51.76 ± 15.41	786.71 ± 36.26
Z veto $M(e_1, e_2) < 78$ GeV	4.87 ± 0.15	36.37 ± 13.90	455.58 ± 20.19
$M(ee\mu) < 90$ GeV	1.25 ± 0.08	36.08 ± 13.88	178.91 ± 16.36
$M(ee\mu) > 40$ GeV	1.22 ± 0.08	36.40 ± 13.86	174.31 ± 16.30
bJets: 0	0.21 ± 0.05	36.80 ± 13.85	103.20 ± 15.42
$E_{\text{T}}^{\text{miss}} < 60$ GeV	0.06 ± 0.02	22.08 ± 8.67	59.79 ± 10.61
$M(\mu, e_2) < 50$ GeV	0.05 ± 0.02	22.08 ± 8.67	58.06 ± 10.57
$M(\mu, e_2) < 30$ GeV	0.05 ± 0.01	15.08 ± 5.33	40.95 ± 7.58
$M(\mu, e_2) < 20$ GeV	0.02 ± 0.01	9.12 ± 4.10	19.11 ± 5.93
$M(\mu, e_2) < 10$ GeV	0.00 ± 0.00	4.67 ± 3.28	7.00 ± 3.81
$M(\mu, e_2) < 5$ GeV	0.00 ± 0.00	0.05 ± 0.92	1.29 ± 1.85

$Z \to \mu\mu$	$Z \to \tau\tau$	Diboson	Triboson
$37\,954\,205.73 \pm 0.00$	$35\,645\,838.18 \pm 0.00$	$122\,653\,547.50 \pm 0.00$	$255\,607.43 \pm 0.00$
779.17 ± 108.78	4813.80 ± 268.38	5139.57 ± 13.63	48.35 ± 0.77
38.17 ± 15.46	1069.84 ± 95.39	3805.69 ± 9.85	42.53 ± 0.71
37.91 ± 15.45	1015.65 ± 93.73	3788.31 ± 9.81	42.41 ± 0.71
35.54 ± 15.39	964.30 ± 88.85	3367.05 ± 9.21	37.82 ± 0.67
1.61 ± 5.97	613.45 ± 63.90	3055.63 ± 8.79	34.81 ± 0.65
1.60 ± 5.96	538.52 ± 58.22	2798.67 ± 8.45	32.51 ± 0.63
-4.61 ± 4.86	128.24 ± 34.18	106.32 ± 2.59	8.83 ± 0.34
-4.61 ± 4.86	128.24 ± 34.18	106.32 ± 2.59	8.83 ± 0.34
0.35 ± 0.31	25.64 ± 7.99	59.29 ± 1.77	8.01 ± 0.33
0.04 ± 0.03	25.28 ± 7.98	58.09 ± 1.75	7.80 ± 0.33
0.02 ± 0.02	7.42 ± 5.71	50.53 ± 1.52	7.63 ± 0.32
0.02 ± 0.02	5.55 ± 5.39	44.68 ± 1.34	7.24 ± 0.30
0.02 ± 0.02	4.96 ± 5.31	17.76 ± 0.75	2.91 ± 0.18
0.00 ± 0.00	5.11 ± 4.35	9.26 ± 0.52	1.43 ± 0.13
0.00 ± 0.00	5.05 ± 4.35	8.99 ± 0.52	1.39 ± 0.13
0.00 ± 0.00	4.28 ± 4.09	8.75 ± 0.51	1.36 ± 0.13
0.00 ± 0.00	3.75 ± 4.08	5.92 ± 0.42	0.77 ± 0.10
0.00 ± 0.00	3.75 ± 4.08	5.71 ± 0.41	0.72 ± 0.09
0.00 ± 0.00	2.99 ± 3.59	3.76 ± 0.35	0.42 ± 0.07
0.00 ± 0.00	-0.40 ± 3.00	1.84 ± 0.28	0.21 ± 0.05
0.00 ± 0.00	-1.23 ± 1.12	0.64 ± 0.15	0.05 ± 0.03
0.00 ± 0.00	-1.08 ± 1.11	0.29 ± 0.12	0.00 ± 0.00

Table B.7.: *Electron channel:* Impact of cuts on the number of background events. The samples are scaled by $\mathcal{L} = 36.1\,\mathrm{fb}^{-1}$. The last cuts are indicating the impact of a *possible* upper cut on the di-lepton mass for different mass hypothesis. This is to indicate the significance that a simple cut and count experiment would yield. However the dilepton mass variable is used as a final signal search variable.

Appendix C.

Impact of signal lepton origin on dilepton invariant mass

The dilepton invariant mass distribution is formed by invariant mass of the subleading lepton ℓ and the single flavour lepton ℓ' in the final state $\ell^{\pm}\ell^{\pm}\ell'^{\mp}\nu$. As this discriminant is supposed to reconstruct the mass of the HNL an implicit assumption is made that the leading lepton in originating from the on-shell W decay. Depending on the mass of the HNL this assumption is justified as for low mass HNL the available energy is lower for the p_{T} of its decay products and hence the leading lepton will in the vast majority of cases originate from the on-shell W boson. However as HNL mass increases so does the available energy for its decay products and hence the lepton p_{T} of the subleading ℓ becomes increasingly competing with the leading lepton p_{T}. In this appendix MC signal samples with increased statistics and additional generator information about the origin of leptons are examined. The impact of the subleading ℓ origin on the dilepton invariant mass distribution is studied both in terms of shape and and its magnitude.

From the Figures presented in the following it can be seen that for HNL masses 5 to 30 GeV the classification of the subleading ℓ to originate from the HNL is only mistaken in less than 15 %. Furthermore it is clear that for 50 GeV signal masses, once the mass actually gets more comparable to the W boson mass, the origin of subleading ℓ changes significantly and is determined to be around 30 to 40 %. However in the same Figures it can be seen that the invariant mass distribution has only a slight shape difference due to the similar kinematics of the leading and subleading ℓ at that point.

As the search presented in this thesis is not applying an upper cut on the dilepton invariant mass in its statistical analysis of background-only and signal-plus-background hypotheses this becomes a non-issue as the full amount of information contained in the dilepton mass disregarding of the origin of the subleading lepton enters the combined pdf. In case one wants to reconstruct though the HNL mass from the visible decay products this is an issue that would need to be taken into acocunt.

In Figure C.1 the findings are presented from the muon channel while in Figure C.2 the same is presented for the electron channel.

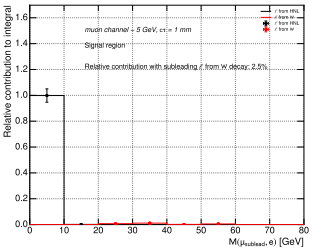

(a) 5 GeV signal point.

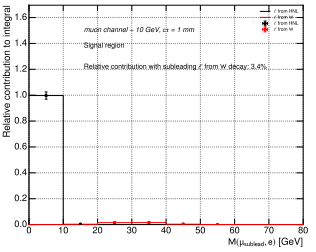

(b) 10 GeV signal point.

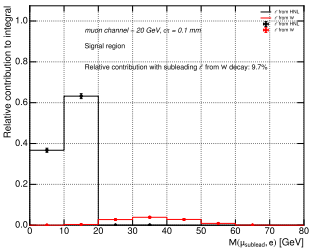

(c) 20 GeV signal point.

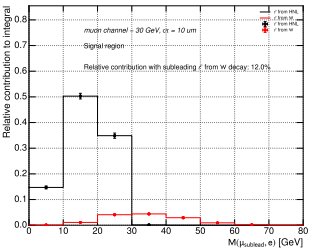

(d) 30 GeV signal point.

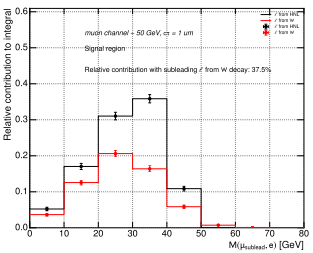

(e) 50 GeV signal point.

Figure C.1.: *Muon Channel.* Impact of lepton origin on dilepton invariant mass distribution.

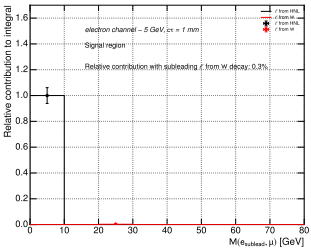

(a) 5 GeV signal point.

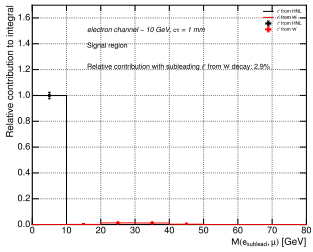

(b) 10 GeV signal point.

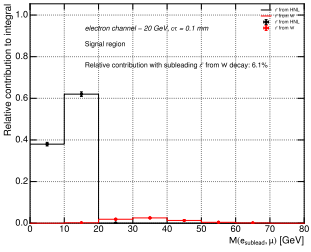

(c) 20 GeV signal point.

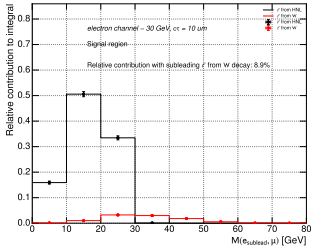

(d) 30 GeV signal point.

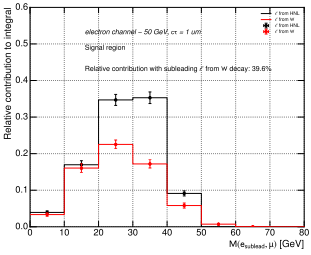

(e) 50 GeV signal point.

Figure C.2.: *Electron Channel.* Impact of lepton origin on dilepton invariant mass distribution.

Appendix D.

Smoothing of JER systematic variation

The Jet Energy Resolution (JER) plays a crucial role in the measurement of jet cross section and $E_{\mathrm{T}}^{\mathrm{miss}}$. It is therefore an important part for most searches at ATLAS. Jets are reconstructed for this search using the anti-k_t algorithm with a radius parameter of $R = 0.4$ and calorimeter clusters as input. As calorimeter jets are reconstructed usually with more than 15 % lower energy than the actual energy (due to their measurement at the EM-scale), one needs to derive a calibration for the energy. This can for instance be done by comparison to track energy information [109]. Depending on the strategy a systematic variation of the JER is the consequence which in turn will have an effect on the reconstruction of jet objects for this search.

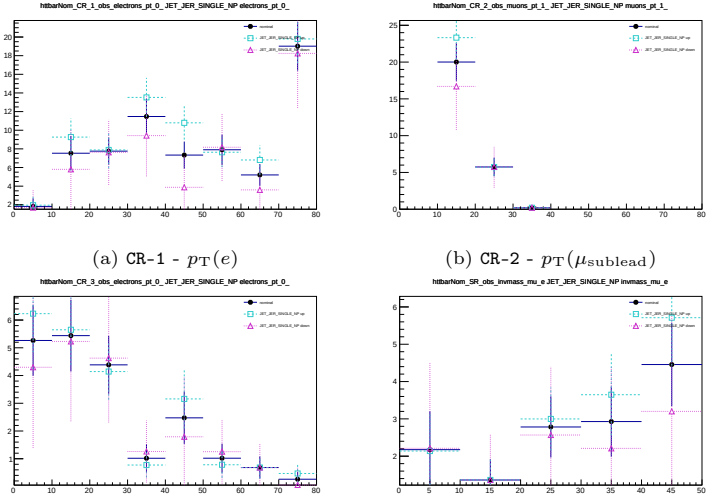

(a) `CR-1` - $p_{\mathrm{T}}(e)$

(b) `CR-2` - $p_{\mathrm{T}}(\mu_{\mathrm{sublead}})$

(c) `CR-3` - $p_{\mathrm{T}}(e)$

(d) `SR` - $M(\mu_{\mathrm{sublead}}, e)$

Figure D.1.: $t\bar{t}$'s nominal and `JER_SINGLE_NP` systematic variations are shown including their statistical uncertainties.

A simultaneous fit of `CR-1`, `CR-2`, `CR-3` and `SR` using pre-fit background distributions as Asimov data showed a constraint on the `JER_SINGLE_NP` systematic for the muon channel. The $\pm 1\sigma$ variation was constrained to approx. $\pm 0.55\sigma$.

There are two reasons for this: For one, the JER uncertainty is known within ATLAS to be largely overestimated as an extrapolation from a Run-1 result [109] and a constr int both in real and Asimov data would therefore be expected. Additionally the single top and $t\bar{t}$ samples, that are affected by the systematic variation, show in some bins large statistical uncertainties and a spread of the

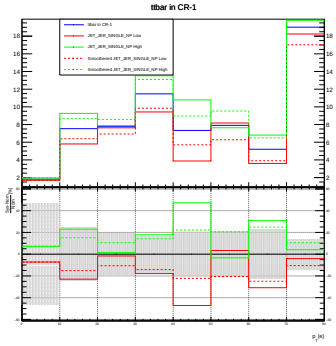

(a) CR-1 - $p_{\mathrm{T}}(e)$

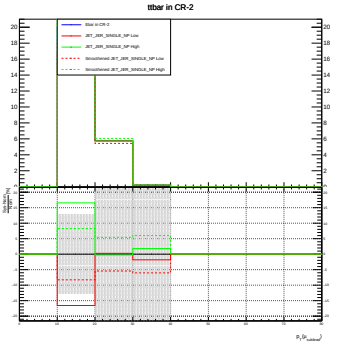

(b) CR-2 - $p_{\mathrm{T}}(\mu_{\mathrm{sublead}})$

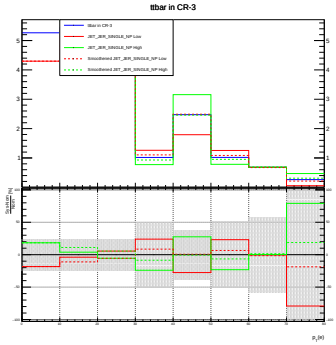

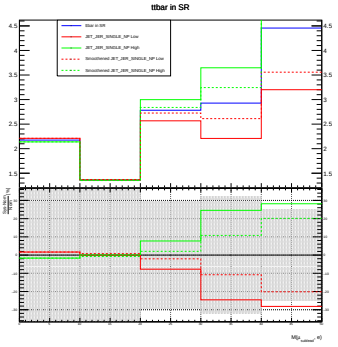

(c) SR - $M(\mu_{\mathrm{sublead}}, e)$

Figure D.2.: $t\bar{t}$'s pre- and post-smoothed JER_SINGLE_NP systematic variations. Dashed lines show the smoothed up- (green) and down (red) variations. Statistical uncertainty of the nominal sample is shown by the Grey background. The systematic variations have uncertainties of same order as nominal but are not shown her e.

same order between them, which can increase the constraining effect if the statistical uncertainty on the Asimov datapoint is smaller than the combined statistical fluctuation of the nominal and systematic variation distributions.

The nominal and systematic variation distributions including their statistical uncertainties are shown in Figures D.1 and D.3 clearly showing the aforementioned behavior. To ensure a stable fit, kernel smoothing has been applied in this search for the JER systematic only using a smoothing library developed by ATLAS. This is the recommended approach by the experiment. The resulting smoothing is shown in Figure D.2 for $t\bar{t}$ and in Figure D.4 for the single top sample. It is clearly visible that large up-down fluctuations have been smoothed.

As a result the JER variation constrain is weakened to $\pm 0.81\sigma$ as shown in Figure 7.22 displaying the final pull constrains on a pre-fit model in both CRs and SR.

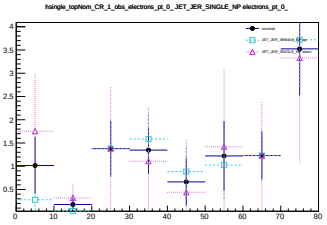

(a) CR-1 - $p_{\mathrm{T}}(e)$

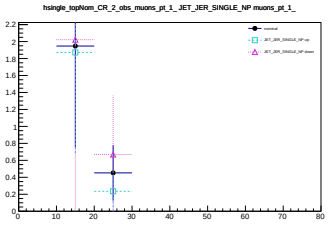

(b) CR-2 - $p_{\mathrm{T}}(\mu_{\mathrm{sublead}})$

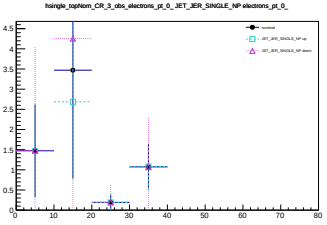

(c) CR-3 - $p_{\mathrm{T}}(e)$

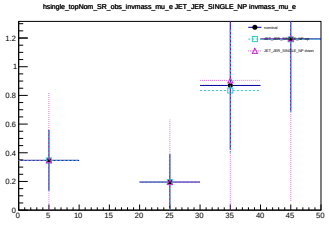

(d) SR - $M(\mu_{\mathrm{sublead}}, e)$

Figure D.3.: Single top's nominal and JER_SINGLE_NP systematic variations are shown including their statistical uncertainties.

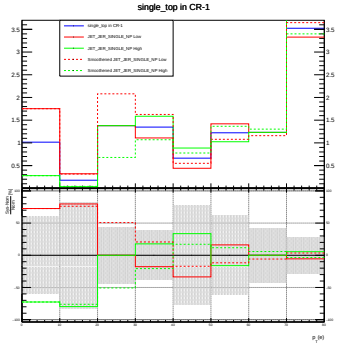

(a) `CR-1` - $p_{\mathrm{T}}(e)$

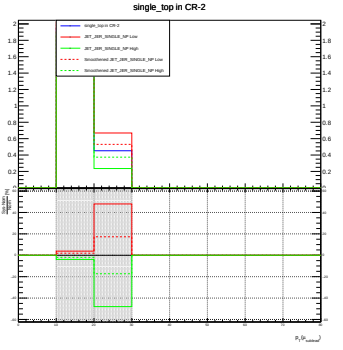

(b) `CR-2` - $p_{\mathrm{T}}(\mu_{\mathrm{sublead}})$

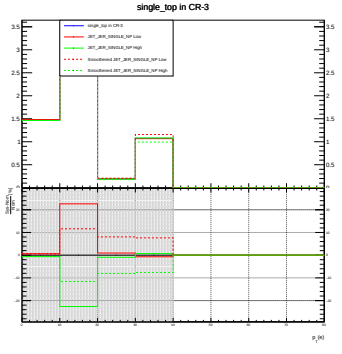

(c) `CR-3` - $p_{\mathrm{T}}(e)$

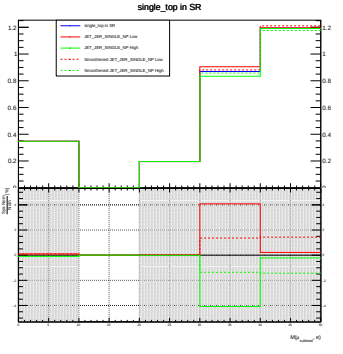

(d) `SR` - $M(\mu_{\mathrm{sublead}}, e)$

Figure D.4.: Single top's pre- and post-smoothed `JER_SINGLE_NP` systematic variations. Dashed lines show the smoothed up- (green) and down (red) variations. Statistical uncertainty of the nominal sample is shown by the Grey background. The systematic variations have uncertainties of same order as nominal but are not shown here.

Appendix E.

Data/MC comparison

In order to show the varying degree of agreement between measured ATLAS data and MC as the signal region gets iteratively selected in the following two sections plots are presented showing p_{T} distributions, as well as $E_{\mathrm{T}}^{\mathrm{miss}}$, the trilepton invariant mass $M(\ell,\ell,\ell')$ and the amount of b jets.

The plots are created applying an inverted trilepton invariant mass cut and therefore show the sidebands at

$$40\,\mathrm{GeV} \geq M(\ell,\ell,\ell') \text{ or } M(\ell,\ell,\ell') \geq 90\,\mathrm{GeV}. \tag{E.1}$$

In table E.1 the differences between the plots and the signal region is described. The resulting plots are presented in in Figure E.4 and in Figure E.8 for the muon channel and electron channel respectively.

Cut	DM-1	DM-2	DM-3	DM-4
$M(\ell,\ell,\ell')$ sideband	✓	✓	✓	✓
no OSSF lepton pairs	✗	✓	✓	✓
b jet veto	✗	✗	✓	✓
$E_{\mathrm{T}}^{\mathrm{miss}}$ cut	✗	✗	✗	✓

Table E.1.: Definition of data / MC comparison regions. All object selection criteria and trigger cuts are applied for each region. The signal region corresponds to DM-4, with the exception of the trilepton invariant mass sidebands. Instead the signal region requires $M(\ell,\ell,\ell')$ to be in the range of 40 to 90 GeV.

E.1. Muon Channel

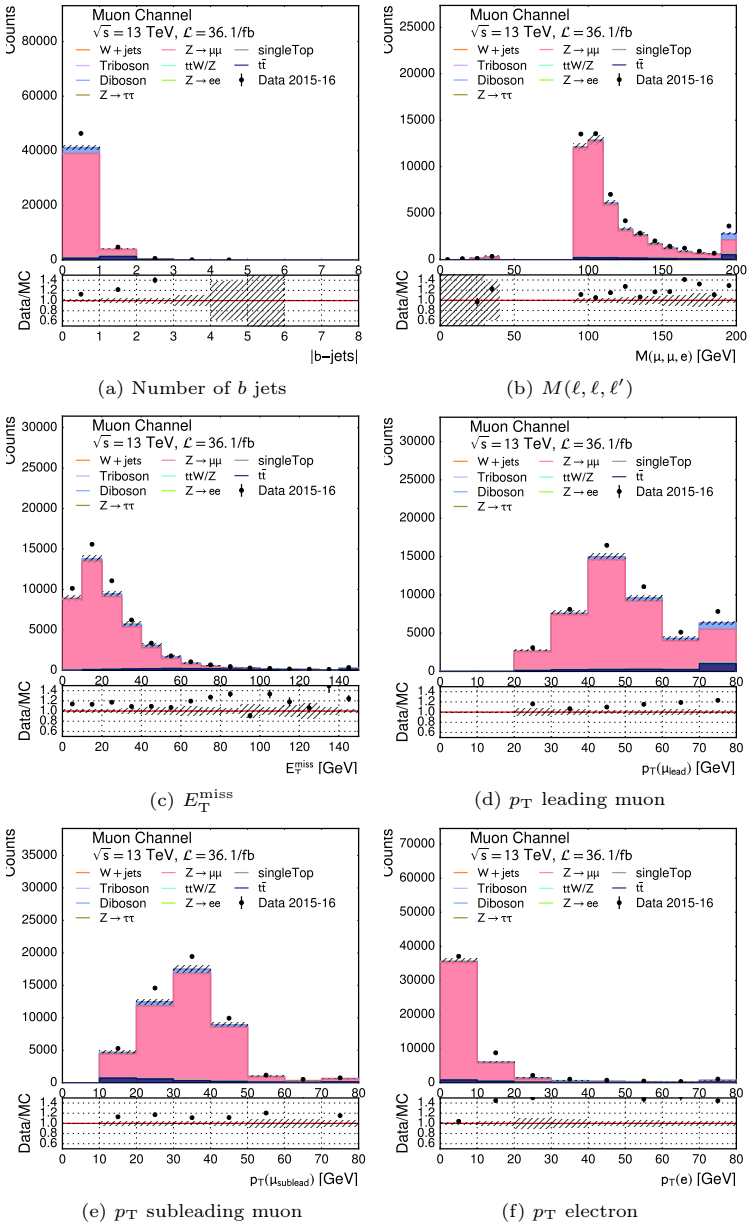

(a) Number of b jets

(b) $M(\ell, \ell, \ell')$

(c) $E_{\mathrm{T}}^{\mathrm{miss}}$

(d) p_{T} leading muon

(e) p_{T} subleading muon

(f) p_{T} electron

Figure E.1.: *Muon Channel.* Comparison of agreement between data and MC backgrounds in `DM-1`. The error bands show combined statistical uncertainties.

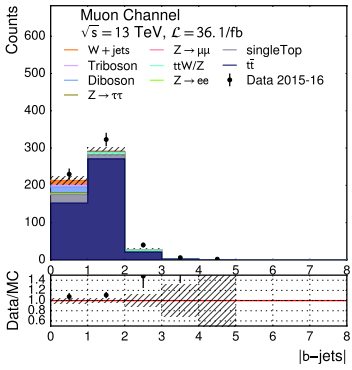

(a) Number of b jets

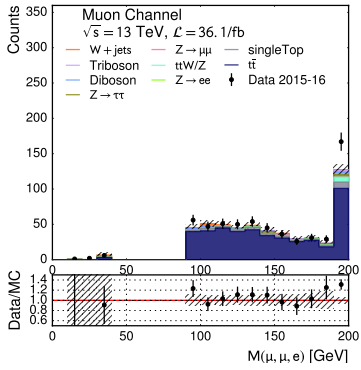

(b) $M(\ell, \ell, \ell')$

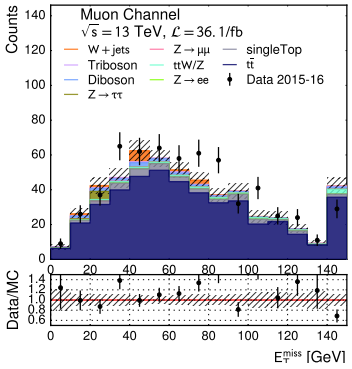

(c) $E_{\mathrm{T}}^{\mathrm{miss}}$

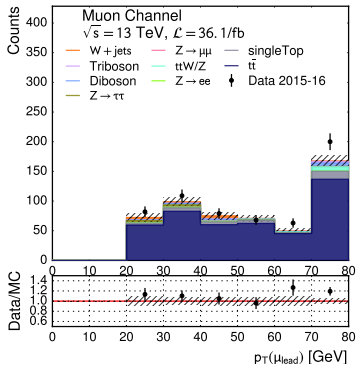

(d) p_{T} leading muon

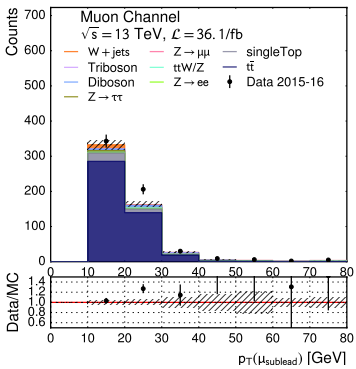

(e) p_{T} subleading muon

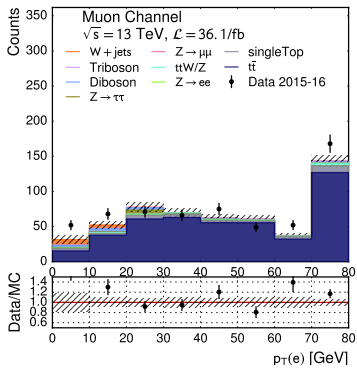

(f) p_{T} electron

Figure E.2.: *Muon Channel.* Comparison of agreement between data and MC backgrounds in `DM-2`. The error bands show combined statistical uncertainties.

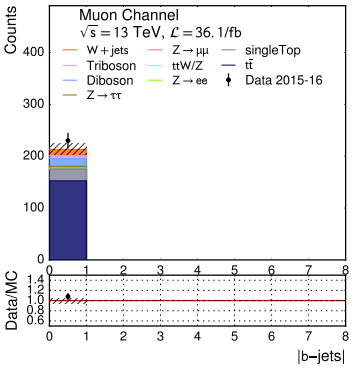

(a) Number of b jets

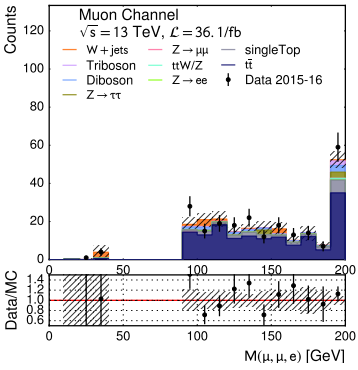

(b) $M(\ell, \ell, \ell')$

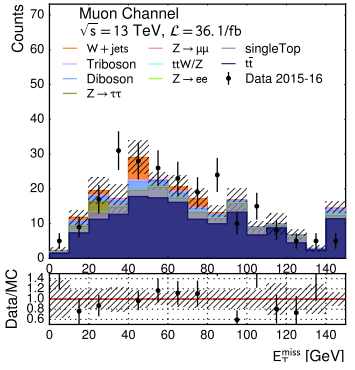

(c) $E_{\mathrm{T}}^{\mathrm{miss}}$

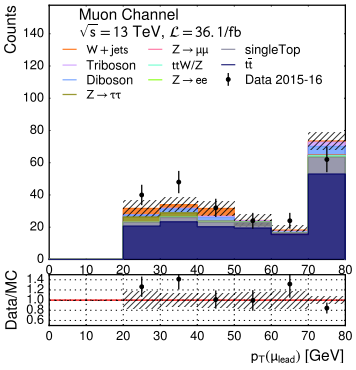

(d) p_{T} leading muon

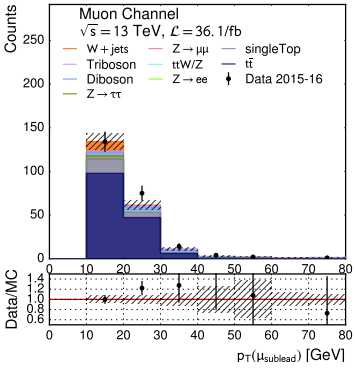

(e) p_{T} subleading muon

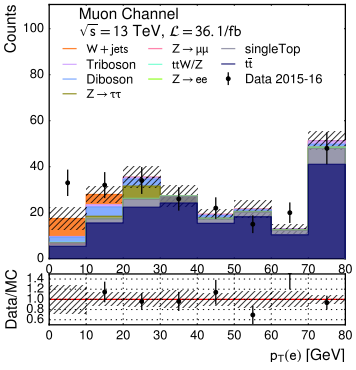

(f) p_{T} electron

Figure E.3.: *Muon Channel.* Comparison of agreement between data and MC backgrounds in `DM-3`. The error bands show combined statistical uncertainties.

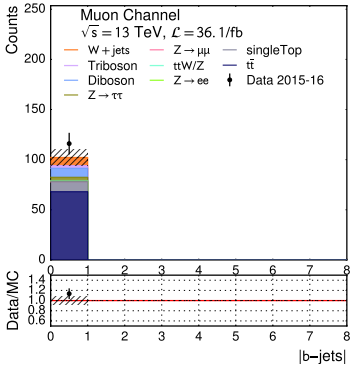

(a) Number of b jets

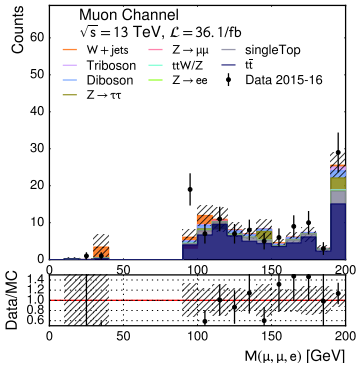

(b) $M(\ell, \ell, \ell')$

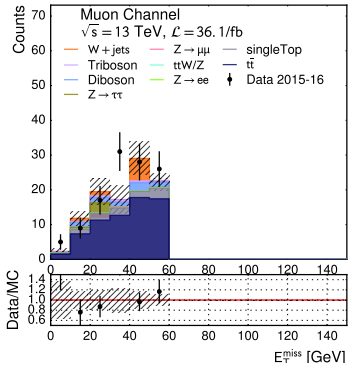

(c) $E_{\mathrm{T}}^{\mathrm{miss}}$

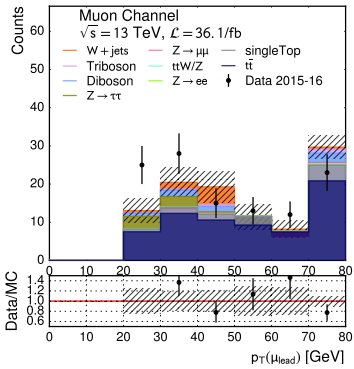

(d) p_{T} leading muon

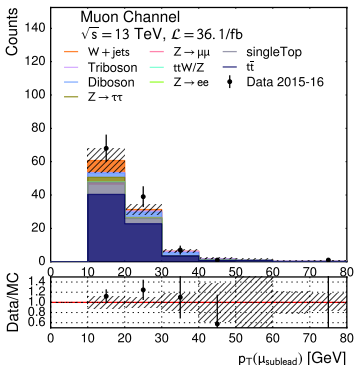

(e) p_{T} subleading muon

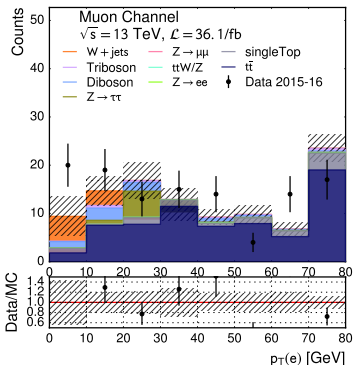

(f) p_{T} electron

Figure E.4.: *Muon Channel.* Comparison of agreement between data and MC backgrounds in `DM-4`. The error bands show combined statistical uncertainties.

E.2. Electron Channel

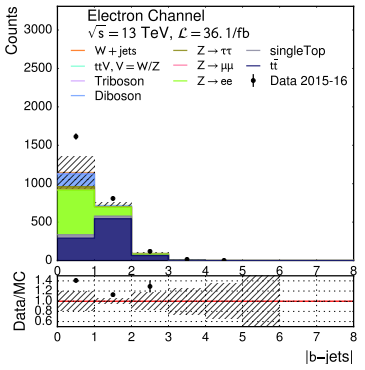

(a) Number of b jets

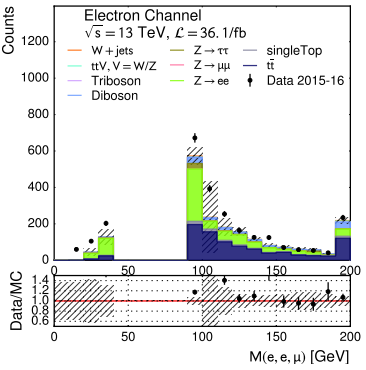

(b) $M(\ell, \ell, \ell')$

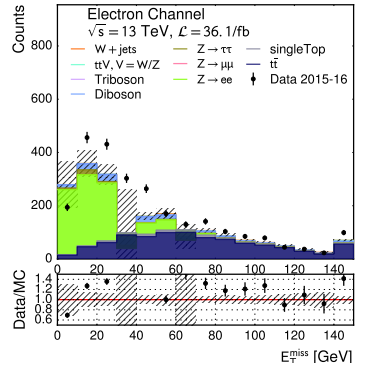

(c) $E_{\mathrm{T}}^{\mathrm{miss}}$

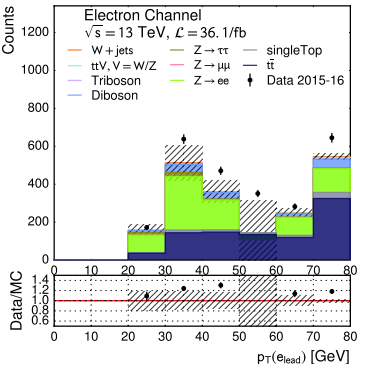

(d) p_{T} leading electron

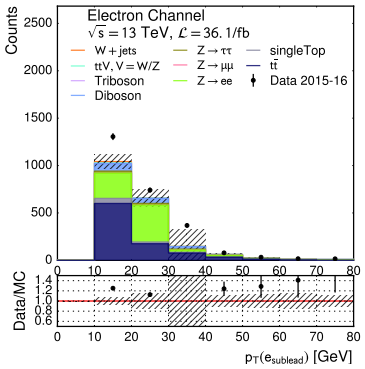

(e) p_{T} subleading electron

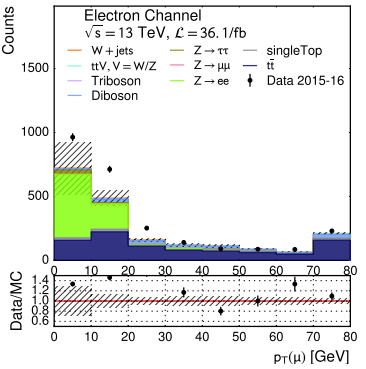

(f) p_{T} muon

Figure E.5.: *Electron Channel.* Comparison of agreement between data and MC backgrounds in `DM-1`. The error bands show combined statistical uncertainties.

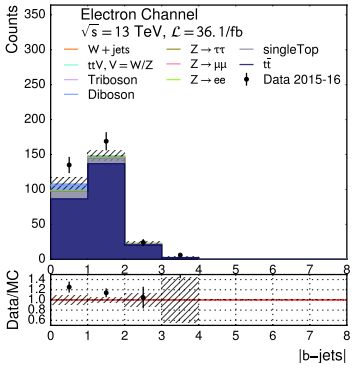

(a) Number of b jets

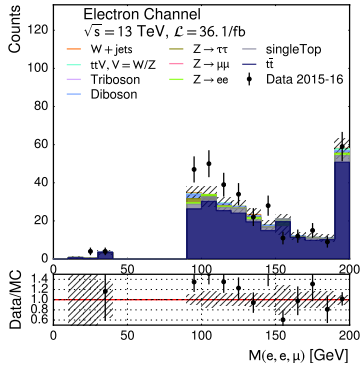

(b) $M(\ell, \ell, \ell')$

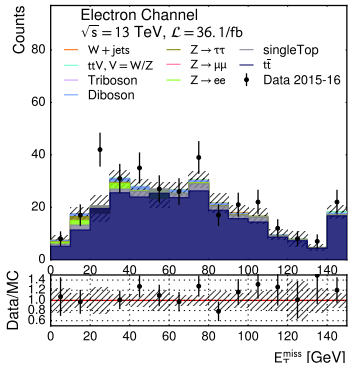

(c) $E_{\mathrm{T}}^{\mathrm{miss}}$

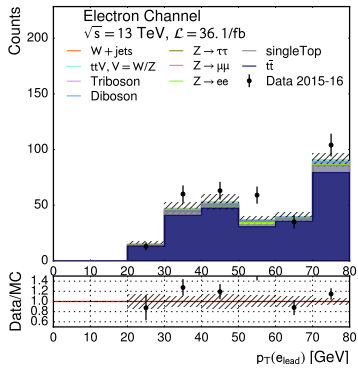

(d) p_{T} leading electron

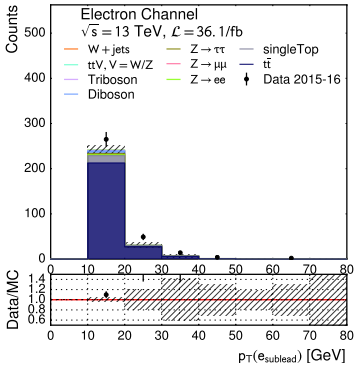

(e) p_{T} subleading electron

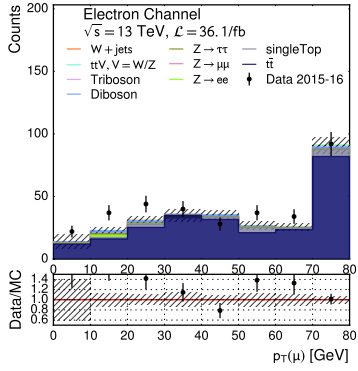

(f) p_{T} muon

Figure E.6.: *Electron Channel.* Comparison of agreement between data and MC backgrounds in `DM-2`. The error bands show combined statistical uncertainties.

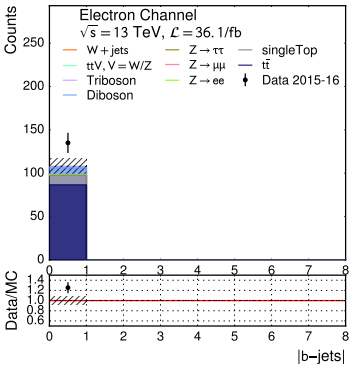

(a) Number of b jets

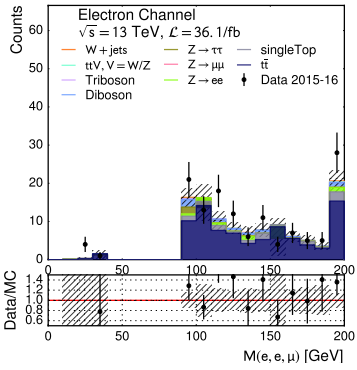

(b) $M(\ell, \ell, \ell')$

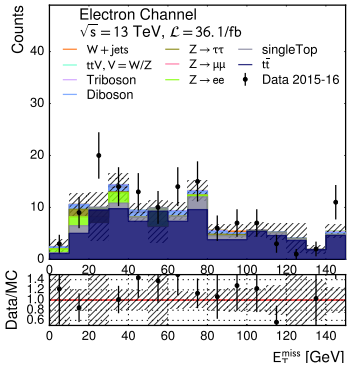

(c) $E_{\mathrm{T}}^{\mathrm{miss}}$

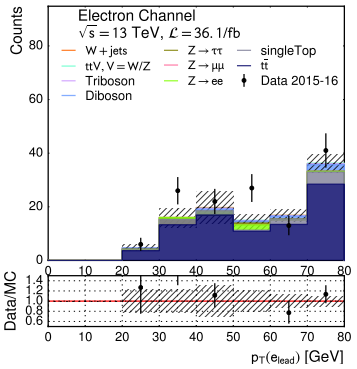

(d) p_{T} leading electron

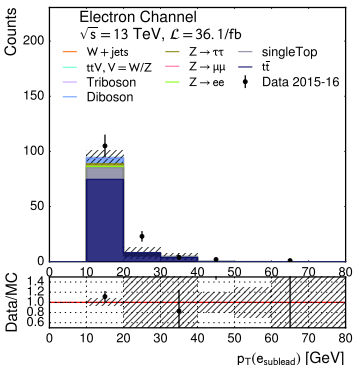

(e) p_{T} subleading electron

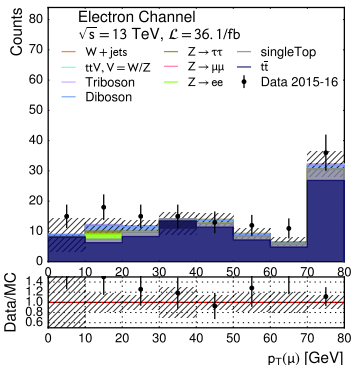

(f) p_{T} muon

Figure E.7.: *Electron Channel.* Comparison of agreement between data and MC backgrounds in `DM-3`. The error bands show combined statistical uncertainties.

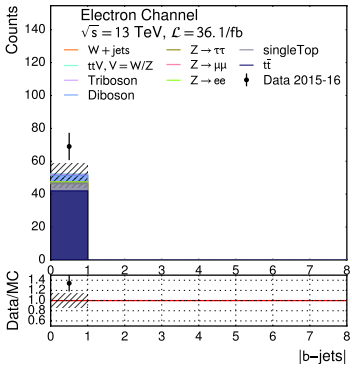

(a) Number of b jets

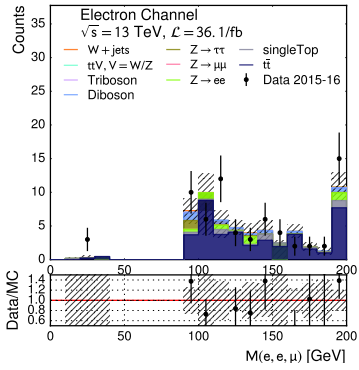

(b) $M(\ell, \ell, \ell')$

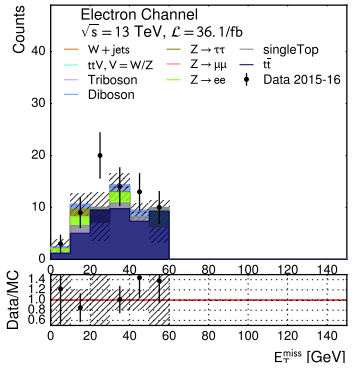

(c) $E_{\mathrm{T}}^{\mathrm{miss}}$

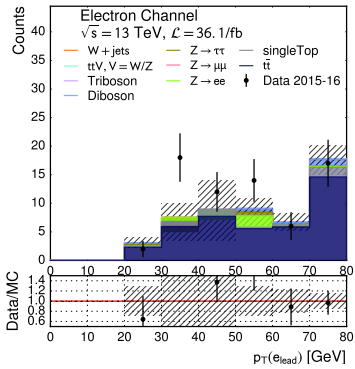

(d) p_{T} leading electron

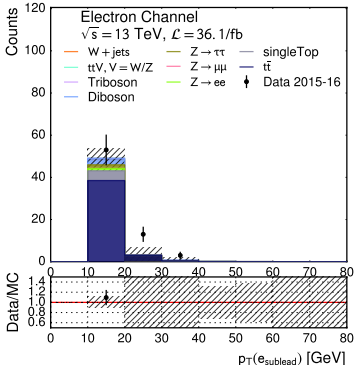

(e) p_{T} subleading electron

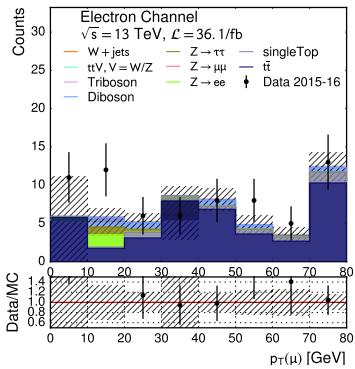

(f) p_{T} muon

Figure E.8.: *Electron Channel.* Comparison of agreement between data and MC backgrounds in `DM-4`. The error bands show combined statistical uncertainties.

List of Figures

List of Tables

Bibliography

[1] NobelPrize.org. Nobel Media AB 2018. *Niels Bohr - Banquet speech*. en. URL: https://www.nobelprize.org/prizes/physics/1922/bohr/speech/ (visited on 12/31/2018) (cit. on p. xi).

[2] Laurie M. Brown. "The idea of the neutrino". en. In: *Physics Today* 31.9 (Dec. 2008), p. 23. ISSN: 0031-9228. DOI: 10.1063/1.2995181. URL: https://physicstoday.scitation.org/doi/10.1063/1.2995181 (visited on 01/09/2019) (cit. on pp. 1, 75).

[3] C. L. Cowan et al. "Detection of the Free Neutrino: a Confirmation". en. In: *Science* 124.3212 (July 1956), pp. 103–104. ISSN: 0036-8075, 1095-9203. DOI: 10.1126/science.124.3212.103. URL: http://science.sciencemag.org/content/124/3212/103 (visited on 01/09/2019) (cit. on p. 1).

[4] The Super-Kamiokande Collaboration and Y. Fukuda et al. "Evidence for oscillation of atmospheric neutrinos". In: *Physical Review Letters* 81.8 (Aug. 1998). arXiv: hep-ex/9807003, pp. 1562–1567. ISSN: 0031-9007, 1079-7114. DOI: 10.1103/PhysRevLett.81.1562. URL: http://arxiv.org/abs/hep-ex/9807003 (visited on 12/29/2018) (cit. on pp. 1, 8).

[5] SNO Collaboration. "Measurement of the Total Active 8B Solar Neutrino Flux at the Sudbury Neutrino Observatory with Enhanced Neutral Current Sensitivity". In: *Physical Review Letters* 92.18 (May 2004). arXiv: nucl-ex/0309004. ISSN: 0031-9007, 1079-7114. DOI: 10.1103/PhysRevLett.92.181301. URL: http://arxiv.org/abs/nucl-ex/0309004 (visited on 12/29/2018) (cit. on pp. 1, 8).

[6] KamLAND Collaboration. "A High Sensitivity Search for $\bar{\nu}_e$'s from the Sun and Other Sources at KamLAND". In: *Physical Review Letters* 92.7 (Feb. 2004). arXiv: hep-ex/0310047. ISSN: 0031-9007, 1079-7114. DOI: 10.1103/PhysRevLett.92.071301. URL: http://arxiv.org/abs/hep-ex/0310047 (visited on 12/29/2018) (cit. on pp. 1, 8).

[7] Particle Data Group et al. "Review of Particle Physics". In: *Physical Review D* 98.3 (Aug. 2018), p. 030001. DOI: 10.1103/PhysRevD.98.030001. URL: https://link.aps.org/doi/10.1103/PhysRevD.98.030001 (visited on 12/29/2018) (cit. on pp. 1, 8, 9).

[8] Susanne Mertens. "Direct Neutrino Mass Experiments". In: *Journal of Physics: Conference Series* 718 (May 2016). arXiv: 1605.01579, p. 022013. ISSN: 1742-6588, 1742-6596. DOI: 10.1088/1742-6596/718/2/022013. URL: http://arxiv.org/abs/1605.01579 (visited on 01/09/2019) (cit. on p. 1).

[9] C. S. Wu et al. "Experimental Test of Parity Conservation in Beta Decay". en. In: *Physical Review* 105.4 (Feb. 1957), pp. 1413–1415. ISSN: 0031-899X. DOI: 10.1103/PhysRev.105.1413. URL: https://link.aps.org/doi/10.1103/PhysRev.105.1413 (visited on 10/24/2018) (cit. on pp. 1, 7).

[10] M. Goldhaber, L. Grodzins, and A. W. Sunyar. "Helicity of Neutrinos". en. In: *Physical Review* 109.3 (Feb. 1958), pp. 1015–1017. ISSN: 0031-899X. DOI: 10.1103/PhysRev.109.1015. URL: https://link.aps.org/doi/10.1103/PhysRev.109.1015 (visited on 10/24/2018) (cit. on pp. 1, 7).

[11] Manfred Lindner, Tommy Ohlsson, and Gerhart Seidl. "See-saw Mechanisms for Dirac and Majorana Neutrino Masses". en. In: *Physical Review D* 65.5 (Feb. 2002). arXiv: hep-ph/0109264. ISSN: 0556-2821, 1089-4918. DOI: 10.1103/PhysRevD.65.053014. URL: http://arxiv.org/abs/hep-ph/0109264 (visited on 01/09/2019) (cit. on p. 1).

[12] Takehiko Asaka and Mikhail Shaposhnikov. "The νMSM, Dark Matter and Baryon Asymmetry of the Universe". In: *Physics Letters B* 620.1-2 (July 2005). arXiv: hep-ph/0505013, pp. 17–26. ISSN: 03702693. DOI: 10.1016/j.physletb.2005.06.020. URL: http://arxiv.org/abs/hep-ph/0505013 (visited on 01/08/2019) (cit. on pp. 1, 11).

[13] Dmitry Gorbunov and Mikhail Shaposhnikov. "How to find neutral leptons of the nuMSM?" In: *Journal of High Energy Physics* 2007.10 (Oct. 2007). arXiv: 0705.1729, pp. 015–015. ISSN: 1029-8479. DOI: 10.1088/1126-6708/2007/10/015. URL: http://arxiv.org/abs/0705.1729 (visited on 06/29/2016) (cit. on pp. 1, 11, 34).

[14] W. Bonivento et al. "Proposal to search for heavy neutral leptons at the SPS". In: *arXiv preprint arXiv:1310.1762* (2013). URL: http://arxiv.org/abs/1310.1762 (visited on 05/10/2016) (cit. on pp. 1, 11).

[15] Eder Izaguirre and Brian Shuve. "Multilepton and Lepton Jet Probes of Sub-Weak-Scale Right-Handed Neutrinos". In: *Physical Review D* 91.9 (May 2015). arXiv: 1504.02470. ISSN: 1550-7998, 1550-2368. DOI: 10.1103/PhysRevD.91.093010. URL: http://arxiv.org/abs/1504.02470 (visited on 01/20/2016) (cit. on pp. 1, 34).

[16] John Dalton. "On the Absorption of Gases". In: *Memoirs of the Literary and Philosophical Society of Manchester* 1.2 (1805), pp. 271–286 (cit. on p. 3).

[17] The ATLAS Collaboration. "Observation of a new particle in the search for the Standard Model Higgs boson with the ATLAS detector at the LHC". In: *Physics Letters B* 716.1 (Sept. 2012). arXiv: 1207.7214, pp. 1–29. ISSN: 03702693. DOI: 10.1016/j.physletb.2012.08.020. URL: http://arxiv.org/abs/1207.7214 (visited on 01/09/2019) (cit. on p. 3).

[18] The CMS Collaboration. "Observation of a new boson at a mass of 125 GeV with the CMS experiment at the LHC". In: *Physics Letters B* 716.1 (Sept. 2012). arXiv: 1207.7235, pp. 30–61. ISSN: 03702693. DOI: 10.1016/j.physletb.2012.08.021. URL: http://arxiv.org/abs/1207.7235 (visited on 01/09/2019) (cit. on p. 3).

[19] MissMJ. *Standard Model of Elementary Particles.svg - Wikipedia, the free encyclopedia*. URL: https://en.wikipedia.org/wiki/File:Standard_Model_of_Elementary_Particles.svg (visited on 12/09/2014) (cit. on p. 4).

[20] *Creative Commons License*. Version CC BY 3.0. Free Software Foundation. URL: https://creativecommons.org/licenses/by/3.0/deed.en (cit. on pp. 4, 8).

[21] Mark Thomson. *Modern particle physics*. Cambridge, United Kingdom ; New York: Cambridge University Press, 2013. ISBN: 978-1-107-03426-6 (cit. on pp. 4–6, 10).

[22] Jeffrey Goldstone, Abdus Salam, and Steven Weinberg. "Broken Symmetries". In: *Physical Review* 127.3 (Aug. 1962), pp. 965–970. DOI: 10.1103/PhysRev.127.965. URL: https://link.aps.org/doi/10.1103/PhysRev.127.965 (visited on 01/08/2019) (cit. on p. 6).

[23] Antonio Pich. "Electroweak Symmetry Breaking and the Higgs Boson". en. In: *Acta Physica Polonica B* 47.1 (2016). arXiv: 1512.08749, p. 151. ISSN: 0587-4254, 1509-5770. DOI: 10.5506/APhysPolB.47.151. URL: http://arxiv.org/abs/1512.08749 (visited on 01/08/2019) (cit. on p. 6).

[24] E. Kh Akhmedov. "Neutrino physics". en. In: *arXiv:hep-ph/0001264* (Jan. 2000). arXiv: hep-ph/0001264. URL: http://arxiv.org/abs/hep-ph/0001264 (visited on 10/09/2018) (cit. on p. 6).

[25] Kismalac. *Neutrino mass hierarchy - Wikipedia, the free encyclopedia*. URL: https://commons.wikimedia.org/wiki/File:NeutrinoHierarchy.svg (visited on 12/29/2018) (cit. on p. 8).

[26] Palash B. Pal R. N. Mohapatra. *Massive Neutrinos in Physics and Astrophysics*. 3rd ed. World Scientific lecture notes in physics 72. World Scientific, 2004 (cit. on pp. 9, 11).

[27] Takehiko Asaka, Steve Blanchet, and Mikhail Shaposhnikov. "The νMSM, Dark Matter and Neutrino Masses". In: *Physics Letters B* 631.4 (Dec. 2005). arXiv: hep-ph/0503065, pp. 151–156. ISSN: 03702693. DOI: 10.1016/j.physletb.2005.09.070. URL: http://arxiv.org/abs/hep-ph/0503065 (visited on 03/10/2016) (cit. on p. 11).

[28] Oleg Ruchayskiy and Artem Ivashko. "Restrictions on the lifetime of sterile neutrinos from primordial nucleosynthesis". In: *Journal of Cosmology and Astroparticle Physics* 2012.10 (Oct. 2012). arXiv: 1202.2841, pp. 014–014. ISSN: 1475-7516. DOI: 10.1088/1475-7516/2012/10/014. URL: http://arxiv.org/abs/1202.2841 (visited on 01/08/2019) (cit. on p. 11).

[29] Oleg Ruchayskiy and Artem Ivashko. "Experimental bounds on sterile neutrino mixing angles". In: *Journal of High Energy Physics* 2012.6 (2012), pp. 1–27. URL: http://www.springerlink.com/index/g86k448710m6g241.pdf (visited on 07/10/2016) (cit. on pp. 11, 35).

[30] Sergey Alekhin et al. "A facility to Search for Hidden Particles at the CERN SPS: the SHiP physics case". In: *arXiv preprint arXiv:1504.04855* (2015). URL: http://arxiv.org/abs/1504.04855 (visited on 01/20/2016) (cit. on pp. 11, 13).

[31] CMS Collaboration. "Search for heavy neutral leptons in events with three charged leptons in proton-proton collisions at $\sqrt{s} = 13$ TeV". en. In: *Physical Review Letters* 120.22 (May 2018). arXiv: 1802.02965. ISSN: 0031-9007, 1079-7114. DOI: 10.1103/PhysRevLett.120.221801. URL: http://arxiv.org/abs/1802.02965 (visited on 01/08/2019) (cit. on pp. 11, 13).

[32] Marco Chianese et al. "Investigating two heavy neutral leptons neutrino seesaw mechanism at SHiP". en. In: *arXiv:1812.01994 [hep-ex, physics:hep-ph]* (Dec. 2018). arXiv: 1812.01994. URL: http://arxiv.org/abs/1812.01994 (visited on 01/08/2019) (cit. on p. 13).

[33] J. Schechter and J. W. F. Valle. "Neutrinoless double-β decay in SU(2)×U(1) theories". In: *Physical Review D* 25.11 (June 1982), pp. 2951–2954. DOI: 10.1103/PhysRevD.25.2951. URL: https://link.aps.org/doi/10.1103/PhysRevD.25.2951 (visited on 01/08/2019) (cit. on p. 12).

[34] Giovanni Benato. "Effective Majorana Mass and Neutrinoless Double Beta Decay". en. In: *The European Physical Journal C* 75.11 (Nov. 2015). arXiv: 1510.01089. ISSN: 1434-6044, 1434-6052. DOI: 10.1140/epjc/s10052-015-3802-1. URL: http://arxiv.org/abs/1510.01089 (visited on 01/08/2019) (cit. on p. 12).

[35] Takehiko Asaka, Shintaro Eijima, and Hiroyuki Ishida. "On neutrinoless double beta decay in the νMSM". en. In: *Physics Letters B* 762 (Nov. 2016). arXiv: 1606.06686, pp. 371–375. ISSN: 03702693. DOI: 10.1016/j.physletb.2016.09.044. URL: http://arxiv.org/abs/1606.06686 (visited on 01/08/2019) (cit. on p. 12).

[36] The ATLAS Collaboration. "The ATLAS Experiment at the CERN Large Hadron Collider". In: *Journal of Instrumentation* 3.08 (Aug. 2008), S08003–S08003. ISSN: 1748-0221. DOI: 10.1088/1748-0221/3/08/S08003. URL: http://stacks.iop.org/1748-0221/3/i=08/a=S08003?key=crossref.b2ac868e8992413771c34191a8138368 (visited on 12/18/2018) (cit. on pp. 15, 21–29).

[37] *The Collaboration*. Mar. 2015. URL: https://atlas.cern/discover/collaboration (visited on 12/17/2018) (cit. on p. 15).

[38] "ATLAS: Letter of intent for a general purpose p p experiment at the large hadron collider at CERN". In: (1992) (cit. on p. 15).

[39] Peilian Liu. "Expected performance of the upgrade ATLAS experiment for HL-LHC". In: *arXiv:1809.02181 [hep-ex, physics:physics]* (Sept. 2018). arXiv: 1809.02181. URL: http://arxiv.org/abs/1809.02181 (visited on 12/17/2018) (cit. on p. 15).

[40] O Brüning et al. *LHC design report. Vol. 1. Vol. 1*. en. OCLC: 723186985. Geneva: CERN, 2004. ISBN: 978-92-9083-224-9. DOI: 10.5170/CERN-2004-003-V-1. URL: https://cds.cern.ch/record/782076 (cit. on pp. 16–19).

[41] Esma Mobs. *The CERN accelerator complex*. en. July 2016. URL: https://cds.cern.ch/record/2197559 (visited on 12/13/2018) (cit. on p. 16).

[42] *LuminosityPublicResultsRun2 < AtlasPublic < TWiki*. URL: https://twiki.cern.ch/twiki/bin/view/AtlasPublic/LuminosityPublicResultsRun2#Pileup_Interactions_and_Data_Tak (visited on 01/01/2019) (cit. on pp. 17, 136).

[43] *Accelerating: Radiofrequency cavities | CERN*. URL: https://home.cern/science/engineering/accelerating-radiofrequency-cavities (visited on 12/17/2018) (cit. on p. 17).

[44] D. Boussard et al. "The LHC superconducting cavities". en. In: *Proceedings of the 1999 Particle Accelerator Conference (Cat. No.99CH36366)*. Vol. 2. New York, NY, USA: IEEE, 1999, pp. 946–948. ISBN: 978-0-7803-5573-6. DOI: 10.1109/PAC.1999.795409. URL: http://ieeexplore.ieee.org/document/795409/ (visited on 12/17/2018) (cit. on p. 17).

[45] "Niobium Films Produced by Magnetron Sputtering using an Ar-He Mixture as Discharge Gas". en. In: (1995), p. 5 (cit. on p. 17).

[46] Massimiliano Ferro-Luzzi, A. MacPherson, and H. Burkhardt. "Proceedings, LHC Lumi Days, LHC Workshop on LHC Luminosity Calibration: Geneva, Switzerland, 13-14 Jan, 2011". In: (2011) (cit. on p. 17).

[47] P. Lebrun. "Cryogenics for the Large Hadron Collider". en. In: *IEEE Transactions on Appiled Superconductivity* 10.1 (Mar. 2000), pp. 1500–1506. ISSN: 10518223. DOI: 10.1109/77.828526. URL: http://ieeexplore.ieee.org/document/828526/ (visited on 12/18/2018) (cit. on p. 19).

[48] *Detector & Technology*. June 2015. URL: https://atlas.cern/discover/detector (visited on 12/18/2018) (cit. on p. 19).

[49] ATLAS Collaboration. *ATLAS Insertable B-Layer Technical Design Report*. ATLAS-TDR-19. URL: https://cds.cern.ch/record/1291633 (cit. on pp. 19, 22).

[50] ATLAS Collaboration. *ATLAS Insertable B-Layer Technical Design Report Addendum*. ATLAS-TDR-19-ADD-1. URL: https://cds.cern.ch/record/1451888 (cit. on p. 19).

[51] *Computer generated image of the ATLAS inner detector*. URL: https://cds.cern.ch/images/CERN-GE-0803014-01 (visited on 12/18/2018) (cit. on p. 21).

[52] The ATLAS experiment. "ATLAS pixel detector electronics and sensors". en. In: *Journal of Instrumentation* 3.07 (July 2008), P07007–P07007. ISSN: 1748-0221. DOI: 10.1088/1748-0221/3/07/P07007. URL: http://stacks.iop.org/1748-0221/3/i=07/a=P07007?key=crossref.33a0c6c0aa4c5a065f2fd60b54d778ca (visited on 12/18/2018) (cit. on pp. 20, 21).

[53] Gunnar Lindström. "Radiation damage in silicon detectors". In: *Nuclear Instruments and Methods in Physics Research Section A: Accelerators, Spectrometers, Detectors and Associated Equipment*. Proceedings of the 9th European Symposium on Semiconductor Detectors: New Developments on Radiation Detectors 512.1 (Oct. 2003), pp. 30–43. ISSN: 0168-9002. DOI: 10.1016/S0168-9002(03)01874-6. URL: http://www.sciencedirect.com/science/article/pii/S0168900203018746 (visited on 12/18/2018) (cit. on p. 21).

[54] *A New Sub Detector for ATLAS*. June 2014. URL: https://atlas.cern/updates/atlas-news/new-sub-detector-atlas (visited on 12/18/2018) (cit. on p. 22).

[55] K. Hanagaki. "ATLAS silicon microstrip tracker operation". In: *Nuclear Instruments and Methods in Physics Research Section A: Accelerators, Spectrometers, Detectors and Associated Equipment*. 7th International ""Hiroshima"" Symposium on the Development and Application of Semiconductor Tracking Detectors 636.1, Supplement (Apr. 2011), S173–S176. ISSN: 0168-9002. DOI: 10.1016/j.nima.2010.04.105. URL: http://www.sciencedirect.com/science/article/pii/S0168900210009599 (visited on 12/18/2018) (cit. on p. 22).

[56] Bartosz Mindur. "ATLAS Transition Radiation Tracker (TRT): Straw tubes for tracking and particle identification at the Large Hadron Collider". In: *Nuclear Instruments and Methods in Physics Research Section A: Accelerators, Spectrometers, Detectors and Associated Equipment*. Proceedings of the Vienna Conference on Instrumentation 2016 845 (Feb. 2017), pp. 257–261. ISSN: 0168-9002. DOI: 10.1016/j.nima.2016.04.026. URL: http://www.sciencedirect.com/science/article/pii/S0168900216301905 (visited on 12/13/2018) (cit. on p. 23).

[57] Esben Klinkby. "Simulation of transition radiation and electron identification ability of the ATLASTRT". en. In: *Nuclear Instruments and Methods in Physics Research Section A: Accelerators, Spectrometers, Detectors and Associated Equipment* 706 (Apr. 2013), pp. 79–82. ISSN: 01689002. DOI: 10.1016/j.nima.2012.05.012. URL: https://linkinghub.elsevier.com/retrieve/pii/S0168900212004998 (visited on 01/02/2019) (cit. on p. 23).

[58] CERN. Geneva. LHC Experiments Committee and LHCC, eds. *ATLAS liquid-argon calorimeter: Technical Design Report*. eng. Technical Design Report ATLAS 2. Geneva: CERN, 1996. ISBN: 978-92-9083-090-0 (cit. on pp. 23–25).

[59] CERN. Geneva. LHC Experiments Committee and LHCC, eds. *ATLAS tile calorimeter: Technical Design Report*. eng. Technical Design Report ATLAS 3. Geneva: CERN, 1996. ISBN: 978-92-9083-091-7 (cit. on p. 24).

[60] J. Abdallah et al. *Design, Construction and Installation of the ATLAS Hadronic Barrel Scintillator-Tile Calorimeter*. eng. 2007 (cit. on p. 24).

[61] A. Artamonov et al. "The ATLAS forward calorimeters". In: *JINST* 3 (2008), P02010. DOI: 10.1088/1748-0221/3/02/P02010 (cit. on p. 25).

[62] A. Yamamoto et al. "The ATLAS central solenoid". In: *Nuclear Instruments and Methods in Physics Research Section A: Accelerators, Spectrometers, Detectors and Associated Equipment* 584.1 (Jan. 2008), pp. 53–74. ISSN: 0168-9002. DOI: 10.1016/j.nima.2007.09.047. URL: http://www.sciencedirect.com/science/article/pii/S0168900207020414 (visited on 12/19/2018) (cit. on p. 26).

[63] D. E. Baynham et al. "Engineering status of the superconducting end cap toroid magnets for the ATLAS experiment at LHC". In: *IEEE Transactions on Applied Superconductivity* 10.1 (Mar. 2000), pp. 357–360. ISSN: 1051-8223. DOI: 10.1109/77.828247 (cit. on p. 26).

[64] ATLAS Collaboration. "Performance of the ATLAS trigger system in 2015". In: *Eur. Phys. J. C* 77 (2017), p. 317. DOI: 10.1140/epjc/s10052-017-4852-3. arXiv: 1611.09661 [hep-ex] (cit. on p. 29).

[65] ATLAS Collaboration. "Measurement of $W^{\pm}$ and Z-boson production cross sections in pp collisions at $\sqrt{s} = 13$ TeV with the ATLAS detector". en. In: *Physics Letters B* 759 (Aug. 2016). arXiv: 1603.09222, pp. 601–621. ISSN: 03702693. DOI: 10.1016/j.physletb.2016.06.023. URL: http://arxiv.org/abs/1603.09222 (visited on 10/08/2018) (cit. on p. 33).

[66] Juan Helo, Martin Hirsch, and Sergey Kovalenko. "Heavy neutrino searches at the LHC with displaced vertices". In: *Physical Review D* 89.7 (Apr. 2014). arXiv: 1312.2900. ISSN: 1550-7998, 1550-2368. DOI: 10.1103/PhysRevD.89.073005. URL: http://arxiv.org/abs/1312.2900 (visited on 01/20/2016) (cit. on p. 34).

[67] Stefan Antusch, Eros Cazzato, and Oliver Fischer. "Displaced vertex searches for sterile neutrinos at future lepton colliders". In: *Journal of High Energy Physics* 2016.12 (Dec. 2016). arXiv: 1604.02420. ISSN: 1029-8479. DOI: 10.1007/JHEP12(2016)007. URL: http://arxiv.org/abs/1604.02420 (visited on 09/14/2017) (cit. on p. 34).

[68] Kyrylo Bondarenko et al. "Phenomenology of GeV-scale Heavy Neutral Leptons". en. In: *arXiv:1805.08567 [hep-ex, physics:hep-ph]* (May 2018). arXiv: 1805.08567. URL: http://arxiv.org/abs/1805.08567 (visited on 07/17/2018) (cit. on p. 34).

[69] Fabian A.J. Thiele. *cHNLdecay*. https://github.com/f-thiele/cHNLdecay. 2018 (cit. on p. 35).

[70] Torbjörn Sjöstrand et al. "An Introduction to PYTHIA 8.2". In: *Computer Physics Communications* 191 (June 2015). arXiv: 1410.3012, pp. 159–177. ISSN: 00104655. DOI: 10.1016/j.cpc.2015.01.024. URL: http://arxiv.org/abs/1410.3012 (visited on 12/03/2018) (cit. on pp. 35, 37).

[71] T. Gleisberg et al. "Event generation with SHERPA 1.1". en. In: (Nov. 2008). DOI: 10.1088/1126-6708/2009/02/007. URL: https://arxiv.org/abs/0811.4622 (visited on 12/03/2018) (cit. on pp. 35, 37).

[72] Simone Alioli et al. "A general framework for implementing NLO calculations in shower Monte Carlo programs: the POWHEG BOX". In: *Journal of High Energy Physics* 2010.6 (June 2010). arXiv: 1002.2581. ISSN: 1029-8479. DOI: 10.1007/JHEP06(2010)043. URL: http://arxiv.org/abs/1002.2581 (visited on 12/03/2018) (cit. on pp. 35, 37).

[73] Paolo Nason. "A New Method for Combining NLO QCD with Shower Monte Carlo Algorithms". In: *Journal of High Energy Physics* 2004.11 (Nov. 2004). arXiv: hep-ph/0409146, pp. 040–040. ISSN: 1029-8479. DOI: 10.1088/1126-6708/2004/11/040. URL: http://arxiv.org/abs/hep-ph/0409146 (visited on 12/03/2018) (cit. on pp. 35, 37).

[74] Stefano Frixione, Paolo Nason, and Carlo Oleari. "Matching NLO QCD computations with Parton Shower simulations: the POWHEG method". In: *Journal of High Energy Physics* 2007.11 (Nov. 2007). arXiv: 0709.2092, pp. 070–070. ISSN: 1029-8479. DOI: 10.1088/1126-6708/2007/11/070. URL: http://arxiv.org/abs/0709.2092 (visited on 12/03/2018) (cit. on pp. 35, 37).

[75] Torbjorn Sjostrand, Stephen Mrenna, and Peter Skands. "PYTHIA 6.4 Physics and Manual". en. In: *Journal of High Energy Physics* 2006.05 (May 2006). arXiv: hep-ph/0603175, pp. 026–026. ISSN: 1029-8479. DOI: 10.1088/1126-6708/2006/05/026. URL: http://arxiv.org/abs/hep-ph/0603175 (visited on 12/03/2018) (cit. on pp. 35, 37).

[76] Anders Ryd et al. "EvtGen: A Monte Carlo Generator for B-Physics". In: (2005) (cit. on pp. 35, 37).

[77] M. Chrzaszcz et al. "TAUOLA of tau lepton decays– framework for hadronic currens, matrix elements and anomalous decays". In: *arXiv:1609.04617 [hep-ph]* (Sept. 2016). arXiv: 1609.04617. URL: http://arxiv.org/abs/1609.04617 (visited on 12/03/2018) (cit. on pp. 35, 37).

[78] Piotr Golonka and Zbigniew Was. "PHOTOS Monte Carlo: A Precision tool for QED corrections in Z and W decays". In: *Eur.Phys.J.* C45 (2006), pp. 97–107. DOI: 10.1140/epjc/s2005-02396-4 (cit. on pp. 35, 37).

[79] Richard D. Ball et al. "Parton distributions with LHC data". In: *Nuclear Physics B* 867.2 (Feb. 2013). arXiv: 1207.1303, pp. 244–289. ISSN: 05503213. DOI: 10.1016/j.nuclphysb.2012.10.003. URL: http://arxiv.org/abs/1207.1303 (visited on 12/03/2018) (cit. on p. 37).

[80] Andy Buckley. "ATLAS Pythia 8 tunes to 7 TeV data". en. In: (), p. 2 (cit. on p. 37).

[81] Hung-Liang Lai et al. "New parton distributions for collider physics". In: *Physical Review D* 82.7 (Oct. 2010). arXiv: 1007.2241. ISSN: 1550-7998, 1550-2368. DOI: 10.1103/PhysRevD.82.074024. URL: http://arxiv.org/abs/1007.2241 (visited on 12/03/2018) (cit. on p. 37).

[82] J. Pumplin et al. "New Generation of Parton Distributions with Uncertainties from Global QCD Analysis". In: *Journal of High Energy Physics* 2002.07 (July 2002). arXiv: hep-ph/0201195, pp. 012–012. ISSN: 1029-8479. DOI: 10.1088/1126-6708/2002/07/012. URL: http://arxiv.org/abs/hep-ph/0201195 (visited on 12/03/2018) (cit. on p. 37).

[83] Peter Zeiler Skands. "Tuning Monte Carlo Generators: The Perugia Tunes". In: *Physical Review D* 82.7 (Oct. 2010). arXiv: 1005.3457. ISSN: 1550-7998, 1550-2368. DOI: 10.1103/PhysRevD.82.074018. URL: http://arxiv.org/abs/1005.3457 (visited on 12/03/2018) (cit. on p. 37).

[84] J. Alwall et al. "The automated computation of tree-level and next-to-leading order differential cross sections, and their matching to parton shower simulations". In: *Journal of High Energy Physics* 2014.7 (July 2014). arXiv: 1405.0301. ISSN: 1029-8479. DOI: 10.1007/JHEP07(2014)079. URL: http://arxiv.org/abs/1405.0301 (visited on 12/03/2018) (cit. on p. 37).

[85] The NNPDF Collaboration et al. "Parton distributions for the LHC Run II". en. In: (Oct. 2014). DOI: 10.1007/JHEP04(2015)040. URL: https://arxiv.org/abs/1410.8849 (visited on 12/03/2018) (cit. on p. 37).

[86] Glen Cowan. "Discovery sensitivity for a counting experiment with background uncertainty". en. In: (2012), p. 8. (Visited on 10/07/2018) (cit. on p. 36).

[87] "Never Lose a Holy Curiosity". In: *LIFE Magazine* (May 1955) (cit. on p. 39).

[88] T. Cornelissen et al. "Concepts, Design and Implementation of the ATLAS New Tracking (NEWT)". en. In: (Mar. 2007). URL: https://cds.cern.ch/record/1020106 (visited on 11/06/2018) (cit. on p. 39).

[89] Atlas Collaboration. "Muon reconstruction performance of the ATLAS detector in proton–proton collision data at $\sqrt{s}$=13 TeV". en. In: (Mar. 2016). DOI: 10.1140/epjc/s10052-016-4120-y. URL: https://arxiv.org/abs/1603.05598 (visited on 11/06/2018) (cit. on pp. 39, 40).

[90] The ATLAS collaboration. "Electron efficiency measurements with the ATLAS detector using the 2015 LHC proton-proton collision data". In: (2016) (cit. on pp. 41–43).

[91] W. Lampl et al. "Calorimeter Clustering Algorithms : Description and Performance". en. In: *CERN Document Server* (Apr. 2008). URL: https://cds.cern.ch/record/1099735 (visited on 11/06/2018) (cit. on p. 41).

[92] T. G. Cornelissen et al. "The global χ^2 track fitter in ATLAS". en. In: *Journal of Physics: Conference Series* 119.3 (2008), p. 032013. ISSN: 1742-6596. DOI: 10.1088/1742-6596/119/3/032013. URL: http://stacks.iop.org/1742-6596/119/i=3/a=032013 (visited on 11/06/2018) (cit. on p. 41).

[93] T. Cornelissen et al. "The new ATLAS track reconstruction (NEWT)". en. In: *Journal of Physics: Conference Series* 119.3 (2008), p. 032014. ISSN: 1742-6596. DOI: 10.1088/1742-6596/119/3/032014. URL: http://stacks.iop.org/1742-6596/119/i=3/a=032014 (visited on 11/06/2018) (cit. on p. 41).

[94] "Jet Calibration and Systematic Uncertainties for Jets Reconstructed in the ATLAS Detector at $\sqrt{s} = 13$ TeV". eng. In: (2015). Ed. by The ATLAS collaboration, p. 29 (cit. on p. 42).

[95] "Tagging and suppression of pileup jets with the ATLAS detector". en. In: *CERN Document Server* (May 2014). URL: https://cds.cern.ch/record/1700870 (visited on 11/07/2018) (cit. on p. 42).

[96] Michela Paganini. "Machine Learning Algorithms for b-Jet Tagging at the ATLAS Experiment". In: *J.Phys.Conf.Ser.* 1085.4 (Oct. 2018), p. 042031. DOI: 10.1088/1742-6596/1085/4/042031 (cit. on p. 42).

[97] "Expected performance of missing transverse momentum reconstruction for the ATLAS detector at $\sqrt{s} = 13$ TeV". en. In: *CERN Document Server* (July 2015). URL: https://cds.cern.ch/record/2037700 (visited on 11/07/2018) (cit. on p. 42).

[98] Michael T. Raggo and Chet Hosmer. *Data Hiding: Exposing Concealed Data in Multimedia, Operating Systems, Mobile Devices and Network Protocols*. en. Google-Books-ID: yMw9if8ybp0C. Newnes, Dec. 2012. ISBN: 978-1-59749-741-1 (cit. on p. 45).

[99] Kyle Cranmer. "Practical Statistics for the LHC". en. In: *arXiv:1503.07622 [hep-ex, physics:physics]* (Mar. 2015). arXiv: 1503.07622. URL: http://arxiv.org/abs/1503.07622 (visited on 01/04/2019) (cit. on pp. 80, 81, 83, 121).

[100] F. James and M. Roos. "Minuit - a system for function minimization and analysis of the parameter errors and correlations". In: *Computer Physics Communications* 10.6 (Dec. 1975), pp. 343–367. ISSN: 0010-4655. DOI: 10.1016/0010-4655(75)90039-9. URL: http://www.sciencedirect.com/science/article/pii/0010465575900399 (visited on 01/05/2019) (cit. on p. 80).

[101] *MINUIT2*. URL: https://root.cern.ch/root/html/MATH_MINUIT2_Index.html (visited on 01/05/2019) (cit. on p. 80).

[102] S. S. Wilks. "The Large-Sample Distribution of the Likelihood Ratio for Testing Composite Hypotheses". EN. In: *The Annals of Mathematical Statistics* 9.1 (Mar. 1938), pp. 60–62. ISSN: 0003-4851, 2168-8990. DOI: 10.1214/aoms/1177732360. URL: https://projecteuclid.org/euclid.aoms/1177732360 (visited on 01/05/2019) (cit. on p. 82).

[103] Gioacchino Ranucci. "The profile likelihood ratio and the look elsewhere effect in high energy physics". en. In: *Nuclear Instruments and Methods in Physics Research Section A: Accelerators, Spectrometers, Detectors and Associated Equipment* 661.1 (Jan. 2012), pp. 77–85. ISSN: 01689002. DOI: 10.1016/j.nima.2011.09.047. URL: https://linkinghub.elsevier.com/retrieve/pii/S0168900211018420 (visited on 01/05/2019) (cit. on p. 82).

[104] Alexander L. Read. "Modified frequentist analysis of search results (The CL(s) method)". In: (2000), pp. 81–101 (cit. on p. 82).

[105] ATLAS Collaboration. "Jet energy scale measurements and their systematic uncertainties in proton-proton collisions at $\sqrt{s} = 13$ TeV with the ATLAS detector". en. In: *Physical Review D* 96.7 (Oct. 2017). arXiv: 1703.09665. ISSN: 2470-0010, 2470-0029. DOI: 10.1103/PhysRevD.96.072002. URL: http://arxiv.org/abs/1703.09665 (visited on 01/03/2019) (cit. on p. 83).

[106] Robert D. Cousins, James T. Linnemann, and Jordan Tucker. "Evaluation of three methods for calculating statistical significance when incorporating a systematic uncertainty into a test of the background-only hypothesis for a Poisson process". In: *Nuclear Instruments and Methods in Physics Research Section A: Accelerators, Spectrometers, Detectors and Associated Equipment* 595.2 (Oct. 2008), pp. 480–501. ISSN: 0168-9002. DOI: 10.1016/j.nima.2008.07.086. URL: http://www.sciencedirect.com/science/article/pii/S0168900208010255 (visited on 01/04/2019) (cit. on p. 83).

[107] Ruth Moore. *Niels Bohr: The Man, His Science, and the World They Changed*. English. Cambridge, Mass: The MIT Press, Mar. 1985. ISBN: 978-0-262-63101-3 (cit. on p. 115).

[108] Ian Sample. "The god of small things". en-GB. In: *The Guardian* (Nov. 2007). ISSN: 0261-3077. URL: https://www.theguardian.com/science/2007/nov/17/sciencenews.particlephysics (visited on 01/09/2019) (cit. on p. 135).

[109] ATLAS Collaboration. "Jet energy resolution in proton-proton collisions at sqrt(s) = 7 TeV recorded in 2010 with the ATLAS detector". en. In: *The European Physical Journal C* 73.3 (Mar. 2013). arXiv: 1210.6210. ISSN: 1434-6044, 1434-6052. DOI: 10.1140/epjc/s10052-013-2306-0. URL: http://arxiv.org/abs/1210.6210 (visited on 01/03/2019) (cit. on p. 155).

Acronyms

νMSM Neutrino Minimal Standard Model. 1, 3, 11, 12

pp proton-proton. 12, 16, 20, 25

CR Control Region. 75, 77, 78, 84, 85, 88, 90, 91, 98, 100, 105, 115–120, 122, 137, 158

ER Estimation Region. 77, 80, 84, 96, 117

SR Signal Region. 63, 64, 75, 77, 105, 106, 115–121, 137, 157–160

ALICE A Large Ion Collision Experiment. 15

ATLAS A Toroidal LHC ApparatuS. 1–3, 15, 17, 19–21, 23, 24, 26, 27, 30–32, 34–36, 39–44, 48, 70, 76, 81–83, 116, 121, 137, 138, 157, 158, 161

ATLFAST ATLAS Fast Simulation. 36

BOOSTER Proton Synchrotron Booster. 16

BSM Beyond the Standard Model. 9

CERN European Organization for Nuclear Research. 15, 16

CMS Compact Muon Solenoid. 1, 3, 12, 13, 15, 33, 121, 123, 124

CSC Cathode-strip Chamber. 28, 29

CST Calorimeter-based Soft Term. 43

DAQ Data Aquisition System. 30

DELPHI Detector with Lepton, Photon and Hadron Identification. 1, 33, 35, 121, 123, 124

EID Electron Identification Criteria. 41, 42

EM calorimeter Electromagnetic Calorimeter. 24, 25, 30

FCal Forward Calorimeter. 24–26

HEC Hadronic End-cap Calorimeter. 24, 25

HL-LHC high-luminosity phase of the LHC. 15

HLT High Level Trigger. 30, 47, 49, 50, 60, 62

HNL Heavy Neutral Lepton. iii, v, 1–3, 10–13, 22, 31–35, 45, 51, 54, 61, 70, 83, 85, 90, 91, 98, 100, 115, 121, 122, 137, 138, 153

IBL Insertable B-Layer. 20, 22, 42

ID Inner Detector. 19–24, 26, 30, 40, 43, 83

IP Impact Parameter. 40, 54–58, 65–73

JER Jet Energy Resolution. 157, 158

JES Jet Energy Scale. 42

JVT Jet Vertex Tagger. 42

L1 Level-1 Trigger. 30, 47, 85

LAr liquid-argon. 20, 24–26

LEP Large Electron-Positron Collider. 17

LHC Large Hadron Collider. iii, v, 1, 15–20, 23, 30, 34, 138, 175

LHC-b Large Hadron Collider beauty. 15

LINAC2 Linear Accelerator. 16

LLH Log-Likelihood. 77, 80, 83, 90, 91, 98, 100, 120

MC Monte Carlo. 31, 35–37, 43, 46, 49–55, 59–63, 65, 69–71, 76, 77, 81–85, 91, 96, 100, 115, 117, 120, 137, 138, 153, 161–169

MDT Monitored Drift Tube Chamber. 28, 29

MS Muon Spectrometer. 19, 20, 27–30, 39, 40, 83

NF Normalization Factor. 82, 85, 88–91, 98–100, 115–117, 122–124, 131, 132, 134, 135, 137

nLLH negative Log-Likelihood. 80

NP Nuisance Parameter. 127, 128

PDF Probability Density Function. 32, 77, 80, 115, 120

PIX Pixel Detector. 20, 39, 41

PMNS Pontecorvo-Maki-Nakagawa-Sakata. 8

PMT Photomultiplier Tube. 25

PS Proton Synchrotron. 16

QFT Quantum Field Theory. 4

QRL Cryogenic Distribution Line. 19

RF radiofrequency. 17, 19

RPC Resistive plate Chamber. 29, 30

SCT Semiconductor Tracker. 20, 22, 39, 41

SF Scale Factor. 44, 46, 47, 70, 71, 82

SM Standard Model. iii, 1, 3–9, 11, 42, 76, 77, 81, 84, 86, 137

SPS Super Proton Synchrotron. 16

TGC Thin Gap Chamber. 29, 30

TRT Transition Radiation Tracker. 20, 23, 41

TST Track-based Soft Term. 43

WP Working Point. 40, 42, 43, 51–53, 61–64, 70, 82, 139–142

Index